2015

Crystal plasticity finite element method simulation of high pressure torsion

Peitang Wei
University of Wollongong

Crystal Plasticity Finite Element Method Simulation of High Pressure Torsion

A thesis submitted in fulfilment of the requirements
for the award of the degree of

Doctor of Philosophy

from

University of Wollongong

by

Peitang Wei
BEng, MEng

School of Mechanical, Materials and Mechatronic Engineering
Faculty of Engineering & Information Sciences

March, 2015

Declaration

I, Peitang Wei, declare that this thesis, submitted in fulfillment of the requirements for the award of Doctor of Philosophy, in the school of Mechanical, Materials and Mechatronic Engineering, University of Wollongong, Australia, is wholly my own work unless otherwise referenced or acknowledged, and has not been submitted for qualifications at any other university or academic institution.

Peitang Wei

March 2015

Acknowledgements

I wish to express my sincere gratitude to my supervisors Professor Anh Kiet Tieu (University of Wollongong), Associate/Professor Cheng Lu (University of Wollongong) and Professor Chao Lin (Chongqing University, China) for their excellent supervision and guidance, continuous encouragement and invaluable advice during my PhD study. All my supervisors' implicit trust in my research abilities not only allowed me to freely pursue my goals, but also gave me an opportunity to learn how to manage time and allocate resources. Without their help I could never have finished this work.

I am grateful to Dr. Hongtao Zhu, Dr. Guanyu Deng, Dr. Lihong Su, Dr. Yong Sun, Dr. Xuan Zheng, Dr. Kuiyu Cheng and Dr. Huaiju Liu for their invaluable advice on my study. My thanks are also extended to Linqing Pei, Xing Zhao, Ning Kong, Jie Zhang, Hui Wang and Liang Zhang. I enjoyed all the coffees, dinners, movies and trips together with you. I feel very lucky to have you guys during my study in Wollongong and I will never forget the time we spent together. Special thanks go to Dr. Min Su for your great help and continuous encouragement.

Finally, I would like to offer my heartfelt thanks to my parents, parents-in-law, my sister, my wife and my son for their continued love, understanding and devotion. Their encouragements always kept me going forward during my study.

Thank you all,

Peitang

List of Publications

(1) **Peitang Wei**, Cheng Lu, Kiet Tieu, Guanyu Deng, Haixia Wang, and Ning Kong. Finite element analysis of high pressure torsion. Steel Research International. 2013, Vol 84, issue (12): 1246-1251.

(2) **Peitang Wei**, Cheng Lu, Kiet Tieu, Guanyu Deng. A study of plastic deformation behavior during high pressure torsion process by crystal plasticity finite element simulation. IOP Conf. Series: Materials Science and Engineering 63 (2014) 012045

(3) **Peitang Wei**, Cheng Lu, Kiet Tieu, Guanyu Deng and Jie Zhang. Modelling of texture evolution of aluminium single crystal in high pressure torsion by crystal plasticity finite element method. Material Research Innovation. (Under review)

(4) Guanyu Deng, Anh Kiet Tieu, Lihong Su, Cheng Lu, **Peitang Wei**, Xianghua Liu. Crystal Plasticity FEM Study on the Influence of Crystallographic Orientation in Copper Single Crystals Subjected to Equal Channel Angular Pressing. Steel Research International. 2013, Vol 84, issue (12): 1258-1266.

Abstract

Severe plastic deformation (SPD) has been the subject of intensive investigations in recent years because of the unique physical and mechanical properties of ultrafine grained (UFG) materials fabricated by this technique. High pressure torsion (HPT) is one of the most widely used SPD techniques. The main aim of HPT processing is to produce extreme grain refinement and the ensuing strengthening of the processed material. There is no longer any doubt that this is achievable with most malleable and even with many hard-to-deform materials, and innumerable experimental results documented in the literatures are a convincing testimony to that. Despite this body of experimental evidence, the deformation mechanisms during the HPT process, which are pivotal in designing the routes to property improvement, are far from being understood. Up to now, a few numerical simulations have been reported. However, these simulations only gave reasonably satisfactory predictions due to the simplifications and shortcomings of the developed models, and are definitely insufficient to fully understand the deformation mechanisms of the HPT process. Therefore, a systematic study on modeling of plastic deformation behavior, texture evolution and grain refinement of the HPT process is essential.

In the present study, a three-dimensional crystal plasticity finite element method (CPFEM) model has been developed to offer a systematic understanding of the plastic deformation behavior, texture evolutions and grain fragmentation of single crystals during the full scale HPT process. The developed CPFEM model has been validated by comparing the simulation results with the experimental observations.

Texture simulation has been carried out for HPT of nickel single crystal which has the initial (001) and (111) orientation. It has been seen that different crystallographic orientations rotated towards different ideal shear texture components with respect to the torsion deformation in HPT. During this process, lattice rotated predominately along the radial direction. While for the initial Cube orientation of (001) nickel single crystal, a noticeable amount of rotation angles around the tangential direction and axial direction have also been observed. Moreover, lattice

did not rotate uniformly during the HPT process, the rotation rate converged when approaching the main components of the ideal shear texture but it diverged while rotated away from the ideal texture components. In addition, for HPT deformation, the material spin was usually larger than other SPD processes due to severe shear deformation. The material spin requirement could be met by either lattice spin or plastic rotation rate. For dominant slip condition, material spin could be mainly or even fully satisfied by plastic rotation rate and thus the lattice spin was very small or even dropped to zero, which led to relatively limited orientation change or even stable orientation with increasing HPT deformation; while for multiple slip condition, each of the slip systems of interest produced a rotation component, the resultant of which was the overall glide rotation rate was small, the lattice must rotate to generate large lattice spin to satisfy the material spin requirement, which led to significant orientation changes. When the resulting overall plastic rotation rate was zero, the lattice spin was equal to the material spin so that the lattice rotated simply in the direction of the imposed material rotation. Dominant slip and multiple slip competed against each other to minimize the total energy consumed in the system, which is assumed to be responsible for texture evolution of nickel single crystal during the HPT process.

Grain refinement simulation of nickel single crystal has also been carried out. The predicted grain maps were capable of reflecting the prominent characteristics associated with grain refinement during the HPT process. It has been found that there were mainly two reasons that were responsible for the grain fragmentation of the nickel single crystal: one was the difference in lattice rotation rate along the radial direction which is the direction of predominant lattice rotation in HPT. The occurrence of divergence in R-axis rotation rate was because lattice did not rotate uniformly with respect to the increasing plastic deformation in HPT; another one was the divergence of rotation angles along the tangential direction, even though much smaller than the R-axis rotations, could also contribute to the formation of grains surrounded by boundaries with high misorientation.

Plastic deformation behavior along the circumferential direction of the initial (001) aluminum single crystal during HPT has also been simulated. It has been found that at the early stage of

deformation, Mises stress and critical resolved shear stress (CRSS) were not homogenously distributed along the circumferential direction and a four-fold-symmetry distribution pattern occurred on the sample surface. Because of the variations in the initial orientation along the circular direction of the disk-shaped single crystal, the introduced plastic strain activated different slip systems at different circumferential positions. Circumferential positions deformed by different slip modes resulted in differences in lattice rotations and crystallographic orientation changes and showed different mechanical behaviors, which is assumed to be responsible for the development of plastic deformation heterogeneity along the circumferential direction of the sample. For higher strains, the non-homogenous distribution of CRSS along the circumferential direction became weak. This was mainly due to that some crystals has almost reached the saturate level of strain hardening while some crystals underwent further hardening. For even higher strains, such a heterogeneous distribution of the CRSS grew even weaker due to the gradual expansion of the saturated strain hardening region during the HPT process.

Notations

AD	Axial direction
AFSE	axisymmetric forward spiral extrusion
ARB	Accumulative roll bonding
a_1	Constant for $f_{\alpha\beta}$ (no junction)
a_2	Constant for $f_{\alpha\beta}$ (Hirth lock)
a_3	Constant for $f_{\alpha\beta}$ (coplanar junction)
a_4	Constant for $f_{\alpha\beta}$ (glissile junction)
a_5	Constant for $f_{\alpha\beta}$ (sessile junction)
$\boldsymbol{B}$	Symmetrical part of the coefficient matrix of velocity gradient
BCC	Body centered cubic
$\boldsymbol{C}$	Fourth order tensor of the elastic modulus
$\boldsymbol{C}_0$	Tensor of elastic moduli
C_i	Deformation inhomogeneity index
CEC	Cyclic extrusion compression
CPFEM	Crystal plasticity finite element method
CRSS	Critical resolved shear stress
$\boldsymbol{D}$	Stretch rate tensor
$\boldsymbol{D}^*$	Elastic part of the stretch rate tensor
$\boldsymbol{D}_{\mathrm{L}}$	Rate of the elastic stretching in the lattice coordinate system
$\boldsymbol{D}^{\mathrm{P}}$	Plastic part of the stretch rate tensor
$\delta\boldsymbol{D}$	Virtual form of the rate of deformation
$\boldsymbol{E}$	Grain strain tensor

$\dot{\boldsymbol{E}}$	Rate of Grain strain tensor
EBSD	Electron backscatter diffraction
ECAE	Equal channel angular extrusion
ECAP	Equal channel angular pressing
ED	Extrusion direction
$\boldsymbol{F}$	Total deformation gradient
$\dot{\boldsymbol{F}}$	Time derivative of the total deformation gradient
$\boldsymbol{F}^{*}$	Elastic part of the total deformation gradient
$\dot{\boldsymbol{F}}^{*}$	Time derivative of the total deformation gradient
$\boldsymbol{F}^{*-1}$	Inverse of $\boldsymbol{F}^{*}$
$\boldsymbol{F}^{\mathrm{P}}$	Plastic part of the total deformation gradient
$\dot{\boldsymbol{F}}^{\mathrm{P}}$	Time derivative of the plastic part of the total deformation gradient
$\boldsymbol{F}^{\mathrm{P}-1}$	Inverse of $\boldsymbol{F}^{\mathrm{P}}$
$\boldsymbol{F}^{(\alpha)\mathrm{P}}$	Contribution of slip system α to $\boldsymbol{F}^{\mathrm{P}}$
$\boldsymbol{F}^{\mathrm{T}}$	Transposition of $\boldsymbol{F}$
FCC	Face centered cubic
FSW	Frictional stir welding
$f_{\alpha\beta}$	Strength of a particular slip interaction between two slip systems α and β
$\boldsymbol{G}$	Skewed part of the coefficient matrix of velocity gradient
g	Orientation matrix
$\boldsymbol{H}$	Fourth order hardening parameter tensor
HAGB	High angle grain boundary
HCP	Hexagonal close packed
HPT	High pressure torsion

HPTT	High pressure tube twisting
$h_{\alpha\beta}$	Instantaneous hardening moduli
h_{s}	Hardening modulus during easy glide
h_0	Hardening modulus just after the initial yield
$\boldsymbol{I}$	Second order unit tensor
$\boldsymbol{K}$	Jacobian matrix
$\boldsymbol{L}$	Velocity gradient
$\boldsymbol{L}^*$	Elastic part of velocity gradient
$\boldsymbol{L}^{\mathrm{P}}$	Plastic part of velocity gradient
$\boldsymbol{L}^{\mathrm{T}}$	Transposition of $\boldsymbol{L}$
LAGB	Low angle grain boundary
MDE	Multiple direct extrusion
MDF	Multidirectional forging
$\boldsymbol{m}^{(\alpha)}$	Normal vector of slip plane of α-th slip system in the current configuration
$\boldsymbol{m}_0^{(\alpha)}$	Normal vector of slip plane of α-th slip system in the reference configuration
N	Number of active slip systems
N	Shape functions
n	Rate sensitive exponent
$\boldsymbol{p}^{(\alpha)}$	Symmetrical part of Schmid factor
q	Latent hardening parameter
$\boldsymbol{q}^{(\alpha)}$	Asymmetrical part of Schmid factor
$\boldsymbol{R}$	Orthogonal rotation tensor
RD	Radial direction

SPD	Severe plastic deformation
SSE	simple shear extrusion
$\boldsymbol{s}^{(\alpha)}$	Slip direction vector of slip plane of α-th slip system in the current configuration
$\boldsymbol{s}_0^{(\alpha)}$	Slip direction vector of slip plane of α-th slip system in the reference configuration
$\boldsymbol{s}^{(\alpha)} \otimes \boldsymbol{m}^{(\alpha)}$	Schmid factor
TD	Tangential direction
TE	Twist extrusion
THPS	Tube high pressure shearing
Δt	Time increment
$\boldsymbol{t}_0$	Kirchhoff stress in the reference configuration
$\dot{\boldsymbol{t}}$	Material rate of Kirchhoff stress
$\dot{\boldsymbol{t}}_1^*$	Rate of the Kirchhoff stress in the intermediate configuration
$\dot{\boldsymbol{t}}_{\mathrm{L}}$	Material rate of the Kirchhoff stress in the lattice coordinate system
$\nabla \boldsymbol{t}$	Kirchhoff stress
$\nabla^* \boldsymbol{t}$	Jaumann rate of Kirchoff stress
$\boldsymbol{U}$	Right stretch tensor
UFG	Ultra-fine grained
$\boldsymbol{V}$	Left stretch tensor
$\boldsymbol{v}$	Velocity of the material point
$\boldsymbol{v}^{\mathrm{n}}$	Nodal velocities
$\delta\boldsymbol{v}$	kinematically admissible virtual velocity field
VPSC	Visco-plastic self-consistent

$\boldsymbol{X}$	Position of material point in the initial configuration
$\boldsymbol{x}$	Position of material point in the current configuration
$\otimes$	Tensor product
α	Slip system α
β	Slip system β
$\gamma^{(\alpha)}$	Shear strain of slip system α
$\gamma_0^{(\alpha)}$	Reference value of shear strain of slip system α
$\dot{\gamma}^{(\alpha)}$	Shear rate of slip system α
$\dot{\gamma}_0^{(\alpha)}$	Reference value of shear rate of slip system α
$\tau^{(\alpha)}$	Resolved shear stress of slip system α
$\tau_{\mathrm{c}}^{(\alpha)}$	Current strength of slip system α
τ_1	Breakthrough stress where large plastic flow begins
τ_0	Initial critical resolved shear stress
$\boldsymbol{\sigma}$	Cauchy stress
$\varphi 1$, φ, $\varphi 2$	Three Euler angles
$\boldsymbol{\Omega}$	Spin tensor
$\boldsymbol{\Omega}^*$	Elastic part of spin tensor
$\boldsymbol{\Omega}^{\mathrm{P}}$	Plastic part of spin tensor

List of Tables

List of Figures

Chapter 1 Introduction

Interest in the use of severe plastic deformation (SPD) to produce ultra-fine grained (UFG) structure of different materials has developed a great deal over the last two decades [1–5]. UP to now, several different SPD processing techniques are available. These include equal channel angular pressing (ECAP) [6–9], high pressure torsion (HPT) [10–14] and accumulative roll bonding (ARB) [15–19] and so on. Compared with the other SPD methods, the most important advantage of the HPT process is that extremely high shear stain can be continuously achieved via simple means [10]. Due to its incomparable straining capacity, HPT has attracted extensive research interest for the fabrication of UFG materials, including pure metals, alloys, intermetallics, metal matrix composites and amorphous alloys [11].

It has been well known that most excellent properties of UFG materials produced by the HPT process are strongly relevant to the micro-scale features, such as crystallgraphic texture, grain size, grain misorientation etc. Up to now, extensively experimental measurements of microhardness [14,20–29], microstructure [20,22,30–42] and texture [43–57] over a wide range of HPT processed materials have been conducted. These experimental measurements revealed that HPT was more effective in producing exceptionally small grain size and a much higher fraction of high-angle boundaries than other SPD technique. The experimental observation is undoubtedly essential to understand the deformation mechanism of HPT. However, it only provides limited information. The comprehensive understanding of the HPT process can only be achieved by combination of advanced experimental technique and accurate modeling.

Until now, a few numerical simulations have been conducted for the HPT process. Most published simulation work used the classic finite element method (FEM) to investigate the geometry change of the sample and distributions of stress and strain during HPT [58–68]. A few pioneering studies have been carried out to understand the deformation behaviors in HPT using models integrated with crystal plasticity theory. Estrin et al. simulated HPT using gradient plasticity modelling [25], in which the constitutive formulation used was based on a phase

mixture model in which the dislocation cell walls and the cell interiors were considered as separate phases with different dislocation densities. They have successfully interpreted the occurrence of a uniform micro-structure as a result of an inherently non-uniform deformation along the radial direction of the HPT sample [69]. Kratochvil et al. interpreted the grain refinement process of HPT within the framework of crystal plasticity [70,71]. However, due to these simpifications (rigid-plasticity, rate-independent and uniform deformation of plane-strain double slip), this model provided only limited valuable information for the grain refinement mechnism of HPT. Hafok and Pippan predicted the crystallographic orientations development of nickel single crystals during the HPT process using a fully constrained Taylor model [48]. The simulation results in [48] revealed that the Taylor-type model failed to give satisfactory predictions compared to the experimental measurements. Lee et al. carried out the FEM simulations of the HPT process based on a dislocation density-based constitutive model [72,73]. They only studied the dislocation density and dislocation cell size evolution with the progressive HPT straining and it is insufficient to fully understand the deformation mechanism during the HPT process.

Limitation of current modelling for the HPT process is that the real HPT process has not been modelled correctly and it has always been over-simplified as simple shear. For a better understanding of the deformation mechanism during the HPT process and for the aim of industrial engineering application of HPT in the future, a crystal plasticity finite element method (CPFEM) model, which has been recognized as one of the best models for the predicting of plastic deformation of crystalline materials [74], is developed to simulate the plastic deformation behavior, texture evolution, and grain refinement during the HPT process.

This thesis consists of 8 chapters set out as follows:

Chapter 2 presents a brief overview of the HPT process. The experimental measurement results of microhardness, microstructure and texture are presented and summarized. The existing models used in the HPT research including the FEM model, analytical model, Taylor-type model and dislocation density based CPFEM model, are introduced. The advantages and disadvantages of the HPT simulation methods are reviewed.

Chapter 3 introduces the three-dimensional FEM model of the HPT process. The evolutions of Mises stress and strain with increasing HPT deformation are presented. The simulation results are compared to the experimental measurements to validate the developed FEM model. This chapter lays a model foundation for CPFEM studies in the following chapters.

Chapter 4 introduces the crystal plasticity theory and rate-dependent hardening model. The procedures of implementing the crystal plasticity constitutive model into the user material subroutine (UMAT) of ABAQUS software are outlined. For the first time, the CPFEM model of the HPT process of single crystals is constructed.

Chapter 5 presents the CPFEM simulations of texture evolution of nickel single crystals during the HPT process. The developed CPFEM models are verified by comparing the simulation results with the experimental measurements. The simulated texture results are investigated in detail to obtain the underlying mechanism.

Chapter 6 presents the CPFEM simulations of grain refinement of nickel single crystal during the HPT process. The main purpose of this chapter is to study how an original single crystal fragments into many differently oriented grains after HPT deformation and to explore the underlying mechanism.

Chapter 7 presents the CPFEM simulations of plastic deformation behaviors of aluminum single crystal during the HPT process. The plastic deformation heterogeneity along the circumferential direction and the underlying mechanism are investigated in detail.

Chapter 8 summarizes the research findings obtained in this thesis and some recommendations for future research are also offered.

Chapter 2 Literature Review

This chapter contains a substantial amount of information on topics considered essential to the understanding of plastic deformation, texture evolution and grain refinement etc. and their underlying mechanisms during the high pressure torsion process.

2.1 Severe Plastic Deformation

The average grain size plays a dominant role in the mechanical and physical properties of crystalline metal materials. Most of these properties benefit greatly from the grain size reduction. Therefore, grain size control has long been recognized as a way to produce material with designed properties. Among the procedures devised for grain refinement, severe plastic deformation (SPD) techniques are of particular interest owing to their exceptional ability of producing bulk ultrafine-grained (UFG) or even nanocrystalline structure materials. Compared with conventional coarse grained materials, UFG materials produced by SPD techniques show excellent physical and mechanical properties such as ultrahigh strength [36,41,75–77], low temperature and/or high strain rate superplasticity [78–80], enhanced fatigue behavior [81,82], and superior corrosion resistance [83], which are comprehensively summarized in the review papers [3–5,11,14]. For these reasons, in recent years, UFG materials have attracted significant interest from many modern industries including aerospace, defense, automotive, medical devices, sports equipment, and micro systems.

Up to now, many different SPD techniques have been developed, such as HPT [20,21,31–33,40,42,84–88], ECAP [6–9,89–98], ARB [15–19,99–102], multidirectional forging (MDF) [103–105], twist extrusion (TE) [106–109] and their derivative process, such as high pressure tube twisting (HPTT) [52,110], tube high pressure shearing (THPS) [111], frictional stir welding (FSW) [112–116], rotary-ECAP [117], cyclic extrusion-compression (CEC) [118,119], multiple direct extrusion (MDE) [120], axisymmetric forward spiral extrusion (AFSE) [121] and simple shear extrusion (SSE) [122–124]. These techniques are fundamentally different, but they all introduce

large plastic strain during deformation to achieve extreme grain refinement without any significant change in the overall dimensions of the work piece. In the following text, several frequently used SPD techniques, namely ARB, ECAP and HPT will be summarized.

ARB was first proposed by Saito et al. [15,99]. The principle of the ARB process is represented systematically in Fig. 2.1 [15]. Stacking of sheets and conventional roll-bonding are repeated in this process. First, a strip is neatly placed on top of another strip. The interfaces of the two strips are surface-treated in advance in order to enhance the bonding strength. The two layers are joined together by rolling, as in the conventional roll-bonding process. Then, the length of the rolled material is sectioned into two halves. The sectioned strips are again surface-treated, stacked and roll-bonded. ARB was successfully applied to a wide range of materials, including commercial-purity (CP) Al, the Al–Mg Al–Mg alloy AA5083 and interstitial-free steel, and was also used to process Al- and Mg-based laminated structures and composites [101]. In addition, ARB can be applied for the production of metal–matrix composites by sheathing mixed powders and subjecting them to a roll-bonding process [16].

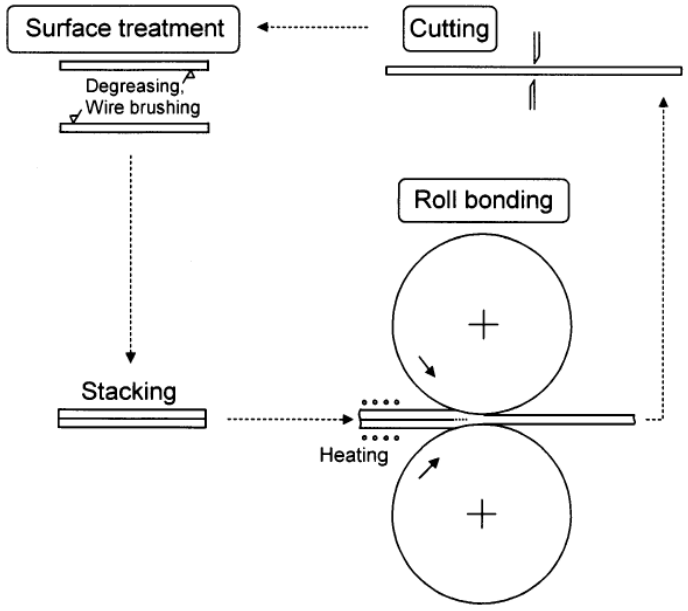

Fig. 2.1 Schematic illustration showing the principle of the ARB process [15].

During the ARB process the microhardness increases rapidly after the first rolling cycle and then it dwindles until it becomes saturated by further ARB cycles, as shown in Fig. 2.2 [19]. The

saturation of hardness at high cycles is caused by the steady-state density of dislocation due to a dynamic balance between the generation and annihilation of dislocation caused by the dynamic restoration phenomena [19]. The ARB process is very effective in grain refinement, and the average grain sizes of about 200 nm and 80 nm can be obtained in AA5083 with an initial average grain size of 25 μm after four and six rolling cycles respectively, as shown in Fig. 2.3 [19].

The greatest technological advantage of ARB is that it makes use of a conventional rolling facility. The main drawback of the ARB process is its poor bond strength, although it can be improved by the application of nano-particles before stacking. Moreover, the ARB process is only suitable for sheet metals [18,102].

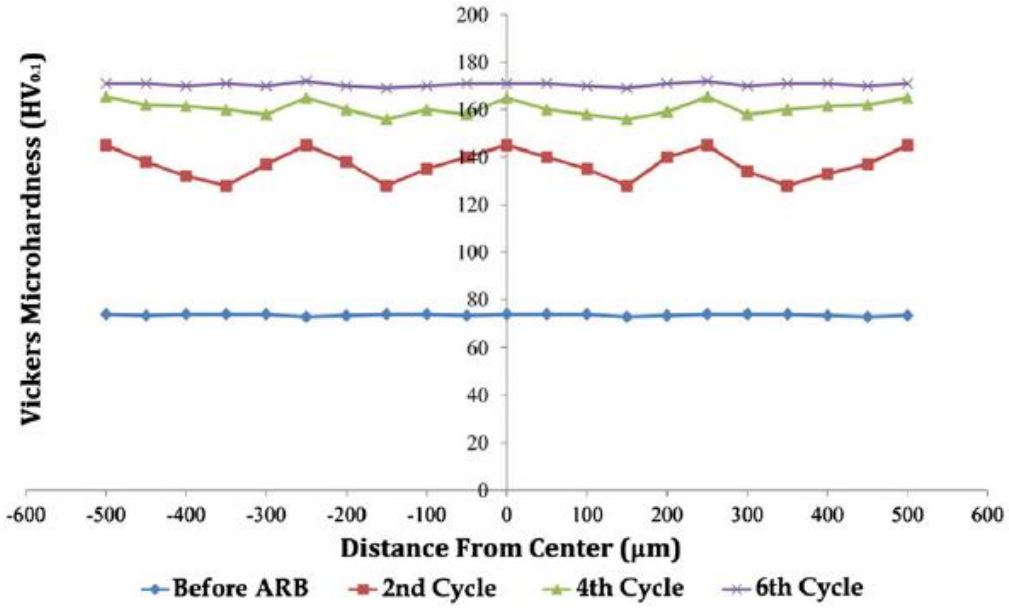

Fig. 2.2 The variation of microhardness along the thickness of the ARB processed AA5083 [19].

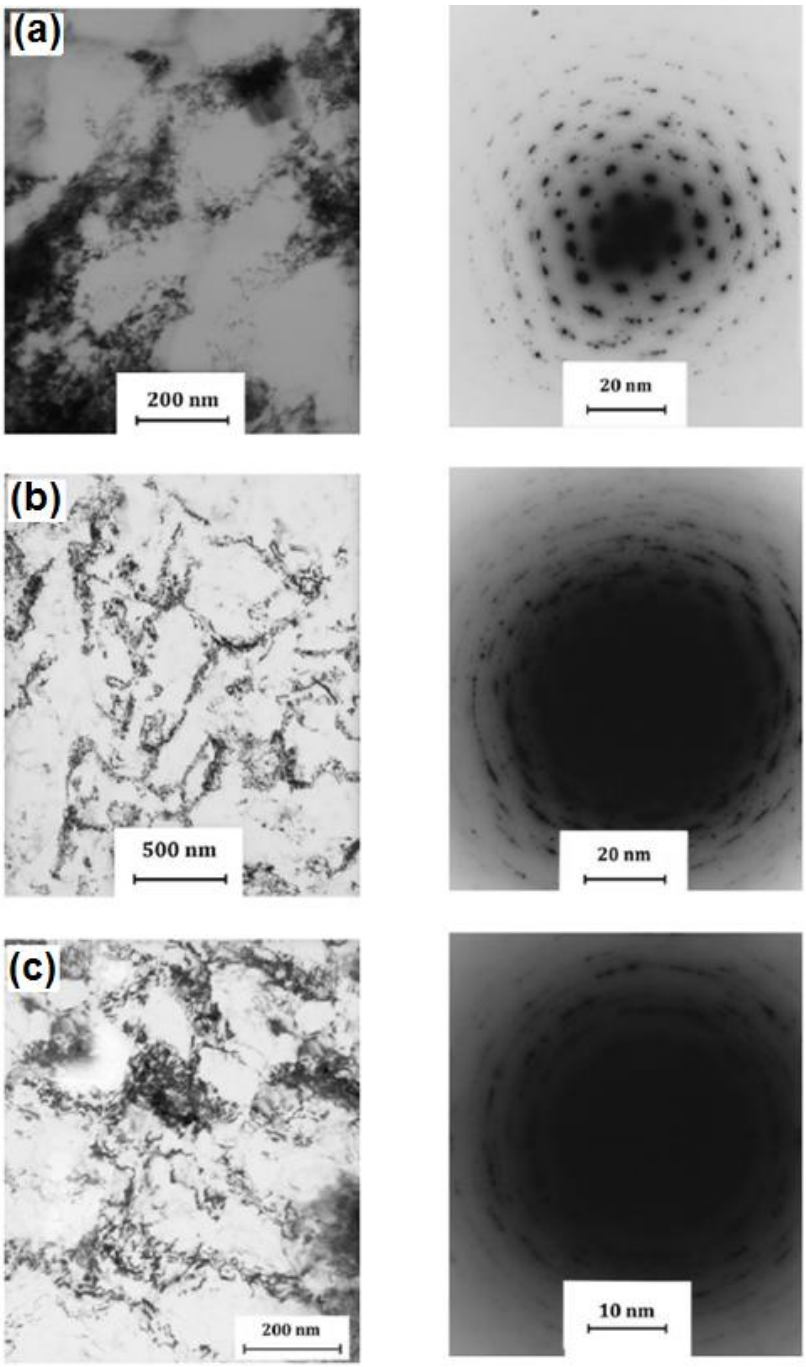

Fig. 2.3 TEM microstructures and the matching SAD patterns of ARB processed AA5083 by (a) 2, (b) 4, and (c) 6 cycles [19].

In practice ARB can be assumed as a plane strain deformation process, which means that the effective plastic strain during ARB can be estimated by [102]:

$$\varepsilon = \frac{2}{\sqrt{3}} \mathrm{N} \ln \frac{\mathrm{h_0}}{\mathrm{h_f}} \tag{2.1}$$

where h_0 is the initial thickness of the stacked sheets, h_f is the final thickness after the ARB process and N is the number of rolling cycles. If the reduction per rolling cycle can be maintained at 50%, Eqn. (2.2) can be simplified to the form [99]

$$\varepsilon = 0.8\mathrm{N} \tag{2.2}$$

ECAP, also called equal channel angular extrusion (ECAE), was first proposed by Segal and his co-workers who wanted to transform simple shear into ordinary and effective production operations [90]. The ECAP process has drawn significant attention since the early of 1990s [8,9,89,95]. The principle of ECAP is illustrated schematically in Fig. 2.4 [92]. In ECAP, a bar shaped billet is pressed through a die that has two channels with an equal cross-section intersecting at an angle ϕ which varies from 60° to 150° [96]. During the ECAP process, the cross-sectional dimensions of the billet remain unchanged, thereby permitting repetitive pressing that leads to accumulation of very large strains. For example, the equivalent (von Mises) strain, ε_{eq}, introduced per pass in ECAP with a 90° angle between the channels amounts to 1.15 [6]. Furthermore, it is possible to initiate different slip systems by rotating the sample between each pass [90]. Different ECAP variants involving rotations of the billet about the pressing axis between the passes are possible, and they generally lead to different results in terms of the microstructure and texture produced. The definitions of these ECAP routes can be found in Ref. [93].

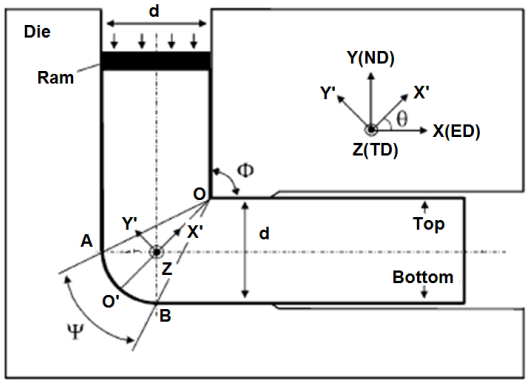

Fig. 2.4 Schematic illustration of the ECAP process [92].

The effective plastic strain during ECAP can be calculated by [8],

$$\varepsilon_N = \frac{N}{\sqrt{3}}\left[2\cot\left(\frac{\phi}{2}+\frac{\psi}{2}\right)+\psi\,\mathrm{cosec}\left(\frac{\phi}{2}+\frac{\psi}{2}\right)\right] \tag{2.3}$$

where ε_N is the accumulated equivalent plastic strain, N is the number of ECAP passes, ϕ is the die channel angle, and ψ is the outer corner angle.

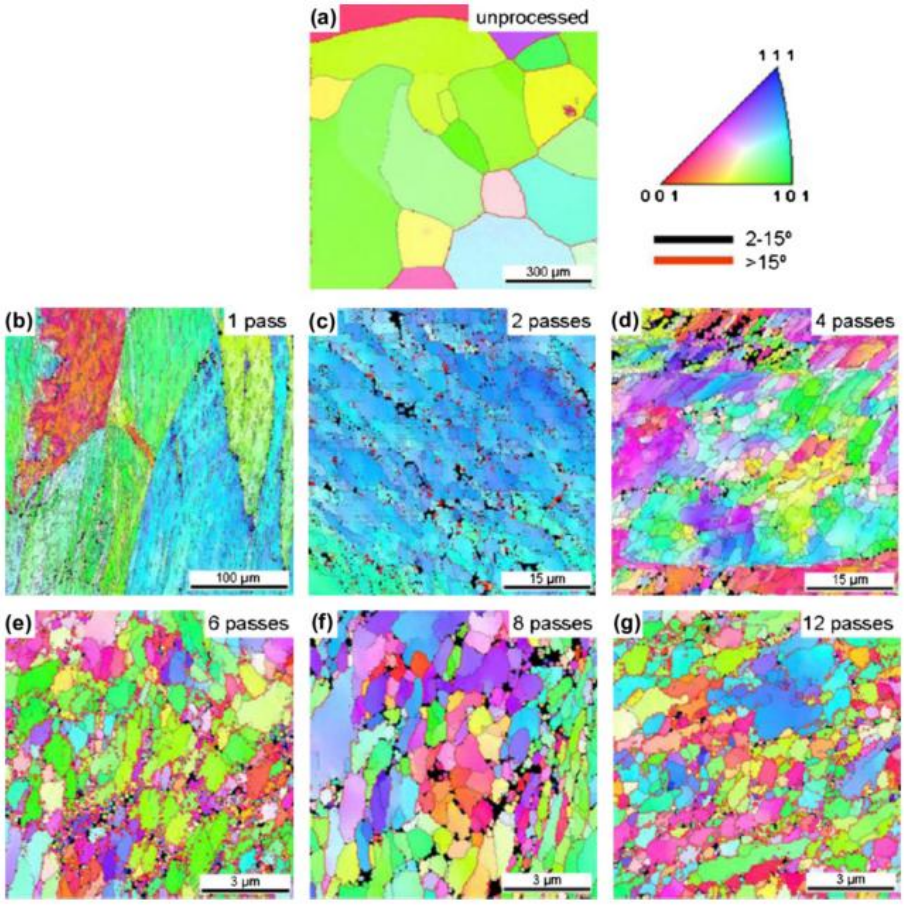

Fig. 2.5 Microstructural evolution in an Al–1% Mg alloy processed by ECAP [98].

The microstructural evolution occurring in FCC metals during processing by ECAP is now well documented, and an example is shown in Fig. 2.5 using OIM with samples of Al–1% Mg solid solution alloy processed by ECAP using route B_C with a die having internal angles of $\phi = 90°$ and $\psi = 20°$ [98]. Fig. 2.5(a) is for the unprocessed material with an initial grain size of 350 µm, and Figs. 2.5(b)–(g) shows samples processed through 1, 2, 4, 6, 8 and 12 passes, respectively. Elongated subgrains could be observed after 1 pass and then an evolution to an ultrafine-

grained structure with grain sizes of ~700 nm after 8 and 12 passes but with some larger grains remaining even after 12 passes. Moreover, the fraction of high-angle boundaries is initially low but increases to ~50% after 4 passes and continues to increase to ~74% after 12 passes.

2.2 High Pressure Torsion

The high pressure torsion process was first investigated by Bridgman early in 1943 [125]. In his experiments, attention was not paid to the microstructure change taking place in severely deformed metals. Another implementation of HPT was carried out by Erbel [126]. The specimen was a short ring with conical faces whose virtual extensions met at the axis of the apparatus. The conical matching faces of the punches had radial teeth to facilitate the application of torque. The ring specimens were constrained from all directions which created a condition closer to hydrostatic pressure. Since the 1990s, HPT experiments have been extensively carried out using devices under high pressure as described in Fig. 2.6 by Valiev et al. [127–129], Zhilyaev et al. [11,20,31,35,130], Horita, pippan et al. [21,37,131,132], Langdon et al. [5,11,14] and many others to produce ultra-fine grained materials. Today this technique is appreciated by many researchers as the one that allows the most efficient grain refinement [4].

The principle of processing by HPT is illustrated schematically in Fig. 2.6 [47]. The thin-disk shaped sample is located between two massive anvils. First, the specimen is subjected to a compressive pressure, P, of several GPa applied on one anvil at room temperature. After that the specimen is subjected to a torsional strain imposed by rotating the other anvil such that the surface frictional forces deform the disk by shear. Due to the specific geometry shape, the main volume of the material is strained in conditions of quasi-hydrostatic pressure. As a result, in spite of large strain values, the deformed sample is not destroyed.

In practice, there are three different types of HPT, which depend upon the geometry of the anvils and the degree of restriction imposed on any lateral flow during the processing operation [11,14,47]. In unconstrained HPT, as shown in Fig. 2.6(a), the anvils are flat so that the material flows outwards in an unconstrained manner during processing. In fully constrained HPT, the disk is placed within a cavity in the lower anvil, a plunger from the upper anvil enters the cavity,

and there is no lateral flow during processing (see Fig. 2.6(c)). In practice, however, most of the HPT processing is now conducted under quasi-constrained conditions as illustrated in Fig. 2.6(b), where the disk is contained within depressions on the inner surfaces of the upper and lower anvils, the disk thickness is slightly larger than the combined depths of the two depressions, and some limited outward flow occurs during torsional straining.

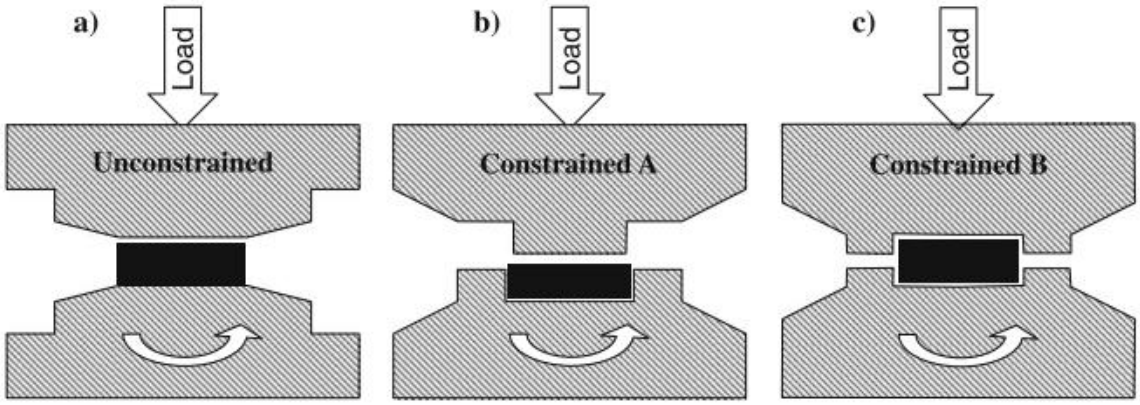

Fig. 2.6 Schematic illustration of the principle of high pressure torsion process of (a) unconstrained HPT, (b) fully constrained HPT and (c) quasi-constrained HPT [47].

The equivalent strain, ε_{eq} , imposed on the disk through the torsional straining is given by the following relationship [11,131,133]:

$$\varepsilon_{eq} = \frac{2\pi Nr}{\sqrt{3}h} \tag{2.4}$$

where N is the rotation numbers, r is the radial distance away from the center of the specimen, and h is the depth of the specimen.

Theoretically HPT can proceed for infinite revolutions. One hundred HPT revolutions, which are usually not difficult to apply in practice, correspond to an equivalent strain of 1800 [10]. Such large strains are impossible to obtain with any other SPD techniques. Moreover, among these SPD methods, early investigations suggested that HPT was more effective in producing equaxied character grains with exceptionally small grain size and could develop homogeneous microstructure with predominately high-angle grain boundaries [5,11]. The HPT process is the focus of this study and will be summarized in the following text.

2.3 Experimental Measurements of HPT Processed Materials

2.3.1 Microhardness evolution during HPT

In order to investigate the mechanical properties of the samples deformed by HPT, the tensile test needs to be conducted. However, since the samples deformed by HPT normally have thin disk shape and it is difficult to fabricate the dog-bone from such a sample. Instead, microhardness examinations are usually carried out by the researchers, mostly by taking measurements of the Vickers's microharness, HV.

For a disk-shaped specimen deformed by HPT technique, the main problem is the non-uniformity of deformation. During HPT straining, according to Eqn. 2.4, the strain applied on the specimen is not identical along the radial direction, the strain values in the disk center should be zero, increasing linearly to reach the maximum at the edge. As a consequence of this variation, the inhomogeneous microhardness distribution is expected. However, this is not supported by numerous microstructural observations and microhardness measurements showing a reasonably uniform distribution of grain dimensions and microhardness, provided the compressive pressure and the number of revolutions of the anvil are sufficiently large. Indeed, as shown in Figs. 2.7 and 2.8, at the early stage of HPT deformation, HV measurements performed along the diameter of HPT-deformed CP Al [34] and Al 1050 [29] revealed lower hardness at the center compared to the periphery region. However, with increasing numbers of HPT turns, the HV values in the center increased and the difference between the center and the edge region decreased. When the applied strain reached a sufficient high level, a reasonable level of homogeneity across the diameters of the disks could be realized. This trend towards microhardness homogeneity has also been reported in many HPT deformed materials, such as, copper and copper alloys [21,30,37,134], high purity Ni [20,22,135], Al and Al alloys [24,26,27,29,136]. It is referred to the review paper [14] for more details. Now this gradual evolution towards homogeneity has already been successfully modeled by Estrin Y etc. using strain gradient plasticity theory [69]. Vorhauer and Pippan [136] explained this discrepancy by the fact that it is virtually impossible to realize an ideal HPT deformation due to the misalignment of the axes of the anvils.

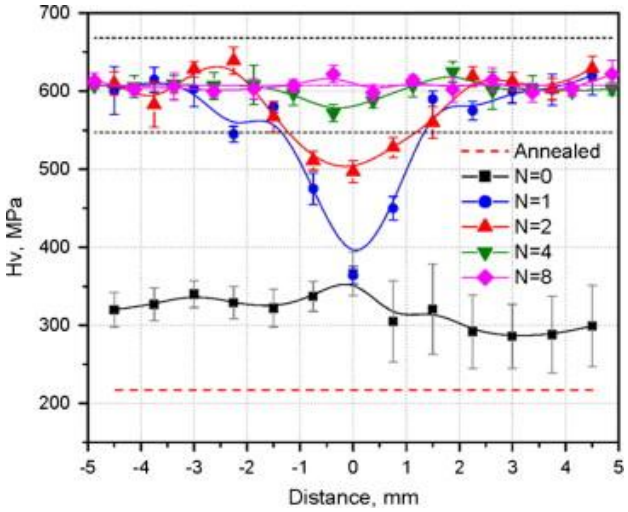

Fig. 2.7 Microhardness distribution across the diameter of a CP Al processed using a constrained HPT facility at 1 GPa up to 8 turns [34].

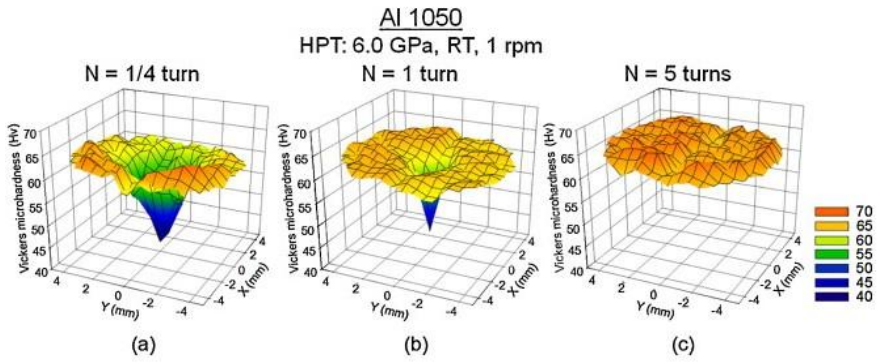

Fig. 2.8 There-dimensional representation of HV microhardness of Al 1050 samples processed by HPT [29].

For different materials produced by HPT, the evolution of homogenous microhardness is anticipated if the stain deformation is large enough, however, there is a significant dichotomy at the early stage of the HPT process which is attributed to the variations in the rates of recovery of these materials, as shown in Fig. 2.9. For materials with low recovery rates, investigations revealed lower values of hardness in the center region and higher values at the edge region in the early stages of torsion straining. The hardening occurred in the absence of any significant recovery as in a wide range of metallic alloys, such as Cu [21,25], Ni [20,22] and

Al alloys [26,137]. On the contrary, the high stacking fault energy in materials such as high-purity aluminum [26,137,138] led to easy cross-slip and rapid recovery, the hardness values were higher in the center region of the disk at low total strains in HPT.

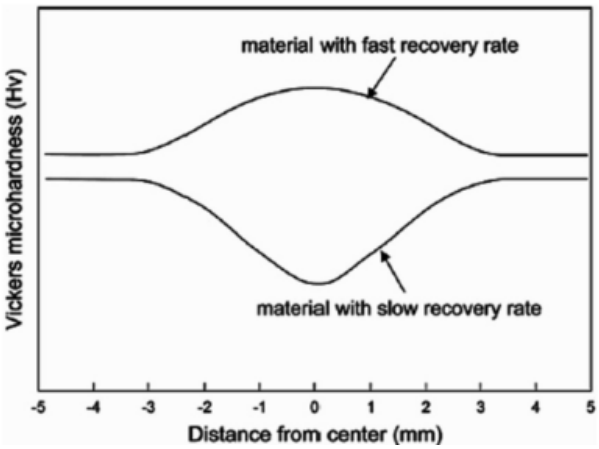

Fig. 2.9 Schematic illustration of the variation of the Vickers microhardness across the disk at low total strains in HPT processing for materials having either slow (lower) or fast (upper) rates of recovery [24].

2.3.2 Microstructure Evolution during HPT

Previously reported studies associated with HPT were devoted extensively to observe the microstructure evolution using various optical microscopes over a wide range of materials. The microstructural characteristics of HPT processed samples have been investigated and were well documented in the review papers [4,5,11,13]. The representative results are shown in Fig. 2.10 where polycrystalline high purity aluminium was subjected to an applied pressure of 1Gpa and then torsionally strained through (a, b) N=1/8 turn, (c) N=1/4 turn and (d) N=1 turn [139]. At the early stage of deformation, the grains subdivided and a network of closed deformation-induced subgrains bounded by LAGBs were formed within these larger grains. Grain size at the center and edge and region was measured as $\sim$250μm. At the center region there was a large average spacing between the subgrain boundaries, at the periphery, however, the average spacing between the low-angle boundaries was very small; With the increasing level of applied strain, the boundary spacing decreased while the boundaries misorientation gradually increased and finally the fraction of grains having high angle boundaries has increased. At this stage the

microstructure was heterogeneous with some regions having subgrains and a high density of dislocations and other regions having ultrafine grains with relatively few dislocations. The grain size at the edge region was reduced to ～5μm; With increasing applied strain, many equiaxed grains having different orientations surrounded by well-defined HAGBs dominated the microstructure. Grain size at the edge region was further reduced to ～2μm. Orlov et al. [140], Hansen et al. [38] and Horita [132] also reported that the similar three stages of microstructure evolution, specifically, the first stage, the transition stage and the saturation stage, could be distinguished during different strain levels of HPT deformation. Hansen et al. [38] and Zhilyaev et al. [31][141], measured the distribution of grain boundary misorientations in ultrafine-grained nickel processed by HPT, as shown in Fig. 2.11. With increasing HPT deformation, high angle grain boundaries were gradually produced, leading to a typical bimodal distribution with one peak appearing at low angles and another peak at high angles.

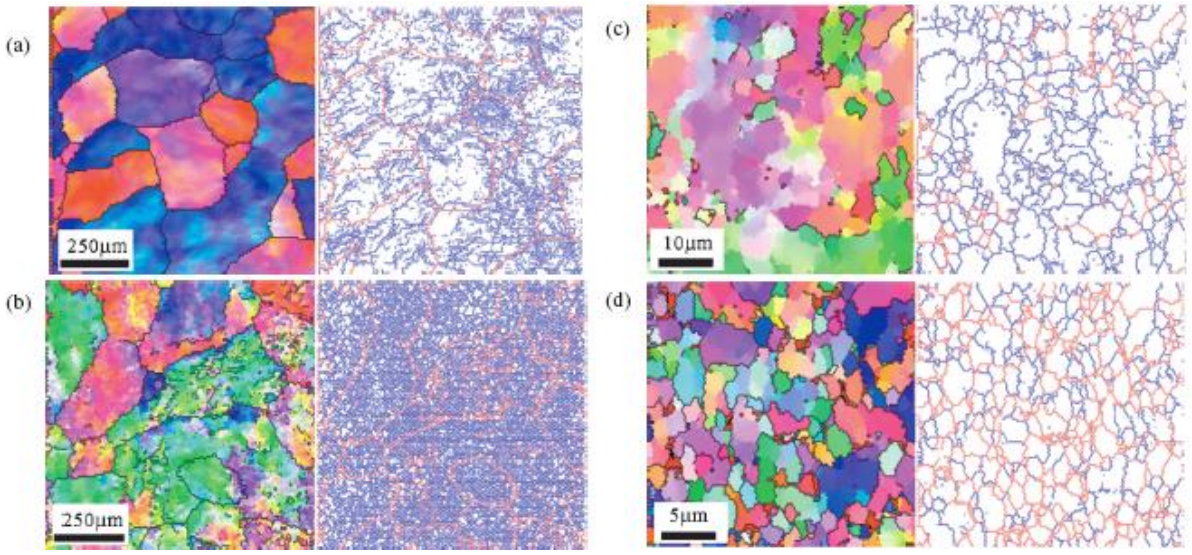

Fig. 2.10 Images obtained by EBSD for disks processed by HPT where (a) shows 1/8 turn near the center, (b) shows 1/8 turn near the edge, (c) shows1/4 turn near the edge and (d) shows 1 turn near the edge [139].

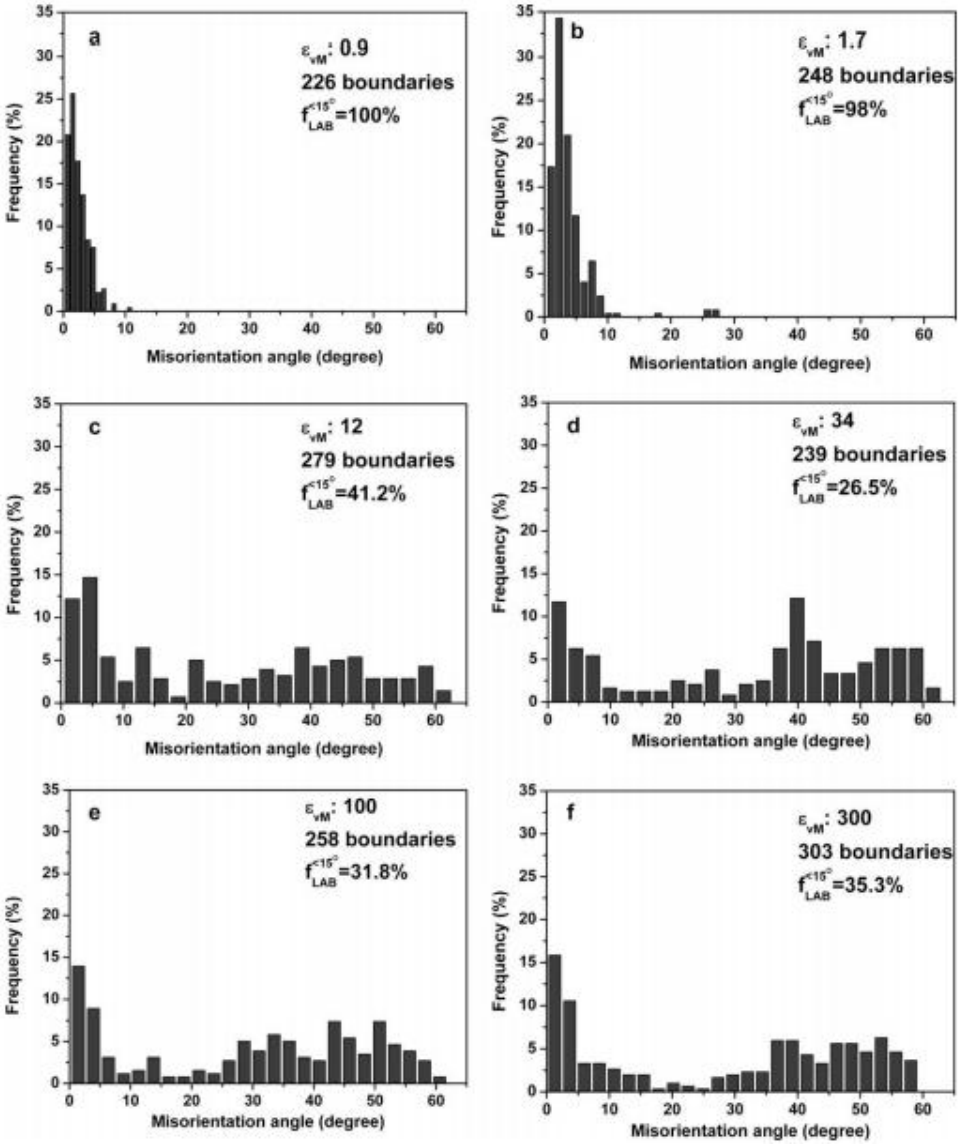

Fig. 2.11 Misorientation angles across boundaries (GNBs and IDBs) for HPT deformed Ni in the form of histograms [38].

In the case of a single crystal, the condition becomes different as the dislocation gliding is not constrained by boundaries and there are no differences between different grains like in polycrystals in the early stage of deformation. The absent of initial boundaries and the effect of the overall initial orientation of the crystals could aid the understanding the microstructure evolution during HPT. So far, single crystals have been widely used in the field of SPD on equal channel angular pressing to investigate the deformation heterogeneity [142–145]. However, single crystal experiments of HPT have been few reported in the literature except for Hafok and

Pippan's work. They performed successive experimental investigations of single crystal nickel [48,146,147]. Fig. 2.12 shows the microstructure evolution of Ni single crystal with increasing HPT straining of (a) 1, (b) 1.5, (c) 2.25, (d) 3, (e) 4, (f) 5, (g) 8, (h) 12 and (i) 32. The EBSD-scans results were obtained in the top view (RD-TD section) with 30 μm X 30 μm. In the case of a single crystal, no boundaries were present in the as-received state. All boundaries, formed during deformation, were induced by plastic strain. In the beginning, the dislocation density increased during deformation and a few low angle boundaries were formed. These boundaries consisted of a band shaped structure aligned in the radial direction, as shown in Fig. 2.12(a). The bands got more pronounced in Fig. 2.12(b). In the centre of this boundary plot, a band bordered by high angle boundaries has evolved, while the interior of the band was subdivided by cell structures consisting of low angle boundaries. Outside the band the initial crystallographic orientation was distorted weakly, indicated by the low density of low angle boundaries. With increasing equivalent strain the bands subdivided, more and more high angle boundaries formed, and the structure in-between transforms to equiaxed cell structures bounded by high angle boundaries. This microstructure decreased its size until the saturation region of the torque curve was reached. Most of the structure elements have developed a minimum structure size which could not be further decreased by deformation, as was apparent through a comparison of Fig. 2.12(g)-(h). The structure size in this region of saturation was around 380 nm, as shown in Fig. 2.13(a). Fragmentation of the original Ni single crystal microstructure led to an increase of the misorientation angle between adjacent structure elements. The obtained misorientation angle distribution for different equivalent strains in Fig. 2.13(b) showed that: at the very low equivalent no high angle boundaries existed, and the distribution showed a strong decline up to a misorientation of approximately 10°. By increasing the equivalent strain the misoriention angle between different structure elements increased and this led to a second peak at a misorientation angle of approximately 53°, indicating the formation of high angle boundaries during deformation.

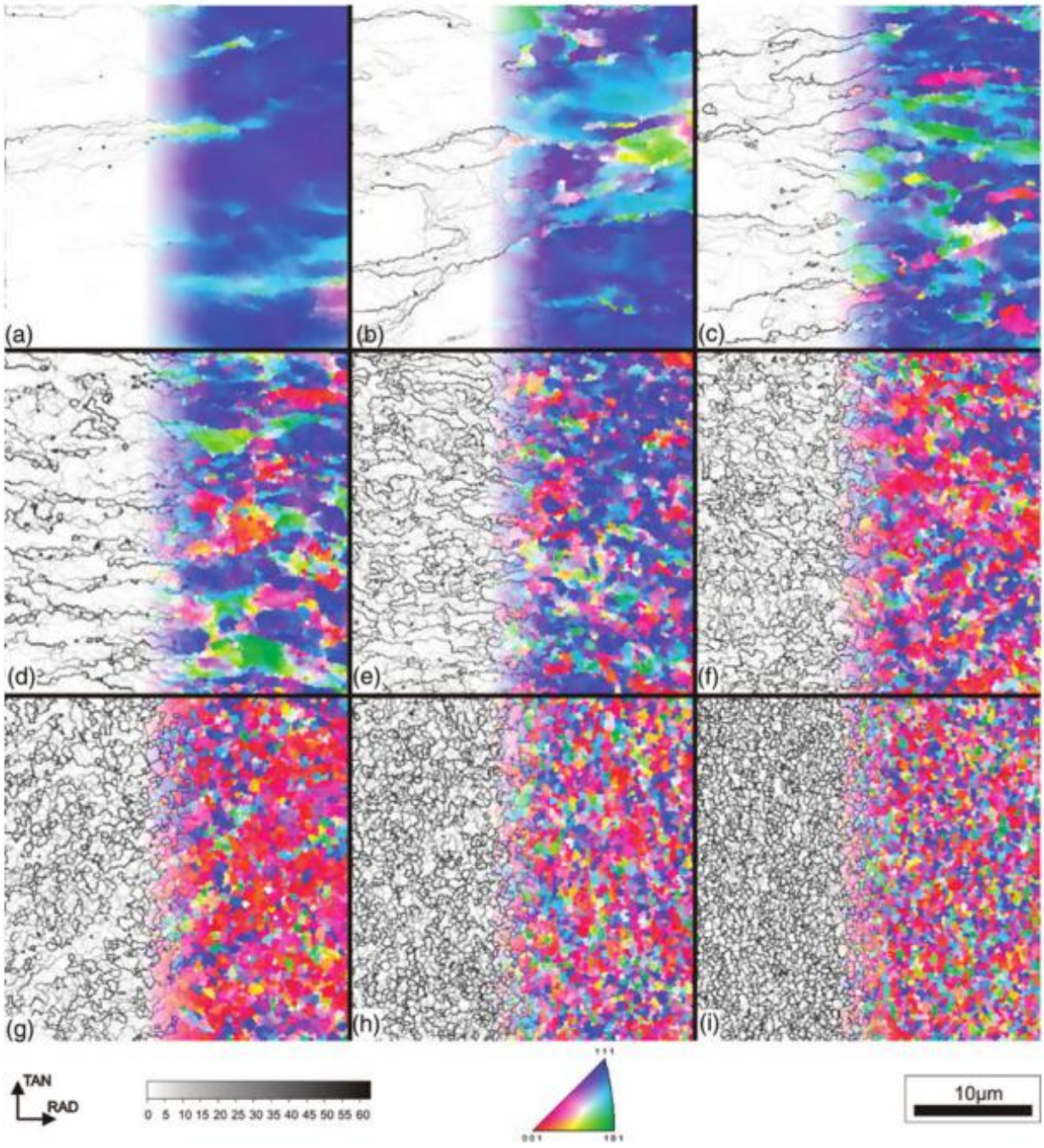

Fig. 2.12 Structure development with increasing equivalent strain of the nickel <111> single crystal recorded in top view. The scans refer to the following equivalent strains (a) 1, (b) 1.5, (c) 2.25, (d) 3, (e) 4, (f) 5, (g) 8, (h) 12 and (i) 32 [48].

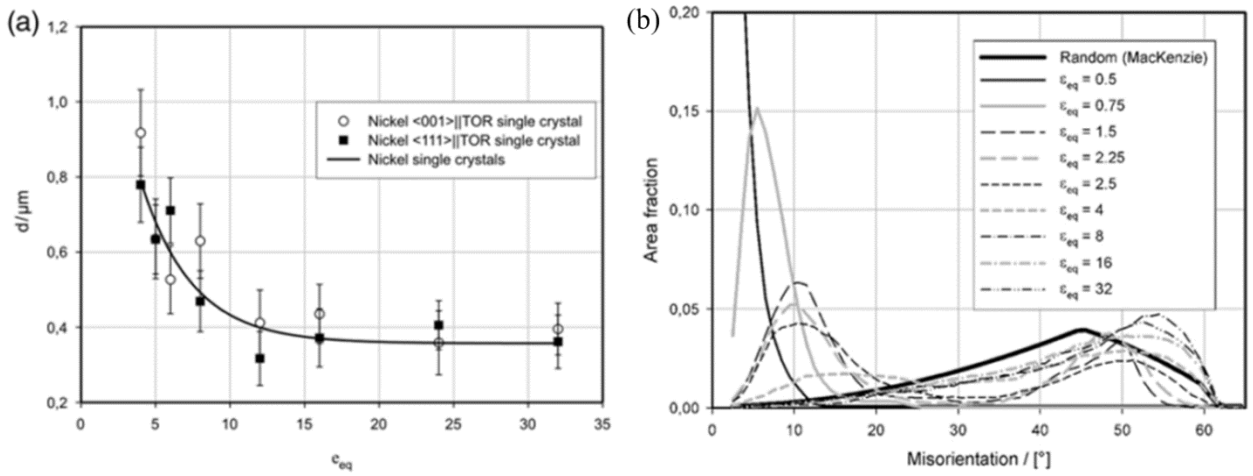

Fig. 2.13 (a) The decrease in structure size with increasing equivalent strain. (b) Misorientation angle distributions recorded at different equivalent strains [48].

The main aim of SPD processing is to produce grain refinement and the ensuing strengthening of the processed material. There is no longer any doubt that this is achievable with most malleable and even with many hard-to-deform materials, and innumerable experimental results documented in the review articles [1–5,11,12,14] are a convincing testimony to that. The existing microstructure evolution theory was obtained based on experimental investigations over a wide range of materials. All these microstructure observations demonstrated a gradual evolution of microstructure with subgrains bounded predominately by LAGBs evolving into an array of ultrafine grains by boundaries predominately having high angles of misorientations. Despite the body of experimental evidence, there are different explanations for the microstructure process from various perspectives, which are summarized as follows:

The most commonly accepted type of grain refinement mechanism due to large strain induced by HPT are based on the notion that a dislocation cell structure, which forms already in the early stages of plastic deformation, gradually transforms to the final fine grain structure [4]. This is believed to occur through continual decrease in the average grain size accompanied by accumulation of misorientation between neighbouring dislocation cells. This mechanism is discussed in detail by Estrin and Vinogradov in the review paper [4].

An alternative explanation would be the source-sink mechanism for dislocations. Accordingly, dislocations can be generated, trapped, or annihilated at the boundaries. During deformation the dislocations glide through the grain and contribute to the local deformation. When the dislocations reach the boundary region they can be trapped or annihilated by other dislocations. The source-sink model can also describe the local deformation in the vicinity of the boundary due to the storage and annihilation of dislocations. A description can be given by considering the boundaries as disclination dipole walls [148]. Dislocations can be trapped or emitted from such a boundary [149]. The continuous increase of dislocation density can be prevented by dynamic recovery due to the rearrangement of dislocations in the boundary layer. For that reason, dynamic recovery could establish a minimum structure size that cannot be further decreased by deformation. For example, Horita and his co-workers [87,132], Ivanisenko et al. [150] investigated the grain refinement phenomenon during the deformation process of high purity Al and Cu and Armco iron in HPT by focusing on the dislocation behavior and the formation of high angle boundaries. They found that the hardness with the straining values could be divided into three stages, as shown in Fig. 2.14(a); during the first stage, the subgrain boundaries formed due to the accumulation of dislocation, during the second stage, the dislocation were absorbed at grain boundaries and misorientation angle increased, and in the third stage, there was a balance between dislocation generation and the absorption at high angle boundaries.

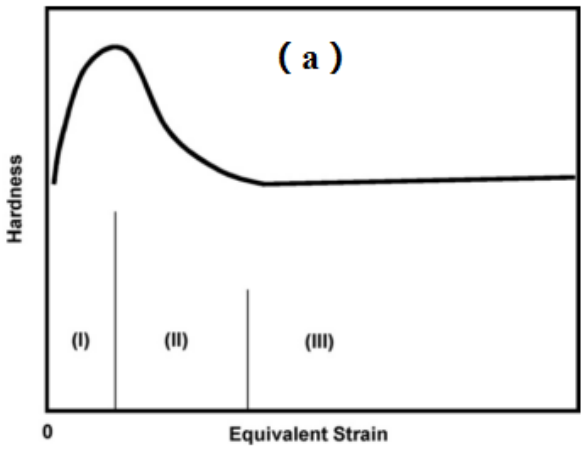

(To be continued)

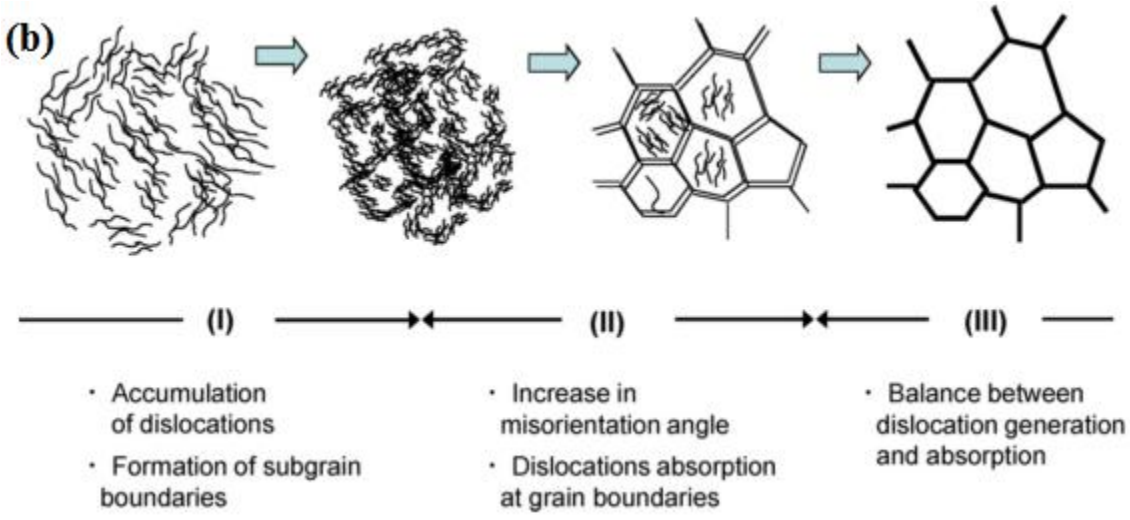

Fig. 2.14 (a) Three regions I, II and III defined in hardness variation with equivalent strain of pure aluminium. (b) Schematic illustration of microstructural evolution with straining along with descriptions occurring in regions I, II and III defined in Fig. 2.14(a) [132].

Pippan et al. proposed the intergranular gliding of dislocations and the crystal lattice rotation model after examining the microstructure of Ni [151,152] and Cu [85] deformed by the HPT process. In order to maintain the continuity during HPT deformation, neighbouring grains will exert stresses on each other so that the local stress field will vary within one grain. As a consequence, different sets of slip systems will be activated within one crystal and thus leading to diverging crystal lattice rotations towards different preferred texture components. With large applied strains, the continual rotation can lead to significant intergranular misorientation. Such a mechanism promotes fragmentation of the microstructure. Barnett and Montheillet [153] learned about boundaries generated during torsion deformation and found that that the new high-angle boundaries were associated with a subgrain rotating away from the parent grain in the same sense and around the radial direction, the main cause of the high-angle boundaries was a difference in rotation rate. Zhilyaev, et al. [31,141] inspected the ultrafine-grained nickel processed by HPT and assured that three deformation processes occurred during the plastic deformation: dislocation slip gave a high fraction of low angle grain boundaries, a rotation mode of deformation led to the creation of high-angle boundaries, and dynamic recovery accompanied by increasing of special GBS (including twins). Among the three

deformation processes, the latter two processes were more pronounced during the HPT process.

On the other hand, the experimental observations of Vinogradov et al. [154] and others [78,155,156] seem to support grain boundary sliding (GBS) at room temperature. In the paper of Vinogradov the micrographs obtained by transmission electron microscopy and atomic force microscopy (AFM) after a tensile test were used to reveal the deformation mechanism of ultrafine-grained nickel and copper produced by ECAP. It was reported that shear bands formed that were oriented 45° to the loading axes. The AFM measurements showed pronounced slip in the grain boundary region, which led to the authors to conclude that deformation was concentrated at the grain boundary and the grain interior remained nearly undeformed. This deformation appeared in the shape of pronounced steps in the boundary region. Due to the high deformation in the boundary region, GBS was proposed as the main deformation mechanism.

Grain refinement by HPT implies the creation of new high angle grain boundaries (HAGBs). According to Sevillano et al. [157], formation of new HAGBs could be accomplished by three mechanisms. The first is the elongation of existing grains during plastic deformation, causing an increase in high angle boundary area; the second is the creation of high angle boundaries by grain subdivision mechanisms; the third is that an elongated grain can be split up by a localization phenomenon such as a shear band. The second mechanism is probably the most important one for HPT deformation. Grain subdivision starts at low to medium strains when grains break up into cells and cell blocks [158]. With increasing strain this substructure evolves towards a lamellar structure. During this process new high angle boundaries are generated. This happens by the simultaneous action of a microstructural and a texture mechanism [159]. The former starts at low deformations and consist in the accumulation of dislocations in the cell and cell block boundaries in which the misorientions gradually increase with increasing strain. Some boundaries remain low angle boundaries but a significant fraction evolves into medium-high angle boundaries mostly in the range 15°-30; the texture mechanism involves different slip system combinations and strain. Different parts of a subdivided grain rotate towards different

end orientations. Large crystal rotations are required to bring the starting texture to the final preferred texture. This can generate very high misorientations in the range 20°-60°.

The fundamental parameters that influence the microstructure development during the HPT process, such as applied hydrostatic pressure [31,137,160], strain hardening [1,2,31,34], stacking fault energy [13,37,150,161] and deformation temperature [152,162] and so on, have also been widely studied.

2.3.3 Texture Evolution during HPT

Texture is defined as preferred orientation and it is very important due to its influence on material properties such as Young's Modulus, Poisson's ratio, strength, ductility, toughness, electrical conductivity, and so on [163]. Texture is commonly represented by Miller indices, pole figure, inverse pole figure or orientation distribution function (ODF). The main advantage of the Miller indices notation is that it highlights important planes {h k l} and directions <u v w> which are parallel to the principle directions in the sample. For example, the notation of {h k l}<u v w> during rolling indicates that the direction <h k l> is parallel to the normal direction (ND) and the direction <u v w> is parallel to the rolling direction (RD). The pole figure is a two dimensional representation of three dimensional orientation information projected from the reference sphere. One direction must be chosen as a pole during projection and ND is typically chosen to be in the north pole of the sphere during rolling. The inverse pole figure is similar to the pole figure and it is the orientation that represents the sample coordinate system in the crystal coordinate system. Inverse pole figures are often used for axial symmetric samples, where only one of the axes is prescribed. ODF is a three dimensional representation of textures and it is able to offer a quantitative evaluation with the help of Euler angles, which are shown in Fig. 2.15 [163]. It should be noted that there are several different conventions for describing the Euler angles, with the most widely used being the Bunge's convention.

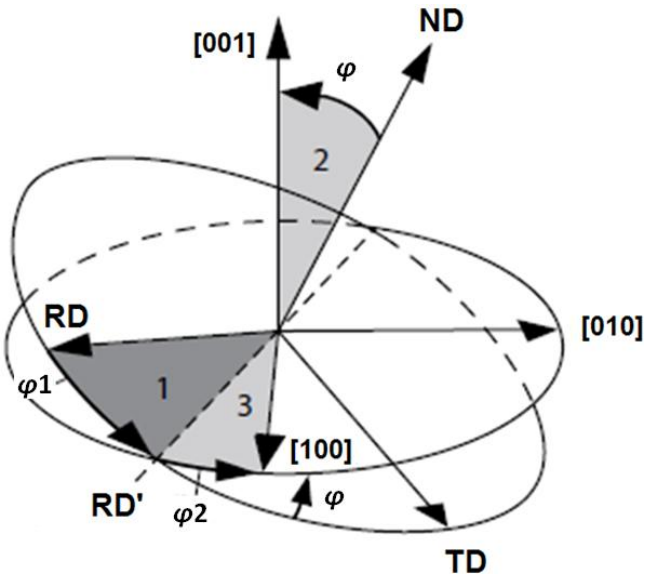

Fig. 2.15 Diagram showing how rotation through the Euler angles φ_1, ϕ, φ_2, in the order 1, 2, 3 as shown describes rotation between the sample and crystal axes [163].

The orientation matrix (g) can be expressed with the three Euler angles as [163]

$$g = g_{\varphi_2} \cdot g_{\varphi} \cdot g_{\varphi_1} \tag{2.5}$$

where the three rotation matrices (g_{φ_2}, g_{φ}, g_{φ_1}) can be written as

$$g_{\varphi_2} = \begin{pmatrix} \cos\varphi_2 & \sin\varphi_2 & 0 \\ -\sin\varphi_2 & \cos\varphi_2 & 0 \\ 0 & 0 & 1 \end{pmatrix} \tag{2.6}$$

$$g_{\varphi} = \begin{pmatrix} 1 & 0 & 0 \\ 0 & \cos\varphi & \sin\varphi \\ 0 & -\sin\varphi & \cos\varphi \end{pmatrix} \tag{2.7}$$

$$g_{\varphi_1} = \begin{pmatrix} \cos\varphi_1 & \sin\varphi_1 & 0 \\ -\sin\varphi_1 & \cos\varphi_1 & 0 \\ 0 & 0 & 1 \end{pmatrix} \tag{2.8}$$

According to the scale of the measured area, texture measurement can be divided into two groups, namely macrotexture analysis and microtexture analysis. Macrotexture represents the bulk texture of a particular sample and is measured from a large number of grains by means of X-ray diffraction or neutron diffraction. Microtexture is measured by Kikuchi patterns with the

electron diffraction under an electron microscope and represents the texture of individual grains. The most widely used measurement is the electron backscatter diffraction (EBSD) technique.

For face-centered cubic (FCC) structured metals, according to [164,165], the ideal orientations of torsion texture could be identified as A/$\overline{\mathrm{A}}$, $\mathrm{A}_1^*/\mathrm{A}_2^*$, B/$\overline{\mathrm{B}}$ and C, the corresponding Miller indices and Euler angles have been summarized, as shown in Tab. 2.1. It should be noted that during the torsion process, the texture indices are defined with respect to the torsional axis and the shear direction. Using this convention, the Miller index {h k l} <u v w> denotes an orientation that has an crystallographic plane {h k l} parallel to the shear plane and an <u v w> direction parallel to the tangential direction. The ideal components of torsion texture have been determined for FCC polycrystalline materials in terms of pole figures shown in Fig. 2.16 [166–168].

Tab. 2.1 Euler angles and Miller indices for the ideal torsion texture components of FCC materials [164,165].

Orientation	Shear plane	Shear direction	ϕ_1	ϕ	ϕ_2
A	$(11\bar{1})$	$[1\bar{1}0]$	0	35.26	45
$\bar{A}$	$(\bar{1}\bar{1}1)$	$[\bar{1}10]$	180	35.26	45
A_1^*	$(11\bar{1})$	$[2\bar{1}1]$	35.26	45	0
A_2^*	$(1\bar{1}1)$	$[\bar{2}\bar{1}1]$	144.74	45	0
B	$(11\bar{2})$	$[1\bar{1}0]$	0	54.74	45
$\bar{B}$	$(\bar{1}\bar{1}2)$	$[\bar{1}10]$	180	54.74	45
C	(100)	$[0\bar{1}1]$	90	45	0

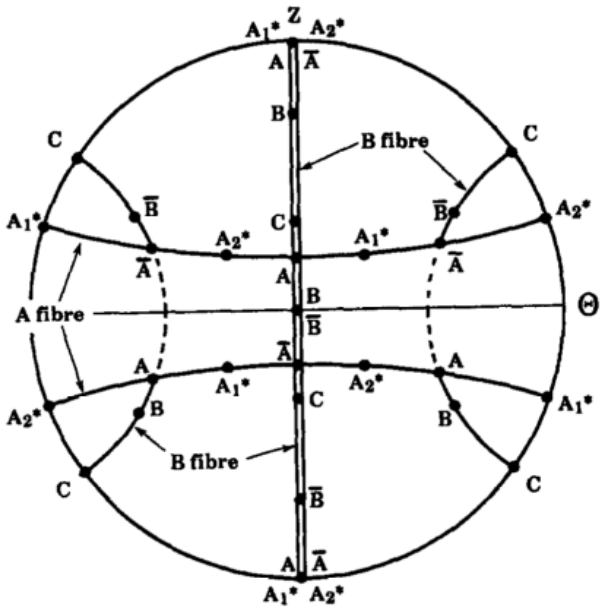

Fig. 2.16 {111} pole figures showing the main ideal orientations and fiber textures for FCC materials [166–168].

For FCC structures, there are two partial fibres which are identified as the A and B fibres respectively, as shown in the form of pole figure in Fig. 2.16 and in terms of ODF in Fig. 2.17 [167,169]. The A fibre corresponds to a common (111) shear plane with rotation of the crystal around the Z (shear plane) axis, while the B fibre is characterized by a common (110) shear direction with rotation around the θ (shear direction) axis of the specimen. The A fibre contains four ideal components of A, $\overline{\mathrm{A}}$, A_1^* and A_2^* while the B fibre contains A, $\overline{\mathrm{A}}$, B, $\overline{\mathrm{B}}$ and C components. The properties of these ideal components were discussed in detail in [153,167,169–171], which shows that the crystallographic rotation field (see Fig. 2.18) for torsion texture possesses a number of interesting features: one is the predominance of single sense rotations around the sample radial direction and another is the lattice rotation rate varies significantly as a function of crystallographic orientation. Crystals oriented between the ideal shear orientations (along φ_1 in Bunge notation) have a high lattice rotation rate, while the rotation rate drops to near zero for orientations that are near the ideal shear orientations. Thus, the lattice rotation rate depends so strongly on orientation that rotating grains near particular ideal orientations can remain near those orientations over appreciable strains.

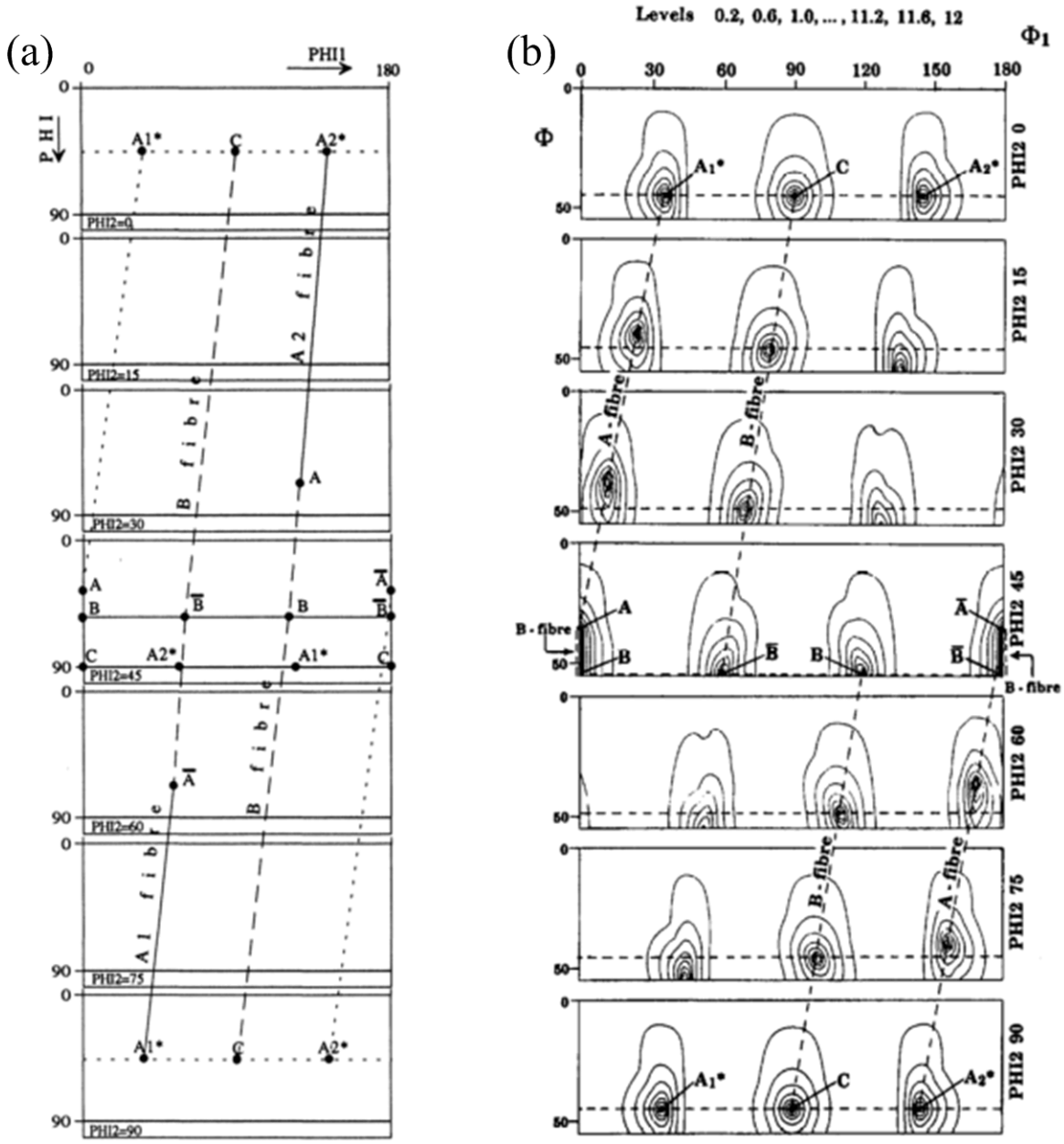

Fig. 2.17 (a) Positions of the ideal components and locations of the three fibres in the ODF sections [169]. (b) orientation persistence map in Euler space (m=0.05) [167].

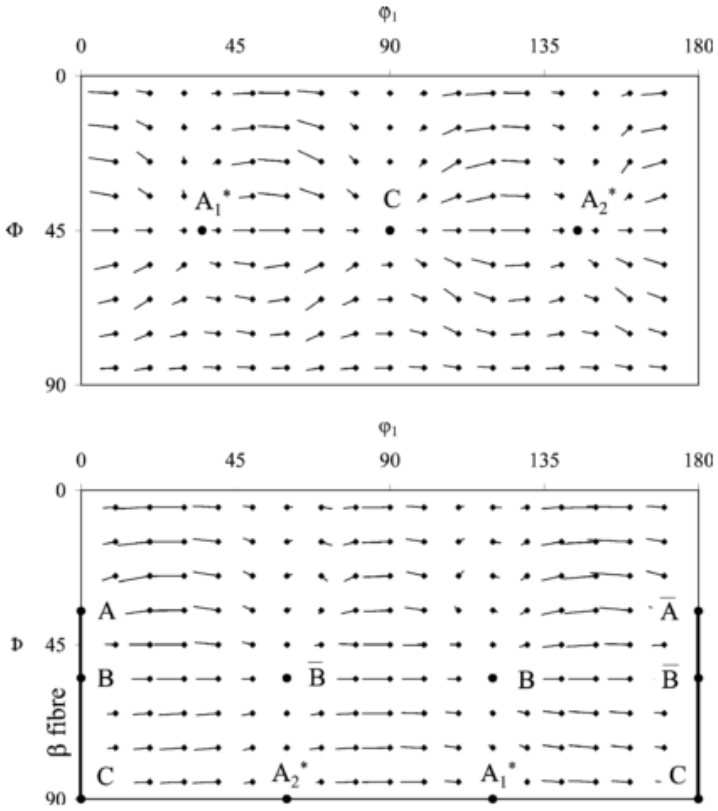

Fig. 2.18 Rotation fields for fixed torsion of fcc material calculated using a full-constraint rate sensitive model (m =0.05) for {111}<110> slip. The plots are in the Bunge ODF notation for the $\Phi_2 = 0°$ and $\Phi_2 = 45°$ sections [153].

Up to now, texture evolution during the HPT process has been studied for a wide range of metals and alloys, such as Pure Al [47,49,52], Pure Ni and single crystal [44,45,47,48,172], Pure Cu and alloys [43,46,54], Mg and alloys [55,173], Ti [43,174], and may other alloys [50,56,57,175–177] and so on. It was found that the ideal texture of polycrystalline materials after HPT could be defined directly from those revealed for the case of above mentioned torsion texture. Generally, the experimental measurements revealed that the texture developed in HPT processed polycrystalline materials possessed the main components of the ideal torsion texture but there were significant variations both in the intensity and in the relative proportion of each individual texture component at different stage of HPT straining. That is to say, different ideal components dominated the developed texture at various strain levels of HPT deformation. At high HPT strains, the typical torsion texture usually could be

developed. Fig. 2.19 shows the representative texture evolution process with increasing HPT deformation, where the aluminum A1050 was subjected to a straining of (a) ε =2, through (b) ε =4, (c) ε =6 up to (d) ε =8 [52]. In order to follow the general strength of texture, the texture component intensities were also calculated and plotted in Fig. 2.20 [52]. It was found that for lower strain level, $\varepsilon = 2$, texture was involved a strong presence of A-fibre orientations which dominated the developed texture. At $\varepsilon = 4$, the A-fibre orientations existed in similar fraction but there was a large increase in the volume fraction of the C component. With the increasing strain, the C-fibre became dominantly stronger with a slightly increase in B-fibre. Further increasing the strain to a shear strain of 20, the C component went up to an intensity of 11 while the increase in the intensity of $\overline{\mathrm{A}}/\overline{\mathrm{B}}$ was also evident where the typical torsion texture formed.

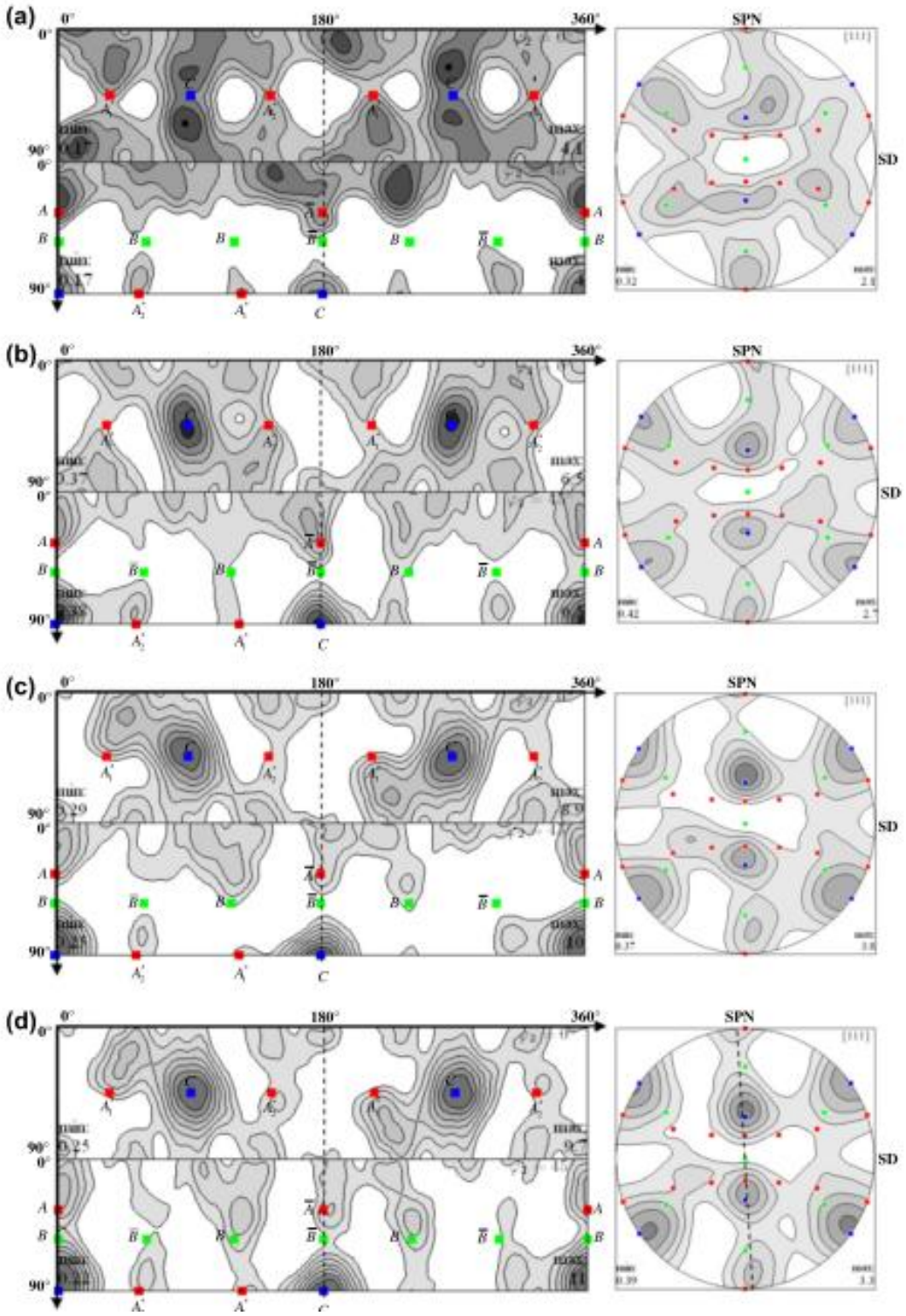

Fig. 2.19 Texture development of the HPTT deformed Al tubes from shear of (a) $\varepsilon = 2$ through (b) $\varepsilon = 4$, (c) $\varepsilon = 6$ up to (d) $\varepsilon = 8$. Intensity levels: 0.7 1.0 1.4 2.0 2.8 4.0 5.6 (x random) [52].

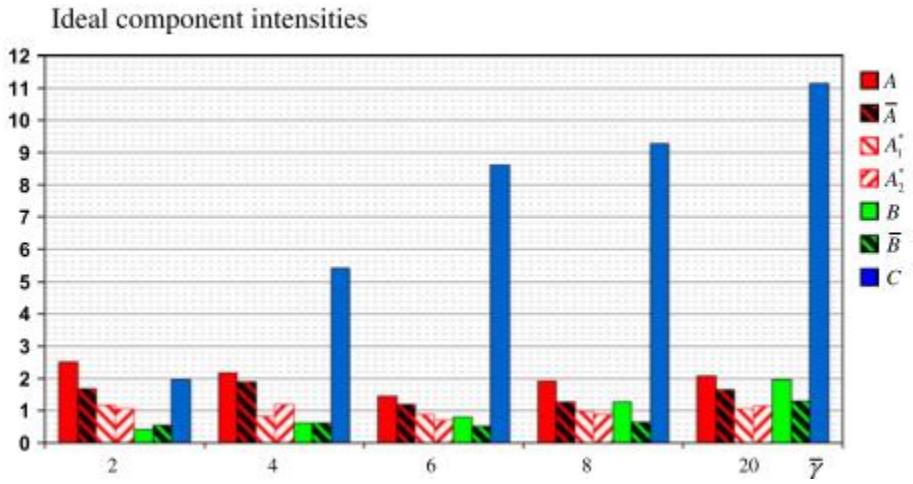

Fig. 2.20 Evolution of the intensities of the ideal texture components as a function of shear (x random) [52].

It is worthy to note that, texture evolutions in single crystals are different from the polycrystalline materials during the early stage of HPT straining. Hafok and Pippan [48,146,147] examined the microtexture evolution of Ni single crystals deformed by HPT, as shown in Fig. 2.21. At relatively small strains levels, in Figs. 2.21(a)-(c), the HPT deformation led to microtexture with a particular streaks orientation distribution connecting the initial crystallographic orientation, white squares in the pole figure, with the first preferred orientation marked by white circles. The first preferred orientation was not stable, as the HPT deformation proceeded, more regions occupied an orientation close to the second preferred orientation marked by white stars in the pole figure, as shown in Fig. 2.21(d). With increasing equivalent strain, the second preferred orientation became smear out (see Fig. 2.21(e)) but a maximum in the centre of the (001) pole figure was still visible, as can be seen in Figs. 2.21(f)-(h). In the saturation region of the torque curve, the crystallographic orientation distribution of Fig. 2.21(i) also illustrated a typical torsion texture.

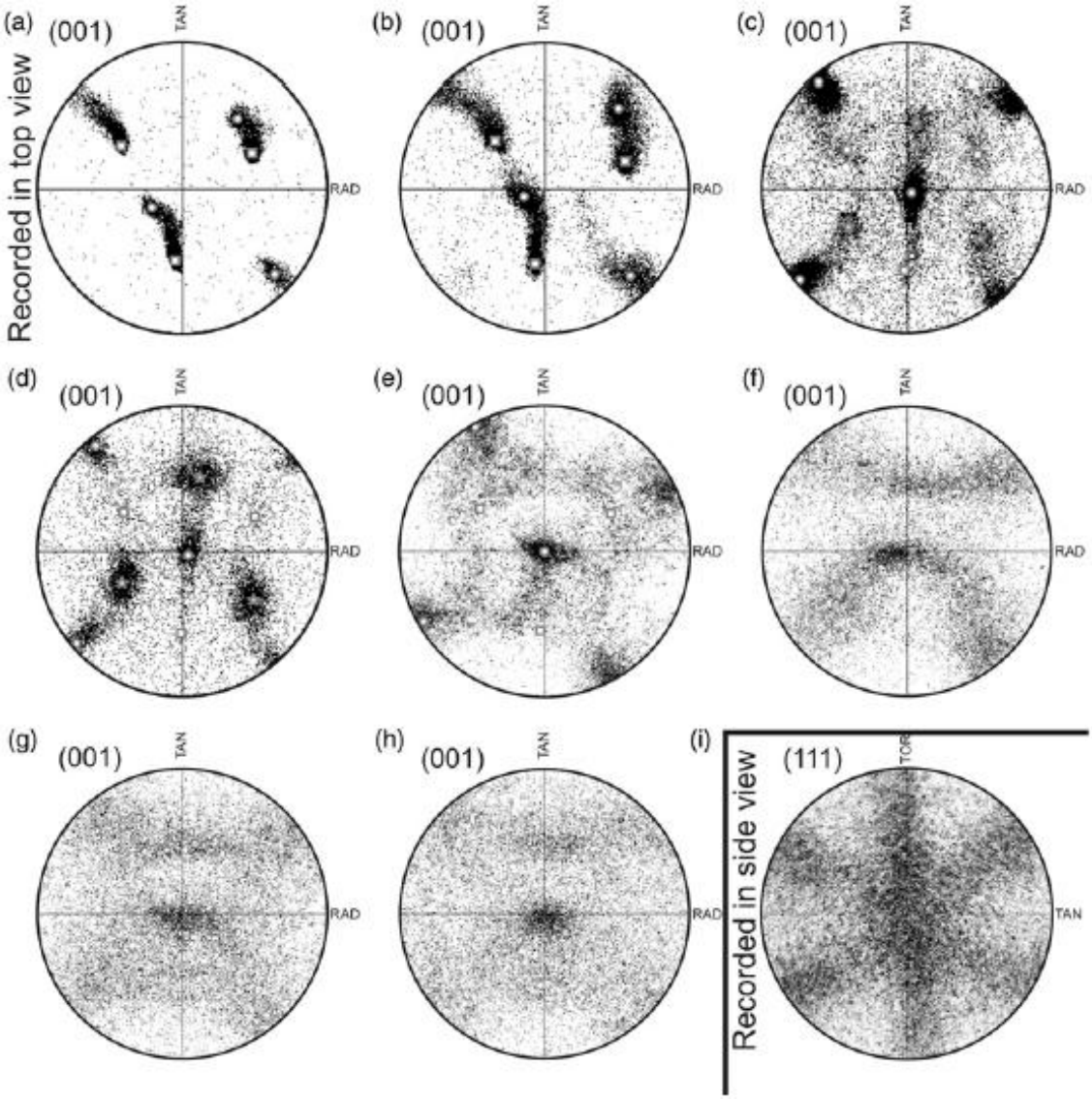

Fig. 2.21 Texture development of the <111> nickel single crystal. The scan size of the evaluated pole figures was 30 μmX30 μm. The (0 0 1) pole figures correspond to an equivalent strain of (a) 1, (b) 2, (c) 2.5, (d) 5, (e) 8, (f) 12, (g) 16, (h) 32 and (i) 32 [48].

2.4. Classic Finite Element Method Simulations of HPT

The classic finite element method (FEM) model has been widely used to simulate the HPT process. The first FEM study of HPT was carried out by Kim et al. [58,59] to investigate the deformation geometry of the pure copper workpiece during the unconstrained HPT process. They found that the normal pressure varied as a function of the distance to the center of the

sample which resulted in the sample thickness decreased with distance from the center. Rosochowski et al. [61] adopted the FEM simulation to investigate the bulk material deformation behavior and the simulation results revealed that the distribution of strain varied through the thickness of the sample. Busquet [178] developed a 3D elastic-plastic model to study the formation mechanisms of tribologically transformed structures of cylindrical samples compressed and sheared between two Bridgeman anvils. Estrin et al. [62] carried out the FEM simulation to study the HPT process for thin samples. They found there was a pronounced strain gradient existing in the sample surface along the radius within the first turn and further predicted that at least eight turns were required to approach uniformity of strain across the sample. Figueiredo, et al. [63–65] adopted the FEM modeling to examine the plastic flow processes and the distribution of temperature in quasi-constrained HPT process. The effective strain distribution along the radial direction on the top surface shown in the Fig. 2.22 indicated that there were low levels of strain near the center of the sample and they increased essentially linearly with the distance from the center to the edge. Moreover, the strain did not vary along the through thickness direction. The mean stresses during processing varied linearly with the distance from the center of the disk such that there were higher compressive stresses in the disk centers and lower stresses at the edges, as shown in Fig. 2.23. Song et al. [68] constructed a FEM model for the quasi-constrained HPT process to investigate the effect of surface friction. They found that friction played an important role in the evolution of effective strain and friction force influenced the effective strain more in the middle and edge regions than in the central region, as shown in Fig. 2.24(a). Furthermore, they reported that there was a critical friction coefficient in which the effective strain varied sharply with increasing friction coefficient, as could be observed in Fig. 2.24(b).

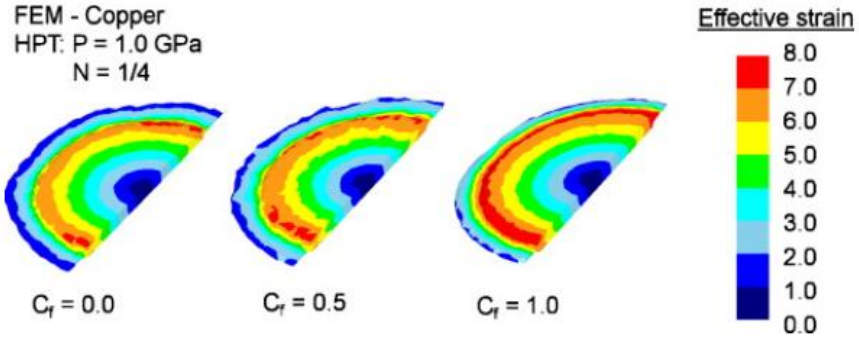

Fig. 2.22 The distributions of the effective strains at the top surfaces of one-half of the disks after a quarter turn of quasi-constrained HPT under an applied pressure of 1.0 GPa [65].

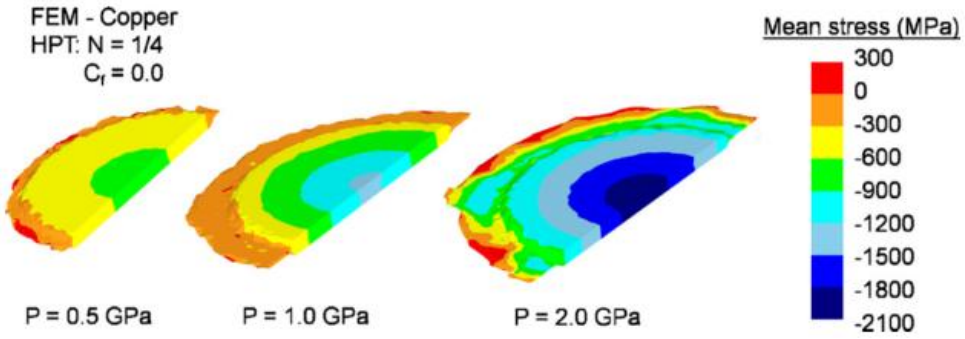

Fig. 2.23 The distribution of mean stresses at the top surfaces of one-half of the disks in simulations considering N = 1/4 turn, C_f = 0.0 and different applied pressures from 0.5 to 2.0 GPa [65].

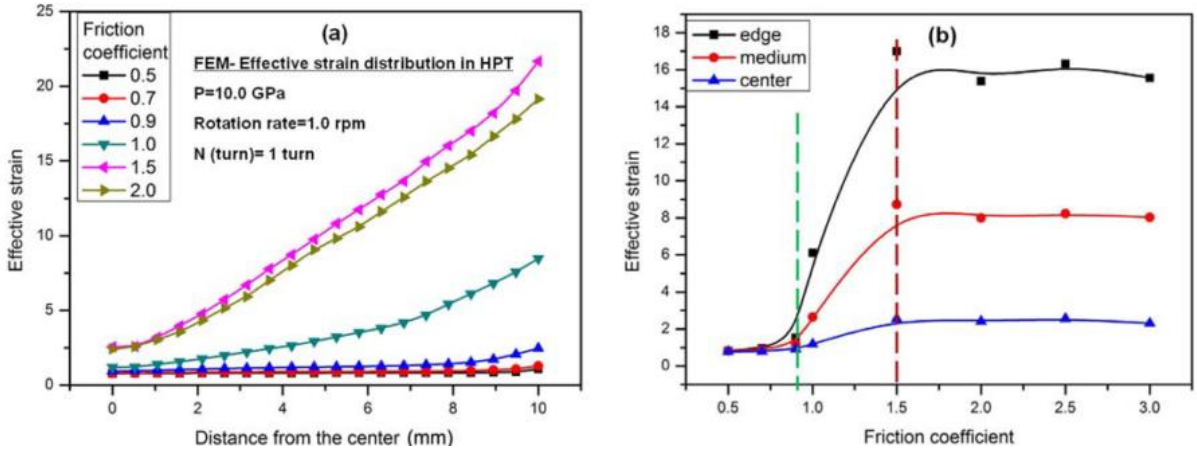

Fig. 2.24 Simulated effective strain distribution on the contact surface of the HPT samples along with the different friction coefficient.

In general, simple continuum-based FEM simulations of the HPT process are capable of providing information of mechanical characteristics of HPT processed materials, such as the characteristics of material flow, the distribution and evolution of the stress and strain, and the changes of sample geometry after deformation. However, unlike the conventional metal forming processes, such as forging, rolling, extrusion and drawing, whose primary purpose is to control the shape and size of workpieces, the HPT process aims at modifying the microstructures and the ensuing properties of the material. Therefore, the most important expected outcomes of simulations of the HPT process are those providing information on the evolution of microstructural features (texture evolution, grain fragmentation, plastic deformation anisotropy) on top of the mechanistic characteristics.

2.5 Crystal Plasticity Modeling of HPT

Up to now, only a few efforts have been devoted to simulate the HPT process adopting crystal plasticity. These studies can be categorized into three groups. The first group was analytical model; the second group was based on the Taylor-type models, and the last group used the CPFEM model.

2.5.1 Analytical Models

The first type of analytical approaches is based on the idea of dislocation density. Estrin et al. [69,179] proposed an analytical model combining the dislocation density based constitutive formulation with a particular gradient plasticity frame to describe the deformation behavior of copper in HPT. This constitutive formulation was based on a phase mixture model in which the material was partitioned in two ‘phases’, the dislocation densities in cell walls and the dislocation densities in cell interior. Two distinct physical mechanisms which give rise to gradient plasticity, the occurrence of geometrically necessary dislocations and reaction stresses, were considered. The found that initially HPT induced a strain non-uniformity that increased during approximately two revolutions, subsequent straining resulted in smoothening of the strain distribution along the specimen radius, and 5 turns were sufficient to obtain a nearly uniform distribution of strain across the entire HPT sample. Also, the predictions of the model

with respect to the evolution of dislocation densities and the ultrafine grain size produced by HPT were in good agreement with experimental results, as shown in Figs. 2.26(a-b) and (c), respectively .

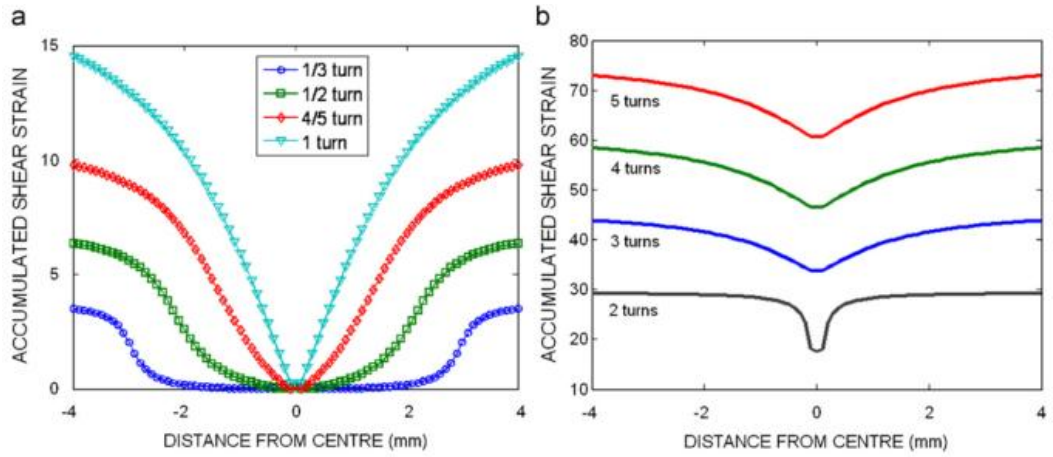

Fig. 2.25 Accumulated equivalent strain versus distance from the specimen center with increasing HPT deformation [69].

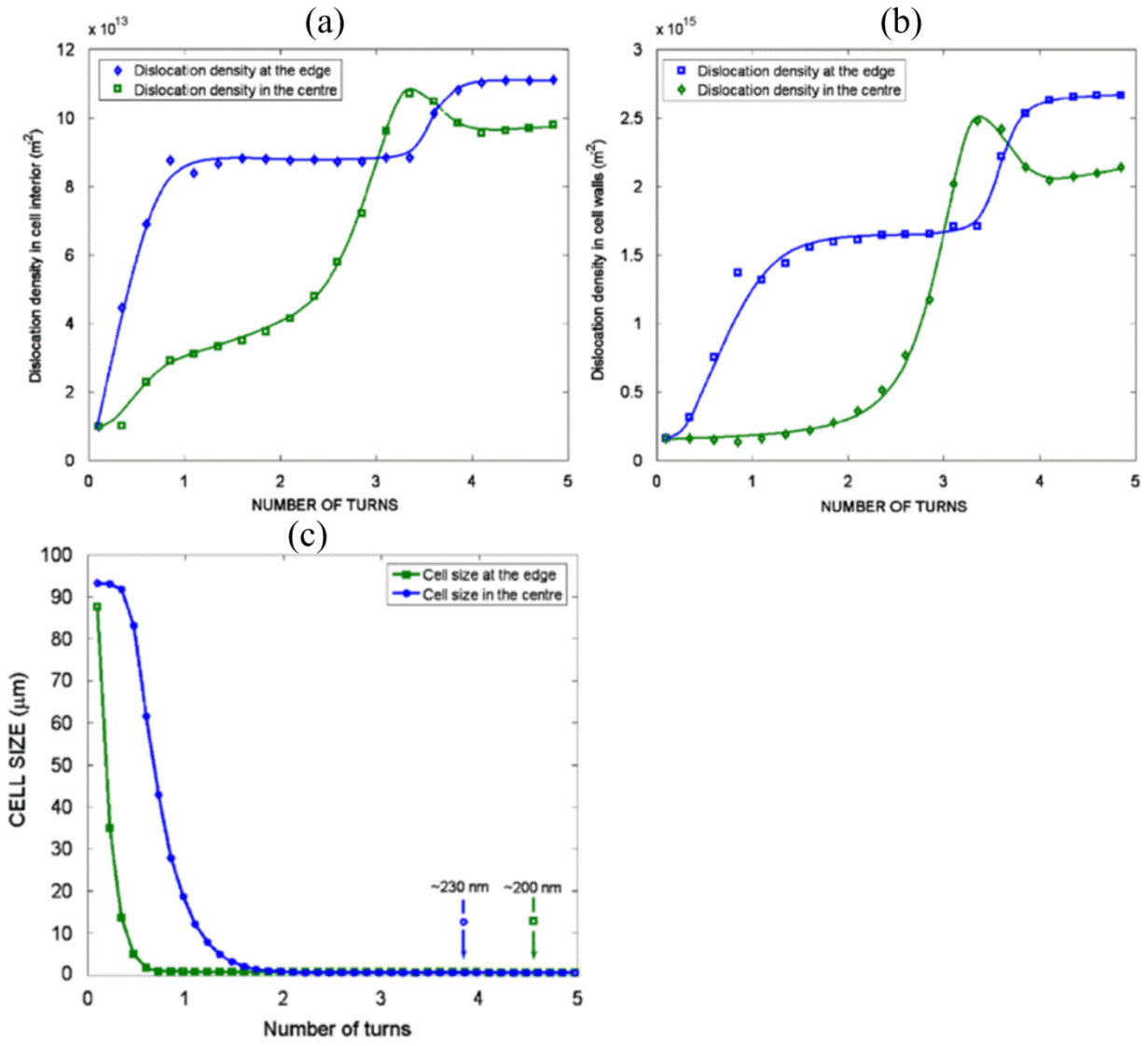

Fig. 2.26 Evolution of the dislocation density in the cell walls and cell interiors and the dislocation cell size at two different locations [69].

Another type of analytical model was recently proposed by Kratochvíl and his co-authors [70,71,180,181] that considered the HPT shearing imposed by torsion was achieved by intergranular glide within the frame work of crystal plasticity to explore a possible mechanism of microstructure evolution in materials deformed by HPT. The evolution of the HPT microstructure was considered only in a rectangular volume element, as shown in Fig. 2.27(a). The proposed model was a simplified version which was restricted to spatially homogenous plane-strain, rigid-plastic deformation achieving by two slip systems (Fig. 2.27(b)), and the rate-

independent material response was considered. They found that to satisfy the imposed HPT loading conditions, the slip systems had to rotate and change their activities during the deformation process and there was a tendency for the double slip to rotate asymptotically towards a steady state of single slip, as shown in Fig. 2.28(a). They assumed that the local variations in the crystal lattice orientation were responsible for the microstructure fragmentation, as shown in Fig. 2.28(b). They further interpretted the size of the subgrains was as the result of a competition between these two tendencies: the internal and dissipative energy tended to decrease the refined structural size, whereas the interface energy of the cell boundaries opposed this tendency. Despite the proposed model have revealed some features about the initiation of the fragmentation and the trends of its evolution, due to too many simplifications of the HPT modelling as mentioned above, the knowledge they presented about the mechanism of the observed fragmentation into the misoriented structural elements during the HPT processing was only qualitative and incomplete.

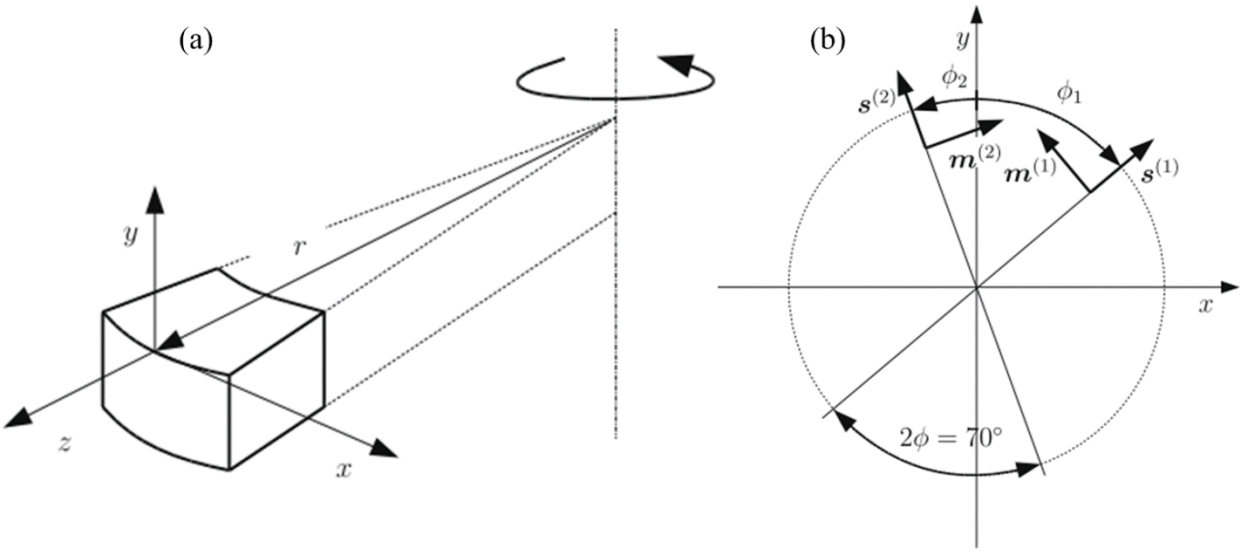

Fig. 2.27 (a) A volume element exposed to HPT. (b) Schematics of asymmetric double slip with $2\emptyset = 70°$ [70].

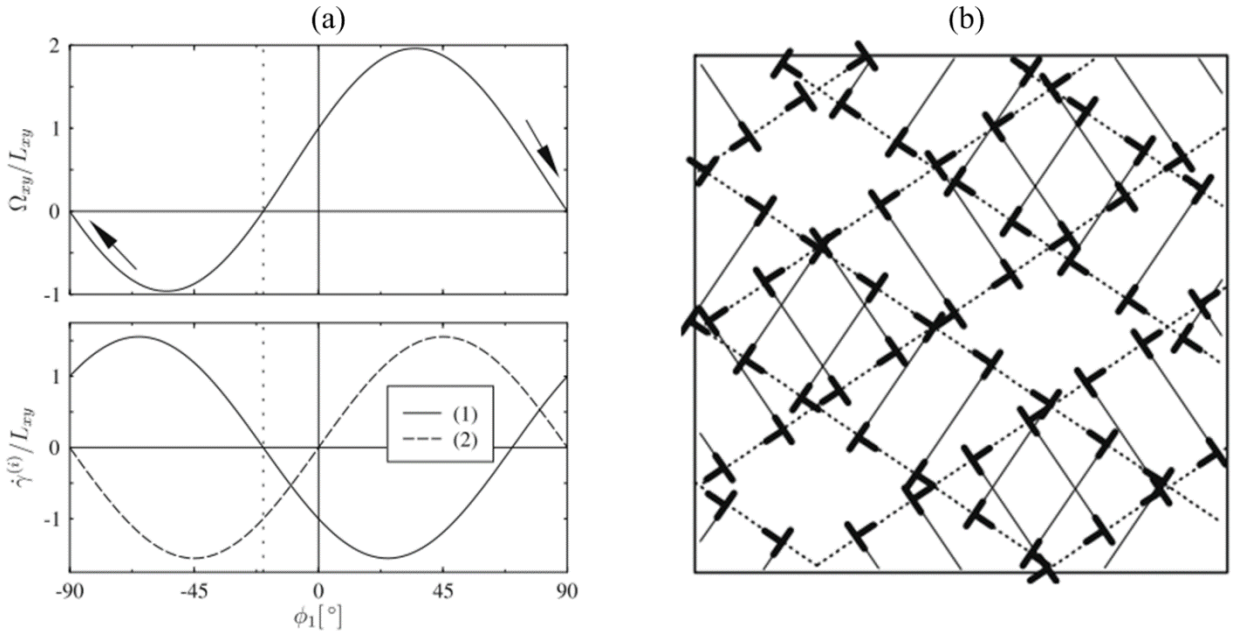

Fig. 2.28 (a) Double slip in simple shear with $2\emptyset = 70°$. The evolution towards the stable single-slip orientations is indicated by arrows. (1) and (2) indicate the slip systems. (b) Visualization of the misoriented microstructure in symmetric double slip [70].

2.5.2 Taylor-type Models

One of the earliest and most widely used crystal plasticity models, referred as fully constrained (FC) model, was proposed by Taylor [182]. In the past decades, this Taylor-type models have been extensively adopted to study the large strain torsion deformation behaviors, such as stress-strain response, shape changes, texture evolution, lattice spin and deformation anisotropy over a wide range of polycrystalline metals [183–194]. However, simulations of the HPT process using Taylor-type models are rarely reported in the literature. In 2008, Hafok and Pippan [48] applied the fully constrained Taylor model to predict the crystallographic orientations development of the initially (111)[11$\bar{2}$] oriented nickel single crystal, as shown in Fig. 2.29. After an equivalent strain of 2.5, the maximum density of calculated poles occupied close to the same orientations shown in the measured pole figure. Moreover, the equivalent strains that correspond to the different orientations were also given. By using the calculated results it can be seen that the (001)[$\bar{1}$10] orientation was maintained over a wide range of equivalent strains ranging from 0.6 to 2.2, indicating a stable orientation and the (111)[$\bar{1}2\bar{1}$]

orientation appeared in the measured pole figure at an equivalent strain of about 3–3.5. However, the computed results deviated from the measured micro-textures in some ways. The preferred orientation was achieved earlier in the experiment than the Taylor modelling. Moreover, the Taylor model was unable to predict the scatter in the radial direction appeared in the measured poles. In Taylor-type models it is assumed that the plastic strain in all the grains of the loaded specimen is the same, and equal to the macroscopically imposed strain. The shape and local neighbourhood of the grains are disregarded. The rotation of a given grain due to the applied external load is not directly affected by the rotation of neighbouring grains. Also, equilibrium between the neighbour grains is not satisfied [195,196]. Therefore, owning to these shortcomings of the Taylor model, usually it gave only reasonable predictions of the texture evolution during the HPT process. In addition, the Taylor type model rapidly becomes inaccurate at large strains [96].

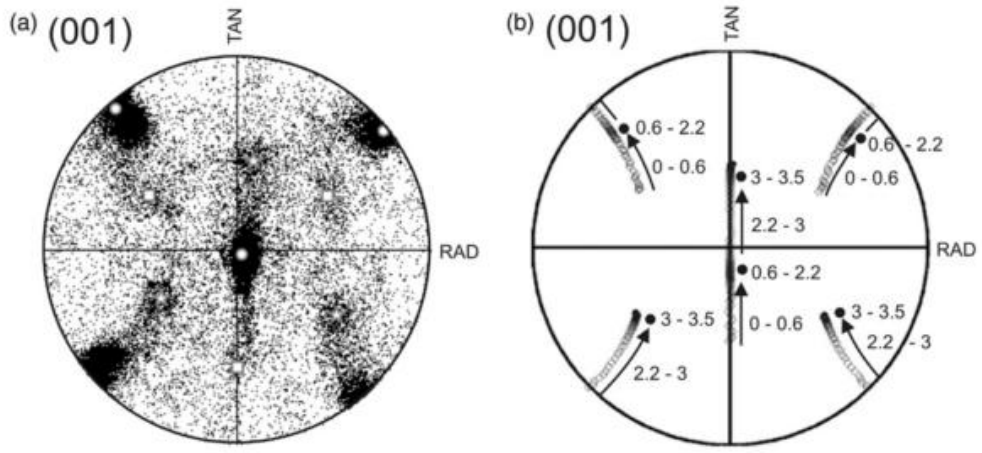

Fig. 2.29 Comparison between a micro-texture measured for the <111> nickel single crystal, (a), and a texture simulation based on the full constrained Taylor model, (b). In the computation, (b), a rough scale is given referring the calculated micro-texture evolution to the equivalent strain [48].

2.5.3 CPFEM Models

The crystal plasticity finite element method, which incorporates the crystal plasticity constitutive law into a finite element framework, is a powerful simulation tool as it combines the FEM's ability of solving complicated boundary problem and CP's ability of taking the

microstructure and deformation mechanisms into account [197]. The FEM serves as the boundary problem solver, while at each integration point the material constitutive model is based on crystal plasticity theory. Unlike the Taylor-type, the CPFEM accounts for the shape and local neighbourhood of the grains, and grain shape change is allowed. The rotation of a given grain due to the applied external load directly affects the rotation of its neighbouring grains. Because of these features, i.e. accounting for local effects, the CPFEM can be potentially used to model local heterogeneity and material failure [198–200]. This is a significant feature of the CPFEM, because the other modelling approaches (Taylor and VPSC) are limited in predicting the material failure caused by local texture effects. Moreover, in the CPFEM, each grain is in direct interaction with the neighbouring grains, and the equilibrium of the forces and the compatibility of the displacements are simultaneously satisfied between them using a weak form of the principle of virtual work in a given finite-volume element [201]. In addition, various constitutive formulations for plastic flow and hardening, based on not only dislocation mechanism, but also other mechanisms such as mechanical twinning [202,203], can be added. This could result in that one type of deformation mechanism occurs at some material points, while other deformation mechanisms or a mixed mechanism may occur at remaining material points.

The first CPFEM simulation was performed by Peirce et al. [204]. With the increase of computation power, CPFEM simulations have been extended from simplified 2-D setups with two or three slip systems for single crystal [204] and polycrystal [205] to 3-D setup with the all the 12 slips system for FCC and complex grain arrangements [206]. The use of CPFEM for FCC materials was well established in [207–209]. A recent comprehensive review of CPFEM has been done by Roters et al. [199]

For the various severe plastic deformation techniques, numerous simulation works using CPFEM have already been carried out to investigate the plastic deformation behavior in ECAP [210–216] and ARB [217–219]. However, up to now, for the HPT process, relatively limited studies based on the CPFEM model have been reported in the literature. Recently, Kim et al. constructed a dislocation density-based finite element model to analyze the large strain

deformation behavior of copper under high-pressure torsion [60,72,73]. This model was based on the concept that the material comprises two 'phases', the dislocation cell walls with dislocation density ρ_w, and the cell interiors with dislocation density ρ_c, which were introduced as scalar internal variables of the model. Ref. [60] only focused on the investigation of deformation geometry of the workpiece and the strain distribution and development during HPT processing, as shown in Fig. 2.30. Therefore, it's not able to reflect the underlying deformation mechanism of HPT processing from the aspect of micro-scale. Refs. [72,73] reported that dislocation density increased with the increasing applied strain and tended to saturation at large strains, as shown in Fig. 2.31. The simulated results for the dislocation density and the grain size agreed with the experimental data, as could be observed in Figs. 2.32(a)-(b), respectively. However, they only studied the evolutions of dislocation density and dislocation cell size with the progressive HPT straining, and it is insufficient to fully understand the deformation mechanism during the HPT process.

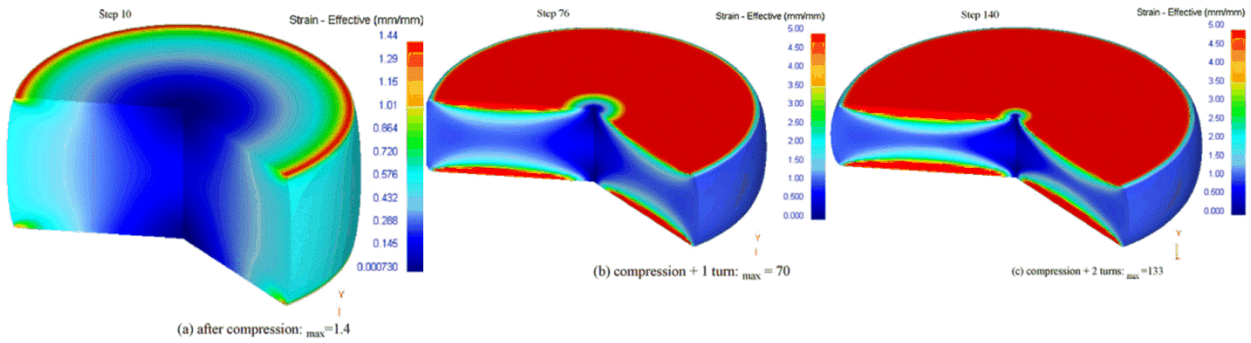

Fig. 2.30 Deformed geometries with effective strain contour (a) after compression: ε_{max}=1.4, (b) compression +one turn: ε_{max} =70 and (c) compression +two turns: ε_{max}=133[60]**.**

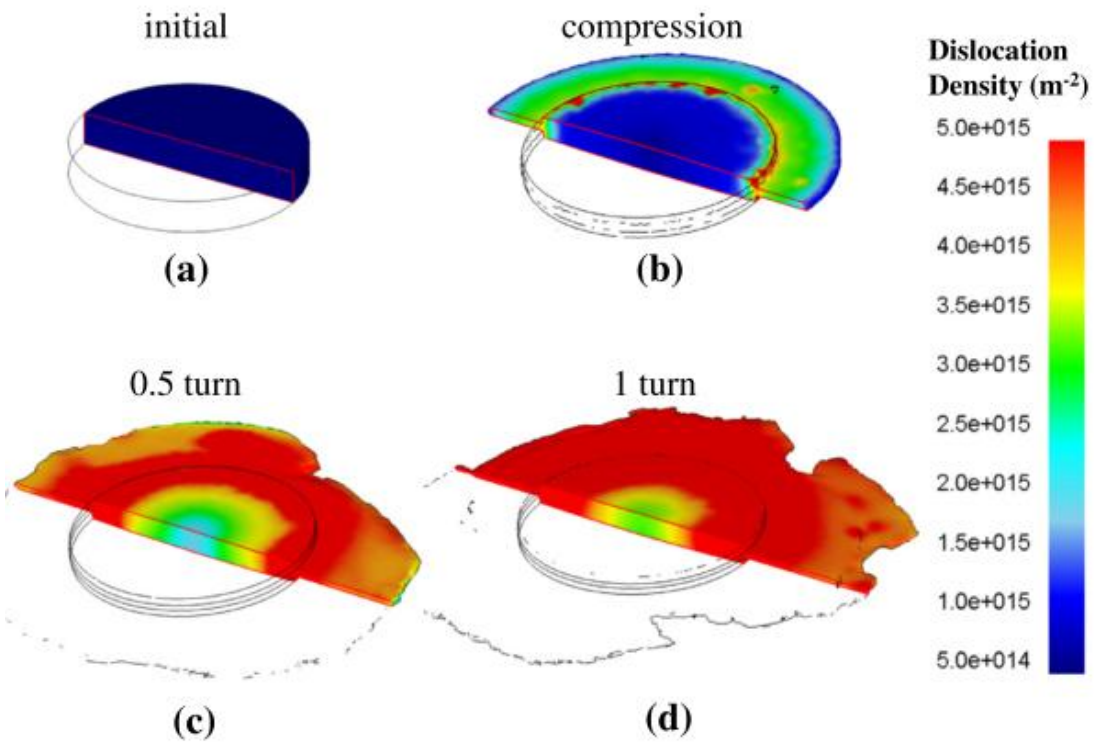

Fig. 2.31 Dislocation density distributions as calculated by FEM: (a) initial, (b) after compression, (c) after 0.5 turn and (d) after 1 turn [73].

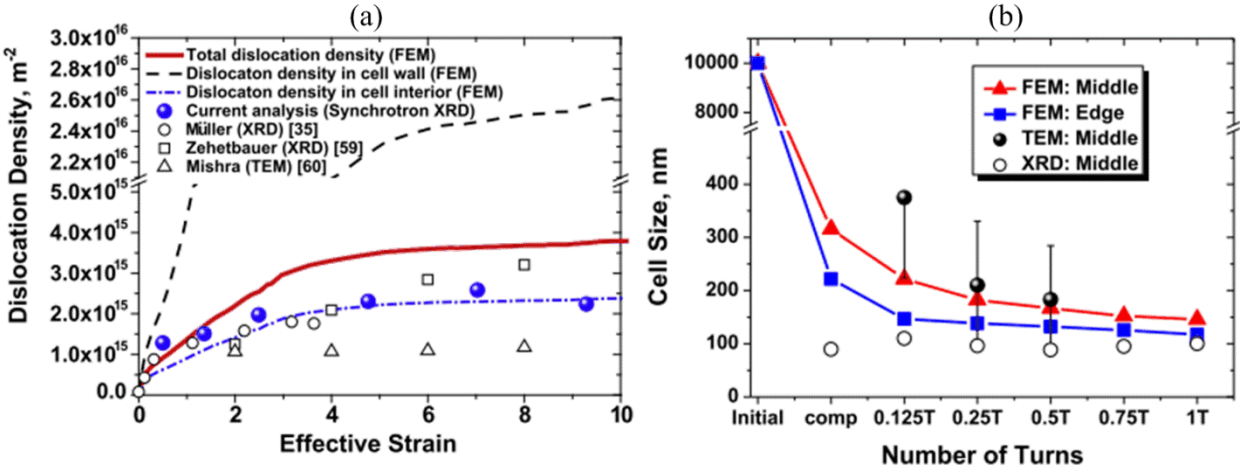

Fig. 2.32 (a) Comparison of dislocation densities from experimental results and FEM simulations for the middle position of the disk samples. (b) Cell size measured by TEM and XRD and calculated by FEM simulations [73].

2.6 Summary and Research Scope of this Thesis

HPT processing is one of the most widely used SPD techniques and is proved to be the most effective in grain refinement and improving the strength of materials. Compared with other SPD processes, the HPT technique offers a large number of advantages [10].

1. Most importantly, extremely high shear stain can be achieved in a very simple way. One revolution of the 0.8-mm-thick sample corresponds to an equivalent strain of 18 at the radius of 4mm. One hundred revolutions, which are usually not difficult to apply, correspond to an equivalent strain of 1800. Such large equivalent strains are basically impossible to be achieved by other SPD methods.
2. Most SPDs offer only a stepwise application of stain while HPT permits a continuous strain without changing the working conditions.
3. HPT permits the SPD of relatively brittle or high-strength materials at low temperatures, at which severe deformation is often impossible.
4. HPT is more effective in producing exceptionally small grain size than other SPD technique and a much higher fraction of high-angle boundaries is shown after deformation by HPT.

Up to now, extensively experimental researches related with the HPT process have been reported for a wide range of materials, including Ni single crystals and alloys, Al and alloys, Cu and alloys, iron, Ti alloys, Mg alloys and so on. The experimental investigations focused on measurements of microhardness, microstructure, texture and mechanical properties, etc. of HPT processed materials. The experimental observations are undoubtedly essential to understanding the deformation mechanism in HPT. However, it only provides limited information. The comprehensive understanding can only be achieved by combination of advanced experimental technique and accurate modeling. Until now, unlikely the ECAP process, only a few numerical simulations have been conducted for the HPT process and the majority of the simulations were carried out using classic elasto-plastic FEM method. Although the elasto-plastic FEM simulations have provided some information of deformation geometry and solid mechanics variables, such as stress, strain, temperature and forming load, they were not capable of reflecting the deformation principles of HPT from micro-scale. Some analytical

models and a full constrain Taylor-type model have been developed to investigate the deformation homogeneity, microstructure fragmentation and texture evolution during the HPT process. Because of their assumptions and simplifications, these models did not give satisfactory predictions. Very recently, the FEM simulation of the HPT process based on a dislocation density-based constitutive model was carried out. However, they only studied the behaviors of dislocation density and dislocation cell size during the HPT process and it was insufficient to fully understand the deformation mechanism of HPT.

In summary, HPT has attracted significant research interests during the last 25 years as this metal forming process provides an opportunity for achieving exceptional grain refinement, often to the nano-scale, and exceptionally high strength. Extensive papers related to the HPT process have been published in the literatures, and the majority of these works dealed with experimental observations and measurements over a wide range of HPT processed materials. To achieve deeper understanding of the experimentally observed material behaviors, a few numerical simulations of HPT have been conducted. However, due the aforementioned problems of these models, they only provided limited valuable information or give unsatisfactory predictions. Moreover, there are still more problems about texture evolution, grain fragmentation and other plastic deformation behaviors needed to be solved.

In this thesis, a CPFEM model, which is regarded as the best model for the simulation of plastic deformation of crystalline materials, has been developed to simulate the HPT process of single crystals. The aims and objectives of this thesis are

(1) to predict the evolution of crystallographic texture with continuous straining during the HPT process, to investigate the characteristics of crystallographic slip and lattice rotation and to further explore the underlying mechanism of crystallographic texture evolution in HPT;
(2) to simulate the grain refinement process of initially single crystals with increasing plastic deformation in HPT, to investigate how an originally single crystal fragments into many different oriented grains after HPT deformation and to reveal the underlying mechanism of grain refinement and the formation of HAGBs in HPT;

(3) to study the plastic deformation anisotropy of HPT deformed single crystals and to figure out the relationship between the microscopic crystallographic orientation, slip activity, lattice rotation and the macroscopic plastic deformation phenomenon.

Chapter 3 Finite Element Analysis of HPT

In this chapter, a FEM model is constructed to simulate the plastic deformation behavior of the HPT process using the commercial software ABAQUS. The major challenge in this simulation is that as the torsion strain is continuously introduced, the mesh becomes significantly distorted by the overall heavy deformation, leading to a deterioration of the numerical accuracy or even encountering a convergence problem. In order to overcome this problem, one of the adaptive meshing techniques, known as mesh to mesh solution (MTMS) mapping analysis [220] is periodically adopted. The Mises stress and equivalent strain distribution and evolution with progressive HPT straining are examined and analyzed in details. To validate the constructed FEM model, the simulation results are compared with the previously published experimental measurements.

3.1 Adaptive Meshing Techniques

Three different adaptive meshing techniques are available in the commercial finite element software ABAQUS: Arbitrary Lagrangian Eulerian (ALE) adaptive meshing, varying topology (VT) adaptive remeshing, and mesh to mesh solution (MTMS) mapping analysis [220]. A brief introduction to these three adaptive meshing techniques is given in the following text.

3.1.1 ALE Adaptive Meshing Analysis

ALE adaptive meshing provides control of mesh distortion. A single mesh definition that gradually becomes smoother within the steps of the analysis has been used. A high quality mesh can be maintained throughout the analysis by allowing the mesh to move independently of the material, even when large deformation or loss of material occurs. In an ALE analysis the element can only be defined as a single material, so a Lagrangian adaptive mesh domain will be created. The domain as a whole will follow the material originally inside it, which is the proper physical interpretation for most structural analyses. ALE analysis in Abaqus/Standard is intended to solve Lagrangian problems and to model the effects of ablation, or wear of

materials. It can also be used in geometrically nonlinear static, steady-state transport, coupled pore fluid flow, and stress, and coupled temperature-displacement procedures. However, the application of ALE analysis in Abaqus/Standard is limited due to the following four reasons. Firstly, initial mesh sweeps cannot be used to improve the quality off the initial mesh definition and secondly, the diagnostic capabilities are limited. Thirdly, this analysis is not intended to be used in general classes of large deformation problems and finally, the material properties of the fluid do not change as a result of smoothing the mesh [220].

3.1.2 VT Adaptive Remeshing Analysis

VT adaptive remeshing involves the iterative generation of multiple dissimilar meshes to determine a single, optimized mesh used throughout the analysis, with the aim of minimizing the number of elements and cost of the solution. Therefore, VT adaptive remeshing can be used to obtain a mesh which provides a balance between the cost of the analysis and the desired accuracy. When incorporating the VT adaptive remeshing into the Abaqus/CAE model, the remeshing rules and the remeshing area should be defined first. Then the error indicator output variables, the sizing method and size constraints are required. A new and smoother mesh in the specified regions will finally be created by sweeping iteratively over the adaptive mesh domain. During each sweep of the mesh, nodes in the domain are relocated based on the current positions of neighboring nodes and elements to reduce element distortion. In a typical sweep a node is moved a fraction of the characteristic length of any element surrounding the node. The increasing number of sweeps leads to the increment of the intensity in each adaptive meshing increment. The default number is one. Finally the neighboring regions will also be remeshed.

VT adaptive remeshing is very helpful to improve the quality of the simulation results, especially in conditions where: (i) it is hard to design an adequately refined mesh near a region of interest; and (ii) it is not certain how refined a mesh is required to reach a particular level of accuracy. However, several limitations of the application exist. For example, Abaqus/CAE is required and only Abaqus/Standard procedures are supported. Besides, only three kinds of elements with

special shapes including planar continuum triangles and quadrilaterals, shell triangles, and quadrilaterals and tetrahedrals can be used [220].

3.1.3 MTMS Mapping Analysis

MTMS mapping is a remeshing analysis technique where a mesh significantly deformed from its original configuration is replaced by a mesh of better quality and the analysis is able to continue. In MTMS mapping, each mesh subsequent to the initial configuration reflects a solution dependent deformed configuration of the model and indicates a component of the overall analysis history. The solution variables will be propagated from one analysis to the next.

When applying the MTMS mapping analysis, it is very important to decide when to remesh. This can be done by examining the magnitude of strains that occur during the phase of the analysis. One possible criterion for remeshing is extreme element distortion in areas where high strain gradients need to be resolved accurately. Another criterion is solution discontinuity. Significant discontinuity suggests that remeshing should have done at an earlier increment before too much distortion occurs, or the meshes are not fine enough.

During the MTMS mapping analysis, all the files needed for restart and the output database must be required for the old job. The interpolation technique is used to obtain the solution variables at the nodes of the old mesh by extrapolating all values from the integration points to the nodes of each element, and then averaging these values over all similar elements abutting each node. Then the location of each integration point in the new mesh is obtained with respect to the old mesh. The variables are interpolated automatically from the nodes of the old element to the integration points of the new element. It should be noted that the boundary conditions are not carried out over from the old mesh to the new mesh. The boundary conditions applied at the beginning of the remeshed analysis should normally be the same as those in effect at the step and increment selected from the initial analysis. Although the boundary conditions can be altered, the problem may fail to converge if the structure is a long way from an equilibrium state. There are no restrictions on applying boundary conditions and loads in the MTMS mapping analysis.

Another advantage of MTMS mapping analysis is that any of the mechanical constitutive models available in ABAQUS can be used and there is no restriction on agreement between material models in the old and new analyses. The application of MTMS mapping analysis is supported for the following five procedures, such as 'Static stress analysis', 'Quasi-static analysis', 'Fully coupled thermal-stress analysis', 'Coupled pore fluid diffusion and stress analysis' and 'Geostatic stress state'. However, it is only suitable for the continuum elements [220].

There are several reasons to choose the MTMS mapping approach in this study:

(1) The ALE analysis is not good at general classes of large deformation problems, whereas the HPT process is one of the severe plastic deformations which definitely belong to the problem of large deformation and therefore the ALE analysis is not suitable in this study [220].
(2) The VT adaptive remeshing analysis is not good at controlling distortion and is only available for the analyses submitted from Abaqus/CAE [220].
(3) The MTMS mapping is suitable to any constitutive models and there is no restriction on agreement between material models in the old and new analyses [220].

3.2 FEM model of HPT

The FEM model of the HPT process was constructed using the commercial software (ABAQUS 6.9-1). As schematically illustrated in Fig. 3.1, it consisted of the sample and the rigid body. The initial dimensions of the disk shaped sample were 10 mm in diameter by 0.8mm in thickness. Compared to the sample, in this study, the lower anvil shown in Fig. 2.6(b) was regarded as a rigid body to restrict the lateral flow of the sample. The radius of the rigid body was 5.01 mm. The sample consisted of pure copper (99.99%) material with a Young's Modulus of 110 Gpa and a Poisson's ratio of 0.34. The stress strain curve of this material can be found in Fig. 3.2 [87]. It was assumed that the hardening behavior of the sample was isotropic and independent of the strain rate and temperature. C3D8R was the type of element chosen for the sample, and 23600 elements and 26895 nodes were generated, as shown in Fig. 3.1(a). The friction coefficient

between the side surface of the sample and internal surface of the rigid body was assumed to be 0.1, which is the value generally used in cold metal forming [59].

The bottom surface of the sample was fixed. During the HPT process, the main functions of the massive pressure are that, on one hand, to ensure that there is no slippage between the surfaces of the die and the sample so that the torsion straining could be accurately introduced to achieve a large strain level; on the other hand, to ensure that the sample is deformed under quasi-hydrostatic pressure condition to prevent the fracture of the processed material so that the material could be deformed continuously without any significant changes in the overall dimensions. The compressive load does not produce any significant variation in the plastic deformation behavior of the processed material and the excellent mechanical properties of HPT processed materials are mainly attribute to the introduced large torsion straining. Therefore, in this study, the pressure was not considered, instead, the torsion was applied directly onto the reference point which was coupled to the top surface of the sample. The other freedoms of the top surface except for the axial rotation were all fixed. By this way, the material of the sample was deformed under quasi fully constrained condition, the torsion straining could be accurately introduced and the shape the sample didn't change.

As the analysis proceeded the mesh of the sample became distorted due to the large torsional strain, so that the simulations became unstable or breakdown. In order to solve this problem, the aforementioned MTMS mapping technique built in ABAQUS was employed. A regular mesh was initially used. After a pre-determined revolution of N=1/8 turn, the simulation was stopped. A new mesh for the deformed sample was consequently generated. MTMS mapping technique was used to transfer all state variable values from the old mesh to the new mesh. The simulation then re-started and the above procedure was repeated until the desired deformation of N=2 turns was reached.

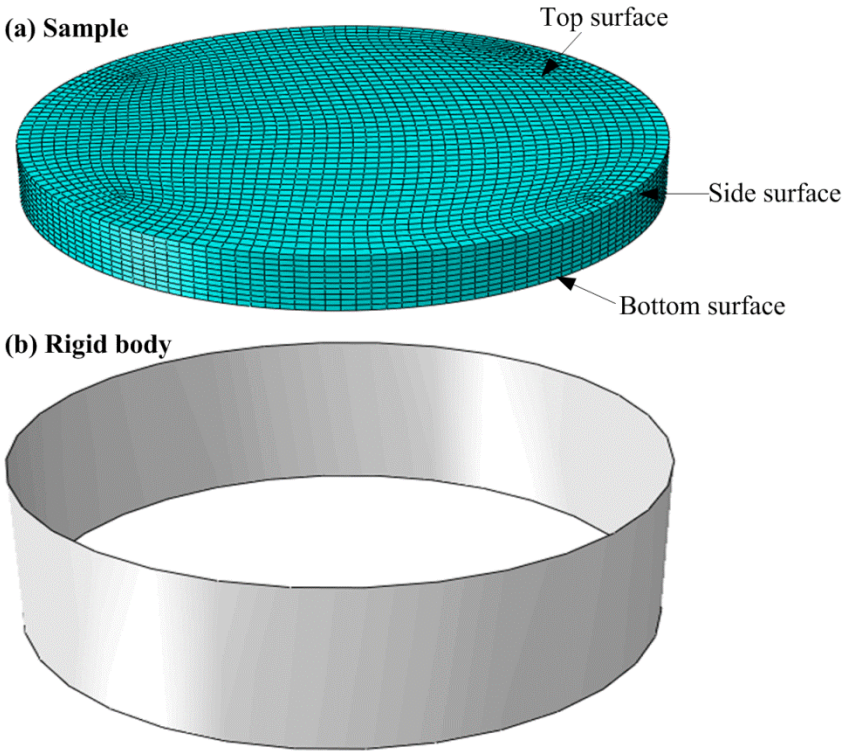

Fig. 3.1 Base FEM model of the HPT process

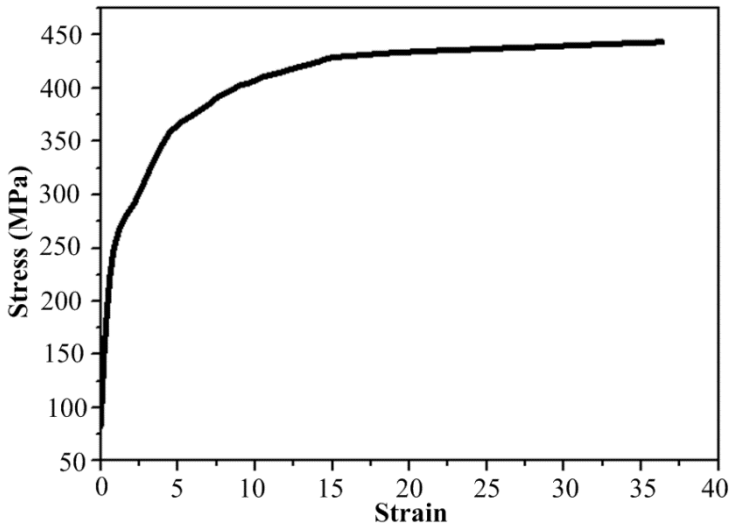

Fig. 3.2 The strain-stress curve of high pure copper [87].

3.3 Results and Discussion

3.3.1 Result of MTMS Mapping

To examine the capability of the MTMS mapping approach, the equivalent strain (variable PEEQ in ABAQUS software) and Von Mises stress results obtained from the N=1/8 turn deformed and the consequently new regenerated meshes were plotted respectively, as shown in Figs. 3.3(a)-(b). The results were recorded along the radial direction ranging from the center of the sample to the edge. Seeing from Fig. 3.3(a), there is an excellent agreement in equivalent strain between the deformed mesh and the new mesh. Meanwhile, the Mises stress results also shows good coincidence apart from the small discontinuity close to core region of the sample as a consequence of the solution mapping algorithm. This indicates that the MTMS mapping approach is an adaptive remeshing method suitable for simulations of the large deformation of the HPT process.

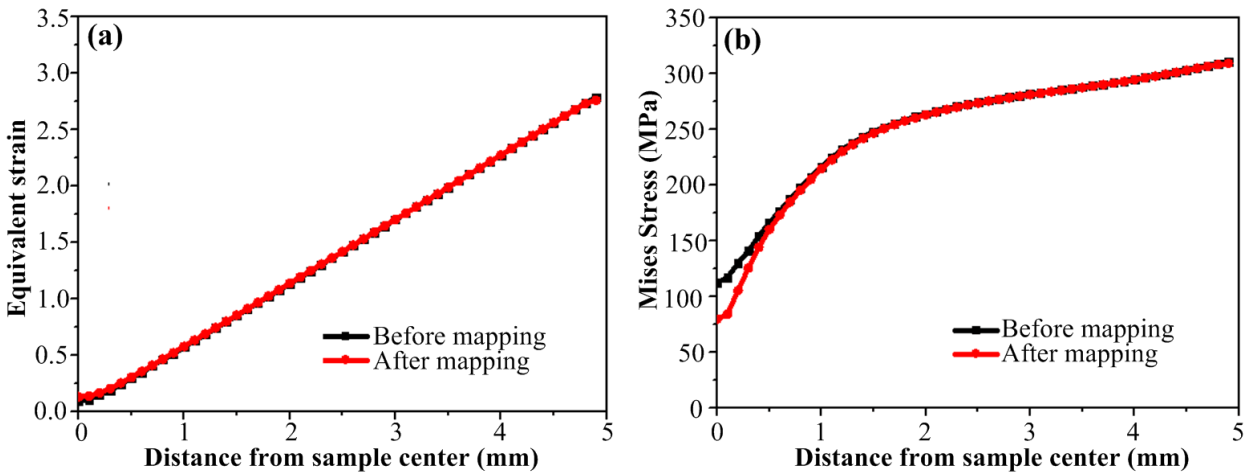

Fig. 3.3 The comparisons of (a) equivalent plastic strain, (b) Mises stress recorded along the radial direction between N=1/8 turn deformed mesh and regenerated new mesh.

3.3.2 Distribution and Evolution of Equivalent Strain

Since the mechanical properties of the HPT deformed material are directly linked to the development of plastic strain induced into the sample, the analysis of the equivalent plastic strain distribution and evolution is addressed in this section. Fig. 3.4 shows the distributions of

the equivalent strain recorded on the half-cut samples for different degrees of rotation from N=1/8 turn to 3/2 turns respectively. Three main features can be observed from the predicted strain distribution results. First, the distributions of strain are relatively similar for all simulations carried out through different numbers of revolutions: a pronounced strain gradient exists along the radial direction on the sample surface and the equivalent strain values are lowest in the center of the sample and highest at the edge. Furthermore, as the deformation proceeds, the introduced equivalent straining increases accordingly. The third important feature is that the distribution of equivalent strain is constant in the through-thickness direction at any position along the radial direction. This is consistent with the previously published experimental measurements [136,151] and numerical simulations [63,65,66,68], in which the phenomenon of homogenous deformation along the thickness direction was also reported.

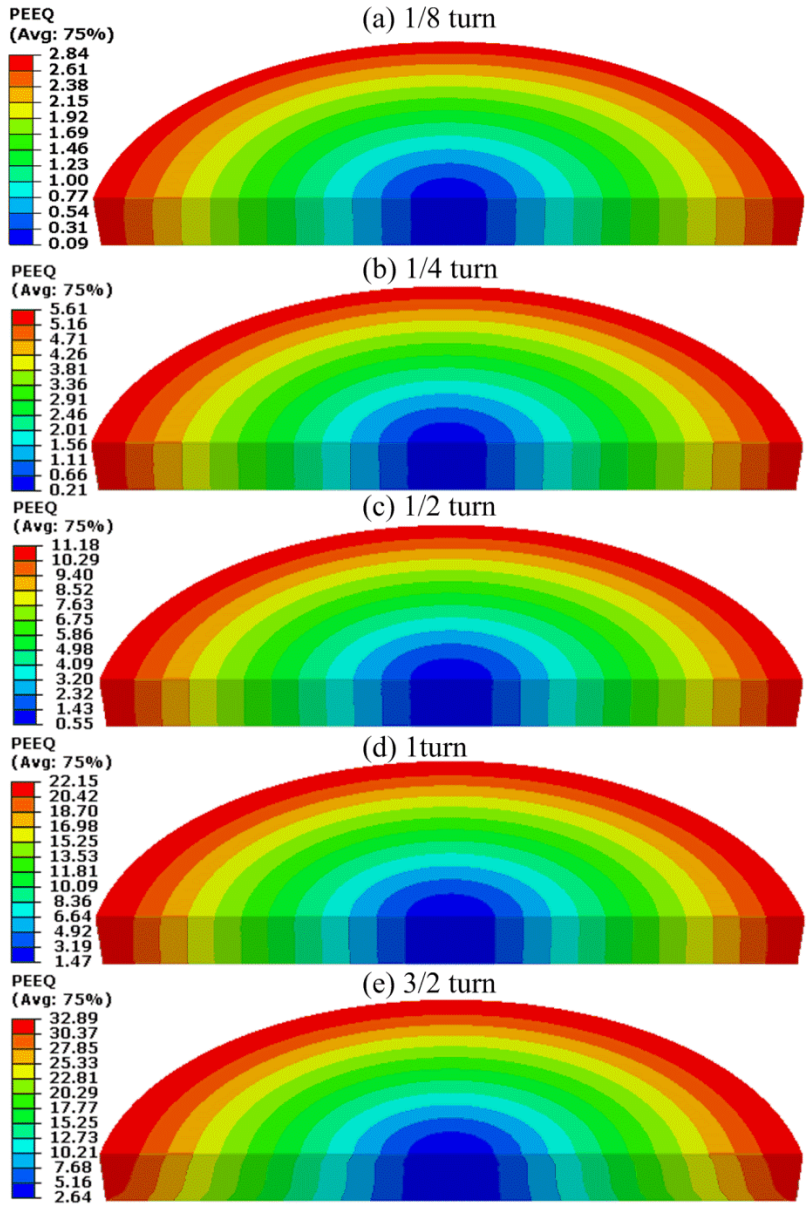

Fig. 3.4 The distributions of equivalent strain recorded on half samples after processing for different revolution numbers of N= (a) 1/8 turn, (b) 1/4 turn, (c) 1/2 turn, (d) 1 turn and (e) 3/2 turns.

In practice, the level of the equivalent strain is dependent upon the amount of rotation imposed on the sample. Fig. 3.5(a) shows the evolution in equivalent strain recoded on the sample radius with increasing sample rotation angles from N=1/8 turn to 3/2 turns. Lower level of strain could be observed near the center of the sample and there is an essentially linear increase away from the center to the edge. It should be noted the values of the equivalent

strain in the edge regions could be identified as reaching around 2.8, 5.5, 11, 22 and 32.6 after processed by increasing revolutions of N=1/8 turn, 1/4 turn, 1/2 turn, 1 turn and 3/2 turns, respectively, indicating that the introduced equivalent strain values increase approximately proportional to the imposed torsion loading.

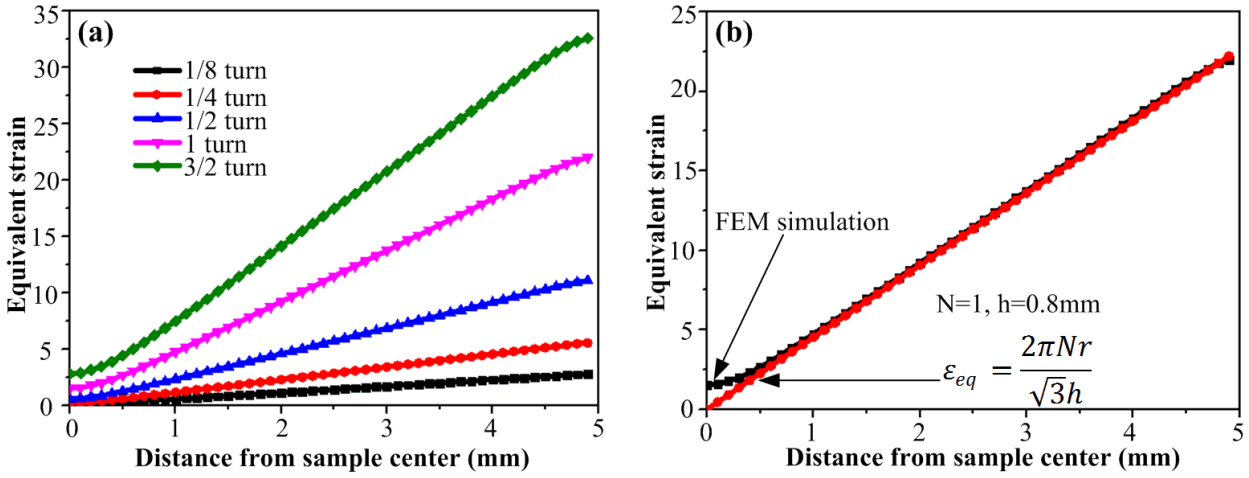

Fig. 3.5 (a) The evolution of equivalent strain as a function of distance from the center of the sample with increasing revolution numbers of N=1/8 turn, 1/4 turn, 1/2 turn, 1 turn and 3/2 turns, respectively. (b) The comparison of equivalent strain results between the ideal theoretical torsion equation and the FEM simulation after N=1 turn HPT deformation.

In the ideal condition of torsion straining, the equivalent strain, ε_{eq}, imposed on the sample, is given by an expression in the form of, $\varepsilon_{eq} = 2\pi Nr/(\sqrt{3}h)$, where N is the number of revolution turns, r is the distance from the center of the sample, and h is the thickness of the sample. This equation implies that the equivalent strain reaches a maximum at the edge of the sample, but reduces to zero at the center of the sample where r=0 mm. To validate the constructed FEM model, the equivalent strain along the sample radius after N=1 turn HPT deformation calculated by the aforementioned equation was plotted, as shown in Fig. 3.5(b). During the calculation, the parameters of N=1 turn and h=0.8 mm were adopted. The comparison between the theoretical equation and the FEM prediction shows that the FEM prediction is in well consistency with the results obtained by the theoretical equation. However, at r=0 mm, the FEM predicted strain does not equal to zero and it increases with the increasing angles of

sample rotation. After being processed by N=1 turn, the values of the equivalent plastic strains around the center region reach more than 2. This is contrary to the prediction of theory of torsion. It should be noted that, to solve the severe mesh distortion problem during the large strain HPT deformation, several remeshing steps were carried out. The new generated elements then acquired an average equivalent strain from the severe deformed old elements at the same location. Therefore, the occurrence of a large number of remeshing steps led to an attenuation in the distribution of strain close to the center of the sample. This explains the high level and curved distributions of equivalent strain near the center of the sample after large sample rotations [63].

3.3.3 Distribution and Evolution of Mises Stress

The distributions of the Von Mises stress recorded on the half-cut samples after deformed by different numbers of revolutions from N=1/8 turn to 3/2 turns were plotted, as shown in Fig. 3.6. The simulation results in Fig. 3.6 provide the clear evidence of the gradual evolution of Mises stress towards the homogenous distribution in the whole disk with increasing number of revolution turns. At the early stage of HPT deformation with N=1/8 turn, as shown in Fig. 3.6(a), the Mises stress in all domain of the sample generally increases and there is a significant variation along the radial direction with much lower values in the center of the sample than the periphery region. The contour plots in Figs 3.6(b)-(c) indicate that an increase in the applied torsion straining gives an overall increase in the Mises stress values along the radial direction, especially at the edge regions of the sample as anticipated suffered from higher strains within this region. After N=1 turn HPT deformation, seeing from Fig. 3.6(d), the outer edge region witnesses no further increase and the Mises stress values are saturated at around 440 MPa. The area of non-uniform deformation decreases as the number of revolutions increase. When the number of sample rotations reaches 3/2 turns, the homogeneity is almost established through the whole disk except for the core region, as shown in Fig. 3.6(e). It is therefore reasonable to conclude from the results recorded in Fig. 3.6, initially the higher Mises stress values are developed around the periphery of the sample, subsequently these regions sweep gradually inwards towards the center of the sample, and ultimately the homogenous distribution across

the whole disk could be anticipated if the torsion straining reaching a sufficiently large level. The similar evolutionary tendency has been widely reported by experimental measurements in [14,24,25,27–29].

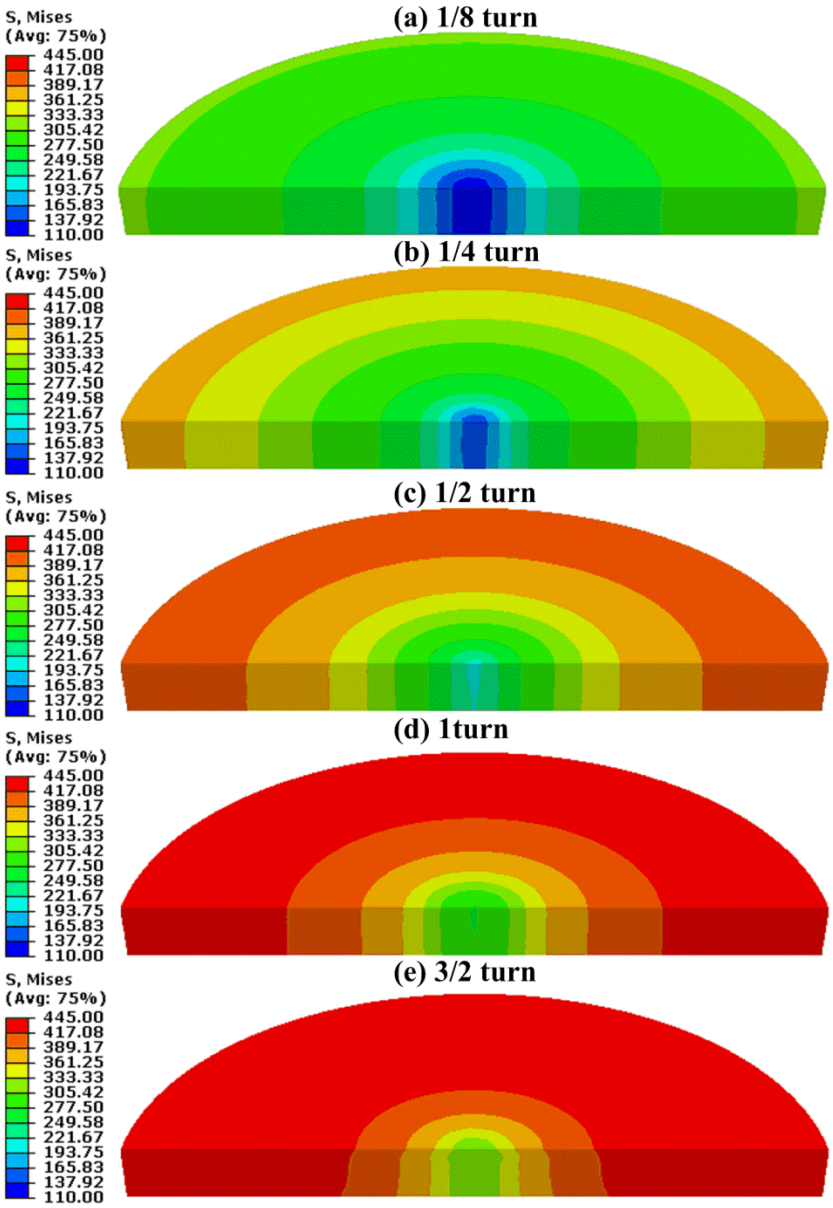

Fig. 3.6 The distributions of Mises stress recorded on half samples after processing for different revolution numbers of N= (a) 1/8 turn, (b) 1/4 turn, (c) 1/2 turn, (d) 1 turn and (e) 3/2 turns.

The evolution of the Mises stress with increasing HPT deformation is more apparently presented in Fig. 3.7 where the Mises stress values were plotted as a function of the distance

away from the center of the sample after processing by various numbers of revolution turns, N, from 1/8 to 3/2. For the condition of N=1/8 turn, it is obvious that the center of the sample is characterized by a lower Mises stress. By contrast, much higher stress values are recorded at the edge region of the sample. Increasing the numbers of HPT revolutions leads to the overall increase in the Mises stress values along the sample radius and the difference between the center and the periphery regions becomes smaller. After N=1 turn HPT deformation, the stress values at the edge of the sample remain essentially constant and almost unchanged, but the central stress values keep on increasing with the increasing number of revolutions. After N=3/2 turns, the results of the Mises stress demonstrate there is a reasonably level of homogeneity across the radius of the sample.

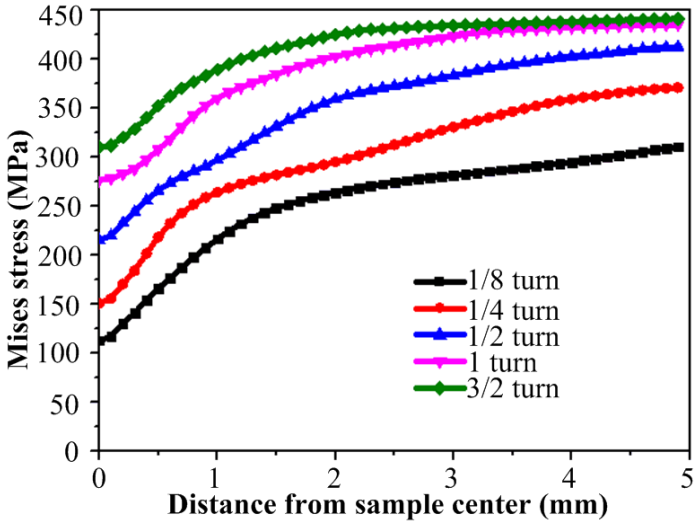

Fig. 3.7 The evolution of Mises stress as a function of distance from the sample center with increasing revolution numbers of N=1/8 turn, 1/4 turn, 1/2 turn, 1 turn and 3/2 turns, respectively.

In order to further validate the proposed FEM model for the HPT process, the experimentally measured hardness results as a function of distance from the center of the sample for different revolutions numbers of N=1/2 turn, 1 turn and 2 turns (See Ref. [87] for more details of the experimental measurements) were plotted to make comparisons with our FEM predictions, as shown in Fig. 3.8(a)-(c), respectively. The left vertical axis stands for the hardness measurements (unit: Hv) while the right vertical axis represents the predicted Mises stress (unit: MPa). Generally, hardness is related to the yield stress or flow stress at a certain strain value.

Hence, hardness can be represented as a function of distance away from the center of the sample. Strictly speaking, hardness cannot replace the stress state of a material. Nevertheless, it is useful to approximately estimate the stress state for large strains from the experimentally obtained hardness values [73].

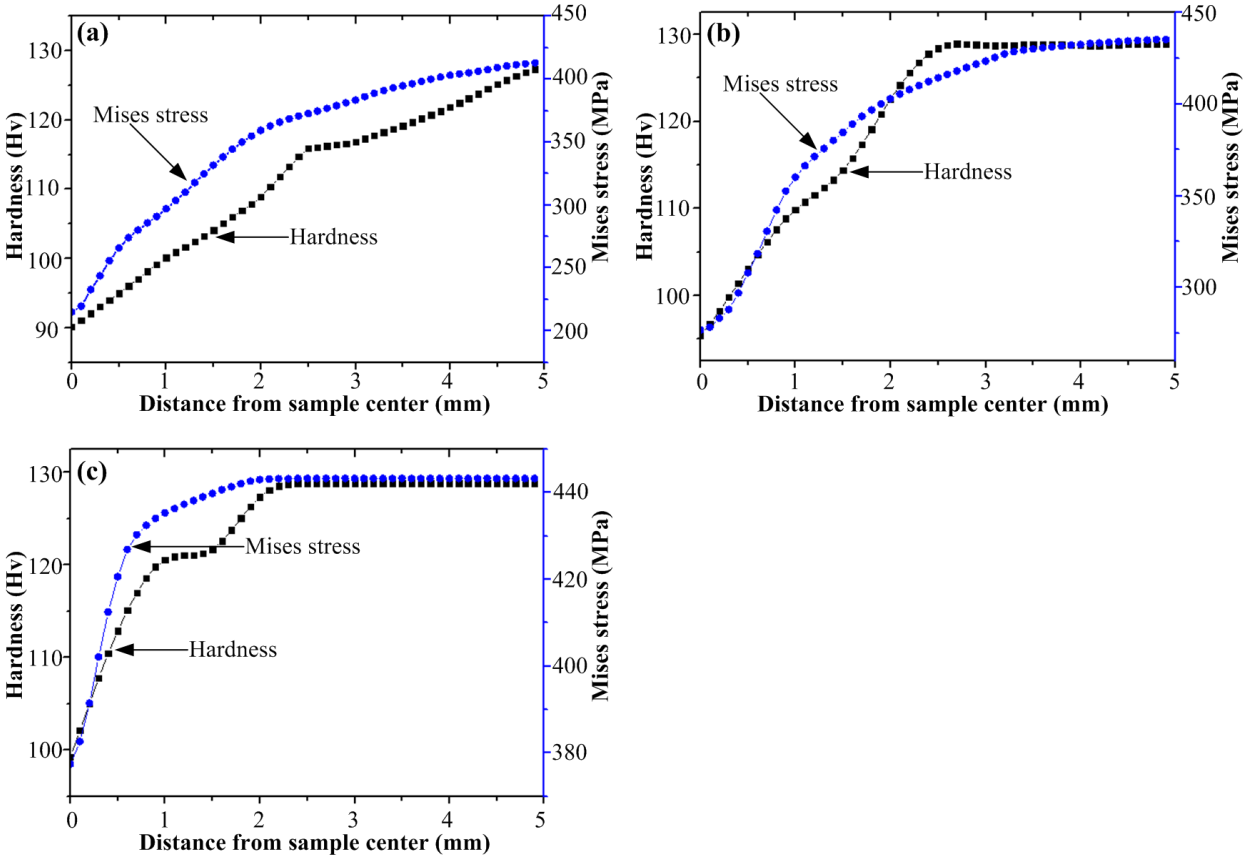

Fig. 3.8 The comparisons between the FEM simulations (Mises stress) and experimental measurements (Hardness) as a function of distance away from the center of the sample for different revolution numbers of N= (a) 1/2 turn, (b) 1 turn and (c) 2 turns.

Fig. 3.8 shows that the results of the measured hardness and the simulated Mises stress are in good consistent at different levels of HPT straining. Close examinations of Fig. 3.8(a) reveal that, after N=1/2 turn deformation, the hardness and the Mises stress show the similar distribution tendency and generally the predicted Mises stress values are slightly higher than the measured hardness. This is mainly because during the whole deformation process of simulation, no slippage between the surfaces of the die and the sample was considered, which is basically

impossible under experimental conditions. When the sample was further deformed to N=1 and 2 turns, the measured hardness and the predicted Mises stress illustrate better coincidence, particularly at regions close to the sample centers and the outer edge regions. In Fig. 3.8(a), at the edge region, the Mises stress and the hardness are ~410 MPa and ~125 Hv respectively and the ratio between them is about 3.3. In the saturated edge regions, in Figs. 3.8(b)-(c), the Mises stress values are ~440 MPa and the hardness are about ~130 Hv with a developed ratio of around 3.4. An empirical relationship between the ultimate tensile strength, σ_0, and Vickers hardness can be expressed by the equation in the form of [221],

$$\sigma_0 = \frac{3}{0.1^{n'-2}} Hv \tag{3.1}$$

Where n' is the exponent in Meyer's law [222], which equals ~2 for fully strain-hardened metals.

Therefore, the Vickers hardness of several metals is proportional to the yield strength, with a proportionality constant of approximately 3. The ratio between the predicted Mises stress of the FEM simulation and the experimentally measured hardness of is ~3.3, which is acceptable compared with the widely used factor of 3.

3.4 Summary

In this chapter, a three dimensional FEM model of the quasi fully constrained HPT process was constructed using commercial software ABAQUS. The distribution and evolution of equivalent plastic strain and Von Mises stress with increasing revolution numbers of HPT deformation were presented and analyzed in detail. The following conclusions could be drawn.

1 Remeshing and mapping solution method of ABAQUS software was adopted to solve the severe mesh distortion problem due to heavy deformation in the simulation of the HPT process. It has been found that the solution values could be accurately mapped from the old deformed meshes to the regenerated new meshes and large angles of sample rotation could be fulfilled. Therefore, the MTMs mapping method provides a solution to investigate plastic deformation

behavior under significantly large strains using FEM simulation, such as the HPT process in this study.

2 The predicted equivalent strain results showed that within the whole volume of the sample the effective strain did not vary along the thickness direction. The equivalent strain values illustrated an approximately linear increase as a function of the distance from the sample center and increased approximately proportional to the increasing imposed torsion loading. There was generally a well consistence in the equivalent strain results between the FEM simulation and those predicted by the theoretical torsion equation.

3 The predicted Mises stress results showed the gradual evolution towards the homogenous distribution across the whole sample. Initially, the significant variation along the radial direction exhibited and there were higher stress values around the edge region. Subsequently there was a tendency of sweeping of these areas of higher stress values from the outer edge region towards the center and the variation along the sample radius diminished gradually. Ultimately, a reasonably level of homogeneity could be developed over the whole sample when the introduced strain reached a sufficiently large level. The predicted Mises stress results by FEM simulation agreed well with the previously reported experimental measurements.

4 Finally, it should be noted that the 3D classic elasto-plastic FEM simulation in this chapter have provided the comprehensive information about the equivalent strain and Mises stress during the HPT process. However, some other vital plastic behaviors such as texture evolution, grain fragmentation and deformation anisotropy, etc., which play the key role in determining the mechanical properties of HPT processed material, are still not well known and should be further investigated in relation with the crystal plasticity theory. The FEM study in this chapter has established a solid model foundation for the crystal plasticity finite element modeling of the HPT process in the following chapters.

Chapter 4 Development of the CPFEM Model of HPT

A 3D CPFEM model has been developed in the thesis to simulate the HPT process. This chapter presents the basic concepts of crystal plasticity theory and implementation of crystal plasticity laws into a commercial FEM framework.

4.1 Crystal Plasticity Theory

As a general scheme of notation, vectors in the subsequent context are written as boldface lowercase letters (e.g., $\boldsymbol{a}$), tensor and matrices are written as boldface capital letters (e.g., $\boldsymbol{A}$). Cartesian components of vectors and tensors are written as, a_i and A_{ij}, respectively. All inner products are indicated by a single dot and the tensor product is indicated as '⊗'. The superscript '-1' of a matrix (e.g., $\boldsymbol{A}^{-1}$) indicates the inverse and the superscript 'T' of a matrix ((e.g., $\boldsymbol{A}^{T}$)) denotes the transposition of this matrix. The summation convention is used for Latin indices but summations over crystallographic slip systems are indicated explicitly. Time derivatives are denoted by superposed dots.

4.1.1 Kinematical Theory

The quantitative description of kinematical theory for the mechanics of elastic-plastic deformation of crystals stems from the early work of Taylor [182] and Hill [223], where they proposed that material flows through the crystal lattice via dislocation motion. The kinematical theory used in the present CPFEM model follows the procedures used by Asaro [224], Asaro and Rice [225] and more recently by Raabe [226–229] and Lu [214–216,230,231].

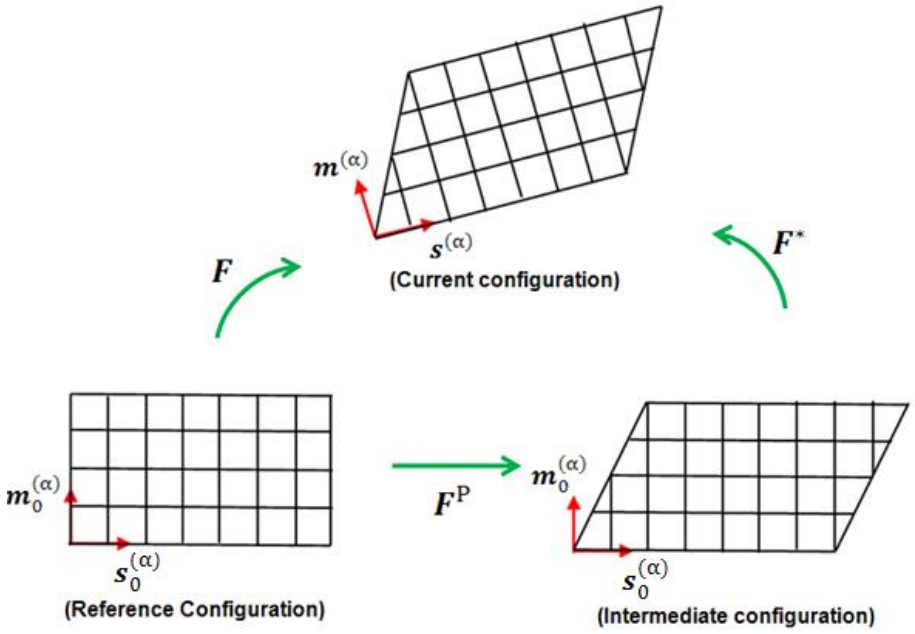

Fig. 4.1 Multiplicative decomposition of the deformation gradient $\boldsymbol{F}$ into plastic deformation part ($\boldsymbol{F}^{\mathrm{P}}$) and elastic deformation part ($\boldsymbol{F}^{*}$).

It has been assumed in this study that crystalline material under load undergoes a crystallographic slip due to dislocation motion on the active slip systems and elastic deformation including stretching and rotating of the crystal lattice [224,225,232,233]. These deformation modes should occur simultaneously during the deformation from a reference configuration to a current configuration. For mathematical treatment convenience it is assumed that there is an intermediate configuration between the reference configuration and the current configuration. As shown in Fig. 4.1, the initial reference configuration corresponds to the undeformed state, the crystallographic slip is assumed to firstly occur from the reference configuration to the intermediate configuration, followed by the elastic stretching and rotation from the intermediate configuration to the current configuration. Therefore, the total deformation gradient can be decomposed into two components as

$$\boldsymbol{F} = \frac{\partial \boldsymbol{x}}{\partial \boldsymbol{X}} = \boldsymbol{F}^{*} \cdot \boldsymbol{F}^{\mathrm{P}} \tag{4.1}$$

where $\boldsymbol{F}$ is the total deformation gradient, $\boldsymbol{x}$ is the position of the material point in the current configuration, $\boldsymbol{X}$ is the position of material point in the initial configuration, $\boldsymbol{F}^{*}$ is the

deformation gradient combined the stretching and rotation of the crystal lattice, and $\boldsymbol{F}^{\mathrm{P}}$ is the deformation due to plastic shearing on crystallographic slip systems and can be written as

$$\boldsymbol{F}^{\mathrm{P}} = \sum_{\alpha=1}^{\mathrm{N}} \boldsymbol{F}^{(\alpha)\mathrm{P}} = \sum_{\alpha=1}^{\mathrm{N}} \boldsymbol{I} + \gamma^{(\alpha)}\left(\boldsymbol{s}_0^{(\alpha)} \otimes \boldsymbol{m}_0^{(\alpha)}\right) \tag{4.2}$$

where $\boldsymbol{F}^{(\alpha)\mathrm{P}}$ is the contribution of α-th slip system to $\boldsymbol{F}^{\mathrm{P}}$, $\gamma^{(\alpha)}$ is the shear strain of α-th slip system, $\boldsymbol{I}$ is a second-order unit tensor and N is the number of active slip systems.

The Green strain tensor can be expressed by

$$\boldsymbol{E} = \frac{1}{2}(\boldsymbol{F}^{\mathrm{T}}\boldsymbol{F} - \boldsymbol{I}) \tag{4.3}$$

In the initial reference configuration, the crystal slip system α is specified by the slip direction $\boldsymbol{s}_0^{(\alpha)}$ lying in a slip plane and normal vector to the slip plane $\boldsymbol{m}_0^{(\alpha)}$. Both $\boldsymbol{s}_0^{(\alpha)}$ and $\boldsymbol{m}_0^{(\alpha)}$ are taken to be unit vectors and are orthogonal.

$$\boldsymbol{s}_0^{(\alpha)} \cdot \boldsymbol{m}_0^{(\alpha)} = 0 \tag{4.4}$$

They do not change during crystallographic slip from the reference configuration to the intermediate configuration but convert with the lattice when the lattice is stretched and rotated. The slip direction vector and the normal vector are defined as $\boldsymbol{s}^{(\alpha)}$ and $\boldsymbol{m}^{(\alpha))}$ in the current configuration, respectively. Under the deformation gradient (**F**) the slip direction is transformed from $\boldsymbol{s}_0^{(\alpha)}$ to $\boldsymbol{s}^{(\alpha)}$, such that

$$\boldsymbol{s}^{(\alpha)} = \boldsymbol{F}^{*} \cdot \boldsymbol{s}_0^{(\alpha)} \tag{4.5}$$

The normal to the slip plane $\boldsymbol{m}_0^{(\alpha)}$ after deformation can be written as

$$\boldsymbol{m}^{(\alpha)} = \boldsymbol{m}_0^{(\alpha)} \cdot \boldsymbol{F}^{*-1} \tag{4.6}$$

It should be noted that $\boldsymbol{s}^{(\alpha)}$ and $\boldsymbol{m}^{(\alpha)}$ are generally not in unit vectors, but remain orthogonal.

$$\boldsymbol{s}^{(\alpha)} \cdot \boldsymbol{m}^{(\alpha)} = 0 \tag{4.7}$$

The current velocity gradient is evaluated from the deformation gradient by

$$\boldsymbol{L} = \frac{\partial \boldsymbol{v}}{\partial \boldsymbol{x}} = \frac{\partial \boldsymbol{v}}{\partial \boldsymbol{X}}\frac{\partial \boldsymbol{X}}{\partial \boldsymbol{x}} = \dot{\boldsymbol{F}}\boldsymbol{F}^{-1} = \boldsymbol{L}^{*} + \boldsymbol{L}^{\mathrm{P}} \tag{4.8}$$

$$\boldsymbol{L}^{*} = \dot{\boldsymbol{F}}^{*} \cdot \boldsymbol{F}^{*-1} \tag{4.9}$$

$$\boldsymbol{L}^{\mathrm{P}} = \boldsymbol{F}^{*} \cdot \dot{\boldsymbol{F}}^{\mathrm{P}} \cdot \boldsymbol{F}^{\mathrm{P}-1} \cdot \boldsymbol{F}^{*-1} \tag{4.10}$$

where $\boldsymbol{v}$ is the velocity of the material point, $\dot{\boldsymbol{F}}$ expresses a time derivative of $\mathbf{F}$, $\boldsymbol{L}^{*}$ is the contribution of the elastic stretching and lattice rotation to $\boldsymbol{L}$ and $\boldsymbol{L}^{\mathrm{P}}$ is the plastic part of the velocity gradient. $\boldsymbol{L}^{\mathrm{P}}$ is related to the shear strain rate $\dot{\gamma}^{(\alpha)}$ of the α-th slip system by

$$\boldsymbol{L}^{\mathrm{P}} = \sum_{\alpha=1}^{\mathrm{N}} \dot{\gamma}^{(\alpha)}\, \boldsymbol{s}^{(\alpha)} \otimes \boldsymbol{m}^{(\alpha)} \tag{4.11}$$

$$\boldsymbol{F}^{\mathrm{P}} = \boldsymbol{I} + \gamma^{(\alpha)} \boldsymbol{s}^{(\alpha)} \otimes \boldsymbol{m}^{(\alpha)} \tag{4.12}$$

The velocity gradient can be uniquely decomposed into a symmetrical part and a skewed-symmetrical part as

$$\boldsymbol{L} = \boldsymbol{D} + \boldsymbol{\Omega} \tag{4.13}$$

$$\boldsymbol{D} = \frac{1}{2}(\boldsymbol{L} + \boldsymbol{L}^{\mathrm{T}}) \tag{4.14}$$

$$\boldsymbol{\Omega} = \frac{1}{2}(\boldsymbol{L} - \boldsymbol{L}^{\mathrm{T}}) \tag{4.15}$$

where $\boldsymbol{D}$ and $\boldsymbol{\Omega}$ are called the stretch rate tensor and spin tensor, respectively. $\boldsymbol{D}$ is generally called the rate of deformation. Corresponding to $\boldsymbol{L}$, the tensors $\boldsymbol{D}$ and $\boldsymbol{\Omega}$ can also be decomposed into the elastic stretching and lattice rotation part ($\boldsymbol{D}^{*}$ and $\boldsymbol{\Omega}^{*}$), and the plastic part ($\boldsymbol{D}^{\mathrm{P}}$ and $\boldsymbol{\Omega}^{\mathrm{P}}$), namely

$$\boldsymbol{D} = \boldsymbol{D}^{*} + \boldsymbol{D}^{\mathrm{P}} \tag{4.16}$$

$$\boldsymbol{\Omega} = \boldsymbol{\Omega}^{*} + \boldsymbol{\Omega}^{\mathrm{P}} \tag{4.17}$$

The components of the two tensors ($\boldsymbol{D}$ and $\boldsymbol{\Omega}$) can be expressed by the velocity $\boldsymbol{v}$ and the coordinate $\boldsymbol{x}$ as,

$$\boldsymbol{D}_{\mathrm{ij}} = \frac{1}{2}\left(\frac{\partial v_{\mathrm{i}}}{\partial x_{\mathrm{j}}} + \frac{\partial v_{\mathrm{j}}}{\partial x_{\mathrm{i}}}\right) \tag{4.18}$$

$$\boldsymbol{\Omega}_{\mathrm{ij}} = \frac{1}{2}\left(\frac{\partial v_{\mathrm{i}}}{\partial x_{\mathrm{j}}} - \frac{\partial v_{\mathrm{j}}}{\partial x_{\mathrm{i}}}\right) \tag{4.19}$$

According to Eqns. (4.8), (4.10), (4.16) and (4.17), $\boldsymbol{L}^{\mathrm{P}}$ can be derived as

$$\boldsymbol{L}^{\mathrm{P}} = \boldsymbol{D}^{\mathrm{P}} + \boldsymbol{\Omega}^{\mathrm{P}} = \boldsymbol{F}^{*} \cdot \dot{\boldsymbol{F}}^{\mathrm{P}} \cdot \boldsymbol{F}^{\mathrm{P}-1} \cdot \boldsymbol{F}^{*-1} \tag{4.20}$$

And then $\boldsymbol{D}^{\mathrm{P}}$ in Eqn (4.16) can be expressed as

$$\boldsymbol{D}^{\mathrm{P}} = \sum_{\alpha=1}^{\mathrm{N}} \boldsymbol{P}^{(\alpha)} \dot{\gamma}^{(\alpha)} \tag{4.21}$$

where $\boldsymbol{P}^{(\alpha)}$ has been defined as

$$\boldsymbol{P}^{(\alpha)} = \frac{1}{2}\left(\boldsymbol{s}^{(\alpha)} \otimes \boldsymbol{m}^{(\alpha)} + \boldsymbol{m}^{(\alpha)} \otimes \boldsymbol{s}^{(\alpha)}\right) \tag{4.22}$$

Similar to $\boldsymbol{D}^{\mathrm{P}}$, the tensor $\boldsymbol{\Omega}^{\mathrm{P}}$ in Eqn. (4.17) can also be expressed as

$$\boldsymbol{\Omega}^{\mathrm{P}} = \sum_{\alpha=1}^{\mathrm{N}} \mathrm{W} \dot{\gamma}^{(\alpha)} \tag{4.23}$$

where $\boldsymbol{W}^{(\alpha)}$ has been defined as

$$\boldsymbol{W}^{(\alpha)} = \frac{1}{2}\left(\boldsymbol{s}^{(\alpha)} \otimes \boldsymbol{m}^{(\alpha)} - \boldsymbol{m}^{(\alpha)} \otimes \boldsymbol{s}^{(\alpha)}\right) \tag{4.24}$$

For convenience, $\boldsymbol{s}^{(\alpha)} \otimes \boldsymbol{m}^{(\alpha)}$ is usually called the Schmid factor. Therefore, $\boldsymbol{P}^{(\alpha)}$ and $\boldsymbol{W}^{(\alpha)}$ are the symmetrical and asymmetrical part of the Schmid factor, respectively.

The derivatives of Eqns. (4.5) and (4.6) yield

$$\dot{\boldsymbol{s}}^{(\alpha)} = \boldsymbol{L}^{*} \boldsymbol{s}^{(\alpha)} = (\boldsymbol{D}^{*} + \boldsymbol{\Omega}^{*}) \boldsymbol{s}^{(\alpha)} \tag{4.25}$$

$$\dot{\boldsymbol{m}}^{(\alpha)} = -\boldsymbol{m}^{(\alpha)} \boldsymbol{L}^{*} = -\boldsymbol{m}^{(\alpha)} (\boldsymbol{D}^{*} + \boldsymbol{\Omega}^{*}) \tag{4.26}$$

By differentiating Eqn. (4.3), the rate of change of Green's Lagrangian strain can be written as

$$\dot{\boldsymbol{E}} = \frac{1}{2}\left(\dot{\boldsymbol{F}}^{\mathrm{T}} \boldsymbol{F} + \boldsymbol{F}^{\mathrm{T}} \dot{\boldsymbol{F}}\right) = \boldsymbol{F}^{\mathrm{T}} \boldsymbol{D} \boldsymbol{F} \tag{4.27}$$

According to the polar decomposition theory, the deformation gradient $\boldsymbol{F}$ in Eqn. (4.1) can be expressed by two alternative forms as

$$\boldsymbol{F} = \boldsymbol{R}\boldsymbol{U} \tag{4.28}$$

$$\boldsymbol{F} = \boldsymbol{V}\boldsymbol{R} \tag{4.29}$$

where $\boldsymbol{R}$ is the orthogonal rotation tensor, $\boldsymbol{U}$ is the right stretch tensor, $\boldsymbol{V}$ is the left stretch tensor. Both tensors $\boldsymbol{U}$ and $\boldsymbol{V}$ are positive definite symmetric tensors. And they have the following properties

$$\boldsymbol{R}^{\mathrm{T}} = \boldsymbol{R}^{-1} \tag{4.30}$$

$$\boldsymbol{U} = \boldsymbol{U}^{\mathrm{T}} \tag{4.31}$$

Therefore, the asymmetric part ($\boldsymbol{\Omega}$) of the velocity gradient in Eqns. (4.15) and (4.17) can be written as

$$\boldsymbol{\Omega} = \dot{\boldsymbol{R}}\boldsymbol{R}^{-1} \tag{4.32}$$

And then $\boldsymbol{R}$ can be expressed by

$$\boldsymbol{R} = \left(\boldsymbol{I} + \frac{1}{2}\boldsymbol{\Omega}\Delta\mathrm{t}\right)\left(\boldsymbol{I} - \frac{1}{2}\boldsymbol{\Omega}\Delta\mathrm{t}\right)^{-1} \tag{4.33}$$

where Δt is the time increment. Accordingly, Eqn. (4.32) can also be expressed as

$$\boldsymbol{\Omega} = \frac{2}{\Delta\mathrm{t}}(\boldsymbol{R} - \boldsymbol{I})(\boldsymbol{R} - \boldsymbol{I})^{-1} \tag{4.34}$$

4.1.2 Constitutive Equations

let $\boldsymbol{t}_0$ is the Kirchhoff stress in the reference configuration at a time t+Δt, and it is also the Kirchhoff stress in the current configuration at a time t. According to the description in Section 4.1.1, deformation occurs first by crystallographic slip from the reference configuration to the intermediate configuration, and then lattice stretching and rotation from the intermediate configuration to the current configuration. It is assumed that the change in stress caused by the slip and lattice stretching is $\dot{\boldsymbol{t}}_0\Delta\mathrm{t}$, where $\dot{\boldsymbol{t}}_0$ is the stress rate in the reference configuration. The

stress $\boldsymbol{t}_0 + \dot{\boldsymbol{t}}_0 \Delta t$ will be rotated to the current configuration. The rotation tensor is $\boldsymbol{R}$. The Kirchhoff stress $\boldsymbol{t}$ in the current configuration can be expressed by

$$\boldsymbol{t} = \boldsymbol{R}(\boldsymbol{t}_0 + \dot{\boldsymbol{t}}_0 \Delta t)\boldsymbol{R}^{\mathrm{T}} \tag{4.35}$$

Taking the time derivative of Eqn. (4.35) it can be obtained as

$$\dot{\boldsymbol{t}} = \boldsymbol{R}\dot{\boldsymbol{t}}_0\boldsymbol{R}^{\mathrm{T}} + \dot{\boldsymbol{R}}(\boldsymbol{t}_0 + \dot{\boldsymbol{t}}_0 \Delta t)\boldsymbol{R}^{\mathrm{T}} + \boldsymbol{R}(\boldsymbol{t}_0 + \dot{\boldsymbol{t}}_0 \Delta t)\boldsymbol{R}^{\mathrm{T}} = \boldsymbol{R}\dot{\boldsymbol{t}}_0\boldsymbol{R}^{\mathrm{T}} + \boldsymbol{\Omega t} - \boldsymbol{t\Omega} \tag{4.36}$$

where $\dot{\boldsymbol{t}}$ is the material rate of Kirchhoff stress in the current configuration. $\boldsymbol{R}\dot{\boldsymbol{t}}_0\boldsymbol{R}^{\mathrm{T}}$ is defined as the Jaumann rate of Kirchhoff stress ($\overset{\nabla}{\boldsymbol{t}}$) on axes that rotate with the material. Therefore, we have

$$\overset{\nabla}{\boldsymbol{t}} = \boldsymbol{R}\dot{\boldsymbol{t}}_0\boldsymbol{R}^{\mathrm{T}} = \dot{\boldsymbol{t}} - \boldsymbol{\Omega t} + \boldsymbol{t\Omega} \tag{4.37}$$

If only the deformation from the intermediate to the current configuration is taken into account then Eqn. (4.37) can be rewritten as

$$\overset{\nabla}{\boldsymbol{t}^*} = \boldsymbol{R}\dot{\boldsymbol{t}}_1^*\boldsymbol{R}^{\mathrm{T}} = \dot{\boldsymbol{t}} - \boldsymbol{\Omega}^*\boldsymbol{t} + \boldsymbol{t\Omega}^* \tag{4.38}$$

where $\overset{\nabla}{\boldsymbol{t}^*}$ is the Jaumann rate of Kirchhoff stress on axes that rotate with the lattice and $\dot{\boldsymbol{t}}_1^*$ is the rate of the Kirchhoff stress in the intermediate configuration.

The difference between Eqns. (4.37) and (4.38) can be obtained as

$$\overset{\nabla}{\boldsymbol{t}^*} - \overset{\nabla}{\boldsymbol{t}} = \sum_{\alpha=1}^{\mathrm{N}} \boldsymbol{\beta}^{(\alpha)}\dot{\gamma}^{(\alpha)} \tag{4.39}$$

where $\boldsymbol{\beta}^{(\alpha)}$ is defined by

$$\boldsymbol{\beta}^{(\alpha)} = \boldsymbol{\Omega}^{(\alpha)}\boldsymbol{t} - \boldsymbol{t\Omega}^{(\alpha)} \tag{4.40}$$

The lattice is elastically stretched along the lattice axis. The lattice stretching can be described in the lattice coordinate system by

$$\dot{\boldsymbol{t}}_{\mathrm{L}} = \boldsymbol{C}_0 : \boldsymbol{D}_{\mathrm{L}} \tag{4.41}$$

where $\dot{\boldsymbol{t}}_{\mathrm{L}}$ is the material rate of the Kirchhoff stress in the lattice coordinate system, $\boldsymbol{D}_{\mathrm{L}}$ is the rate of the elastic stretching in the lattice coordinate system, $\boldsymbol{C}_0$ is the elastic moduli tensor.

Provided the rotation tensor between the lattice coordinate system and the current configuration is $\boldsymbol{R}_{\mathrm{L}}$, the elastic deformation rate $\boldsymbol{D}^*$ in the current configuration can be linked to $\boldsymbol{D}_{\mathrm{L}}$ by the following equation

$$\boldsymbol{D}^* = \boldsymbol{R}_{\mathrm{L}}\boldsymbol{D}_{\mathrm{L}}\boldsymbol{R}_{\mathrm{L}}^{\mathrm{T}} \tag{4.42}$$

The rate of Kirchhoff stress in the intermediate configuration can be expressed by

$$\dot{\boldsymbol{t}}_1^* = \boldsymbol{R}^{\mathrm{T}}\boldsymbol{R}_{\mathrm{L}}\dot{\boldsymbol{t}}_{\mathrm{L}}\boldsymbol{R}_{\mathrm{L}}^{\mathrm{T}}\boldsymbol{R} \tag{4.43}$$

Therefore, according to Eqns. (4.38) and (4.43), the Jaumann rate $\overset{\nabla}{\boldsymbol{t}^*}$ can be written as

$$\overset{\nabla}{\boldsymbol{t}^*} = \boldsymbol{R}_{\mathrm{L}}\dot{\boldsymbol{t}}_{\mathrm{L}}\boldsymbol{R}_{\mathrm{L}}^{\mathrm{T}} \tag{4.44}$$

Eqns. (4.42) and (4.44) can be rewritten as

$$\boldsymbol{D}_{\mathrm{L}} = \left(\boldsymbol{R}_{\mathrm{L}}^{\mathrm{T}}\otimes\boldsymbol{R}_{\mathrm{L}}^{\mathrm{T}}\right) : \boldsymbol{D}^* \tag{4.45}$$

$$\dot{\boldsymbol{t}}_{\mathrm{L}} = \left(\boldsymbol{R}_{\mathrm{L}}^{\mathrm{T}}\otimes\boldsymbol{R}_{\mathrm{L}}^{\mathrm{T}}\right) : \overset{\nabla}{\boldsymbol{t}^*} \tag{4.46}$$

Substituting Eqns. (4.45) and (4.46) into Eqn. (4.41) yields

$$\overset{\nabla}{\boldsymbol{t}^*} = \boldsymbol{C} : \boldsymbol{D}^* \tag{4.47}$$

$$\boldsymbol{C} = (\boldsymbol{R}_{\mathrm{L}}\otimes\boldsymbol{R}_{\mathrm{L}}) \cdot \boldsymbol{C}_0 \cdot \left(\boldsymbol{R}_{\mathrm{L}}^{\mathrm{T}}\otimes\boldsymbol{R}_{\mathrm{L}}^{\mathrm{T}}\right) \tag{4.48}$$

where $\boldsymbol{C}$ is the fourth order tensor of the elastic modulus,

Substituting Eqn. (4.47) into Eqn. (4.39) gives

$$\overset{\nabla}{\boldsymbol{t}} = \boldsymbol{C} : \boldsymbol{D} - \sum_{\alpha=1}^{\mathrm{N}}\left(\boldsymbol{C} : \boldsymbol{p}^{(\alpha)} + \boldsymbol{\beta}^{(\alpha)}\right)\dot{\gamma}^{(\alpha)} \tag{4.49}$$

It was assumed that slip is the only plastic deformation mechanism. The resolved shear stress on each slip system can be used as the vital variable to evaluate plastic flow. The resolved shear stress $\tau^{(\alpha)}$ can be calculated from

$$\tau^{(\alpha)} = \boldsymbol{p}^{(\alpha)} : \boldsymbol{t} \tag{4.50}$$

Taking the time derivative gives

$$\dot{\tau}^{(\alpha)} = \left(\boldsymbol{C} : \boldsymbol{P}^{(\alpha)} + \boldsymbol{\beta}^{(\alpha)}\right) : (\boldsymbol{D} - \sum_{\beta=1}^{N} \boldsymbol{p}^{(\beta)} \dot{\gamma}^{(\beta)}) \tag{4.51}$$

The relationship of the Cauchy stress $\boldsymbol{\sigma}$ and the Kirchhoff stress is

$$\boldsymbol{t} = \mathrm{J}\boldsymbol{\sigma} \tag{4.52}$$

and J is defined as

$$\mathrm{J} = \frac{1}{|\boldsymbol{F}|} \tag{4.53}$$

The derivative of Eqn. (4.52) can be written by

$$\dot{\boldsymbol{t}} = \mathrm{J}\dot{\boldsymbol{\sigma}} + \dot{\boldsymbol{\sigma}}\mathrm{J} = \mathrm{J}\dot{\boldsymbol{\sigma}} + \mathrm{J}\mathrm{tr}(\boldsymbol{D})\boldsymbol{\sigma} \tag{4.54}$$

Substituting Eqns. (4.52) and (4.54) into Eqns. (4.35), (4.37), (4.49) and (4.51) yields the constitutive law based on the Cauchy stress

$$\boldsymbol{\sigma} = \boldsymbol{R}\left(\boldsymbol{\sigma}_0\left(1 + \mathrm{tr}(\boldsymbol{D})\right)\right)\boldsymbol{R}^{\mathrm{T}} + \overset{\nabla}{\boldsymbol{\sigma}}_0 \Delta t \tag{4.55}$$

$$\overset{\nabla}{\boldsymbol{\sigma}} = \boldsymbol{C} : \boldsymbol{D} - \mathrm{tr}(\boldsymbol{D})\boldsymbol{\sigma} - \sum_{\alpha=1}^{N}(\boldsymbol{C} : \boldsymbol{P}^{(\alpha)} + \boldsymbol{\Omega}^{(\alpha)}\boldsymbol{\sigma} - \boldsymbol{\sigma}\boldsymbol{\Omega}^{(\alpha)})\dot{\gamma}^{(\alpha)} \tag{4.56}$$

$$\dot{\tau}^{(\alpha)} = \left(\boldsymbol{C} : \boldsymbol{P}^{(\alpha)} + \boldsymbol{\Omega}^{(\alpha)}\boldsymbol{\sigma} - \boldsymbol{\sigma}\boldsymbol{\Omega}^{(\alpha)}\right) : (\boldsymbol{D} - \sum_{\beta=1}^{N} \boldsymbol{P}^{(\beta)} \dot{\gamma}^{(\beta)}) \tag{4.57}$$

4.1.3 Hardening Model

To overcome the long standing problem of non-uniqueness in the choice of the active slip systems which are inherent in conventional rate-independent theory, the rate-dependent constitutive law has been developed. The rate-dependent law was first introduced by

Hutchinson [234] in 1976 to study the steady creep properties of polycrystalline materials. Since then it has been successfully used by Asaro [224], Pierce, Asaro and Needleman [235], Toth et al. [236] and Neale and Harven [183,184] in their researches. Recently, the rate-dependent theory has been extensively applied in crystal plasticity finite element studies to model various deformation techniques [200,215,230,231,237–241]. This study follows the above mentioned rate-dependent law, the shear strain rate $\dot{\gamma}^{(\alpha)}$ on a slip system is assumed to be related to the resolved shear stress $\tau^{(\alpha)}$ by Power law as follows:

$$\dot{\gamma}^{(\alpha)} = \dot{\gamma}_0^{(\alpha)} \mathrm{sgn}(\tau^{(\alpha)}) \left| \frac{\tau^{(\alpha)}}{\tau_c^{(\alpha)}} \right|^n \tag{4.58}$$

and

$$\mathrm{sgn}(x) = \begin{cases} -1, & x < 1 \\ 1, & x \geq 1 \end{cases} \tag{4.59}$$

where $\dot{\gamma}_0^{(\alpha)}$is the reference value of the shear strain rate which is taken to be a constant for all slip systems. n denotes the rate sensitive exponent and the rate insensitivity limit is n →infinite. Both parameters $\dot{\gamma}_0^{(\alpha)}$ and n are the material characters. Parameter $\tau_c^{(\alpha)}$ is a variable used to describe the current strength of the slip syatem α, also known as the critical resolved shear stress. The shear rate in each slip system is uniquely determined by the power law in Eqn. (4.58)

The flow stress $\tau_c^{(\alpha)}$ for each slip system increases with plastic deformation due to work hardening. The hardening curve needs to be determined for each possible slip system so that $\tau_c^{(\alpha)}$ can be expressed as a function of the plastic shear in that slip system. Fig. 4.2 shows a typical shear stress and shear strain curve for a FCC crystal with the tensile axis oriented with a standard triangle, and where it reflects three different stages [242]. Stage-1 is the easy glide stage where the corresponding hardening rate is very low and almost constant. By contrast, Stage-2 is a rapid hardening stage where the hardening rate is also almost constant, but much higher than in Stage-1. Stage-3 is a parabolic hardening region where the hardening rate decreases continuously until fracture occurs.

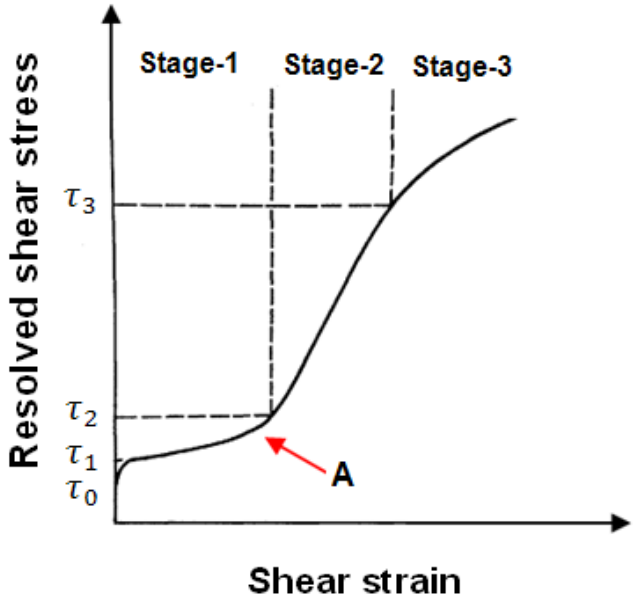

Fig. 4.2 A typical curve of resolved shear stress versus shear strain in a slip system for a FCC single crystal. (Point 'A' denotes where secondary slip commences) [242].

When more than one slip system is active, hardening in each slip system is a function of slip on all the active slip systems, the rate of increase of the flow stress $\tau_c^{(\alpha)}$ has therefore been specified as

$$\dot{\tau}_c^{(\alpha)} = \sum_{\beta=1}^{N} h_{\alpha\beta}\dot{\gamma}^{(\beta)} \tag{4.60}$$

where the matrix $h_{\alpha\beta}$ contains the hardening moduli for each slip system. $h_{\alpha\alpha}$ is known as self hardening (hardening of a slip system during deformation) while $h_{\alpha\beta}$ $(\alpha \neq \beta)$ is known as latent hardening (hardening of a slip system due to the hardening in another slip system)

There have been many proposals for the analytical representation of the instantaneous hardening moduli $h_{\alpha\beta}$. The simplest proposal was the 'isotropic' hardening law by Taylor (1934) [195,196]. According to this law all slip systems harden equally when deformation occurs. This isotropic hardening is unable to predict the experimental observation that inactive or latent slip systems often harden more than the slip system that is active during deformation; Hutchinson (1970) [243] proposed a simple latent hardening law by assuming that the off-diagonal terms in the matrix of hardening moduli are different from the diagonal values. Peirce, Asaro, and

Needleman (1982) [232] proposed a model that also provides latent hardening, while for self-hardening they used the mathematical property of hyperbolic secant function to reach a peak value of hardening and then saturate. That is to say, self-hardening starts with a higher initial hardening and vanishes after reaching a saturation resolved shear stress. Bassani and Wu (1991) [242,244] used a different expression for the hardening moduli to describe the three stages of hardening of crystalline materials in Fig. 4.2. This model was based upon the analytical characterization of the hardening moduli at any stage during deformation. Their expression for self and latent hardening depends on the shear strains $\gamma^{(\alpha)}$ of all slip systems.

$$h_{\alpha\alpha} = \left[(h_0 - h_s)\mathrm{sech}^2\left(\frac{(h_0-h_s)\gamma^{(\alpha)}}{\tau_1-\tau_0}\right) + h_s\right]\left[1 + \sum_{\substack{\beta=1 \\ \beta\neq\alpha}}^{N} f_{\alpha\beta}\tanh\left(\frac{\gamma^{(\beta)}}{\gamma_0}\right)\right] \qquad (4.61)$$

$$h_{\alpha\beta} = \mathrm{q}h_{\alpha\alpha} \qquad \alpha \neq \beta \qquad (4.62)$$

$h_{\alpha\beta}$ is instantaneous hardening moduli that include the self-hardening of each system (α=β) and latent hardening (α≠β). The parameter q is a latent hardening parameter and γ_0 is the reference value of slip. γ is the resolved shear strain and τ_0 is the initial critical resolved shear stress. τ_1 is the breakthrough stress where large plastic flow begins and h_0 is the hardening modulus just after the initial yield, while h_s is the hardening modulus during easy glide. Parameter $f_{\alpha\beta}$ represents the magnitude of the strength of a particular slip interaction between two slip systems α and β and it depends on the geometric relationship between two slip systems. The factors $f_{\alpha\beta}$ are given in terms of five constants [244]:

(i) a_1 (no junction): the resultant Burgers vector from slip systems α and β is parallel to the original one;

(ii) a_2 (Hirth lock): the resultant Burgers vector is not energetically admissible;

(iii) a_3 (coplanar junction): the resultant Burgers vector is on the same slip plane as the original ones;

(iv) a_4 (glissile junction): the resultant Burgers vector is energetically admissible and on one of the two slip planes;

(v) a_5 (sessile junction): the resultant Burgers vector is energetically admissible but not on either of the two slip planes.

Many comparative studies of the various hardening laws mentioned above have been carried out to simulate the finite and large strain deformation behaviors by Wu et al. [185], Havner and Lin [184], Kumar and Yang [245], Siddiq and Schmauder [246]. These simulation results indicated that the Bassani & Wu model could reflect the three-stage hardening of FCC crystals more exactly. Recently, the Bassani and Wu hardening law has been successfully employed to predict the deformation behavior and texture evolution in large strain ECAP process by crystal plasticity modeling [214–216]. Therefore, in this study, the hardening model of Bassani and Wu was adopted to simulate the HPT process.

4.2 Development of the CPFEM Model

4.2.2 Fundamental Equations of FEM

It is well known that the equilibrium for problems neglecting the body forces can be expressed by the virtual work principle in rate form

$$\int_V \boldsymbol{\sigma} : \delta\mathbf{D}\mathrm{d}V = \int_S \mathbf{f} \cdot \delta\mathbf{v}\mathrm{d}S \tag{4.63}$$

Where $\boldsymbol{\sigma}$ is the Cauchy stress; $\delta\boldsymbol{D}$ is the virtual form of the rate of deformation; V is the volume of the solid body in the current configuration; $\boldsymbol{f}$ is the surface traction per unit of the current area; $\delta\boldsymbol{v}$ is the kinematically admissible virtual velocity field and S is the bounding surface of the volume V.

According to FEM theory, a solid body is divided into n elements, where each element is associated with m nodal points. The velocity field in each element is interpolated by interpolation functions $\mathbf{N}$ (shape functions), which link the velocity field ($\boldsymbol{v}$) to the nodal velocities ($\boldsymbol{v}^{\mathrm{n}}$) as follws,

$$\boldsymbol{v} = \mathbf{N}\boldsymbol{v}^{\mathrm{n}} \tag{4.64}$$

The interpolation for the rate of the deformation $\boldsymbol{D}$ and spin tensor $\boldsymbol{\Omega}$ can be expressed as

$$\boldsymbol{D} = \boldsymbol{B}\boldsymbol{v}^{\mathrm{n}} \tag{4.65}$$

$$\boldsymbol{\Omega} = \boldsymbol{G}\boldsymbol{v}^{\mathrm{n}} \tag{4.66}$$

$\boldsymbol{B}$ and $\boldsymbol{G}$ are the symmetrical part and the skewed part of the coefficient matrix of velocity gradient, respectively.

Normally the surface tractions ($\boldsymbol{f}$) in Eqn. (4.63) are the force (or stress) boundary conditions. If $\boldsymbol{f}$ is the function of the nodal velocities, it can be written by

$$\boldsymbol{f} = \boldsymbol{T}\boldsymbol{v}^{\mathrm{n}} \tag{4.67}$$

where $\boldsymbol{T}$ is a matrix.

Therefore, the equilibrium equation (Eqn. (4.63)) can be rewritten as

$$\int_{\mathrm{V}} \mathbf{B}^{\mathrm{T}}\boldsymbol{\sigma}\mathrm{dV} : \delta\mathbf{v}^{\mathbf{n}} = \int_{\mathrm{S}} \mathbf{N}^{\mathrm{T}}\mathbf{f}\mathrm{dS} : \delta\mathbf{v}^{\mathbf{n}} \tag{4.68}$$

Since the $\delta\boldsymbol{v}^{\mathbf{n}}$ are arbitrary, one obtains

$$\int_{\mathrm{V}} \mathbf{B}^{\mathrm{T}}\boldsymbol{\sigma}\mathrm{dV} = \int_{\mathrm{S}} \mathbf{N}^{\mathrm{T}}\mathbf{f}\mathrm{dS} \tag{4.69}$$

The above non-linear equations are functions of the nodal velocities ($\boldsymbol{v}^{\mathbf{n}}$). They form the basis of the displacement-based finite element method. Eqn. (4.69) can be rewritten by:

$$\mathbf{F}(\mathbf{v}^{\mathbf{n}}) = \int_{\mathrm{V}} \mathbf{B}^{\mathrm{T}}\boldsymbol{\sigma}\mathrm{dV} - \int_{\mathrm{S}} \mathbf{N}^{\mathrm{T}}\mathbf{f}\mathrm{dS} = \mathbf{0} \tag{4.70}$$

The Newton algorithm is in general used to solve the non-linear equations (Eqn. (4.70)). An iteration process is performed. In i+1$^{\mathrm{th}}$ iteration step the nodal velocities are updated by

$$\boldsymbol{v}_{i+1}^{n} = \boldsymbol{v}_{i}^{n} - \boldsymbol{K}^{-1}\boldsymbol{F}(\boldsymbol{v}_{i}^{n}) \tag{4.71}$$

$$\boldsymbol{K} = \boldsymbol{F}'(\boldsymbol{v}_{i}^{n}) \tag{4.72}$$

where $\boldsymbol{v}_i^n$ and $\boldsymbol{v}_{i+1}^n$ are the nodal velocities for i iteration step and i+1 iteration step, respectively; $\boldsymbol{K}$ is the Jacobian matrix, which is the derivative of $\boldsymbol{F}(\boldsymbol{v}^n)$ with respect to $\boldsymbol{v}^{\mathrm{n}}$ at $\boldsymbol{v}^{\boldsymbol{n}} = \boldsymbol{v}_i^n$. To solve Eqn. (4.71) $\boldsymbol{K}$ must be developed. It can be expressed by:

$$\mathbf{K} = \int_{\mathrm{V}} \mathbf{B}^{\mathrm{T}} \frac{\mathrm{d}\boldsymbol{\sigma}}{\mathrm{d}\mathbf{v}^{\mathrm{n}}} \mathrm{dV} - \int_{\mathrm{S}} \mathbf{N}^{\mathrm{T}} \mathbf{T} \mathrm{dS} \tag{4.73}$$

For the rate-dependent materials, accordingly, the constitutive relationship can be described in incremental form as follows

$$\overset{\nabla}{\boldsymbol{\sigma}} = \boldsymbol{H} : \boldsymbol{D} \tag{4.74}$$

$\boldsymbol{H}$ is the fourth order hardening parameter tensor. The derivative of the Cauchy stress with respect to $\boldsymbol{v}^{\mathrm{n}}$ can be calculated as follows

$$\frac{\mathrm{d}\boldsymbol{\sigma}}{\mathrm{d}\boldsymbol{v}^{\mathrm{n}}} = \frac{\mathrm{d}\overset{\nabla}{\boldsymbol{\sigma}}}{\mathrm{d}\boldsymbol{v}^{\mathrm{n}}} + \frac{\mathrm{d}\boldsymbol{W}}{\mathrm{d}\boldsymbol{v}^{\mathrm{n}}}\boldsymbol{\sigma} - \boldsymbol{\sigma}\frac{\mathrm{d}\boldsymbol{W}}{\mathrm{d}\boldsymbol{v}^{\mathrm{n}}} \tag{4.75}$$

The Jacobian matrix ($\boldsymbol{K}$) can be expressed as

$$\mathbf{K} = \int_{\mathrm{V}} \mathbf{B}^{\mathrm{T}} (\mathbf{G}\boldsymbol{\sigma} - \boldsymbol{\sigma}\mathbf{G} + \mathbf{H} : \mathbf{B}) \mathrm{dV} - \int_{\mathrm{S}} \mathbf{N}^{\mathrm{T}} \mathbf{T} \mathrm{dS} \tag{4.76}$$

The hardening parameter tensor $\boldsymbol{H}$ must be calculated based on the constitutive law to determine $\boldsymbol{K}$.

4.2.2 Implementation of Crystal Plasticity Theory in FEM

In this study, the crystal plasticity constitutive model was implemented into the implicit finite element code Abaqus/Standard using the user material subroutine (UMAT), where the material properties can be defined and the data can be exchanged with Abaqus [247]. UMAT has two functions. The first one is to make sure that the stress state of the material is at the current increment and calculate all state variables. The second function is to calculate the Jacobian matrix of the current material configuration. The stability and rate of convergence are significantly influenced by the material constitutive model.

In the developed CPFEM model, the following seven groups of data need to be provided in the input file [248]:

(i) Elastic moduli of materials;

(ii) Number of sets of potentially activated slip systems considered;

(iii) Initial crystallographic orientations in the sample coordinate system;

(iv) Shear strain rate depending on the resolved shear stress and current strength;

(v) Self and latent hardening moduli;

(vi) The forward gradient time integration parameter and the parameter determining whether the small deformation theory or the theory of finite strain and finite rotation is used in the analysis;

(vii) Parameters for the iteration method.

ABAQUS/Standard is a displacement-based finite element code. In ABAQUS/Standard the loading history is divided into many steps. In each step the deformation is assumed to be static. The flowchart of the procedures in UMAT is shown in Fig. 4.3, which include

1. Through the interface ABAQUS/Standard provides UMAT: stresses ($\boldsymbol{\sigma}$), logarithmic strains ($\int_0^t \boldsymbol{D}\mathrm{d}t$), increments of logarithmic strains ($\boldsymbol{D}\Delta t$), rotation increments ($\boldsymbol{R}$), time increment (Δt), constants, solution dependent variables, and so on. The constants include elastic moduli, parameters charactering the slip system, materials parameters in the hardening model and forward gradient time integration parameter. All the constant can be modified in the ABAQUS input file or through ABAQUS/CAE interface. The solution dependent variables include the slip directions ($\boldsymbol{s}$), normals to slip planes ($\boldsymbol{m}$), shear strain rates ($\dot{\gamma}$), resolved shear stresses (τ) and critical resolved shear stress (τ_c) on all slip systems.
2. Calculate the elastic moduli ($\boldsymbol{C}$) in the global system by Eqn. (4. 48).
3. Calculate the rotation tensor ($\boldsymbol{R}$) from the local crystal system to the global system by Eqn. (4. 34).

4. Determine the slip systems using inputted parameters charactering the slip systems if UMAT is called at the first time; if not, skip this step.
5. Calculate the Schmid factor ***P***, ***W*** by Eqns. (4.22) and (4.24) respectively.
6. Calculate the shear strain rate $\dot{\gamma}$ and its derivation by Eqns. (4.58-4.59).
7. Calculate the hardening modulus $h_{\alpha\beta}$ by Eqns. (4.61-4.62).
8. According to the Taylor expansion of Eqn. (4.58) to calculate $\Delta\gamma^{(\alpha)}$with time increment Δt.
9. Update the solution dependent state variables and the stresses.

Accordingly, all the variables and Jacobian matrix can be obtained by the related equations obtained at the end of the step. All the calculated variables will be transferred to the next step as entries, and then the iteration of the next increment will be calculated. Otherwise, the time increment will be estimated and iterated. This procedure will be repeated and finally terminated until the desired deformation is finished.

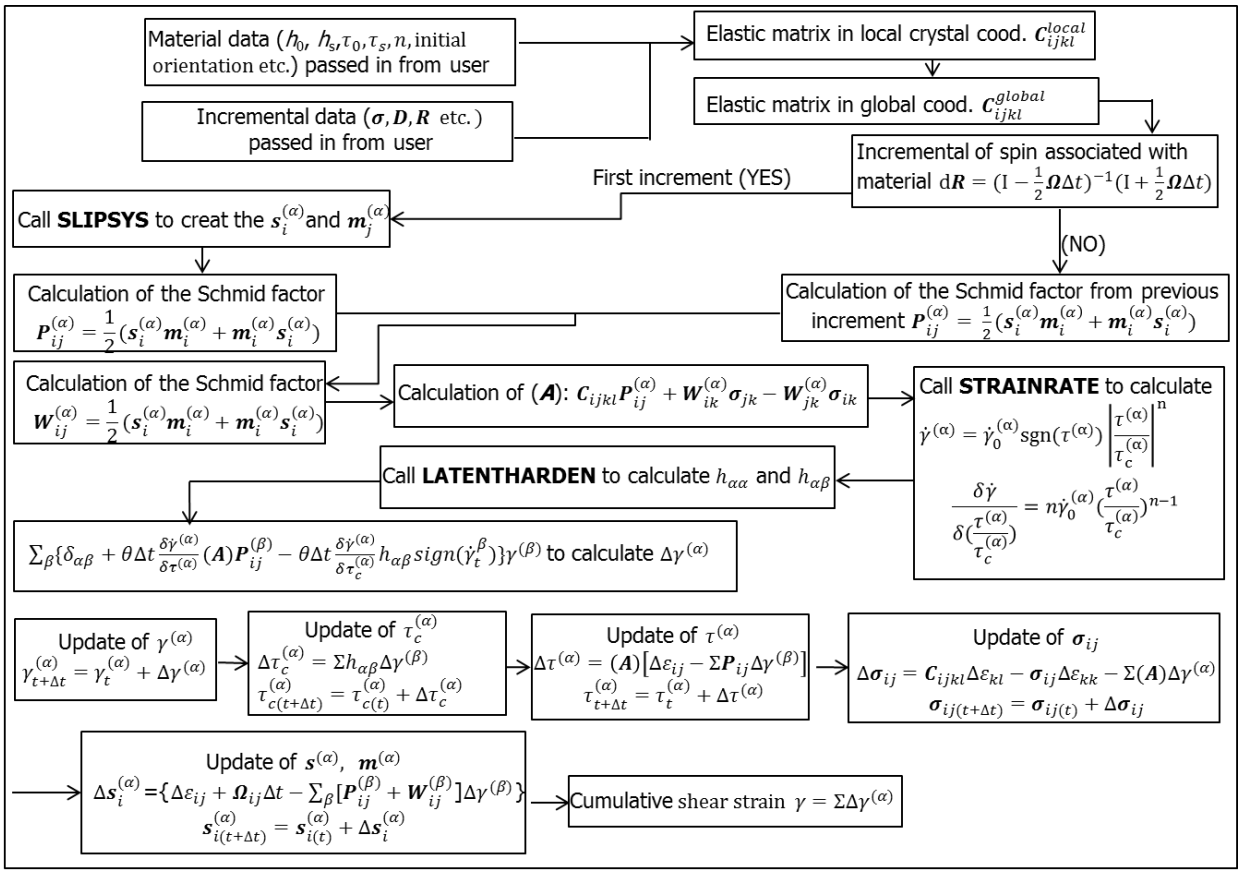

Fig. 4.3 The flowchart for UMAT

4.3 CPFEM Model of HPT

Three-dimensional CPFEM simulations of the HPT process of nickel and aluminum single crystals were carried out in this thesis. In this section, the base model information is presented and the input parameters of the constitutive laws are given.

The geometry of the sample and the die, the meshes of the sample and the boundary conditions were all the same with that used in FEM simulation described in Chapter 3. Two coordinate systems, global system C_g (X, Y, Z) and local system C_l (R, θ, Z), are shown in Fig. 4.4. The local R, θ and Z axes represents the radial, circumferential and axial directions at a given location in the global system, respectively. The global coordinate system was used in the simulation, while the local coordinate system was often used in the data analysis. Two initial crystallographic orientations of the single crystal discs, (001) and (111) orientation, were adopted. The (001) orientation was initially oriented with the (001) crystallographic plane parallel to the shear plane and [010] crystallographic direction parallel to the shear direction, as shown in Fig. 4.4. Similarly, the (111) orientation was initially oriented with the (111) crystallographic plane parallel to the torsion axis. The angular values φ stand for the rotation angles away from the fixed X axis around the axial direction on the shear plane. It should be noted that due to the deformation exerted on the small metallic discs, the initial orientation of the single crystal is rotated around the torsion axis as a function of φ. However, the initial orientation is constant within a layer whose plane normal lies parallel to the shear direction. In the deformed materials with FCC structure, it is assumed that slips occur on the {111} slip planes along the <110> slip directions. Their combination defines 12 different slip systems as indicated in the Tab. 4.1, namely a1-d3, respectively.

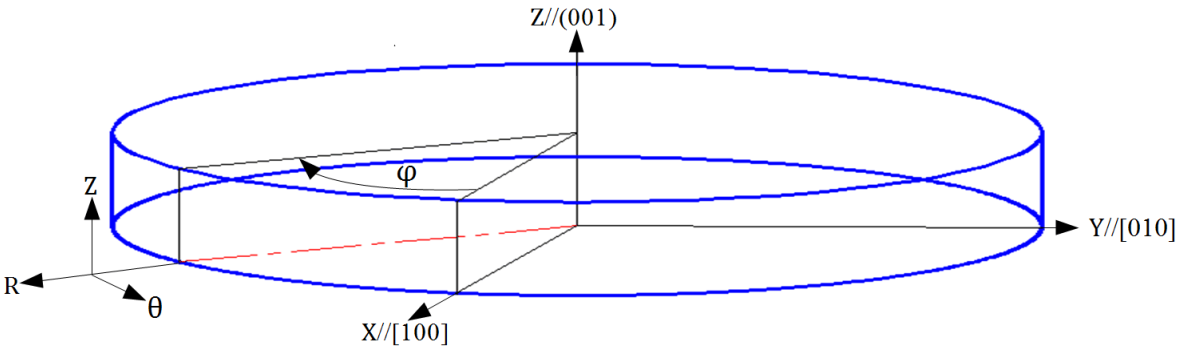

Fig. 4.4 Schematic view of a single crystalline disc that is subjected to HPT deformation

Tab. 4.1 Notations of the slip systems for the FCC materials considered in this study.

Number	Slip system	Slip plane	Slip direction
1	a1	(1 1 1)	[0 -1 1]
2	a2	(1 1 1)	[1 0 -1]
3	a3	(1 1 1)	[-1 1 0]
4	b1	(-1 1 1)	[1 0 1]
5	b2	(-1 1 1)	[1 1 0]
6	b3	(-1 1 1)	[0 -1 1]
7	c1	(1 -1 1)	[0 1 1]
8	c2	(1 -1 1)	[1 1 0]
9	c3	(1 -1 1)	[1 0 -1]
10	d1	(1 1 -1)	[0 1 1]
11	d2	(1 1 -1)	[1 0 1]
12	d3	(1 1 -1)	[-1 1 0]

4.4.1 Nickel Single Crystal

In this study, the HPT process of nickel single crystal was firstly simulated by the developed CPFEM model. A series of constitutive parameters of the simulated nickel material need to be determined. According to the study by Moosbrugger and his co-workers [249,250], the factors $f_{\alpha\beta}$ for nickel material in the Eqn. (4.61) were set as: a1=a2=a3=0.4, a4=0.75 and a5=1. The other material parameters used in the hardening model are listed in Tab. 4.2. They were evaluated by fitting the simulated stress-strain curve with the experimental results under plane strain compression. The elastic moduli tensor for nickel material has been expressed as

$$C_{ij} = \begin{bmatrix} C_{11} & C_{12} & C_{12} & 0 & 0 & 0 \\ C_{12} & C_{11} & C_{12} & 0 & 0 & 0 \\ C_{12} & C_{12} & C_{11} & 0 & 0 & 0 \\ 0 & 0 & 0 & C_{44} & 0 & 0 \\ 0 & 0 & 0 & 0 & C_{44} & 0 \\ 0 & 0 & 0 & 0 & 0 & C_{44} \end{bmatrix} \tag{4.77}$$

where C_{11}=246500 MPa, C_{12}=147300 MPa, and C_{44}=124700 MPa, respectively; they were taken from the research conducted by Freund and Suresh [251], Zhang and Shang [252] and Raabe et al. [253].

Tab. 4.2 The strain rate sensitivity component and parameters in the hardening law for nickel single crystal.

n	$\dot{\gamma}_0$ (s^{-1})	h_0 (MPa)	h_s (MPa)	τ_1 (MPa)	τ_0 (MPa)
50	0.001	61.8	0.01	26.7	17.5
[254,255]	[252,254,255]	[252]	[252]	[252]	[252]

4.4.2 Aluminium Single Crystal

In this study, the HPT process of aluminium single crystal was also simulated. Franciosi et al. obtained the slip system interaction parameters a1-a5 by conducting the latent hardening experiment using aluminum single crystal [256]. The factors $f_{\alpha\beta}$ for aluminium in the Eqn. (4.61)

could be chosen as: a1=a2=a3=1.75, a4=2, and a5=2.25. Three elastic moduli for aluminium material were C_{11}=112000 MPa, C_{12}=66000 MPa and C_{44}=28000 MPa. The other material parameters used for the hardening law are listed in Tab. 4.3, which were identified by fitting the simulated stress-strain curve with the experimental measurements of single crystal aluminum under plane strain compression [257,258]. Recently, these material parameters have been successfully applied in the CPFEM simulations of rolling [230], tensile deformation [231] and ECAP process [214–216].

Tab. 4.3 The strain rate sensitivity component and parameters in the hardening law for aluminum single crystal.

n	$\dot{\gamma}_0$ (s^{-1})	h_0 (MPa)	h_s (MPa)	τ_1 (MPa)	τ_0 (MPa)
300	0.0001	100	0.01	6.3	6

4.4.3 Results of Remeshing during CPFEM simulation

In the CPFEM modelling of the HPT process, the mesh deforms with the material. As the plastic straining is continuously introduced into the sample, the mesh becomes so severely distorted from its original configuration that they no longer provide a good discretization of the analysis or even encounter a convergence problem. When the severe distortion occurs, it is necessary to re-mesh: to create a new mesh to continue the analysis and to map the old- model solution to the new mesh.

In this thesis, a regular mesh was initially used, as shown in Fig. 3.2(a). After a pre-determined revolution angle of N=1/4 turn, the simulation was stopped. A new mesh for the deformed sample was consequently generated. Mesh-to-mesh solution mapping technique built in ABAQUS was used to transfer all state variable values from old mesh to new mesh. The simulation then re-started and the above procedure was repeated. Several steps of remeshing were needed until the desired deformation was reached.

To verify the efficiency of remeshing during the CPFEM simulation of HPT, two positions on the initially un-deformed nickel single crystal, specifically, R=4.5mm,$\theta = 0^{\circ}$, Z=0.75 mm and R=4.5mm, $\theta = 90^{\circ}$, Z=0.75 mm, were chosen for analysis. These positions rotated with respect to the Z axis on the shear plane simulating the changes in crystallographic orientation. At each remeshing step, the crystallographic orientations of the old deformed mesh and the consequently new generated mesh were collected for comparison. Figs. 4.5-4.6 show the comparisons of crystallographic orientation between old and new mesh of these two positions recorded at different remeshing steps when the sample underwent (a) 45°, (b) 78°, (c) 102°, (d) 130°, (e) 146°, (f) 170° revolution angles of HPT deformation, respectively. Figs. 4.5-4.6 indicate that at any step of remeshing the crystallographic orientation of the new mesh are in good agreement with those of the old mesh. This demonstrates that the remeshing method works well and is suitable for the CPFEM simulation of the large deformation of the HPT process.

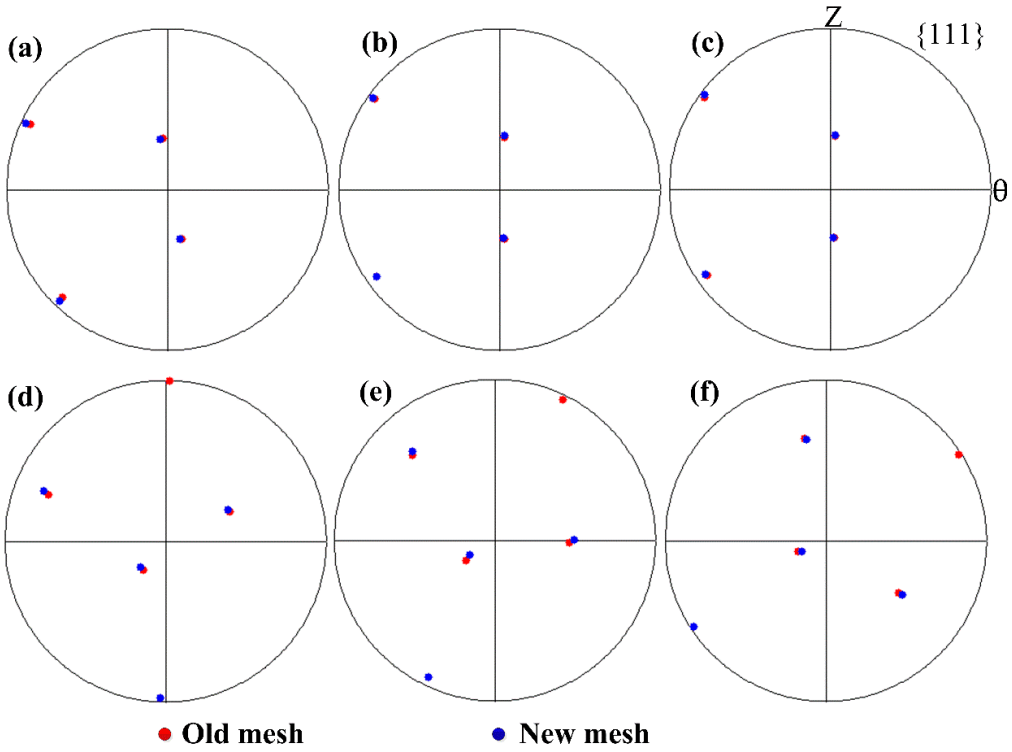

Fig. 4.5 The comparisons of crystallographic orientation between old and new mesh of position R=4.5mm,$\theta = 0^{\circ}$, Z=0.75 mm recorded at different remeshing steps when the sample underwent (a) 45°, (b) 78°, (c) 102°, (d) 130°, (e) 146°, (f) 170° revolution angles of HPT deformation, respectively

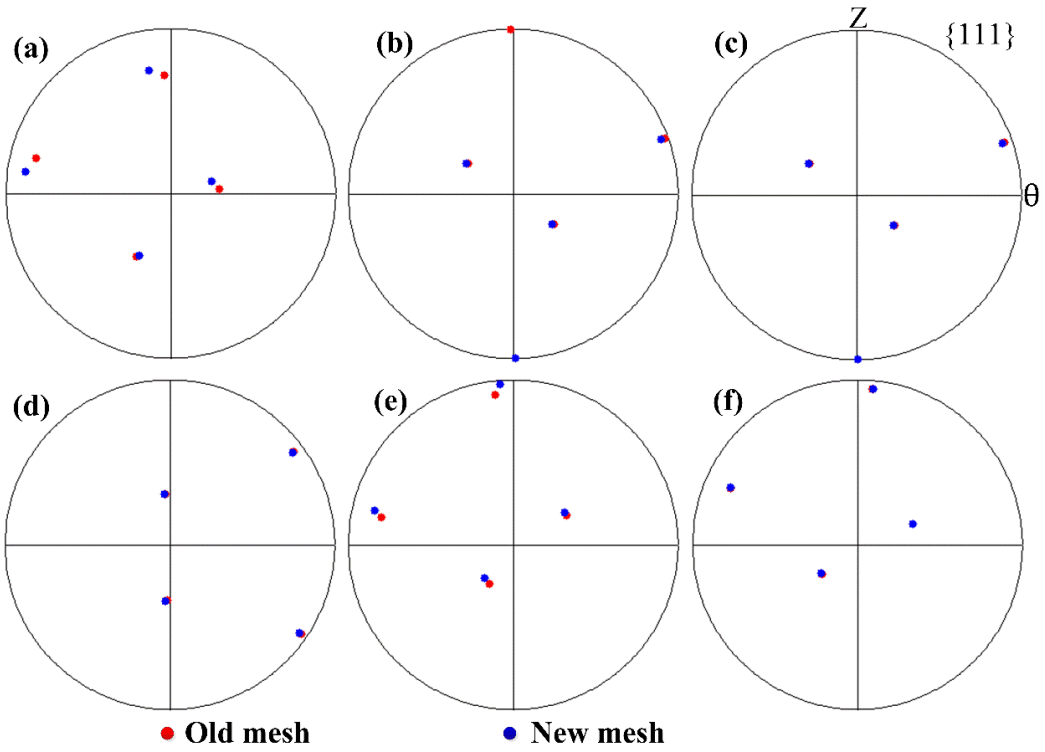

Fig. 4.6 The comparisons of crystallographic orientation between old and new mesh of position R=4.5mm,$\theta = 90^{\circ}$, Z=0.75 mm recorded at different remeshing steps when the sample underwent (a) 45°, (b) 78°, (c) 102°, (d) 130°, (e) 146°, (f) 170° revolution angles of HPT deformation, respectively

4.4 Summary

This chapter is summarized as follows:

(1) The development of a CPFEM model has been introduced. In the model used in this study the deformation has been decomposed into two parts: crystallographic slip due to dislocation on the active slip systems and elastic deformation that includes stretching and rotation of the crystal lattice. The rate-dependent material constitutive law has been applied to overcome the problem of non-uniqueness in the choice of active slip systems which is inherent in the rate-independent theory. The hardening model proposed by Wu and Bassani has also been used because it can accurately capture the three different hardening stages in a slip system and it is also proven to be better than other hardening models in texture predictions.

(2) The detailed implementation of crystal plasticity constitutive model into the user defined material subroutine (UMAT) of commercial finite element code (ABAQUS) has been described.

(3) For the first time, the CPFEM model of the HPT process of single crystals has been constructed by applying the UMAT to the developed FEM model in Chapter 3. The developed CPFEM model will be employed to simulate the texture evolution, grain fragmentation and plastic deformation behaviors of single crystal discs during the HPT process in the following chapters.

Chapter 5 Investigation of Texture Evolution of Nickel Single Crystal during HPT by CPFEM Simulation

In this chapter, the developed CPFEM model is employed to simulate the evolution of crystallographic texture of nickel single crystals during the HPT process. The texture evolution process and the underlying mechanism will be discussed in detail.

5.1 Introduction

It has been known since long time that the major deformation behaviors such as grain refinement and work hardening are strongly related to crystallographic texture [96,259–263]. Up to now, texture evolution during the HPT process has been experimentally studied over a wide range of metals and alloys, such as Pure Al [47,49,52], Pure Ni and single crystal [44,45,47,48,53], Pure Cu and alloys [43,46,54], Pure Mg and alloys [55,173], Ti [43,174] and many other alloys [50,56,57,175–177]. It has been found that the texture formed during the HPT process could be defined directly from those revealed for the case of torsion texture, but there were significant variations both in the intensity and in the relative proportion of each individual ideal component at different stages of HPT straining. Therefore, different ideal components dominated the developed texture at various strain levels of HPT processing. After processed to the sufficiently large strain level, the typical torsion texture usually could be developed.

Crystallographic texture (orientation distribution) and its evolution during forming is a quantity that is inherently connected with plasticity theory. Hence, in addition to the experimental studies, computer modelling is another important and useful tool to interpret the texture evolution. According to the Refs. [199,211,213], crystal plasticity models have enjoyed major

successes in predicting the evolution of the underlying crystallographic texture in single-phase cubic metals subjected to a broad range of low temperature deformation processing operations. Deformation texture modelling started with the Taylor model assuming all constituent crystals of the polycrystal at a material point in the sample experience the exact same deformation history (same as the macroscopically imposed deformation history at that material point). It is now well established that the Taylor-type models produce only reasonably good predictions of texture evolution in the deformed sample. Furthermore, the texture sharpness is significantly overestimated. In addition, they are not satisfactory in texture predictions at large plastic deformation. Later, more sophisticated models such as the advanced Lamel models considering local grain neighbourhood relaxations and visco-plasticity self-consistent (VPSC) models considering the interaction of an ellipsoidal grain with the surrounding medium, have been developed with improved performance in texture predictions. However, the predicted textures are usually too strong, not much different from the Taylor-type model predictions. Meanwhile, the crystal plasticity finite element method (CPFEM) model has been developed by incorporating polycrystal plasticity constitutive equations into FE programs. With this method, grains are represented by finite elements and the deformation of the individual grains is influenced not only by the macroscopic boundary conditions but also by its interactions with other grains in both short and long-range. Because the CPFE models satisfy stress equilibrium and strain compatibility (in the weak numerical sense), it has been proven in various deformation modes that this method can give significantly better texture predictions than the Taylor, Lamel and VPSC models.

During the recent decades, a great deal of interest has been devoted to numerically simulate the HPT process. The majority of published simulation works used the classic FEM method where the adopted materials were assumed to behave as isotropic work-hardening solids [58–66,68,264]. The simulation results have presented some plastic deformation characteristics of the HPT process, such as, the distribution of temperature, the evolution of mean normal stress, equivalent strain and strain rate, the geometrical change after deformation and so on. However, the classic elasto-plastic FEM simulations were unable to predict texture evolution and had few effects in exploring the underlying deformation mechanism.

Theoretical or numerical studies of the HPT process, especially using models integrated with crystal plasticity theory, are very limited. A few pioneering works have been performed to understand the material behaviour in HPT. Estrin et al. [69,179] simulated the HPT process using the gradient plasticity modelling. The constitutive formulation they used was based on a phase mixture model in which the dislocation cell walls and the cell interiors were considered as separate phases with different dislocation densities. Lee et al. [72,73] made further developments based on Estrin's model by embedding the dislocation density-based constitutive model into a finite element code. The aforementioned investigations focused on the prediction of cell/grain size evolution with the accumulation of dislocation density and did not study the texture evolution process. Kratochvil and his co-workers [70,71,180,181] established a simplified crystal plasticity model for the HPT process which was based on the assumption of uniform deformation of plane-strain double slip. They adopted the rotations of slip systems to interpret the microstructure evolution and they did not carry out the texture study either. Hafok and Pippan [48] constructed a fully-constrained Taylor model, which assumed that the local strain rate was equal to the macroscopic strain rate, to simulate the crystallographic orientations development of nickel single crystal during the HPT process. Owning to well-known shortcomings of the Taylor model, they did not give satisfactory texture predictions.

In this chapter, a 3D crystal plasticity finite element model, which incorporates crystal plasticity constitutive equations together with Bassani & Wu hardening modulus into the finite element framework, was developed to simulate the crystallographic texture evolution during the HPT process of initially (001) and (111) oriented nickel single crystals. The single crystal is chosen because it eliminates the effect of grain boundary and grain-grain interaction. The predicted texture results are compared with the currently available experimental measurements. The material deformation, slip activities, and the lattice rotations with increasing applied torsion strain are presented and analysed in detail to reveal the underlying mechanism of crystallographic texture evolution in HPT.

5.2 Simulation Procedure

The simulation model was given in Chapters 3 and 4. In this Chapter, the nickel single crystal with initial (001) and (111) orientations were adopted. The values of various material parameters in the constitutive laws employed in this study were given in Chapter 4. In the deformed nickel material, slips occur on the {111} planes and in the [110] directions. Their combination defines 12 slip systems, as shown in Fig. 5.1(a). For easy reading of the textures, a {111} figure recorded on θ-Z plane was prepared (see Fig. 5.1(b)) that shows the locations of the main components of the ideal shear texture for FCC metals (after [166–168]). In the HPT simulation, the mesh-to-mesh solution mapping technique built in ABAQUS was employed to solve the extremely mesh distortion problem caused by large torsion deformation.

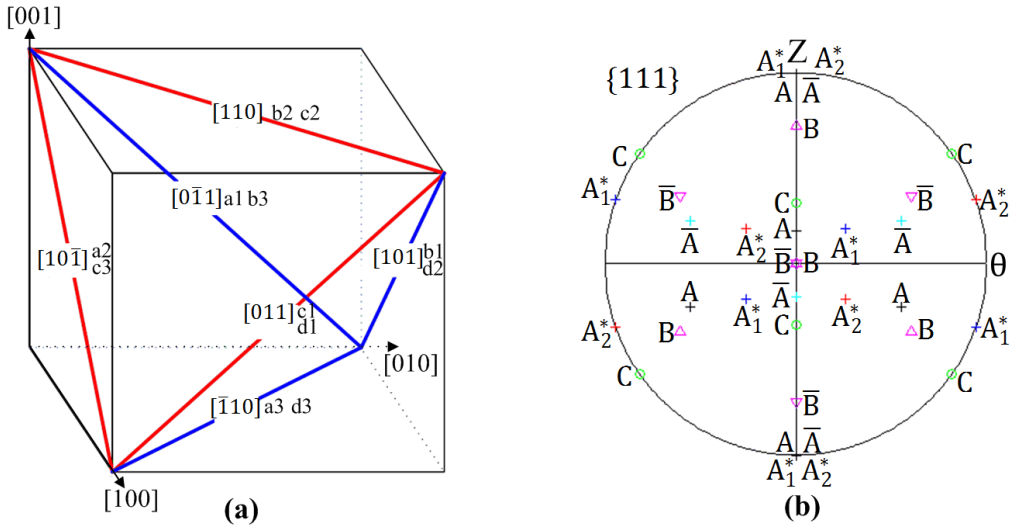

Fig. 5.1 (a) The 12 slip systems of the FCC metals. (b) The main components of the ideal shear texture and their positions on the {111} pole figure recorded on the θ — Z plane.

5.3 Simulation Results

5.3.1 Strain Distribution

Fig. 5 2 shows the distributions of true strain (Variable LE in ABAQUS software) on the top surface of the sample with initial (001) orientation after subjecting to 30° revolution angles HPT

deformation. The strain remains relatively small at the center of the sample and it increases with the distance away from the center. The maximum strain located at the edge of the sample is around 1.4. In addition, close examinations reveal there are slight differences in the strain distribution along the circumferential direction close to the edge region. A distribution pattern with four-fold symmetry, namely four more strained regions separated by four less-strained regions with intervals of $\varphi = 90°$, could be observed around the sample periphery. Here φ refers to the angles of the material flowing away from the fixed X axis around the torsion axis on the shear plane, as shown in Fig. 5.2. The similar strain distribution results on the section of the sample have been previously revealed by [265–267], which reported that the torsion deformation of a cylinder/tubular sample with respect to a [001] axis gave rise to the formation of four more strained zones along the circumference of the sample by using a micro-macro anisotropic viscoplasticity model and experimental observations.

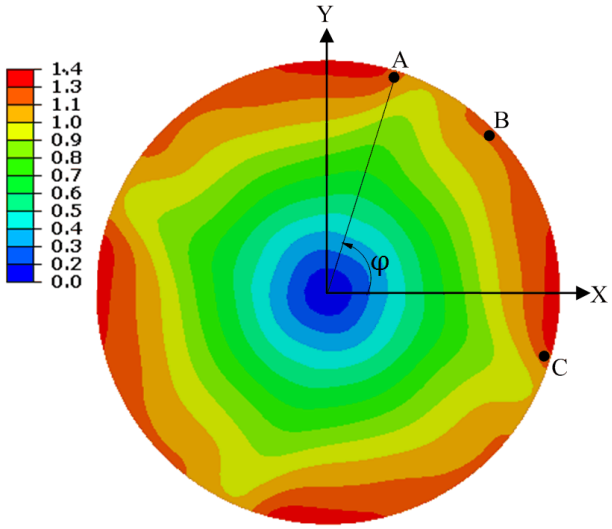

Fig. 5.2 The predicted strain distribution on the surface of (001) nickel single crystal after 30° revolution angles HPT deformation.

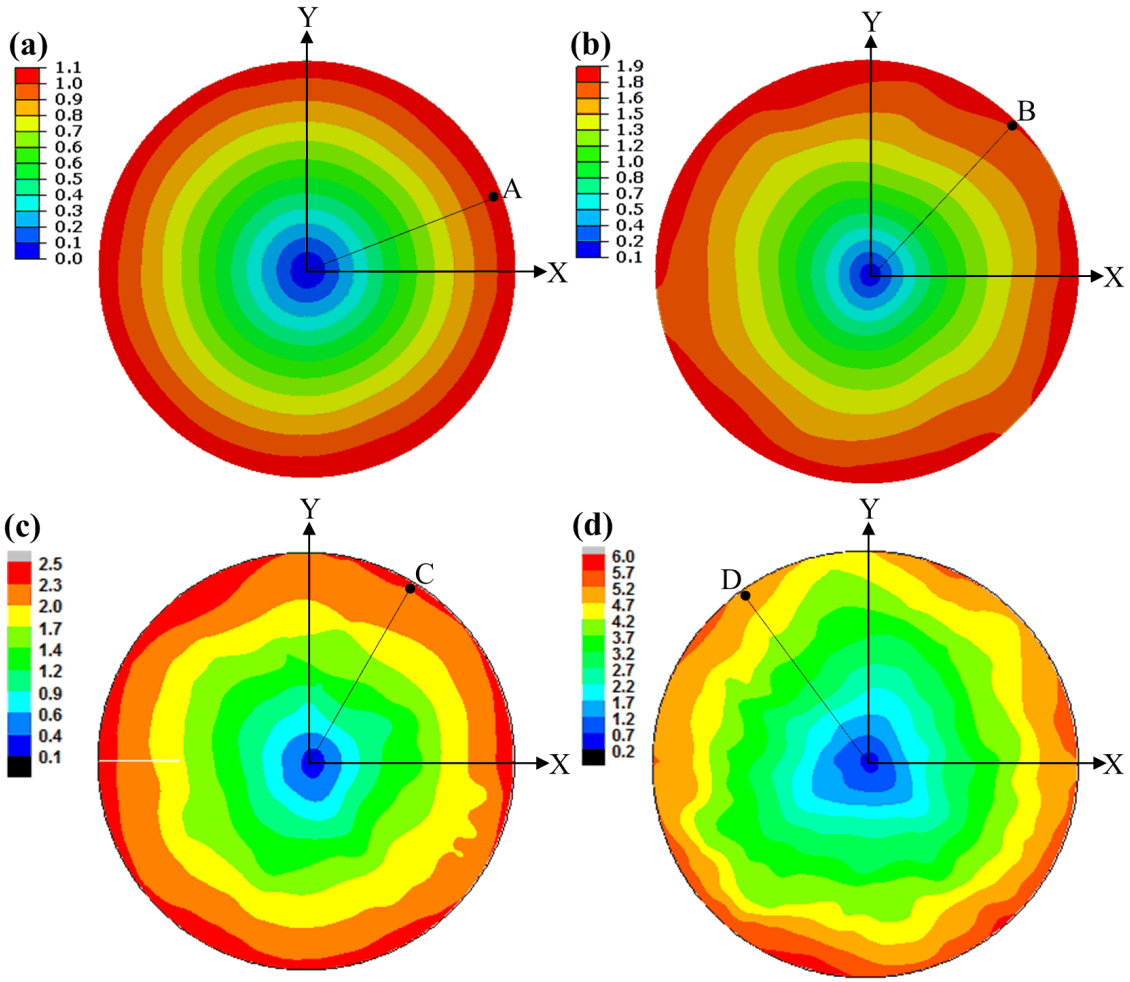

Fig. 5.3 The predicted strain distributions on the surfaces of the initial (111) nickel single crystal after increasing revolution angles HPT deformation of (a) 22.5°, (b) 45°, (c) 60° and (d) 125°.

Fig. 5.3 plots the evolution of strain distribution on the surface of initial (111) nickel single crystal as a function of increasing revolution angles of HPT deformation of 22.5°, 45°, 60° and 125°. Fig. 5.3(a) shows that after 22.5° degrees of HPT deformation the sample is approximately homogeneously deformed along the circumferential direction and the strain increases from the centre of the sample to the edge region at a maximum value of ~1. After further deformation, in Figs. 5.3(b)-(d), the similar tendency of increasing strain with the distance from the centre of the sample could be clearly observed and the corresponding maximum strain values at the edge regions after 45°, 60° and 125° deformation are ~2, ~2.5, and ~6 respectively. Moreover, close to the sample peripheries, the slight differences in the strain distribution along the

circumferential direction could also be seen in Figs. 5.3(b)-(d), which exhibit three-fold strain distribution patterns of less strained and more strained zones with intervals of about $\varphi = 120°$. These zones have also been predicted by classical crystal plasticity simulation in [266].

5.3.2 (001) Nickel Single Crystal

Ref. [48] have reported the texture measurements at different sample positions along the circumferential direction of the (001) nickel single deformed to an equivalent strain between 1.4-1.6. In order to verify the developed CPFEM model, the predicted and measured pole figures reported in Ref. [48] were compared. It is noted that Ref. [48] did not give the specific positions where the texture measurements took place. In this study we may reasonably conclude these specific positions according to the initial orientations, as marked by A ($\varphi = 75°$), B ($\varphi = 45°$) and C ($\varphi = -15°$) in Fig. 5.2. Figs. 5.4(a)-(c) respectively shows the texture results of these three different positions along the tangential direction. The first column pole figures are experimental measurements corresponding to an equivalent strain between 1.4 and 1.6, while the second and third columns are simulations results after $30°$ revolution angles HPT deformation with an equivalent strain of about 1.4 (see Fig. 5.2). The scan size of the experimental measurements were around 200 μm x 200 μm while the predicted pole figures were plotted over an area of about 1000 μm x 200 μm which only consist of several meshes. The pole figures of the first and second columns are the experimental measurements and simulations of {001} crystallographic planes projected onto the R-θ planes. The horizontal axis and vertical axis in the pole figures represent the local radial direction (R) and circumferential direction (θ), respectively. Since the main components of the ideal torsion texture are normally presented in terms of {111} pole figure in the tangential direction and in the direction of torsion axis, as shown in Fig. 5.1(b), to compare the texture results with the ideal torsion texture, such {111} pole figures recorded on $\theta - Z$ planes were also plotted, as shown in the third column of Fig. 5.4. It should be noted that, at each studied position, the two pole figures of the second and third column represent the same distribution of crystallographic orientation with respect to the sample coordinate system. In the pole figures, the initial orientation and the orientation after deformation are indicated by black squares and dots respectively. The locations of the

ideal torsion texture components are also shown and visualized by different symbols in the pole figures of the third column. An {hkl} <uvw> orientation used in this study signifies that the {hkl} crystallographic plane coincides with the shear plane and that the <uvw> crystallographic direction is aligned with the shear direction. The A partial fibre could be indexed as {111} <uvw>, the B partial fibre as {hkl} <110> and C orientation as {001} <110>, which is just a special position of B fibre.

The pole figures shown in Fig. 5.4(a) are the texture results developed at Position A. The initial orientation of this position is identified to be close to (001) orientation (ideal C component) after comparing it with the ideal torsion texture components. The lattice rotations during HPT deformation process have changed the initial crystallographic orientation to positions indicated by black dots. The red circles represent the position of a (111) orientation (ideal A_1^* component). It can be seen from Fig 5.4(a) both the experiment and the simulations indicate that the crystallographic orientations after HPT deformation rotate away from the initial C component progressively and then occupy positions close to the ideal A_1^* orientation. It should be noted that there are fewer points in the simulated pole figures than the measured results as the dimension of the elements is much larger than the resolution applied in the experiments. If we consider Fig. 5.4(b), obtained at position B, it's readily to see that the initial orientation of this position also rotates away from the ideal C orientation by about $30°$ around the sample torsion axis. The pole figure of experiment shows that the developed orientations rotate away from the initial orientation progressively and occupy an orientation close to the (011) orientation marked by red circles. The predicted texture also reveals that the introduced stains during HPT deformation cause the initial orientation to rotate close to the (011) orientation. Small deviations between the experimental and predicted texture are observed as there are absent of orientations close to the initial orientation in the predicted pole figures. This is due to that the initial orientation of the experimental measurement deviated slightly from the simulation. The texture results depicted in Fig. 5.4(c) were obtained from position C. The initial orientation of this position is again close to the ideal C component. The pole figures illustrate a similar texture results with position A recorded in Fig. 5.4(a). The experimental pole figure reveals that some orientations have just rotated away from the initial C orientation, while the other orientations

rotate considerably and occupy positions close to the ideal A_1^* orientation (indicated by red circles). The simulates are capable of predicting both orientations in the pole figures

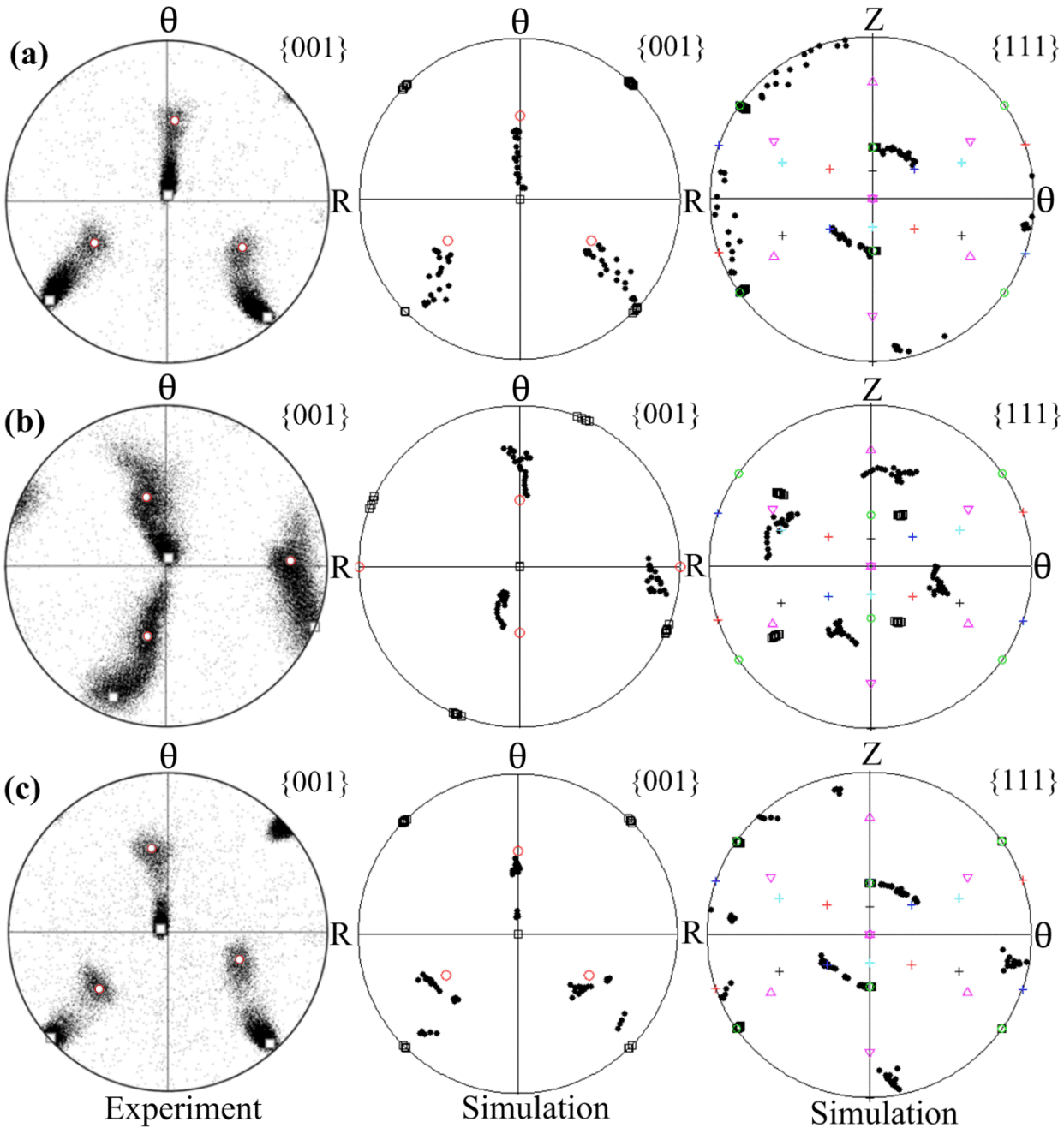

Fig. 5.4 Pole figures of the initial (001) nickel single after 30° revolution angles of HPT deformation at various positions along the tangential direction (a) position A $\varphi = 75°$, (b) position B $\varphi = 45°$ and (c) position C $\varphi = -15°$. (Positions A-C have been given in **Fig. 5.2**)

5.3.3 (111) Nickel Single Crystal

Fig. 5.5 shows the texture evolution of the initial (111) nickel single crystal with increasing HPT deformation. The texture results were obtained at four different positions of different strain levels, as labelled A-D respectively in Figs. 5.3(a)-(d). The same analytical method applied to the (001) nickel single crystal was used here. The first column pole figures in Figs. 5.5(a)-(d) are experimental measurements corresponding to an equivalent strain of 1, 2, 2.5 and 5 respectively [48], while the second and third columns are simulations results after $22.5°$, 45°, 60° and 125° degrees of HPT deformation with an equivalent strain of $\sim$1.1, $\sim$1.9, $\sim$2.5 and $\sim$5 respectively (see Fig. 5.3). The scan size of the experimental measurements was approximately 30 μm x 30 μm while the predicted pole figures were plotted over an area of about 1000 μm x 200 μm. The first and second columns are the experimental measurements and simulation predictions of {001} pole figure recorded on the R-θ planes. The third column is simulation predictions of {111} pole figures recorded on $\theta - Z$ planes corresponding to each pole figure in the second column. The initial crystallographic orientation of the (111) nickel single crystal is $(111)[11\bar{2}]$ (ideal A_2^* component) and is denoted by black squares in the pole figures. The resulting orientations at different strain levels are indicated by black dots.

It could be seen from the pole figures in Fig. 5.5(a), after $22.5°$ revolution angles HPT deformation, at position A, the crystallographic orientations change gradually away from the initial A_2^* orientation and rotate towards a certain preferred orientation. Compared to the predicted results, the measured orientations are observed to rotate moderately faster. After 45° degrees of HPT deformation, at position B, the pole figures in Fig. 5.5(b) show that the HPT deformation leads to a texture with a particular orientation distribution. Both the experimental measurement and simulation predictions reveal that the developed orientations indicated by black dots, change progressively from the initial orientation, black squares in the pole figures, to the orientation marked by red circles, which are the positions of the (001) orientation (ideal C component). Some poles in the pole figures of Fig. 5.5(b) have already reached the position of the first favoured orientation of ideal C component. When further deformed to 60° revolution angles, at Position C, the measured and predicted pole figures all show that the resulting

orientations have concentrated into the ideal C orientation. It should be noted that the in the experimental pole figure of Fig. 5.5(c), a few poles extend to the next preferred orientation whereas in the predicted pole figures such an extension could not be observed. After the angles of sample rotation increase to 125°, at position D, the measured and predicted pole figures in Fig. 5.5(d) show a weak ideal C orientation and a strong orientation close to the second preferred orientation marked by red stars which could be recognized as A_1^* component of ideal shear texture, indicating that most developed orientations have already rotated into the favoured A_1^* orientation.

It can be seen from Figs. 5.4 and 5.5 that the simulated pole figures have captured the main features of the experimental measurements reported in Ref. [48]. The good coincidence between the experimental measurements and simulation predictions demonstrate that the developed CPFEM model in this study could predict the developed texture during the HPT process.

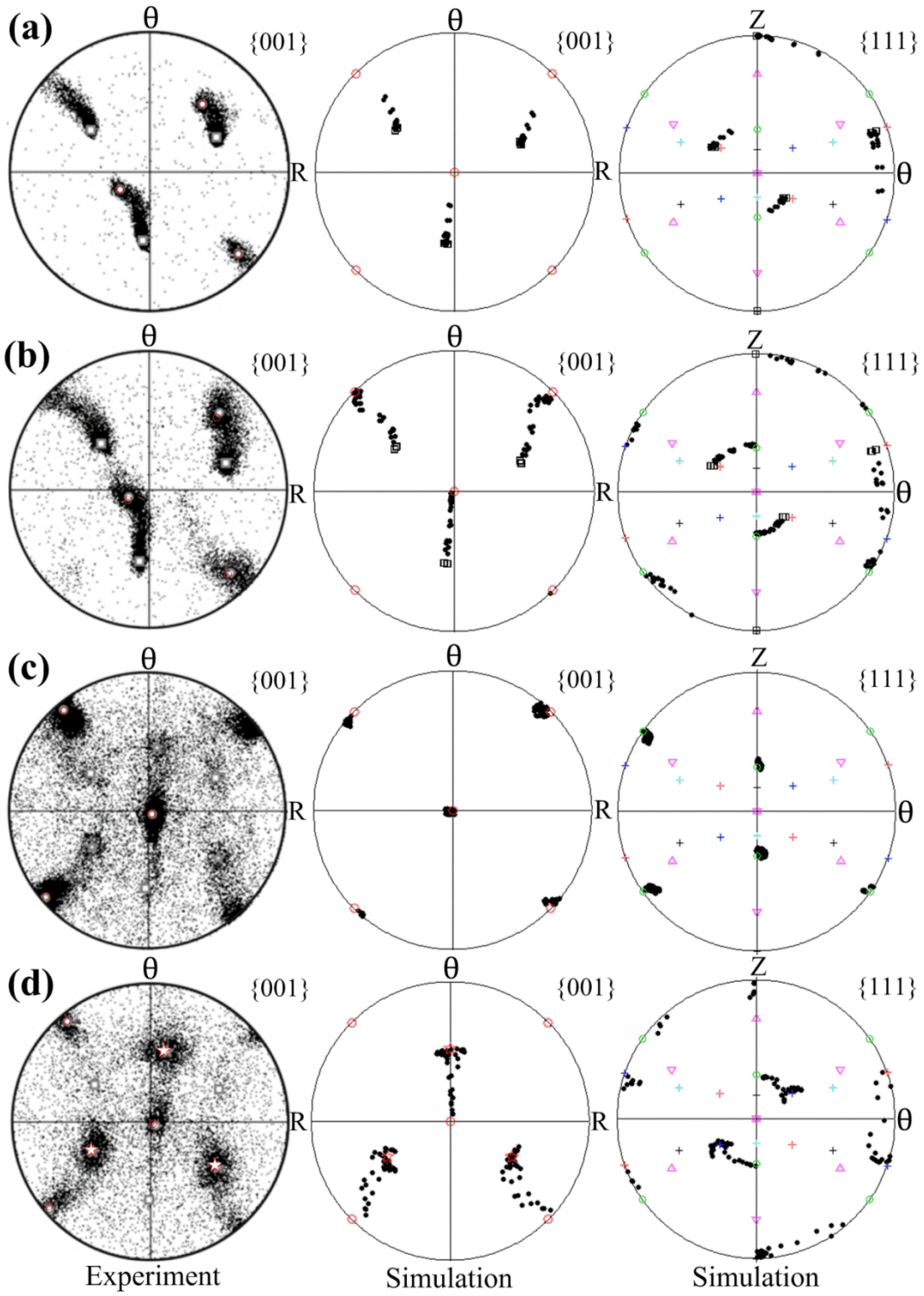

Fig. 5.5 Pole figures of the initial (111) nickel single after increasing revolution angles of HPT deformation of (a) 22.5°, (b) 45°, (c) 60° and (d) 125° (These pole figures correspond to positions of A ($\varphi = 22.5°$), B ($\varphi = 45°$), C ($\varphi = 60°$) and D ($\varphi = 125°$). These positions have been given **Fig. 5.3**)

5.4 Mechanism of Texture Evolution

5.4.1 Initial C Orientation of the (001) Nickel Single Crystal

To understand how the texture evolved from the initial C crystallographic orientation to the preferred A_1^* orientation in Fig. 5.4(a), the changes for the initial C orientation of the (001) nickel single crystal at different stages of HPT deformation were plotted, as shown in Fig. 5.6. All the orientations are presented by means of {111} pole figures recoded on θ-Z planes. In this study, only one mesh was considered as a representation. Under un-deformed condition, the initial C orientation is marked by black dots in the pole figure, as shown in Fig. 5.6(a). The orientations developed at different stages of HPT deformation are represented by red dots in the pole figures of Figs. 5.6(b)-(f), respectively. In Fig. 5.6(b), referring to 12° degrees of HPT deformation, one can see that the developed orientation rotates only minorly away from the initial C orientation. Further HPT deformation results in considerable lattice rotations and the developed orientations change significantly to occupy different positions in the pole figures, as shown in Figs. 5.6(c)-(d) where the sample undergoes about 18°, 23° degrees of HPT deformation respectively. Fig. 5.6(e) shows that after 32° degrees of HPT deformation the resulting orientation approaches the A_1^* component of the ideal shear texture and finally approximately occupies the position of ideal A_1^* orientation after a sample rotation of 40°, as shown in Fig. 5.6(f). For the convenience of interpretation, the orientations depicted in Figs. 5.6(b)-(f) are labeled as 1-5 respectively in the following context.

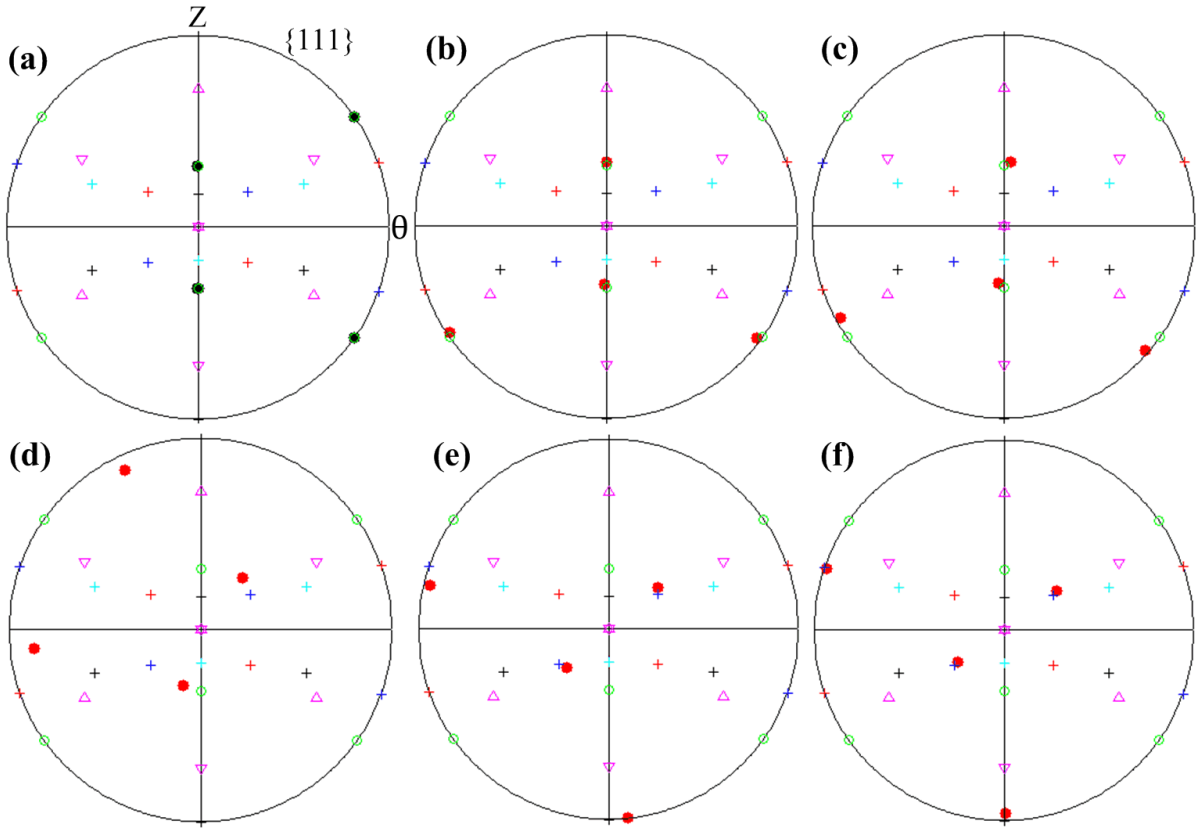

Fig. 5.6 The predicted orientation changes for the initial C orientation of (001) nickel single crystal as a function of increasing revolution angles HPT deformation of (a) 0°, (b) 12°, (c) 18°, (d) 23°, (e) 32° and (f) 40°. The orientations depicted in Figs. 5.6(b)-(f) are labeled as 1-5 respectively in the following context.

The series of pole figures in Fig. 5.6 indicate that, with increasing HPT deformation, the lattices rotate progressively to accommodate the continuously introduced plastic deformation, leading to the crystallgraphic orientation changes of the initially C oriented crystal. In order to describe the rotation of the crystallographic orientation quantitatively during the HPT process, the misorientation of the initially C oriented crystal relative to the initial orientation was calculated and partitioned into three components which represent the rotation angles around R, θ, and Z axes of the local polar coordinate system, respectively. The partition method proposed by Wert et al. [268] was adopted and adjusted to the local polar coordinate system. Fig. 5.7 shows the results of lattice rotation angles along the R, θ, and Z axes with increasing HPT deformation. The horizontal axis of this figure represents the various levels of deformation in the form of revolution angles. The vertical axis of this figure stands for the lattice rotation angles. The

positive value of the lattice rotation angle means the counter-clockwise rotation while negative value means the clockwise rotation. The resulting orientations labeled by 1-5 in Fig. 5.6 are visualized by green circles at their corresponding stain levels, as shown in Fig. 5.7.

It can be seen from Fig. 5.7 that the rotation angles around R axis are significantly larger than the other two axes. A small amount Z-axis lattice rotation angles could be observed over only a short strain range while the rotation angles along the θ axis basically remain zero. This result is confirmed by previous experimental observations and simulations reported in [153,166,167], which revealed the predominance of single sense lattice rotations around the sample radial direction during the torsion deformation process. According to the evolution of lattice rotation along the radial direction shown in Fig. 5.7, the deformation process could be roughly divided into three stages: The initial stage I with nearly absence of lattice rotation, which ranges from 0° to 12° degrees of HPT deformation; a middle stage II during which the R-axis lattice rotation angles increase progressively to $\sim 50°$. This stage ranges from $12°$ to around $38°$ HPT deformation; the final stage III with almost no further lattice rotation for the left strain range. Orientation 1 of Fig. 5.6(b) locates in stage I and therefore a nearly initial C orientation has been observed in the pole figure. Orientations 2 locates at the beginning of stage II when the crystal becomes initially rotated and ∼5° R-axis lattice rotation could be seen in the pole figure of Fig. 5.6(c). Orientations 3 positions about in the middle of stage II when the lattice rotation along the R axis increases dramatically, $\sim 30°$ R-axis rotation angles have been seen in the corresponding pole figures of Fig. 5.6(d). Orientations 4 locates at the end of stage II and is about to enter stage III, until when the crystal has already underwent a large lattice rotation and ∼50° rotations angles along the R axis could be found in the pole figure recorded in Fig. 5.6(e). It's worth noting that in stage II the crystallographic orientation does not rotate uniformly with increasing plastic deformation, specifically, when initially leaving the ideal C component and about to enter the ideal A_1^* component, the lattice rotates at a relatively small rate, whereas away from the preferred orientations, the lattice rotation becomes significantly faster. This is again consistent with the experimental observations and simulations reported in [153,166,167] which revealed that the crystallographic rotation vectors converged adjacent to the main torsion deformation texture components and when rotated away from the ideal

components the divergence occurred. Orientations 5 positions in stage III, the R-axis rotation angles are ~55° and once more illustrate relatively limited increase within the left strain range.

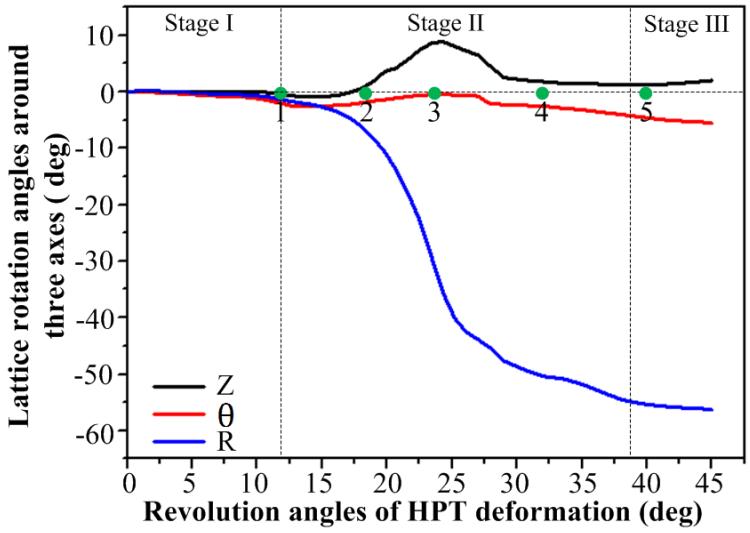

Fig. 5.7 The predicted lattice rotations around R, θ and Z axes for the initial C orientation of (001) nickel single crystal as a function of increasing revolution angles HPT deformation.

Fig. 5.8 shows the predicted results of six components of material strain rate (D), three components of material spin (Ω), resolved shear strain rates on twelve slip systems and three components of lattice spin (Ω^*) for the initial C orientation of the (001) nickel single crystal as a function of increasing applied HPT deformation. Under the condition of our simulation, one end of the sample was fixed while the opposite end twisted an angle under hydrostatic pressure. The material flowed away from its initial position on the shear plane as the plastic deformation proceeded. Therefore the strain rate component $D_{\theta z}$ plays the main role during the whole plastic deformation process, while the other components are almost zero, as shown in Fig. 5.8(a). Accordingly, the material spin component $\Omega_{\theta z}$ (Ω_R) is much larger than the other two components at any rotated position (see Fig. 5.8(b)). According to the Refs. [215,269], the predominant material spin tensor, Ω_R, could be satisfied by two components: Ω^p caused by the slip and Ω_R^* by the lattice rotation and stretching. Ω_R^* represents the rate of rotation of the crystallographic orientation. The changes of resolved strain rates on twelve slip systems and the lattice spin components are presented in Figs. 5.8 (c)-(d) respectively, and they will be combined with the results in Figs. 5.8 (a)-(b) to explore the underlying mechanism of the

crystallographic orientation changes for the initial C orientation of (001) nickel single crystal during the HPT process.

The deformation process is also divided into three stages, same with that in Fig. 5.7. It can be seen from Fig. 5.8(c), during stage I, the major feature is that only two slip systems, namely b2 and c2, which share the same crystallographic direction of [110] (see Fig. 5.1(a)), are activated. All the material strain rates ($\mathrm{D}_{\theta\mathrm{Z}}$) in Fig. 5.8(a) are concentrated into these two predominant slip systems and therefore the magnitudes of resolved shear strain rate of b2 and c2 are significantly large. Under this condition, the dominant two slip systems can generate a sufficiently large plastic rotation (Ω^{p}) to meet the requirement of the whole material rotation (Ω_{R}) (see Fig. 5.8(b)). Thus the lattice rotation (Ω_{R}^{*}) is not necessary and remains almost zero (see Fig. 5.8(d)), leading to the crystal has a near-initial C orientation with increasing applied torsion straining in stage I (see orientations 1).

During the early period of stage II, Fig. 5.8(c) shows that the magnitudes of resolved shear strain rate on the primary slip systems b2 and c2 grow even larger. Meanwhile, another two slip systems, namely a1 and a2, are initially activated successively. Therefore multiple slip systems are simultaneously functioned. It can be seen from Fig. 5.1(a) that the activated slip systems a1, a2, and b2 (c2) are all oriented along different directions and form 120° angles with each other. They provide opposing contributions to the overall plastic rotation (Ω^{p}). However, during the early period, the resolved shear strain rates of a1 and a2 are so small that they only induce limited disturbance to the dominant slip of b2 and c2, resulting in a smaller overall plastic rotation (Ω^{p}) than stage I. Thus a slight increase in lattice rotation (Ω_{R}^{*}) can be seen at the early period of stage II in Fig. 5.8(d) and a relatively small amount of R-axis lattice rotation of $\sim$5° have been observed for orientations 2. As the deformation continues, the resolved shear strain rate on the dominant slip systems b2 and c2 decreases gradually to zero, while the strain rates of a1 and a2 increase continuously and their disturbance capacity grows further. The functioned slip systems possess almost the similar amount of strain rates but are oriented along different directions. This results in a very small overall plastic rotation (Ω^{p}). Therefore the lattice has to rotate significantly (Ω_{R}^{*}) (see Fig. 5.8(d)) to meet the material rotation (Ω_{R})

requirement induced by HPT deformation and a considerable amount of lattice rotations of $\sim 30^{\circ}$ have been seen for orientation 3. Afterwards, accompanied by the decrease in the resolved strain rates of a1 and a2, another two differently-oriented slip systems, d1 and d2, are activated so that the multi-slip condition continues within the middle period of stage II. During the latter period of stage II, the strain rates of slip systems a1 and a2 evolve gradually smaller, while the strain rates of slip systems d1 and d2 become larger and tend to play a dominant role with increasing plastic deformation, producing an ever-increasing overall plastic rotation (Ω^{p}). Accordingly, the lattice rotates at a decreasing rate of Ω_{R}^{*} (see Fig. 5.8(d)) and a slightly further increase in R axes rotation has been observed for orientation 4 at the latter part of stage II.

Fig. 5.8(c) shows that, during stage III, the disturbance of slip systems a1 and a2 basically vanishes, d1 and d2 have become the dominant slip systems that produce a given amount of overall glide rotation (Ω^{p}) capable of satisfying the demands of the whole material rotation (Ω_{R}). There is again a near-zero lattice rotation (Ω_{R}^{*}) in Fig. 5.8(d) and orientation 5 illustrates relatively limited further lattice rotation for the left strain range in Fig. 5.7. Seeing from Fig. 5.1(a), slip systems d1 and d2 position in the same crystallographic plane of $(11\bar{1})$ and form the same angle with $[112]$ crystallographic direction. The $(11\bar{1})[112]$ orientation is well known as A_{1}^{*} component of the ideal simple shear texture.

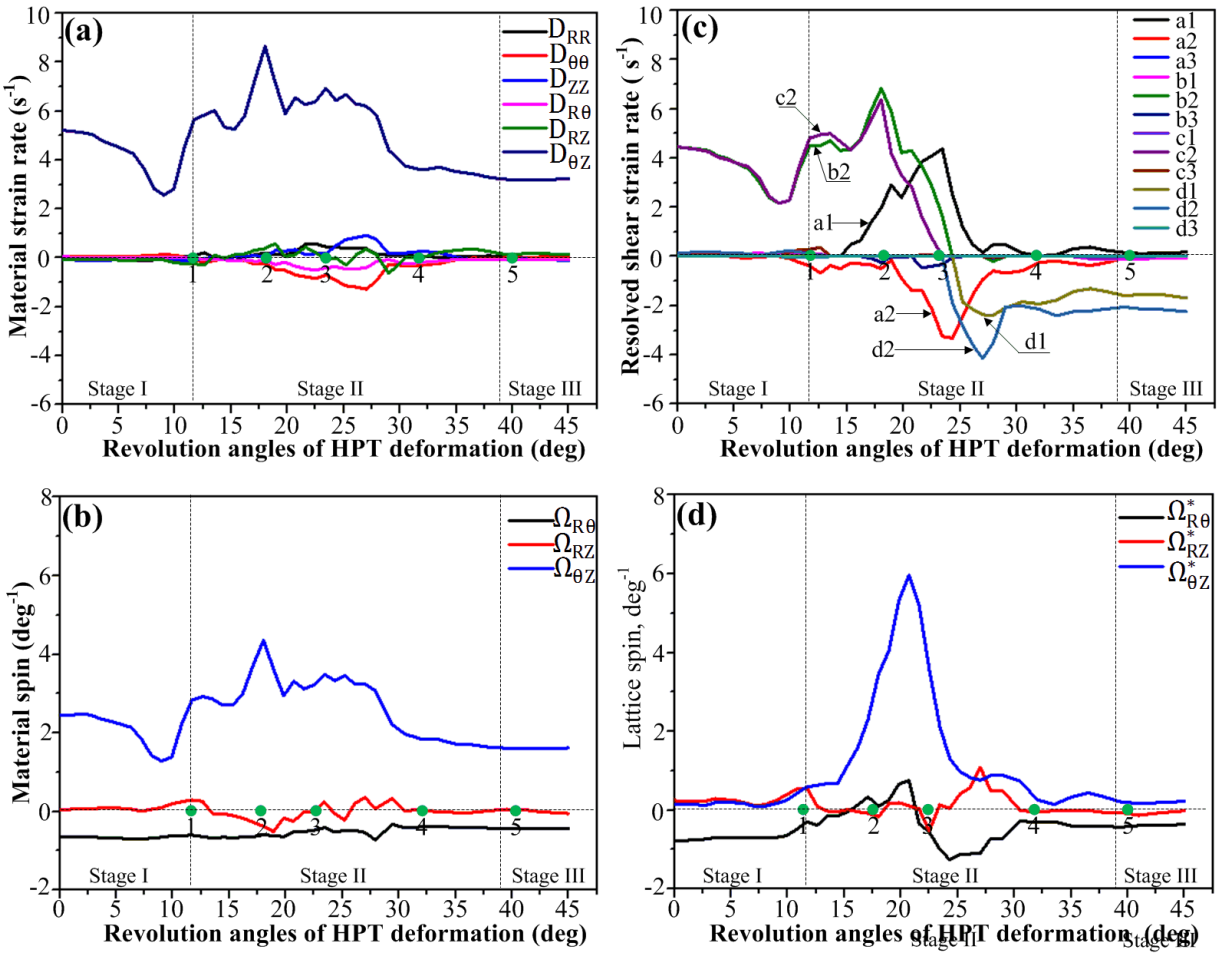

Fig. 5.8 The predicted results for the initial C orientation of (001) nickel single crystal as a function of increasing revolution angles HPT deformation. (a) Material strain rate, (b) Material spin, (c) Resolved shear strain rate and (d) Lattice spin.

5.4.2 Initial Cube Orientation of the (001) Nickel Single Crystal

The Cube orientation (001)[100] plays a central role in industrial thermo-mechanical processes. Enormous interests have been devoted to study the behavior of the Cube texture component in various deformation modes, as discussed in the Ref. [270]. In this section the initial Cube orientation of the (001) nickel single crystal deformed by the HPT process was investigated. The similar analytical method for the initial C orientation was applied.

Fig. 5.9 shows the predicted {111} pole figures for the initial Cube orientation of the (001) nickel single crystal at different stages of HPT deformation. The initial cube orientation is represented

by black dots, as shown in Fig. 5.9(a). The resulting orientations developed at different strain levels are indicated by red dots in the corresponding pole figures recorded in Figs. 5.9(b)-(g).

The effect of the increasing torsion strain on the initial Cube orientation is firstly shown in Figs. 5.9(b)-(c), which corresponds to the 6° and 12° revolution angles HPT deformation respectively. The predicted orientations rotate significantly away from their initial position in a clockwise direction due to continuous lattice rotations and locate around the position of rotated cube orientation in the pole figures. This agrees well with the results reported by Toth et al. [144]. They experimentally examined the texture after ECAP of an initially cube-oriented nickel single crystal and found that the texture showed strong rotated cube component in the billet. The developed rotated cube orientation is unstable. As the deformation proceeds, the crystallgraphic orientation keeps on rotating to accommodate the increasing introduced plastic strain. Figs. 5.9(d)-(f) respectively shows that after 22.5°, 27° and 33° degrees of HPT deformation, the poles rotate progressively and occupy positions that differ greatly from the rotated cube orientation. When the sample is further deformed, the orientations rotate gradually into a certain preferred crystallographic orientation. One can see from Fig. 5.9(g) the initially cube oriented crystal has the orientation close to the C component of the ideal torsion texture when the sample undergoes 42° revolution angles HPT deformation. Such a rotation has also been reported by Toth et al. [144]. They found by experimental measurements and crystal plasticity modeling that the orientation deviating from the exact cube orientation, just like the orientations in Figs. 5.9(b)-(c), rotated into the C texture component. For the convenience of interpretation, the orientations depicted in Figs. 5.9(b)-(g) are labeled as ①-⑥ respectively in the following context.

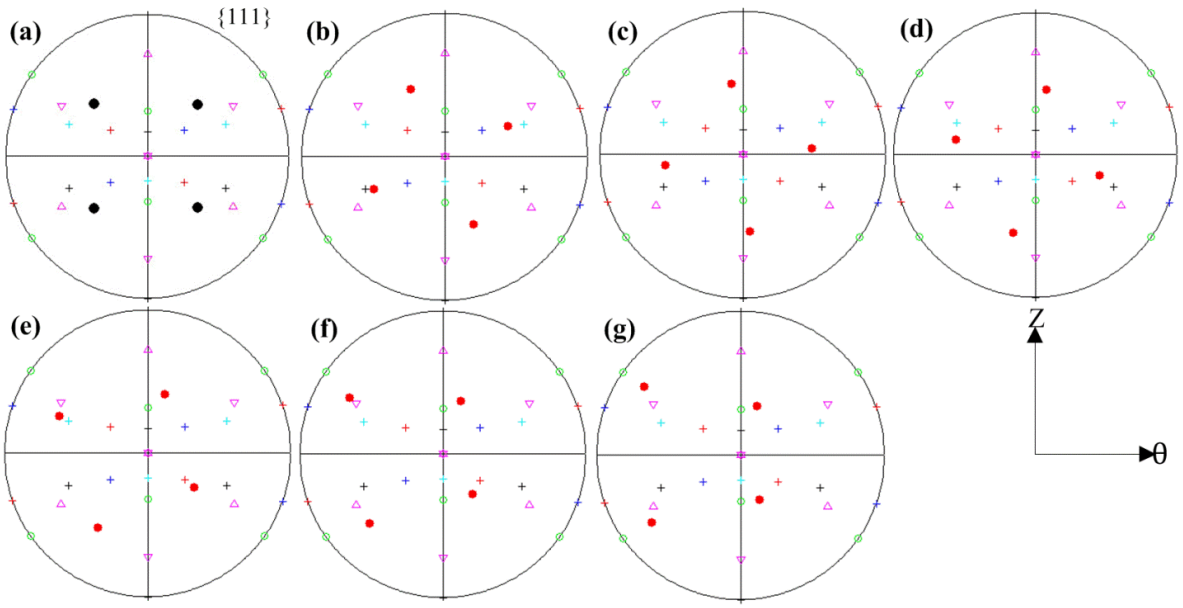

Fig. 5.9 The predicted orientation changes for the initial Cube orientation of (001) nickel single crystal as a function of increasing revolution angles HPT deformation of (a) 0°, (b) 6°, (c) 12°, (d) 22.5°, (e) 27°, (f) 33° and (g) 42°. The orientations depicted in Figs. 5.9(b)-(g) are labeled as ①-⑥ respectively in the following context.

The lattice rotation angles around the R, θ, and Z axes for the initial Cube orientation of (001) nickel single crystal as a function of increasing revolution angles HPT deformation were studied and are shown in Fig. 5.10. The predicted orientations ①-⑥ in Figs. 5.9(b)-(g) were marked by green circles at their corresponding strain positions. The predominant lattice rotation along the R axis during the whole process could also be observed, as that illustrated in Fig. 5.7. Similarly, according to the evolution of R-axis rotations in Fig. 5.10, the deformation process could be roughly divided into three stages: the initial stage I ranging from 0° to about 17° degrees of HPT deformation; the middle stage II from 17° to around 38°; and the final stage III for the left strain range.

In stage I, the R-axis lattice rotation presents an approximately linear increase to ~50° as applied plastic strain increases. By contrast, the θ and Z-axes lattice rotations remain basically unchanged apart from a minor increase in the θ-axis rotation at the end of this stage. This means that during this stage the lattice rotation is almost simply around the radial direction.

Orientations ① and ② locate in stage I, ~20° and ~40° R-axis rotation angles have been observed in the corresponding pole figures of Figs. 5.9(b)-(c). In stage II, the lattice rotation becomes very different. It is no longer taking place simply around the R axis but around all three axes. The R-axis rotation angles increase continuously at a smaller rate than stage I to ~85°. Accompanying with the R-axis rotation, the θ and Z-axes rotation angles illustrate a relatively small increment in the beginning, followed by a considerable increase and then tend to level off. Close inspections reveal that the θ and Z-axes rotation angles both reach to ~30° at the end of this stage. Orientations ③-⑤ locate in stage II. In addition to the main rotation along radial direction, a noticeable amount of θ and Z-axes lattice rotations have also been observed for these predicted orientations. For example, orientation ⑤, obtained after 33° degrees of HPT deformation, reveals the combination rotations of ~80° along R axis, ~20° along the θ axis and ~20° along the Z axis. In stage III, the lattice rotations around all three axes slow down dramatically to converge and show relatively limited further increase for the left strain range. Orientation ⑥ positions in this stage and ~90° R-axis rotation angles have been found in the pole figure (see Fig. 5.9(g))

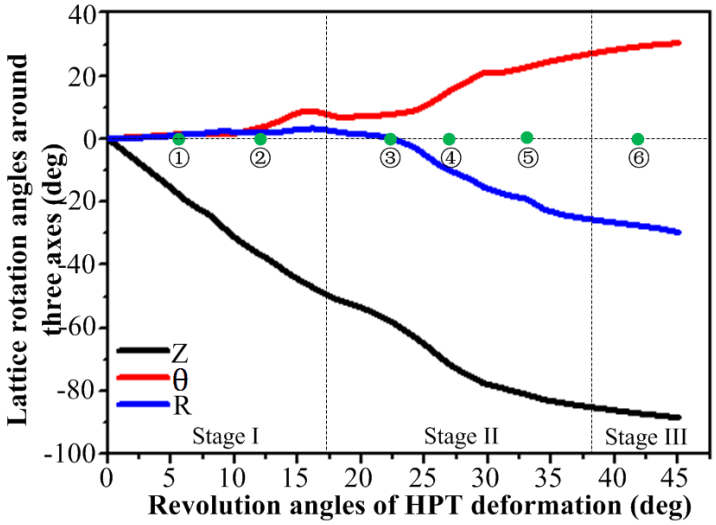

Fig. 5.10 The predicted lattice rotations around R, θ and Z axes for the initial Cube orientation of (001) nickel single crystal as a function of increasing revolution angles HPT deformation.

The evolutions of the six material strain rate (D) components, three material spin (Ω) components, resolved shear strain rate ($\dot{\gamma}^{(\alpha)}$) on twelve slip systems, and the three lattice spin

(Ω^*) components for the initial Cube orientation of (001) nickel single crystal with respect to the increasing HPT deformation were also examined and the results are given in Fig. 5.11. The six predicted orientations described in Figs. 5.9(b)-(g) were labeled out at their corresponding strain levels. Figs. 5.11(a)-(b) show that the components of material strain rate $\mathrm{D}_{\theta\mathrm{Z}}$ and material spin $\Omega_{\theta\mathrm{Z}}$ change with regards to the increasing plastic deformation and their magnitudes are much larger than their counterparts at any rotated position. Meanwhile, at certain strains, there are moderate increases in the components D_{RZ} and Ω_{RZ} whereas the remaining material components remain basically unchanged at relatively small values.

At the beginning of stage I, eight slip systems are simultaneously activated having relatively large resolved shear strain rates, as shown in Fig. 5.11(c). Then the strain rates of four of the all eight slip systems, a1, b2, c1 and d3, increase with the plastic straining while the reminders decrease gradually to zero. As the deformation proceeds, the resolved shear strain rates on a1, b2, c1 and d3 decrease from their peak values progressively to zero, meanwhile, another four differently oriented slip systems, namely a2, b1, c3 and d2, are initially activated to co-operate. In general, the multi-slip of eight slip systems takes place during this stage. Each of the slip systems of interest produces a rotation component, the resultant of which is the overall glide rotation (Ω^{p}) is near-zero because the slip vectors are all differently oriented (see Fig. 5.1(a)). The lattice rotation (Ω_{R}^*) is almost equal to the material rotation (Ω_{R}) during stage I ($\Omega_{\mathrm{R}}^*/\Omega_{\mathrm{R}} \simeq 1$), as shown in Figs. 5.11(b) and (d). Therefore the lattice rotates simply in the direction of the imposed material rotation of the radial direction and the R-axis rotation angles increase approximately linearly. The initial Cube orientation recorded in Fig. 5.9(a) have been found rotating simply along the R axis to occupy the positions of orientations ① and ②, namely rotated cube orientation in Figs. 5.9(b)-(c). This is in good coherence with the results that have been published previously for torsion deformation. Rose and Stüwe [271] published experimental results for initially strongly cube oriented textured tubes in torsion for copper. They have found that the texture was simply rotated with the rigid body rotation. The plastic deformation, however, was not large. Toth and Jonas [272] showed by analytical modeling that in simple shear of cube orientation the plastic spin was zero so that the lattice spin was equal to the rigid body spin for any rotated position of the initially cube oriented crystal, therefore it

rotated in the direction of the imposed rigid body rotation. The same result has been found in the present work, at least up to an imposed rotation angle of the sample by 17° (see Fig. 5.10). At this position, the Cube orientation has rotated by ∼50° around the radial direction.

At the early period of stage II, with the resolved strain rates of slip systems a2, b1, c3, and d2 diminish gradually to zero, another three differently oriented slip systems, namely a3, c2 and d1, are activated and the multiple slip situation maintains. Accordingly, the lattice is further rotated mainly around radial direction at a smaller rate than stage I to compensate for the difference between material rotation (Ω_{R}) and plastic rotation (Ω^{p}). It should be noted that at the end of stage I and the early period of stage II, a moderate increase in Ω_{θ}^{*} could be observed in Fig. 5.11(d). It's reasonable to expect that this is responsible for the slight increase in the θ-axis lattice rotation for orientation ③ which occupied positions deviating from the rotated cube orientation in the pole figure of Fig. 5.9(d). During the middle region of stage II, as shown in Fig. 5.11(c), the slip condition becomes very different. There are four slip systems operating together. Of them, slip systems c1 and d1 share the same [011] crystallographic direction (see Fig. 5.1(a)) and both possess significantly large strain rates. They can produce a large amount of plastic rotation (Ω^{p}); meanwhile, slip systems a3 having significantly large strain rate and c2 with moderately large strain rate, are differently oriented and both form 120° angles with c1 (d1) (see Fig. 5.1(a)), which therefore apply strong disturbance to c1 and d1. Under such circumstances, a large amount of lattice rotation (Ω_{R}^{*}) is needed to satisfy the requirement of material rotation (Ω_{R}), as shown in Fig. 5.11(d), and ∼70° R-axis rotation angles have occurred for orientations ④. At the latter period of stage II, the resolved shear strain rate of slip system a3 decreases gradually while the strain rates of c1 and d1 remain relatively large. The disturbance capacity of a3 grows weaker gradually, leading to an increasing overall plastic rotation (Ω^{p}). The dependence of the material rotation (Ω_{R}) upon the lattice rotation (Ω_{R}^{*}) reduces accordingly. Thus a smaller lattice rotation (Ω_{R}^{*}) is needed to meet the material rotation demand during this period, as shown in Fig. 5.11(d). It's worth noting, during stage II, components Ω_{θ}^{*} and Ω_{Z}^{*} both present a moderate increase to reach a peak value and then decrease gradually in Fig. 5.11(d), which is supposed to contribute to the considerable increase of θ and Z-axes lattice rotations in Fig. 5.10. Thus a noticeable amount of lattice rotations along

θ and Z axes have been observed for orientations ④ and ⑤ in addition to the further R-axis rotations in the pole figures of Figs. 5.9(e)-(f).

In stage III, c1 and d1 become the primary slip systems that dominate the plastic deformation, which produces a sufficiently large plastic rotation (Ω^{p}) to almost fully satisfy the demands of the whole material rotation (Ω_{R}). A near-zero lattice rotation (Ω_{R}^{*}) therefore could be observed in Fig. 5.11(d). Orientation ⑥ locate in this stage, which occupied positions close to the ideal C orientation in the pole figure of Fig. 5.9(g) and illustrated relatively limited further increase in R-axis lattice rotation in Fig. 5.10.

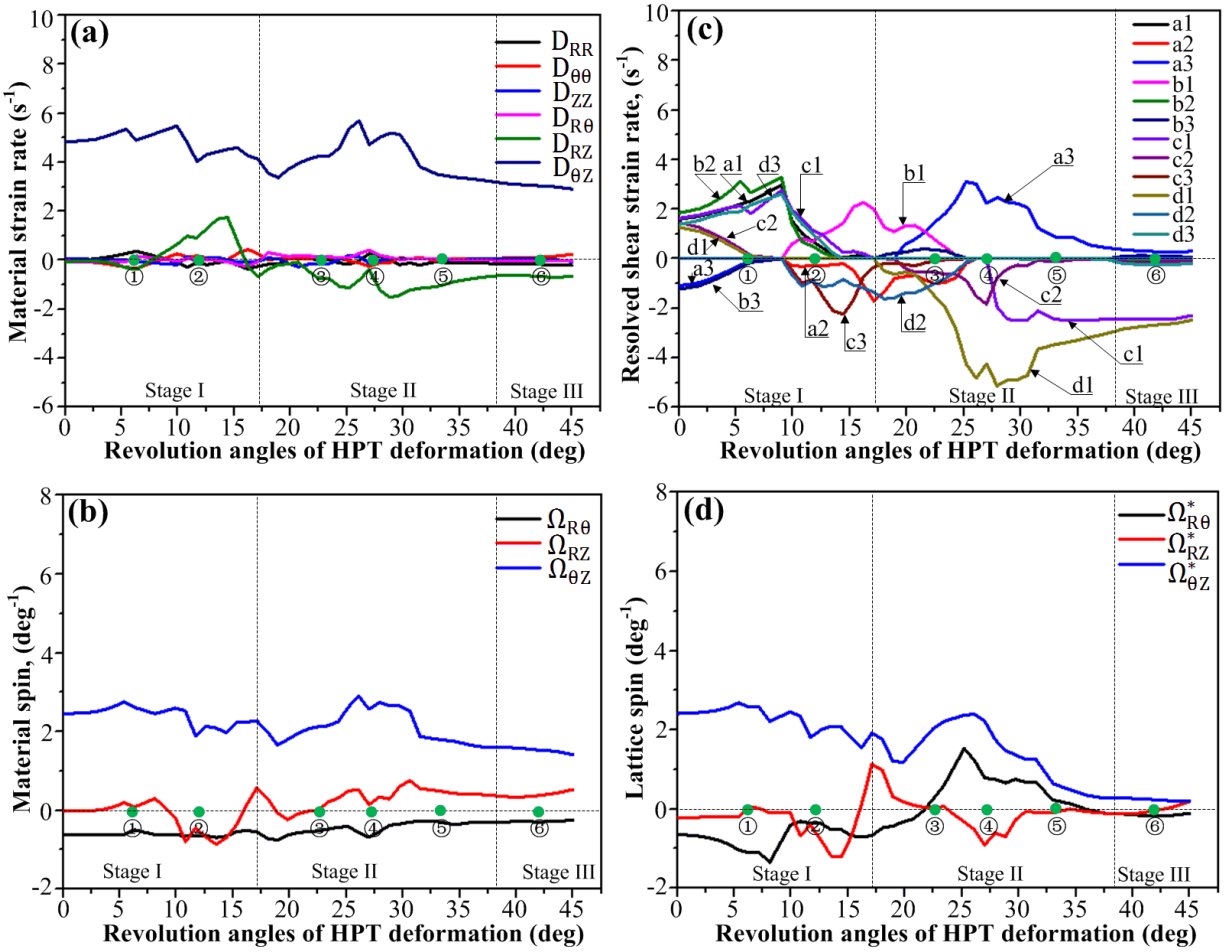

Fig. 5.11 The predicted results for the initial Cube orientation of (001) nickel single crystal as a function of increasing revolution angles HPT deformation (a) Material strain rate, (b) Material spin, (c) Resolved shear strain rate and (d) Lattice spin.

5.4.3 Initial (111) Nickel Single Crystal

To understand the texture development process depicted in Figs. 5.5(a)-(d), the changes of the initial A_2^* crystallographic orientation of the (111) nickel single crystal with increasing sample rotation angles from 0° to 130° were plotted, as shown in Fig. 5.12. The initial A_2^* orientation is marked by black dots in Fig. 5.12(a). The orientation developed after 28° degrees of HPT deformation is shown in Fig. 5.12(b). It is seen that the crystal has rotated significantly away from the initial A_2^* orientation. Fig. 5.12(c) shows the resulting orientation after 60° revolution angles HPT deformation where the predicted poles have already rotated into the first preferred orientation, namely the ideal C component. The crystal is capable of maintaining the C texture component with increasing plastic deformation and is observed to still have this orientation in Fig. 5.12(d) when subjected to 100° angles of sample rotation, indicating that the C orientation is a relatively stable orientation during the HPT process. This simulation result is consistent with the experimental observations and Taylor type modeling conducted by Hafok and Pippan [48] who also reported that the ideal C component could be maintained over a large range of straining in HPT. When further deformed, the rotation of the crystallographic orientation continues. After 120° degrees of deformation, the orientation in Fig. 5.12(e) is seen to occupy positions deviating greatly form the ideal C orientation and tend to rotate towards the next favored orientation. One can see from Fig. 5.12(f) that the second preferred orientation, namely the ideal A_1^* component, has already been approached in the pole figure when the sample undergoes 130° revolution angles of rotation. For convenience, the developed orientations recoded in Figs. 5.12(b)-(f) are indexed by (1)-(5) respectively.

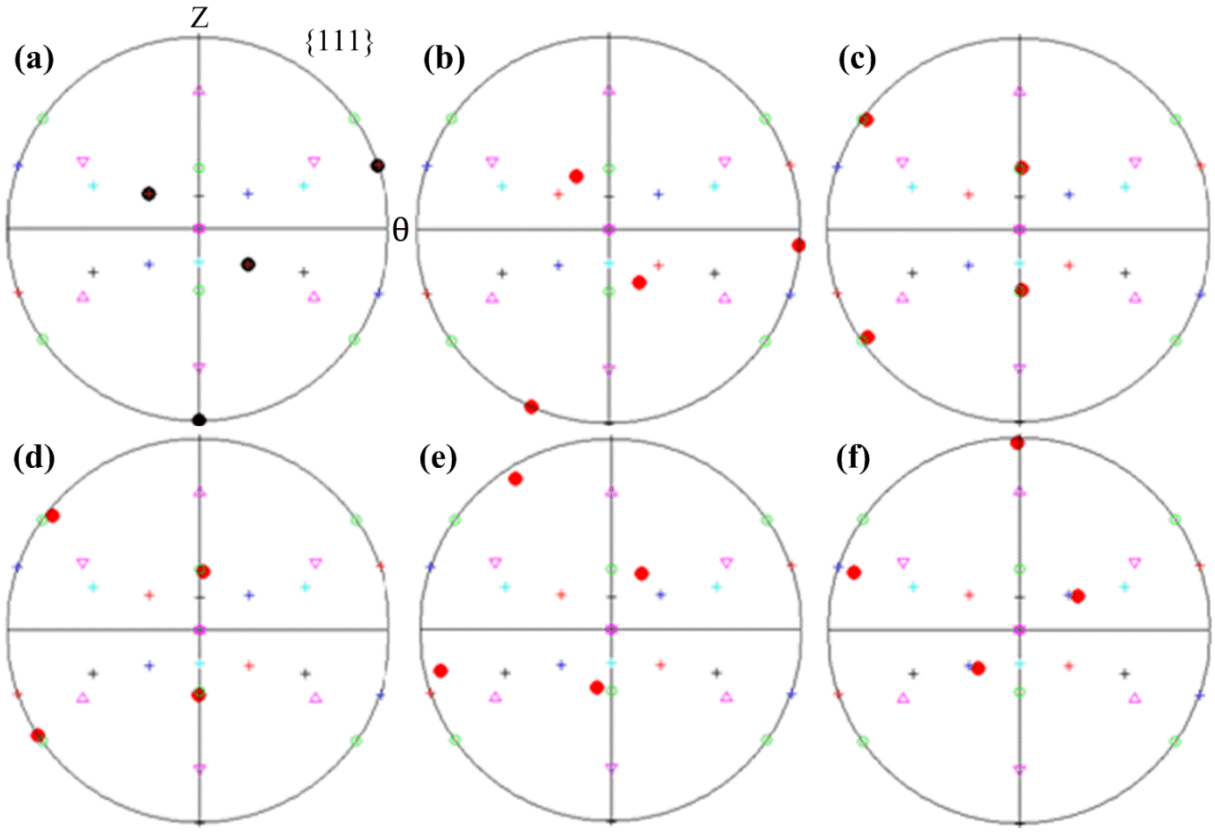

Fig. 5.12 The predicted orientation changes for the initial A_2^* orientation of (111) nickel single crystal as a function of increasing revolution angles HPT deformation of (a) 0°, (b) 28°, (c) 60°, (d) 100°, (e) 120° and (f) 130°. The orientations depicted in Figs. 5.12(b)-(f) are labeled as (1)-(5) respectively in the following context.

Fig. 5.13 illustrates the lattice rotations around R, θ, and Z axes for the initial A_2^* orientation of (111) nickel single crystal as a function of increasing degrees of HPT deformation. It can be seen form Fig. 5.13 that the lattice rotates predominately along the radial direction whereas the θ and Z axes rotation angles are negligibly small, which is similar to that depicted in Fig. 5.7. Moreover, R-axis lattice rotation is characterized by five distinctly different sub-regions including three stable-state / quasi-stable-state regions (region A_2^*, C and A_1^*) with almost absent of lattice rotation and two transient regions between two adjacent stable regions where the R-axis rotation angles increase dramatically, as shown in Fig. 5.13. The A_2^* region ranges from 0°-20° degrees of HPT deformation, the C region ranges from about 50° to 110° and the A_1^* region ranges from around 130° to the remaining strain.

The predicted orientations (1)-(5) recorded in Figs. 5.12(b)-(f) were also marked by green circles at their corresponding strain positions, as shown in Fig. 5.13. Orientation (1) locates in the transient region between the stable regions A_2^* and C, and ~23° R-axis rotation angles could be observed in the pole figure of Fig. 5.12(b). Orientations (2)-(3) position in the stable C region and the R-axis rotation angles are both ~55°, as shown in the corresponding pole figures of Figs. 5.12(c)-(d). Orientation (4) locates in the transient region between the stable regions C and A_1^* and the R-axis rotation angles reach ~75° in the pole figure of Fig. 5.12(e). Orientation (5) positions in the stable region A_1^* where ~110° R-axis rotation angles exist in the pole figure (see Fig. 5.12(f)).

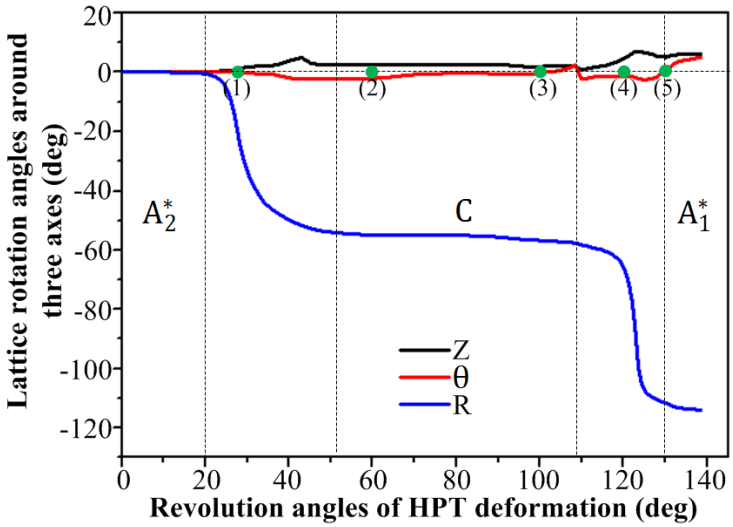

Fig. 5.13 The predicted lattice rotations around R, θ and Z axes for the initial A_2^* orientation of (111) nickel single crystal as a function of increasing revolution angles HPT deformation.

Figs. 5.14(a)-(d) respectively show the evolutions of the six material strain rate (D) components, three material spin (Ω) components, the resolved shear strain rate ($\dot{\gamma}^{(\alpha)}$) on twelve slip systems and the three lattice spin (Ω^*) components for the initial A_2^* orientation of (111) nickel single crystal with respect to the increasing revolution angles HPT deformation. The three stable regions (A_2^*, C and A_1^*) and the resulting orientations (1)-(5) depicted in Figs. 5.12(b)-(f) were also given in Fig. 5.14.

For the three stable regions, the major characteristic in Fig. 5.14(c) is that two slip systems dominate the plastic deformation of these regions, specifically, they are a1 and a2 (on the same (111) crystallographic plane) for A_2^* region, b2 and c2 (share the same [110] crystallgraphic direction) for C region and d1 and d2 (on the same $(11\bar{1})$ crystallographic plane) for A_1^* region. The magnitudes of the resolved shear strain rates of the dominant slip systems are relatively large as all the introduced material strain rates $\mathrm{D}_{\theta Z}$ are concentrated on the primary slip systems. Under these circumstances, the dominant slip systems are capable of generating a sufficiently large overall plastic rotation (Ω^{p}) that could fully satisfy the requirements of material spin (Ω_{R}), so that lattice rotation (Ω_{R}^*) is not needed. Thus lattice rotation (Ω_{R}^*) is basically zero for these three stable regions, as shown in Fig. 5.14(d). The R-axis rotation angles of orientations (2)-(3) in region C and orientation (5) in region A_1^* were observed to be stabilized at $\sim 55°$ and $\sim 110°$ respectively in Fig. 5.13.

For the two transient regions, the slip condition in Fig. 5.14(c) becomes complicated and is featured by multiple slips. Close inspections reveal that slip systems a1, a2, d1 and d2 and slip systems d1, d2 and b2 (c2) are successively functioned in the transient region between the stable regions A_2^* and C; while for the transient region between the stable regions C and A_1^*, slip systems b2 (c2), a1 and a2 and slip systems a1, a2, d1 and d2 are successively co-operate. The functioned slip systems possess almost the similar amount of resolved shear strain rates but the slip vectors are seen to be all different oriented in Fig. 5.1(a). Under these conditions, they provide opposing contributions to the overall plastic rotation (Ω^{p}) and result in a relatively small Ω^{p}, so that the lattice has to rotate to compensate for the difference between material rotation (Ω_{R}) and plastic rotation (Ω^{p}). Thus one can see clearly from Fig. 5.14(d) that the lattice rotations (Ω_{R}^*) are significantly large for these two transient regions. Orientations (1) and (4) locate in these two transient regions and are observed to have already rotated significantly away from the ideal A_2^* and C texture components respectively along the radial direction in the pole figures of Figs. 5.12(c) and (e).

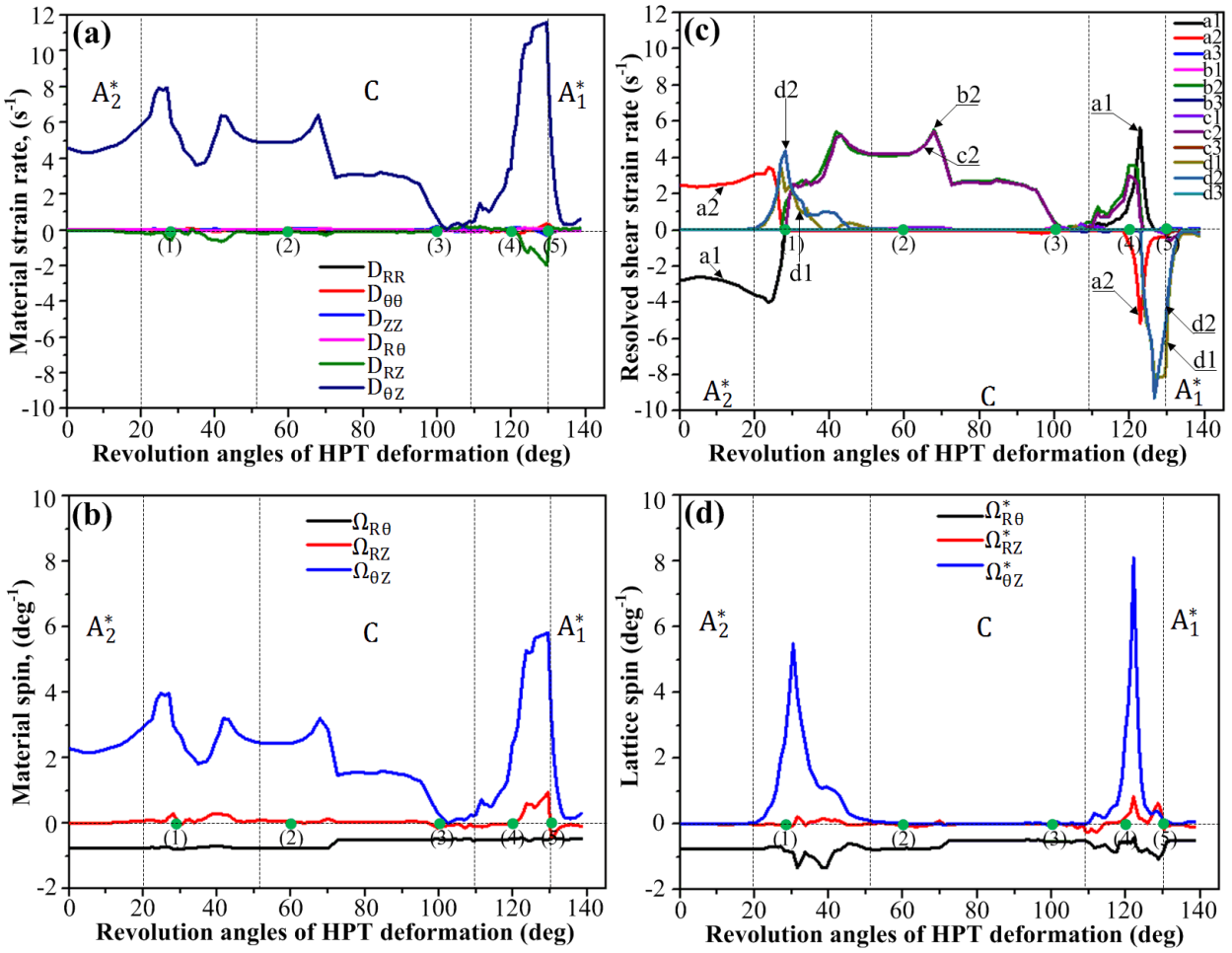

Fig. 5.14 The predicted results for the initial A_2^* orientation of (111) nickel single crystal as a function of increasing revolution angles HPT deformation (a) Material strain rate, (b) Material spin, (c) Resolved shear strain rate and (d) Lattice spin.

5.5 Summary

1. For the first time, a CPFEM model integrated with Bassani & Wu hardening modulus, has been established to investigate the texture evolution of (001) and (111) nickel single crystals during the HPT process. The texture results predicted by the developed CPFEM model were in good coherence with the previously published experimental measurements.

2. The simulation results showed that different crystallographic orientations rotated towards different ideal shear texture components with respect to the torsion deformation in HPT.

During this process, lattice rotated predominately along the radial direction. While for initial Cube orientation of (001) nickel single crystal, a noticeable amount of θ and Z-axes rotation angles could also be observed in this study. Moreover, lattice did not rotate uniformly during the HPT process, the rotation rate converged when approaching the main components of the ideal shear texture but it diverged between the ideal shear orientations.

3. The evolution of the initial C and Cube orientation of the (001) nickel single crystal and initial A_2^* orientation of the (111) nickel single crystal were analysed in detail to explore the underlying mechanism for texture evolution during the HPT process. For HPT deformation, material spin was usually larger than other deformation techniques due to severe shear deformation. The material spin requirement could be met by either plastic rotation rate or lattice spin. The lattice spin, which is the difference between material spin and the plastic rotation rate, was controlled by the plastic rotation rate. Under dominant-slip condition, material spin could be mainly or even fully satisfied by plastic rotation rate and thus the lattice spin was very small or even dropped to zero, which led to relatively limited orientation change or even stable orientation with increasing HPT deformation; while for multi-slip condition, each of the slip systems of interest produced a rotation component, the resultant of which was the overall glide rotation rate was small, the lattice must rotate to generate large lattice spin to satisfy the material spin requirement, which led to significant orientation changes. When the resulting overall glide rotation rate was zero, the lattice spin was equal to the material spin so that the lattice rotated simply in the direction of the imposed rigid body rotation. Dominant slip and multiple slip competed against each other to minimize the total energy consumed in the system, which is assumed to be responsible for texture evolution of nickel single crystal during the HPT process.

Chapter 6 Investigation of Grain Refinement of Nickel Single Crystal during HPT by CPFEM Simulation

In this chapter, the developed CPFEM model is extended to simulate the grain refinement process of nickel single crystals during the HPT process. The grain fragmentation process of nickel single crystals in HPT and the underlying mechanism will be discussed in detail.

6.1 Introduction

Conventional heavy deformation processes, such as rolling, drawing and extrusion, can result in significant grain refinement, but the structures formed usually have low angle grain boundaries [11]. However, UFG materials processed by the SPD processes, especially HPT, are characterised by smaller grains that are mainly surrounded by high angle grain boundaries. It has been well known that most excellent properties of UFG materials are relevant to the substantially small grains and high angle grain boundaries. Therefore, a comprehensive understanding of the grain refinement mechanism and formation of high angle grain boundaries will facilitate development of a new generation of UFG materials.

The existing grain refinement theories are generally obtained based on experimental investigations of the evolution of microstructure in the HPT-deformed materials [38,53,139,140,273,274]. The most commonly accepted type of grain refinement mechanism due to large strain induced by HPT are based on the notion that a dislocation cell structure, which forms already in the early stages of plastic deformation, gradually transforms to the final fine grain structure [4]. This is believed to occur through continual decrease in the average grain size accompanied by accumulation of misorientation between neighbouring dislocation cells. Recently, the two-dislocation density model, based on the above grain refinement theory,

has been employed to simulate the HPT process [69,72,73]. In this model, the constitutive formulation was based on a phase mixture model where the dislocation cell walls and the cell interiors were considered as separate 'phases' [4]. Estrin et al. [69] applied this model to resolve the controversial issue of the occurrence of a uniform microstructure as a result of an inherently non-uniform deformation during the HPT process. Lee et al. [72,73] used this model to investigate the cell/grain size evolution with the accumulation of dislocation density. Both simulations have proved that the two-dislocation density model was a good tool for describing and predicting the evolution of microstructure during the HPT process.

An alternative explanation would be the source–sink mechanism for dislocations [148,149,275,276]. During deformation the dislocations glide through the grain and contribute to local deformation. When the dislocation reaches the boundary region it can be trapped or annihilated by other dislocations, producing misorientation between the adjacent grain fragments. Horita and his co-workers investigated the microstructural evolution of high purity Al [132] and Cu [87] processed by HPT and proposed that the grain refining mechanism in HPT follows the microstructural evolution as dislocation accumulation, formation of subgrain boundaries, enhancement of misorientation angle, absorption of dislocations at high angle boundaries and establishment of a steady state due to a balance between dislocation generations by HPT and dislocation absorption at high angle boundaries.

On the other hand, the experimental observations of Pippan [85,151,152] and others [153,157,159,161] favored the intergranular gliding of dislocations and the crystal lattice rotation model in HPT. In order to maintain compatibility during HPT deformation, different sets of slip systems would be activated in different regions of a grain and thus leading to strong heterogeneities in the local lattice rotation within the single grain. Different regions of a grain under deformation rotate towards a number of distinctly different orientations. The formation of boundaries is accompanied by the rotation of individual structural elements, which promotes fragmentation of the microstructure in the HPT process [277,278]. Crystal plasticity modelling, based on the assumption that crystalline material under load undergoes a crystallographic slip due to dislocation motion on the active slip systems and elastic deformation including

stretching and rotating of the crystal lattice, has been used extensively to describe the grain refinement of SPD processes, such as ECAP [210,279–281]. However, for the HPT process, quite few studies have been reported in the literature. Hafok and Pippan [48] applied a full constrained Taylor model to predict the development of crystallographic orientation of nickel single crystal during the HPT process. Owning to well-known shortcomings of the Taylor model, it gave only reasonable predictions of the texture evolution and did not study the grain refinement. Accepting that HPT shearing is achieved by intergranular glide [85,151,152], Kratochvíl and his co-authors [70,71,180,181] attempted to interpret the fragmentation process within the framework of crystal plasticity. They found that the basic feature of substructure formation was the effective rotation of the double slip and the local variations in the crystal lattice orientation were mainly responsible for the microstructure fragmentation. They interpreted the size of the subgrains as the result of a competition between the internal and dissipative energy which tended to decrease the refined structural size and the interface energy of the cell boundaries opposed this tendency. Despite that the proposed model revealed the initiation of the fragmentation and the trends of its evolution, due to these simpifications (The evolution of the HPT microstructure was simulated by considering a rectangular volume element volume which was subjected to the spatially homogenous plane-strain, rigid-plastic deformation carried by double slip. The rate-independent material response was considered), the model provided only limited valuable information on the grain refinement mechanism during the HPT process.

Since severe plastic deformation has occurred in HPT, and it will definitely lead to the fragmentation process of HPT deformed materials. In this study, a 3D crystal plasticity finite element model which assumes that slip is the plastic deformation mechanism was developed to simulate the grain fragmentation of (001) nickel single crystal during the HPT process. Grain maps detected at different stage of HPT deformation are presented. The main purpose of this work is to study how an original single crystal fragments into many different oriented grains after HPT deformation and to explore the underlying mechanism.

6.2 Simulation Procedure

The CPFEM model of the HPT process adopted for texture study in Chapter 5 was further used to investigate the grain refinement behavior. In this study the initially (001) oriented nickel single crystal was selected for the grain refinement simulation. At each level of strain, the grain detection method followed that proposed by Bachmann et al. [282], we recall the principle procedures of this method first as follows:

(1) The resulting data including the measurement locations and orientations of the interested domain obtained from the experimental measurements are imported for preparation, as shown in Fig. 6.1(a). A two dimensional region was considered, where the measurement locations are marked by black dots and their corresponding orientations are displayed as directions for simplicity.

(2) Voronoi decompositions of the measurement locations in the selected domain are conducted. This results in a series of Voronoi cells, as shown in Fig. 6.1(b). Each Voronoi cell carries its own orientation information and the information about the vertices and edges of the cells are stored in the corresponding incidence matrices.

(3) These incidence matrices are used to find all the adjacency pairs. Each pair has two Voronoi cells which share a common edge. The adjacency pairs record which of the measurement locations are adjacent, i.e., the position of potential grain boundaries. These neighborhood relationships are illustrated in Fig. 6.1(c) where the neighbouring Voronoi cells are linked by hatched red lines.

(4) The common edge between two adjacent Voronoi cells is checked to see whether it is an actual grain boundary. In their study, the term misorientation refers to the minimum angle θ_{min} among all the crystallographically equivalent rotations that bring the lattices of adjacent grains into coincidence. The common edge is defined as a grain boundary if the corresponding misorientation angle exceeds a given threshold angle θ_c. More specifically, if the misorientation $\theta_{\min}$ between orientations in measurement locations A and B is smaller than θ_c, A and B are identified as being within the same grain, their common edge is not a grain boundary. The adjacent measurements that are not separated by a grain boundary are then linked together by bold red lines, as shown in Fig. 6.1(d). Otherwise, if $\theta_{\min} \geq \theta_c$, they consider A and B two

different grains and the common edge between them as a grain boundary. The grain boundaries between two neighbouring Voronoi cells are denoted by bold black lines, as shown in Fig. 6.1(e).

(5) A grain is defined as a region in which the misorientation of at least one neighbouring measurement location is smaller than the threshold angle θ_c. By following this grain characterization rule, all the developed grains could be detected, as shown in Fig. 6.1(f).

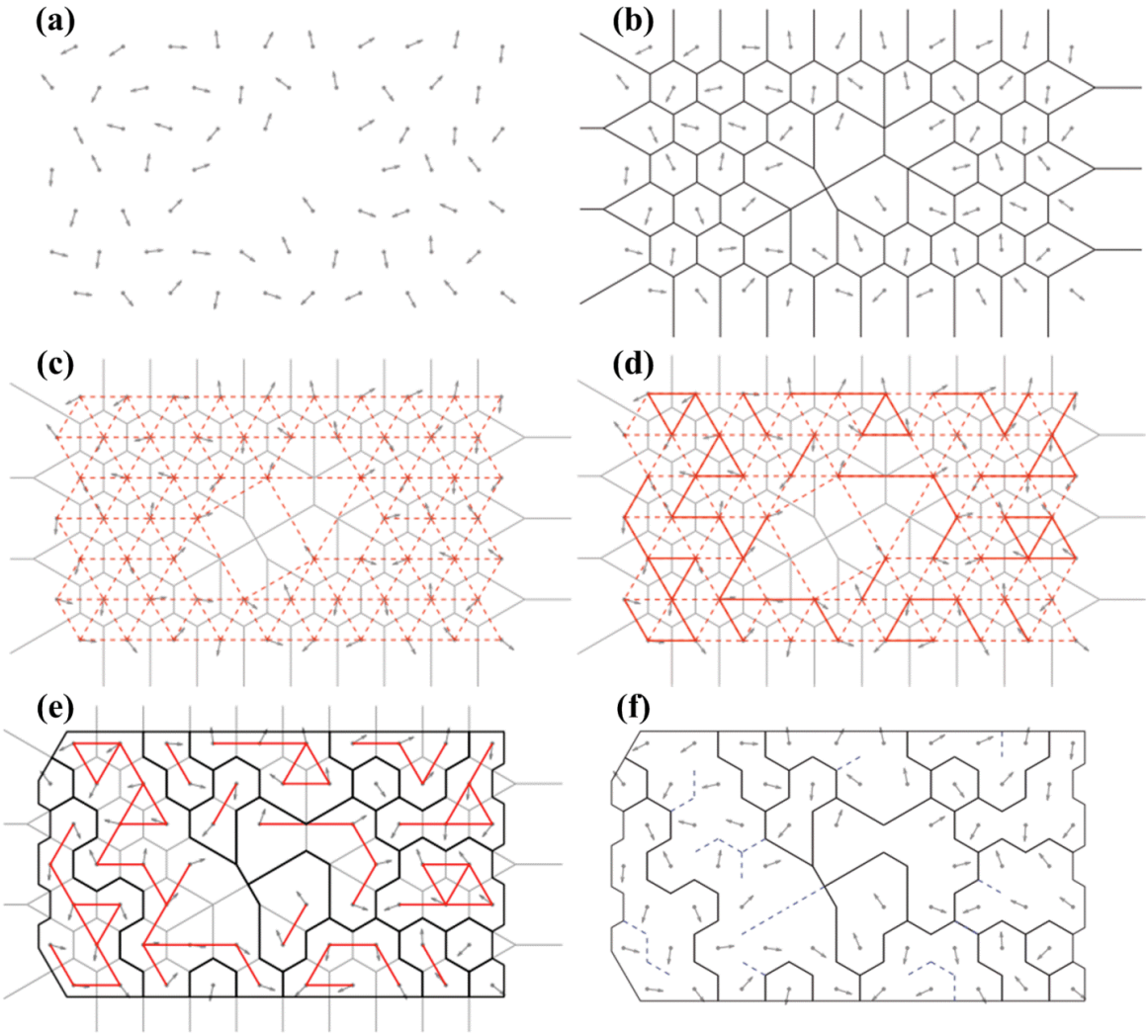

Fig. 6.1 A schematic diagram of grain detection from EBSD data [282]. (a) Location and orientation data of a rectangular domain. (b) The Voronoi decomposition of the measurement locations. (c) The neighborhood relationships of the Voronoi cells (d) Adjacent measurements that are not separated by a grain boundary are linked by bold red lines. (e) Adjacent measurements that are separated by a grain boundary. The grain boundaries are represented by bold black lines. (f) Resulting partition displaying the detected grains.

At each stage of HPT deformation, the EBSD data including locations of integration points and the corresponding orientations obtained from the CPFEM simulations was imported to reconstruct the grain map. All the predicted grain maps were recorded at rectangular regions in the same tangential direction of $\varphi = 75°$. The shear direction is approximately the same within the selected region and it is convenient for the obtained results to be expressed in the polar coordinate systems. For each selected region, the horizontal direction is the radial direction (RD) while the vertical direction refers to the axial direction (AD), as shown in Fig.6.2. The length of the rectangular region spreads from 4-5mm from the center of the sample and the width covers the whole thickness of the sample. Overall 23660 elements were generated for the disk-shaped sample. In the selected region, there were RD=6 and AD=10 elements in the radial and axial direction, respectively (see Fig. 6.2). Potentially, this mesh permits fragmentation into a maximum of RD X AD grains in the selected cross-section. The meshes used here are expected to be too coarse to represent the grain-scale deformation. However, we do expect the meshes to be able to capture the prominent features associated with grain fragmentation during the HPT process.

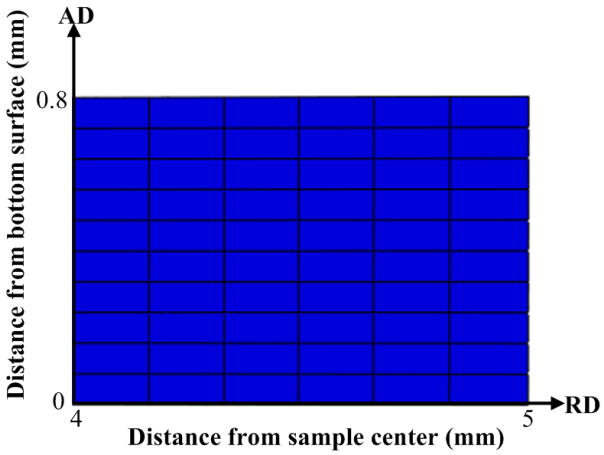

Fig. 6.2 Schematic description of the region selected for grain detection.

6.3 Detection and Description of Grain Refinement

In this study the evolution of grain subdivision and the corresponding crystallographic texture of (001) nickel single crystal with increasing strain levels of HPT deformation of N=1/8 turn, 1/4

turn, 3/8 turn and 1/2 turn were predicted by the developed CPFEM model. The results are shown in Fig. 6.3. In all the resulting grain maps, the colors of each grain were determined by their mean orientation, as illustrated in the unit triangle. High angle grain boundaries (HAGB) surrounding the developed grains with misorientation larger than 13° were depicted by black lines. The corresponding textures were presented in terms of {111} pole figures which were recorded on $\theta - Z$ planes. In all the pole figures, the resulting orientations obtained at different levels of strain were marked by black dots and the positions of main components of ideal torsion texture were also visualized using different symbols. The starting material was nickel single crystal which was oriented with the (001) crystallographic plane lying parallel to the Z axis. Therefore, only one grain, colored dark red, could be observed in Fig. 6.3(a).

The effect of increasing plastic strain on the grain fragmentation is initially illustrated in Fig. 6.3(b), referring to N=1/8 turn deformation. Fig. 6.3(b) shows that grain refinement has already taken place in the original single crystal. On the left side of the map, which is away from the edge of the sample, three lamellar substructures are developed which are delineated by HAGBs located close to the top surface and at one third of the sample thickness, respectively. The major axes of the substructures are almost parallel to the radial direction. The interior of the substructures are clear without the alternation of local domain orientations because only the mean orientation of each grain was computed. Meanwhile, a few differently oriented grains appear at the area close the edge of the sample ranging from 4.7mm∼5mm in sample radius. The morphology and size of these grains differ significantly, some grains retain a lamellar structure, while some substructures are further deformed to smaller sizes, especially close to the sample surface. The poles in the pole figure mainly concentrate around two orientations but spread slightly around the rotated position, which corresponds to the two large grains on the left side of the grain map in Fig. 6.3(b). Meanwhile, a minor presence of the isolated poles due to grain subdivision could also be observed.

After further deformation to N=1/4 turn, at the left side of the selected R-Z plane, more grains with typical lamellar shapes surrounded by HAGBs could be observed in Fig. 6.3(c). The major axes of these grains are aligned in the radial direction while the sizes decrease compared to

that in Fig. 6.3(b). The same tendency of an increasing number of grains while approaching the sample periphery is also seen. Smaller grains are visible near the edge of the sample and their appearances are similar to that formed after N=1/8 turn deformation. The developed orientations becomes more complex in the pole figure of Fig. 6.3(c) with ever increasing isolated poles could be cleared observed. Moreover, further torsion straining contributes to the formation of a combination of A_1^* and A_2^* components of the ideal torsion texture which align the {111} crystallographic planes with the axial direction.

As HPT deformation proceeds, the process of grain subdivision continues. After N=3/8 turn torsion deformation, Fig. 6.3(d) shows that the grain refinement evolves gradually from the edge of the sample to the center. Many fairly small grains with various orientations surrounded by HAGBs are developed. Close examinations reveal that about eight grains has already formed in the axial direction, which is close to the number of mesh layers through the whole thickness. Meanwhile, lamellar substructures could be still observed, especially in the middle of the cross-plane. The corresponding crystallographic orientation distribution in the pole figure of Fig. 6.3(d) reveals that the ideal C component dominates the developed texture at this particular level of strain.

As the accumulative straining reaching a relatively high level of N=1/2 turn, as shown in Fig. 6.3(e), the selected region is characterized by polycrystals with an array of much finer substructures bounded by HAGBs. The variations in grain size decrease significantly and deformation-induced grains tend to be more homogenously distributed in the selected R-Z plane. The resulting orientations in the pole figure of Fig. 6.3(e) represent a strong ideal torsion texture revealed for the case of shear deformation in FCC metals.

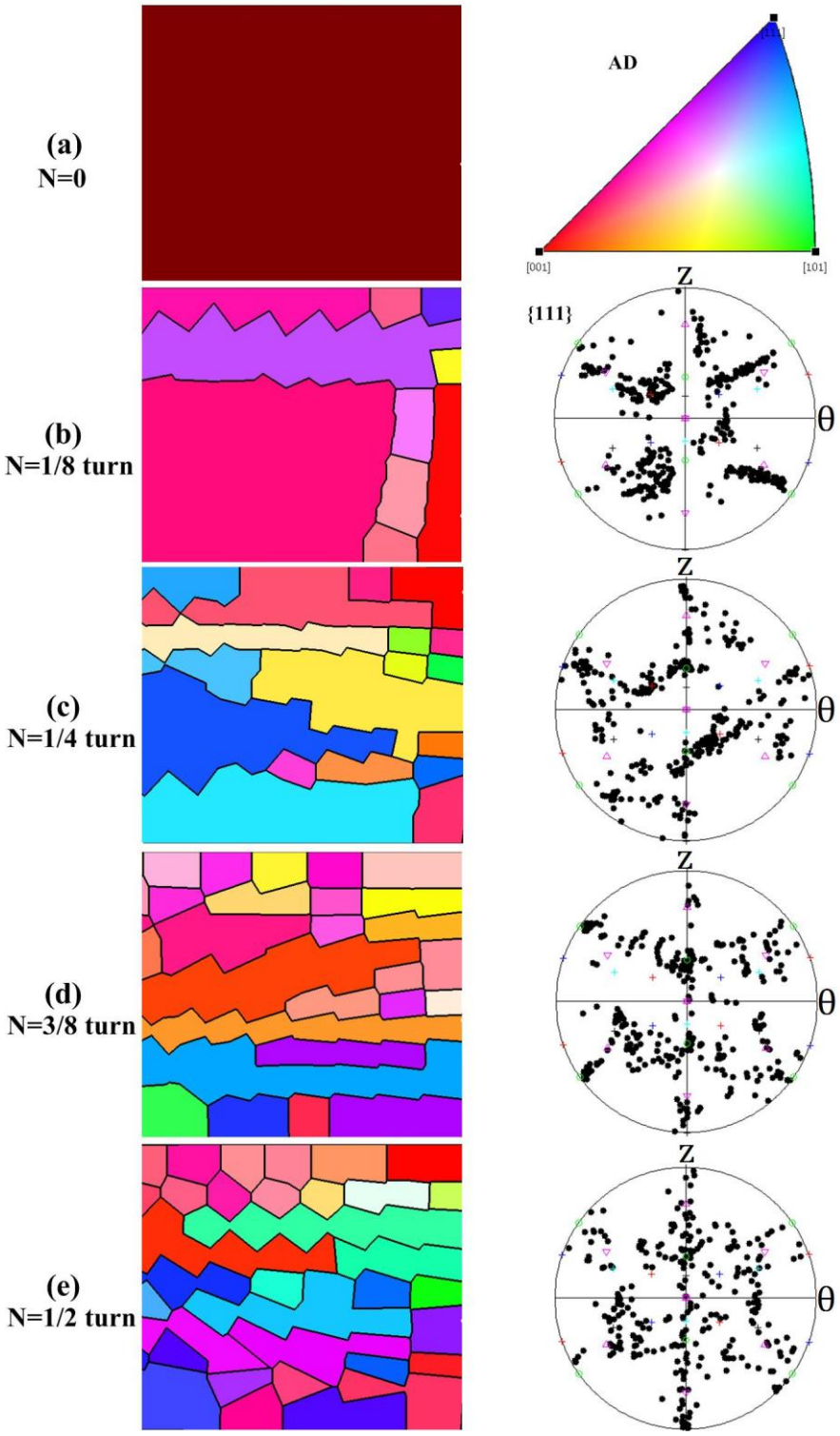

Fig. 6.3 The detected grain maps and the corresponding crystallographic texture of (001) nickel single crystal after subjected to (a) N=0, (b) N=1/8 turn, (c) 1/4 turn, (d) 3/8 turn and (e) 1/2 turn HPT deformation.

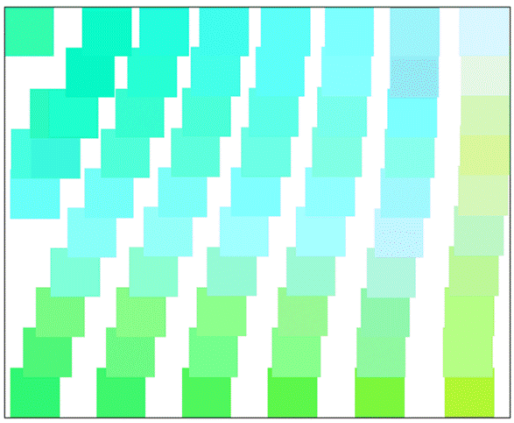

Fig. 6.4 The orientation map recorded on the R-Z plane after 1/16 turn HPT deformation.

The simulation results in the present work obtained by the developed CPFEM model are capable of predicting the prominent characteristics associated with grain refinement during the HPT process. Pippan et al. [152] experimentally examined the orientation map of a copper single crystal after initially deformed by HPT to an equivalent strain of about 0.7. They found there were continuous changes in the color, i.e., the continuous changes in the crystal orientation from top to bottom surface. Such a continuous change in the grain color could also be predicted by the developed CPFEM model, as shown in Fig. 6.4 (N=1/16 turn), in which this change in crystal orientation along the axial direction is clearly visible while the HAGB is not formed. Moreover, for larger strains, our simulation results in Figs. 6.3(b)-(e) showed that the lamellar shaped substructures could be observed with the major axes lying approximately along the radial direction. This is consistent with the experimental observations made by Orlov et al. [140]. They analyzed the experimental observations together with many other reports and then constructed a geometrical analogy model to illustrate the microstructure morphology changes with respect to the observational directions. While on the R-Z plane, they found that the deformation induced grain were lamellar and clearly elongated along the radial direction. Furthermore, Figs.6.3 showed the evolution of the grain refinement process with increasing HPT deformation was quite obvious. The grain refinement process initialized at the periphery of the sample and then evolved inwards towards the center of the sample. There was a tendency for the fraction of substructures surround HAGBs to increase while the grain size decreased

with increasing plastic deformation. The original single crystal has fragmented into many fine volumes of widely different orientations in the cross section investigated.

It should be noted that in our simulation, due to limitations in the number of meshes, only a few grains formed in deformation which were considered for any discussion of texture. In Fig. 6.3, the A_1^* and A_2^* components emerged after N=1/4 turn deformation, the C component dominated the texture developed after N=3/8 deformation and finally a typically ideal torsion texture formed after N=1/2 turn deformation. The simulation results of the evolution of local texture in the present work are in good coherence with the results published previously for HPT/torsion deformation. In 1985, Jonas et al. [283] investigated the texture development during torsion testing and found that in the FCC case the A-fibre texture set predominated at small strains, the C component replaced it at intermediate strains, and the A-fibre was reintroduced at large strains. Orlov, et al. [49] and Langdon et al. [53] used the EBSD technique to investigate the crystallographic texture formation process in pure aluminum and nickel subjected to HPT deformation. Similar to our simulation results, they reported that during HPT deformation, the developed texture varied in a symmetrical manner with increasing strain: for lower strain, the texture was dominated by the orientation mainly belong to A-fibre; with the increasing strain, the A-fibre decreased and the C-fibre became dominately stronger; further increasing the strain, the texture indicated a strong ideal torsion texture. At small strains, the initial grain refinement has just occurred, according to [53,283], the Taylor strain compatibility should be strict and the formation of a combination of the A_1^*/A_2^* texture in Fig. 6.3(c) was expected; for larger strains, the C shear texture in Fig. 6.3(d) usually formed under a relaxed strain compatibility and was generally associated with the formation of elongated grain structures [49,53,54,283]; for even higher strains, the predicted ideal torsion texture in Fig. 6.3(e) agreed well with many other experimental observations of single crystal and polycrystalline materials deformed by HPT [43,44,47,48,52,54]

6.4 Mechanism of Grain Refinement

In order to explore the underlying mechanisms of grain refinement during the HPT process, especially how one single crystal fragments into many different oriented portions in the beginning, the predicted grain map after N=1/8 turn deformation in Fig.6.3(b) and the corresponding crystallgraphic orientations were re-examined and analyzed in detail. For convenience, the detected grains were indexed from 1 to 10 respectively, as shown in Fig. 6.5. To help interpreting the grain refinement process, the orientation of individually predicted grain was plotted in terms of (111) pole figure recorded on the θ-Z plane, as shown in Figs. 6.6(a)-(j) respectively. In each pole figure, the predicted orientations of the meshes inside each grain were denoted by black dots and the corresponding initial orientations were marked by red asterisks. All the developed orientations will be discussed in detail in the following context. The investigations of grain refinement mechanism were carried out along two directions: one is the radial direction and the other one is the axial direction.

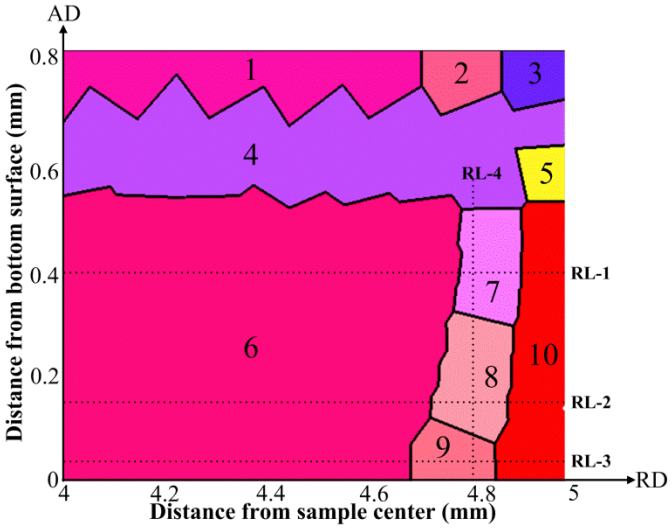

Fig. 6.5 The predicted grain map after N=1/8 turn HPT deformation. The detected grains are indexed from 1 to 10 respectively.

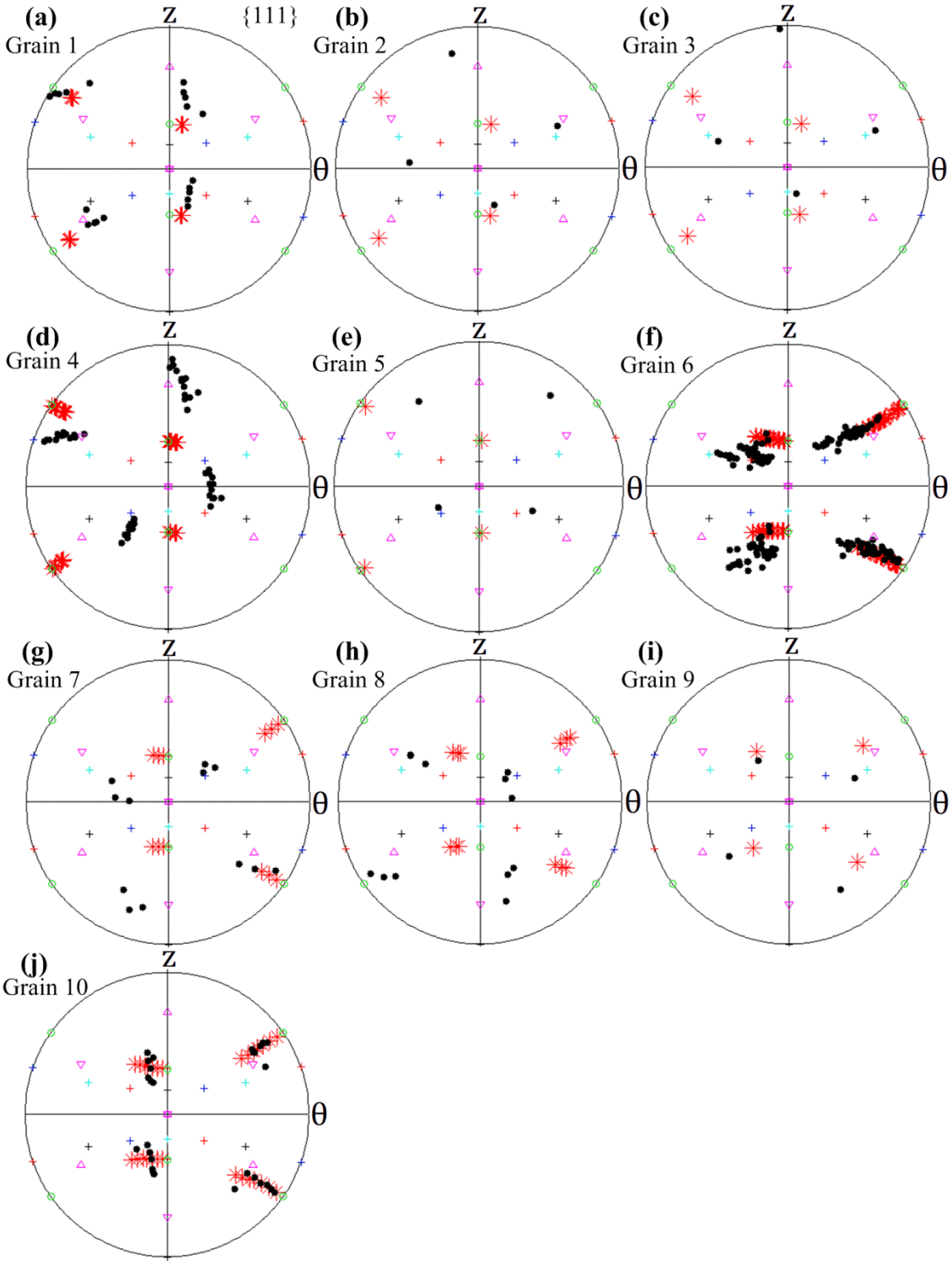

Fig. 6.6 The predicted {111} pole figures of the various detected grains recorded in **Fig. 6.5**.

6.4.1 Grain Refinement along the Radial Direction

The grain refinement process along the radial direction was examined first. The neighbouring grains along the radial direction with decreasing distance from the top surface in Fig. 6.5, specifically, Grains 1, 2 and 3, Grains 4 and 5, Grains 7 and 10, Grains 8 and 10, Grains 9 and 10, were comparatively analyzed in terms of {111} pole figures and lattice rotation angles, as shown in Fig.6.7 and 6.8 respectively. It should be noted that there were more than one mesh inside some of the detected grains. In this study, for each grain, only one mesh which was just adjacent to the HAGB sounded the detected grain was selected for analysis. The resulting {111} pole figures in Fig.6.7 were all recorded on θ-Z planes. The initial orientations were marked by red asterisks. The developed orientations of the detected grains after 45° sample rotation deformation were denoted by thick dots of different colors and the grain ID for each color was also given in Fig.6.7. In each pole figure, one can see from Fig.6.7 that the grains selected for analysis has almost the same initial orientation. The lattice rotation angles of detected grains relative to the initial orientations were calculated and partitioned into three components which represent the rotation angles around the R, θ and Z axis, respectively. The R, θ and Z axes lattice rotation angles were plotted as a function of increasing HPT deformation to 45° revolution angles (N=1/8 turn), as shown in Fig. 6.8.

Figs. 6.7(a) and 6.8(a) show the grain refinement process close to the sample top surface. The initial orientation of this region approaches to the C component of the ideal torsion texture. Originating from this orientation, one can see from Fig. 6.8(a) that all the lattices rotate predominately along the radial axis to accommodate the increasing plastic deformation. Grain refinement does not take place until $\sim$40° revolution angles HPT deformation. After 45° deformation, the lattice rotation angles along the R axis exhibit obvious divergences due to the strain gradient existing along the radial direction, leading to the formation of these grains, namely, Grains 1, 2 and 3, in Fig. 6.7(a). Seeing from Fig. 6.7(a), Grain 3 has the orientation close to the ideal $\overline{\mathrm{A}}$ component which aligns the $(\overline{1}\overline{1}1)$ crystallographic plane with the shear plane. Therefore Grain 3 was colored in blue in the predicted grain map of Fig. 6.5. While the orientations of Grains 1 and 2, developed at less strained positions, are proceeding towards the

same preferred orientation of $\overline{\mathrm{A}}$ at distinctly varying degrees. All the lattices in this region rotate towards the same preferred orientation, therefore, the misorientation angles between Grains 1, 2 and 3 are not too large.

The region located ~0.2mm from the top surface was examined in the same way. The initial orientation changes to occupy the positions of the ideal C component. The lattice rotation results recorded in Fig. 6.8(b) indicate a steady period with no lattice rotation at the early stage of HPT deformation, followed by significant increases along the radial direction. Grain subdivision occurs after ~25° HPT deformation, since when the less strained lattice tends to once more stop rotating to stabilize at the next favored orientation, whereas the more strained lattice continues to rotate at a fast rate. Close examinations reveal there are $\sim 40°$ variations in the R-axis lattice rotation after 45° HPT deformation which are responsible for the development of Grains 4 and 5 in this region. The orientation of Grain 4 that developed at less strained position is identified to being close to the A_1^* ($\{11\overline{1}\}[2\overline{1}1]$) component in Fig. 6.7(b), and was colored in light blue in Fig. 6.5. The orientation of Grain 5 that developed at more strained position occupies positions greatly away from the A_1^* in the pole figure. The misorientation between the developed Grain 4 and 5 is reasonably large.

The development processes of Grains 1, 2 and 3 as well as Grains 4 and 5 indicate that the main reason of grain subdivision lies in the R-axis lattice rotation, the divergence in rotation rate along radial direction contributes to the formation of these grains. The reason for the occurrence of divergence in R-axis rotation rate is that the lattice does not rotate uniformly with respect to the shear deformation in HPT, as described in Chapter 5.

As the distance from the top surface increase, the initial orientations of the regions along the radial direction gradually rotate away from the ideal C components, as shown in Figs. 6.7 (c)-(e). Regardless of the variations in the initial orientation, the R-axis lattice rotations shown in Figs. 6.8 (c)-(e) illustrate a similar tendency of approximately linear increase with increasing plastic deformation, meanwhile, there is basically no divergence between adjacent positions. It is reasonable to expect from the aforementioned analysis that no grain refinement should occur in these regions further away from the top surface. However, after 45° HPT deformation, it is

surprising to observe that at each region the resulting crystallographic orientations of the adjacent two positions occupy obviously different locations in the corresponding pole figures shown in Figs. 6.7(c)-(e). Further examinations of the lattice rotations in Figs. 6.8 (c)-(e) reveal that, accompanying with the predominant R-axis lattice rotations, a noticeable amount of lattice rotation angles along the θ axis also occurs. Specifically, after 45° HPT deformation, the amount of accumulative θ-axis rotation angles are ∼-5° of Grain 7 and ∼-45° of Grain 10 (see Fig. 6.8(c)), ∼25° of Grain 8 and ∼-50° of Grain 10 (see Fig. 6.8(d)) as well as ∼-10° of Grain 9 and ∼-45° of Grain 10 (see Fig. 6.8(e)). Therefore, at these regions further away from the top surface, although the single sense R-axis lattice rotations still dominate the plastic deformation behavior of the HPT process, however, it has almost no influence on determining the grain subdivision. Instead, it is the θ-axis lattice rotation that plays a key role in the grain refinement process. When comparing the detected grains developed at various regions, the misorientation angles between Grains 9 and 10 are moderately large because of the same sense and small variations in θ-axis lattice rotations, followed by Grains 7 and 10 as the θ-axis divergence grows larger and the very large misorientation angles are developed between Grains 8 and 10 which occurs by large amount of rotations but opposite sense about θ-axis.

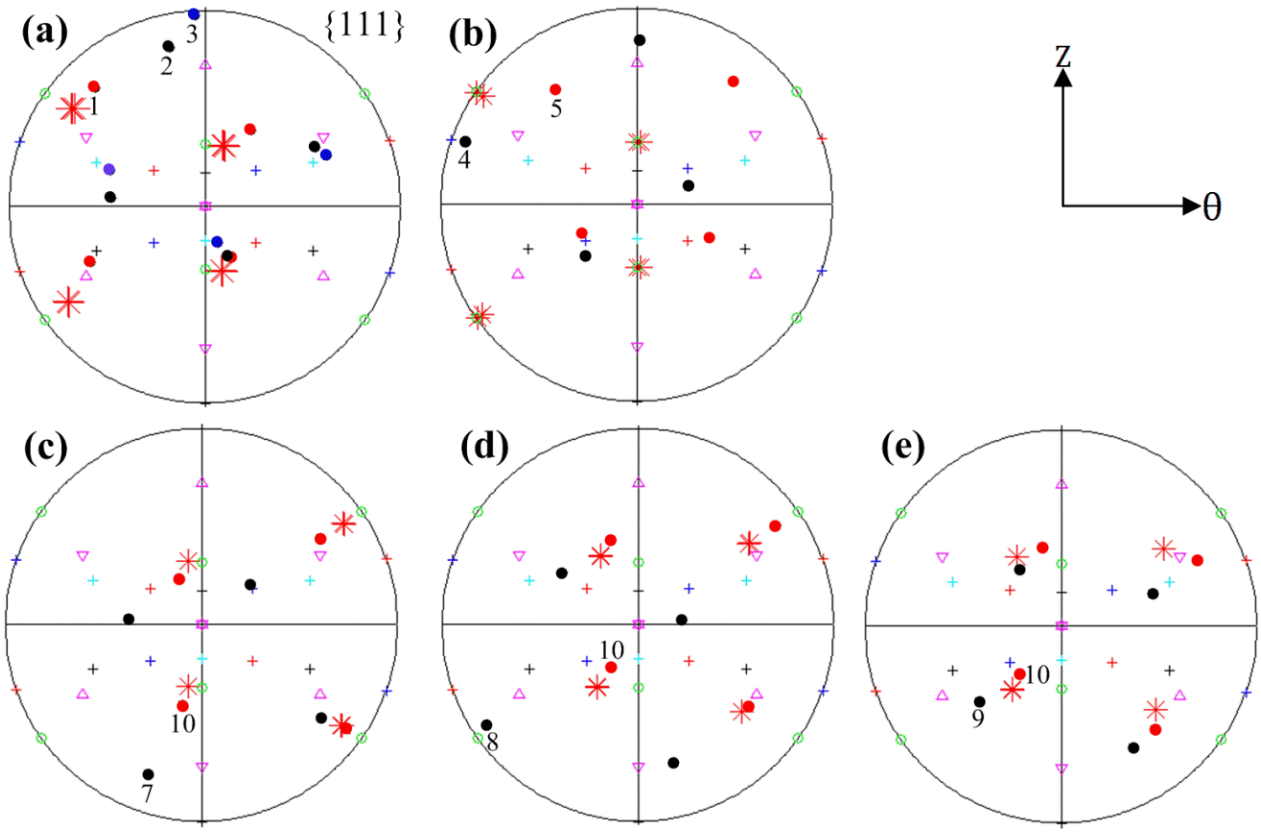

Fig. 6.7 The predicted {111} pole figures of the detected grains along the radial direction. (a) Grains 1, 2 and 3, (b) Grains 4 and 5, (c) Grains 7 and 10, (d) Grains 8 and 10 and (e) Grains 9 and 10

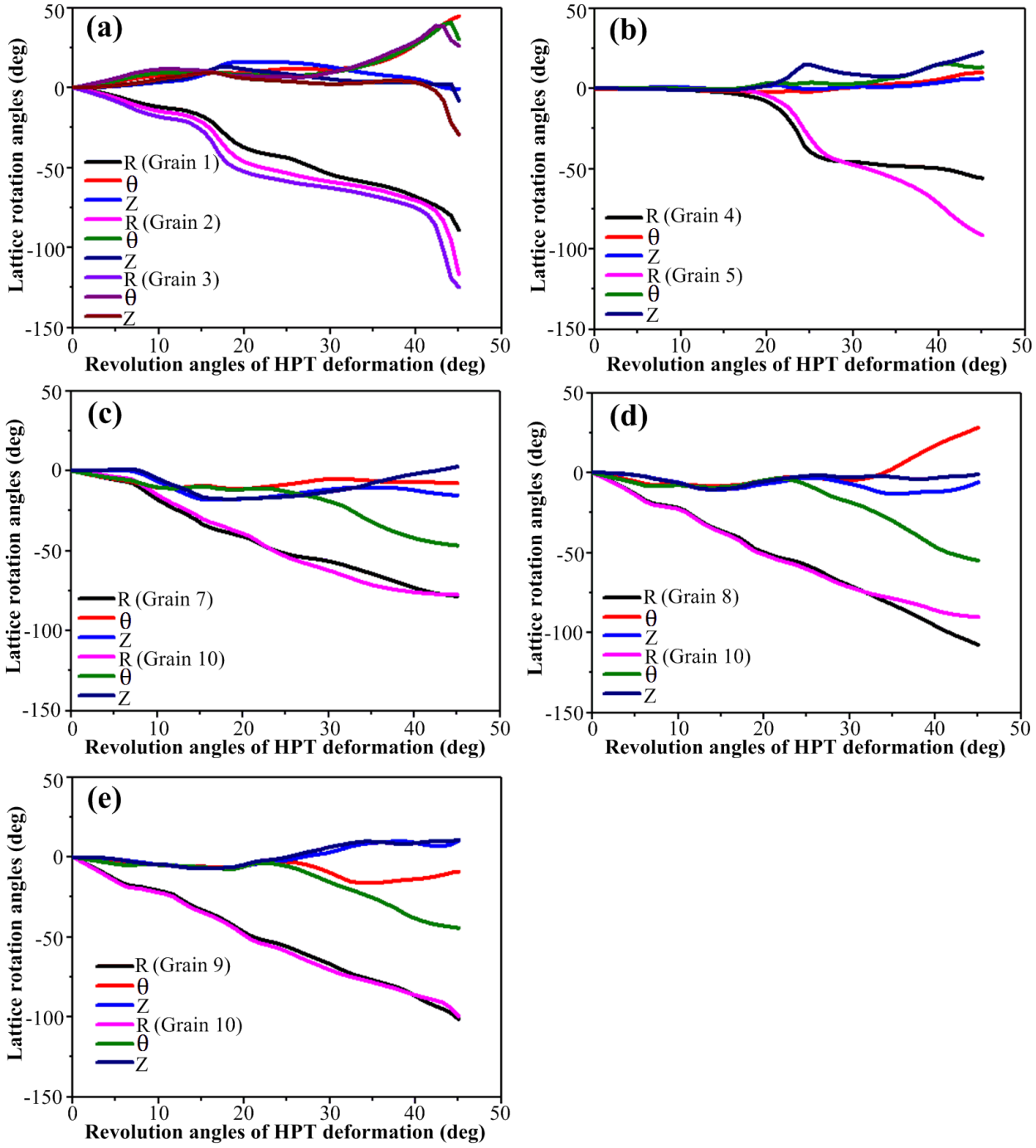

Fig. 6.8 The predicted lattice rotation angles of the detected grains along the radial direction. (a) Grains 1, 2 and 3, (b) Grains 4 and 5, (c) Grains 7 and 10, (d) Grains 8 and 10 and (e) Grains 9 and 10

To achieve a comprehensive understanding of grain fragmentation along the radial direction, larger regions were examined to take Grain 6 into account. Figs. 6.9(a)-(c) show the predicted lattice rotations recorded on various reference lines of RL-1, RL-2, and RL-3 respectively after

45° revolution angles HPT deformation. The positions of these reference lines were given in Fig. 6.5. Two main characteristics of the lattice rotation results can be seen from Fig. 6.9. First, the formation of HAGBs that bounded Grains 6 and 7, Grains 6 and 8 as well as Grains 6 and 9 are mainly attributed to the distinct variations lying in θ-axis lattice rotations while the influences of R and Z-axis rotations could be basically neglected, just like that described in Figs. 6.8(c)-(e). Furthermore, only slight differences of the rotation angles around all three axes could be found for the detected Grains 6 and 10.

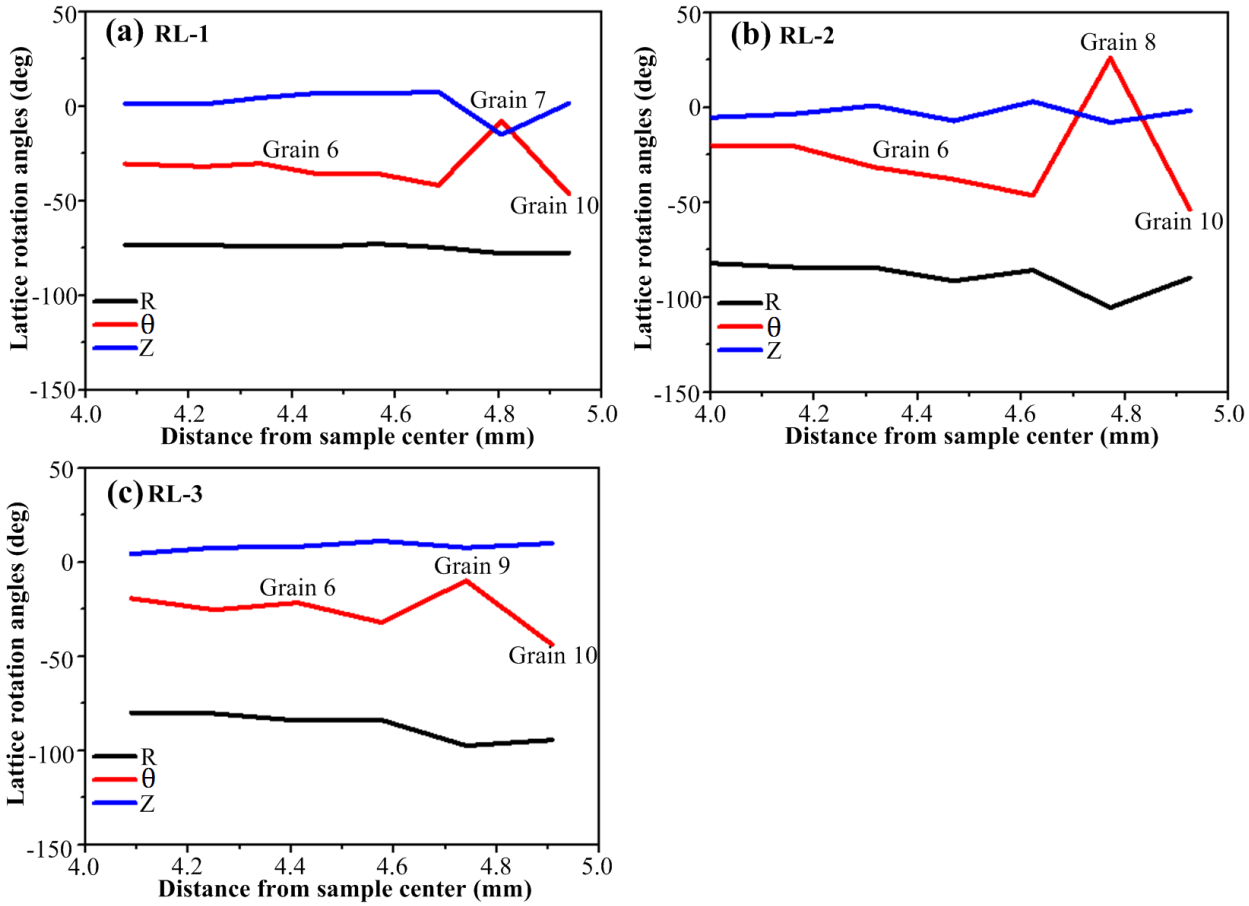

Fig. 6.9 The predicted lattice rotation angles after 45° revolution angles HPT deformation of various reference lines (a) RL-1, (b) RL-2 and (c) RL-3.

6.4.2 Grain Refinement along the Axial Direction

In Fig.6.5, close to the sample periphery where the adjoining grains along the axial direction having varying thickness distances, Grains 3 and 4, Grains 4 and 5, and Grains 5 and 10 were selected for comparative analysis to investigate the grain refinement process along the axial

direction. The same method used in the radial direction analysis was adopted. The resulting {111} pole figures and lattice rotation angles along the R, θ and Z axis are presented in Fig. 6.10 and Fig. 6.11 respectively. In each pole figure of Fig. 6.10, one can see that the initial orientations of the detected grains are slightly different due to the intrinsic properties of the disk-shaped single crystal and the inherent characteristics of material flow during the HPT process.

At the edge region close to the sample top surface, Fig. 6.10(a) shows that the initial orientations of the neighbouring two positions are slightly different and occupy positions gradually toward the ideal C component. Due to slight differences in the initial orientation, Fig. 6.11(a) shows grain subdivision occurs early at low strain level compared to that recorded in Fig. 6.8. The divergence in R-axis lattice rotations becomes relatively visible after 45° degrees of HPT deformation with the amount of ∼55°. Meanwhile, the moderate divergences in θ and Z axis rotations could also be observed in Fig. 6.11(a). The large difference in R-axis rotation together with the moderate variations in the θ and Z axis contribute to the formation of distinctly misoriented grains along the axial direction in this region, namely, Grain 3 and 4. It can be seen from Fig. 6. 10(a) Grain 3 has the orientation close to the $\overline{\mathrm{A}}$ component of the ideal torsion texture while Grain 4 has the orientation just rotated away from the ideal A_1^* component.

Figs. 6.10(b) and 6.11(b) show the grain refinement process along the axial direction at ∼0.15mm from the top surface. The initial orientations occupy the positions of the ideal C component at slightly varied extents. When initially deformed, as shown in Fig. 6.10(b), one lattice is considered to be stable and illustrates no rotation while the other lattice has rotated predominately along the radial direction to accommodate the increasing plastic strain. Accordingly, the divergence in the R-axis rotation angles gradually expands and reaches ∼35° after 20° degrees of deformation. Following that, the lattice with the stable initial orientation begins to rotate. The divergence in the R-axis rotations between the two adjacent positions progressively diminishes to zero after ∼35° angles of sample rotation, indicating the adjacent two positions have almost the same orientation. As the deformation proceeds, the divergence

in R-axis lattice rotations once more increases and is about 20° after 45° degrees of deformation. As a consequence, Grains 4 and 5, form in this region, as shown in Fig. 6.10(b), which occupy different positions in the pole figure.

Further examinations were conducted at ~0.25mm from the top surface. The initial orientations locate in the positions of ideal C component with minor differences in Fig.6.10(c). The tendencies of lattice rotation around all three axes recorded in Fig. 6.11(c) are similar to that of Fig. 6.8(d). Through the deformation process, the lattice rotations around the R axis are much larger than those around the θ and Z axes but the difference between the adjacent two positions is not large. The Z-axis lattice rotations are relatively small so that their influences could be basically neglected. The major difference lies in the θ axis where the accumulative lattice rotation angles around the θ axis are ~10° for Grain 5 and ~-50° for Grain 10 after 45° degrees of deformation. Therefore the large variation in the θ-axis lattice rotation dominates the grain fragmentation process in this region. Seeing from Fig. 6.10(c), the orientation of Grain 5 has rotated further away from the ideal A_1^* component, while the orientation of Grain 10 has just rotated close to the ideal C component and was colored in red in Fig. 6.5. The misorientation angles of Grains 5 and 10 are significantly large.

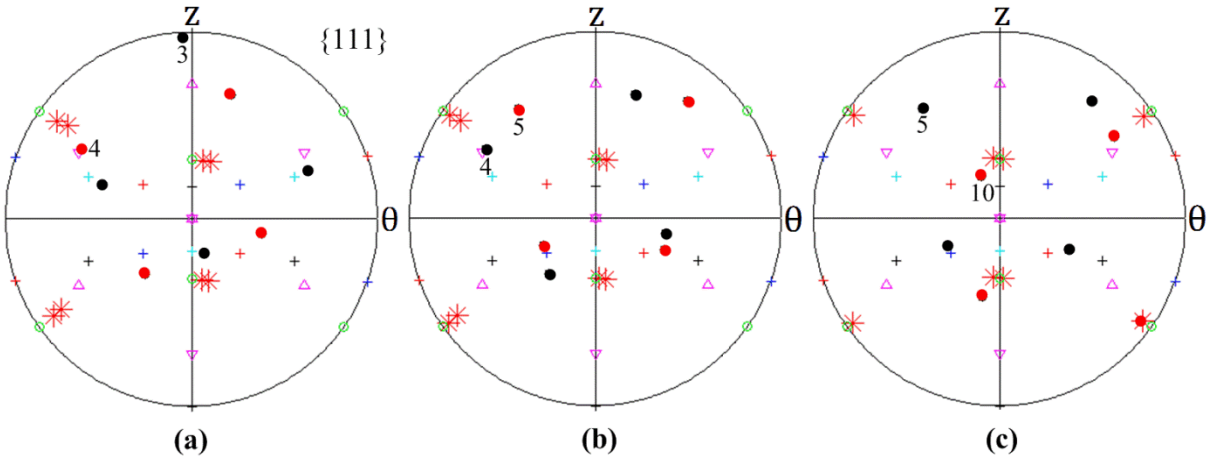

Fig. 6.10 The predicted {111} pole figures of the detected grains along the axial direction. (a) Grains 3 and 4, (b) Grains 4 and 5 and (c) Grains 5 and 10.

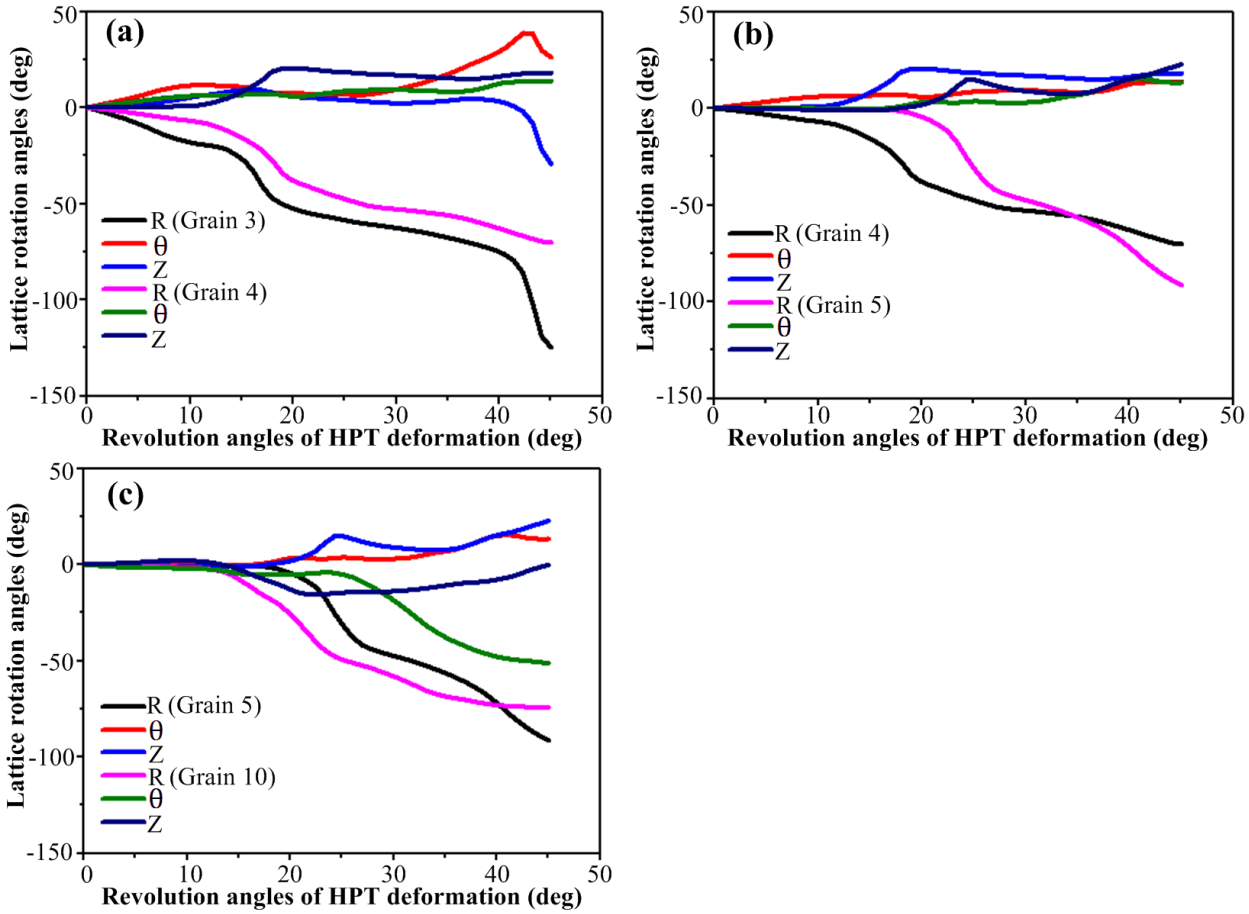

Fig. 6.11 The predicted lattice rotation angles of the detected grains along the axial direction. (a) Grains 3 and 4, (b) Grains 4 and 5 and (c) Grains 5 and 10.

Figs. 6.12 and 6.13 respectively shows the results of orientations and lattice rotations of the adjacent grains along the axial direction at ~0.25mm from the sample periphery, that is, Grains 2 and 4, Grains 4 and 7, Grains 7 and 8 and Grains 8 and 9. The lattice rotations recorded in Fig. 6.13(a) indicate a similar tendency as Fig. 6.8(b) and Fig. 6.11(a). After 45° degrees of deformation, the main divergence is the R-axis lattice rotation and the corresponding values are ~50°. This causes Grains 2 and 4 to form, as shown in Fig. 6.12(a). Fig. 6.13(b) shows that for the adjacent positions, the variation of R-axis lattice rotation is about ~15° and the divergence of θ-axis lattice rotation is ~20° after 45° angles of sample rotation. The developed Grains 4 and 7 in Fig. 6.12(b) are seen to occupy positions significantly different from each other in the pole figure. The lattice rotations become very different in Fig. 6.13(c), nearly equal amount of divergences around all three axes could be observed after 45° HPT deformation, which

operates together to contribute to the development of Grains 7 and 8 in Fig. 6.12(c). Grain refinement close to the bottom surface is obviously illustrated in Fig. 6.13(d), which reveals that the opposite sense lattice rotations along the θ axis is mainly responsible for the formation of Grains 8 and 9 (see Fig. 6.12(d)) in the region.

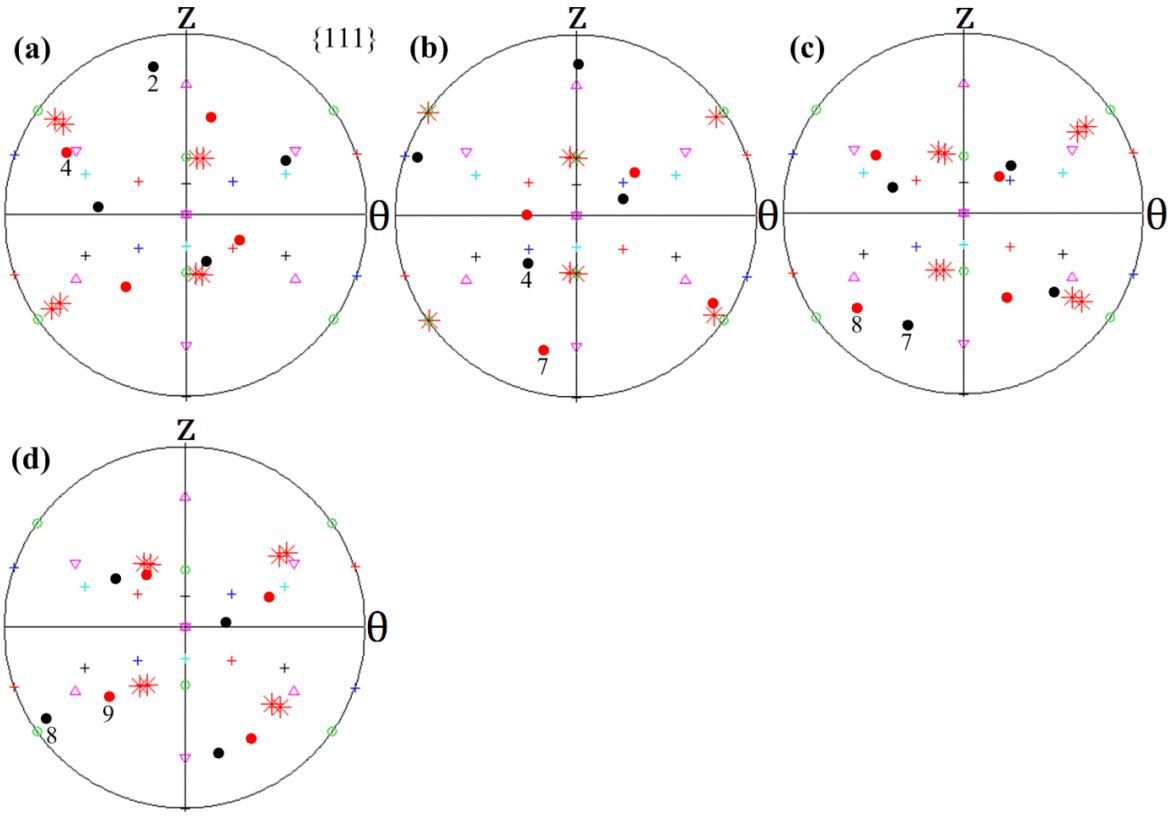

Fig. 6.12 The predicted {111} pole figures of the detected grains along the axial direction. (a) Grains 2 and 4, (b) Grains 4 and 7, (c) Grains 7 and 8 and (d) Grains 8 and 9.

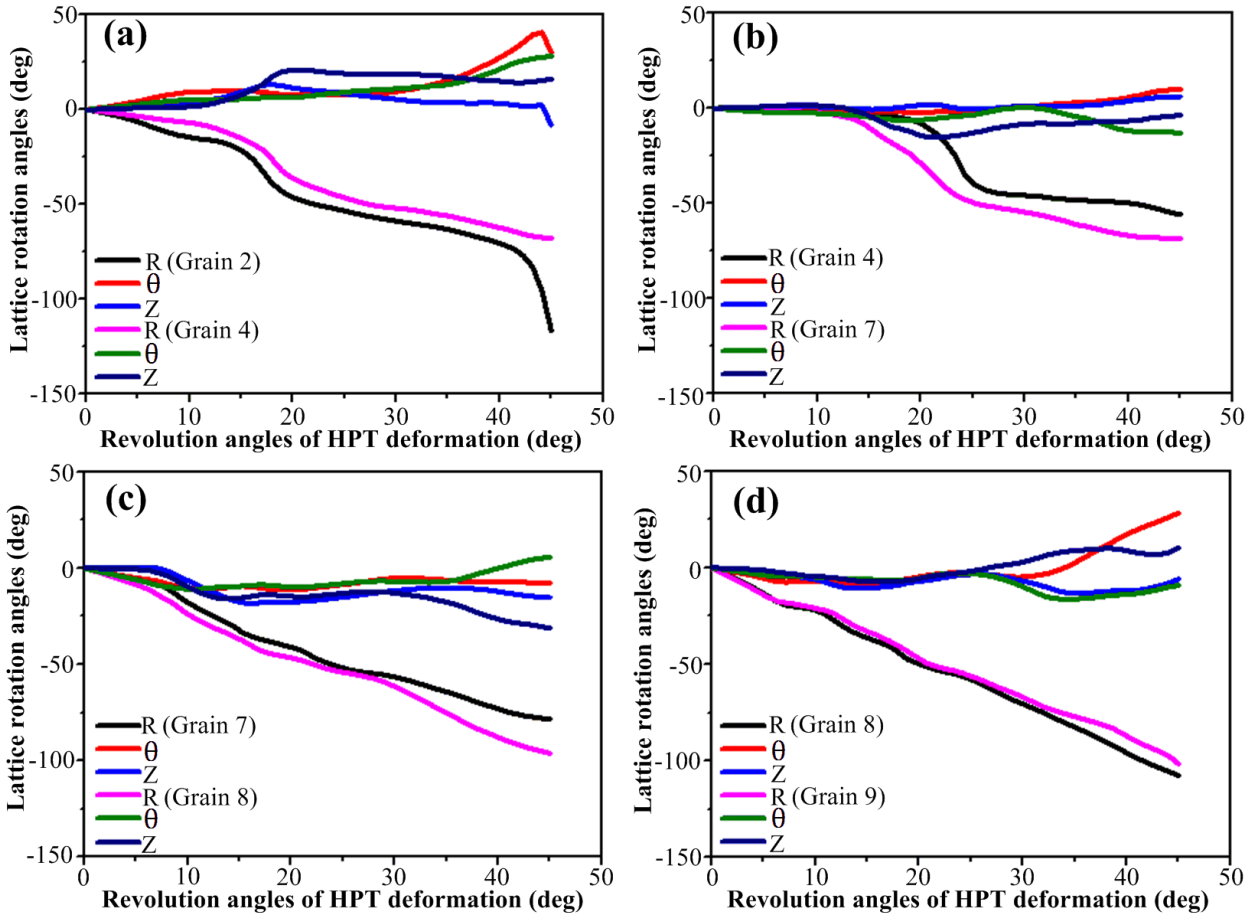

Fig. 6.13 The predicted lattice rotation angles of the detected grains along the axial direction. (a) Grains 2 and 4, (b) Grains 4 and 7, (c) Grains 7 and 8 and (d) Grains 8 and 9.

It is worth noting from Figs. 6.13(b)-(d) that the lattice rotations along the θ axis were involved for the two adjacent positions to be split up into different orientation branches. The function of the θ-axis lattice rotations in grain subdivision along the axial direction is better illustrated in Fig. 6.14, which shows the predicted lattice rotations after 45° degrees of deformation of the pre-defined reference line RL-4. The location of RL-4 was given in Fig. 6.5. Seeing from Fig. 6.14, each adjacent grains has the various amounts of opposite sense lattice rotations along the θ axis. Specifically, the lattice rotation angles around the θ axis are ~10° for Grain 4 and ~-15° for Grain 7, ~-8° for Grain 7 and ~6° for Grain 8 as well as ~30° for Grain 8 and ~-10° for Grain 9 after 45° revolution angles HPT deformation.

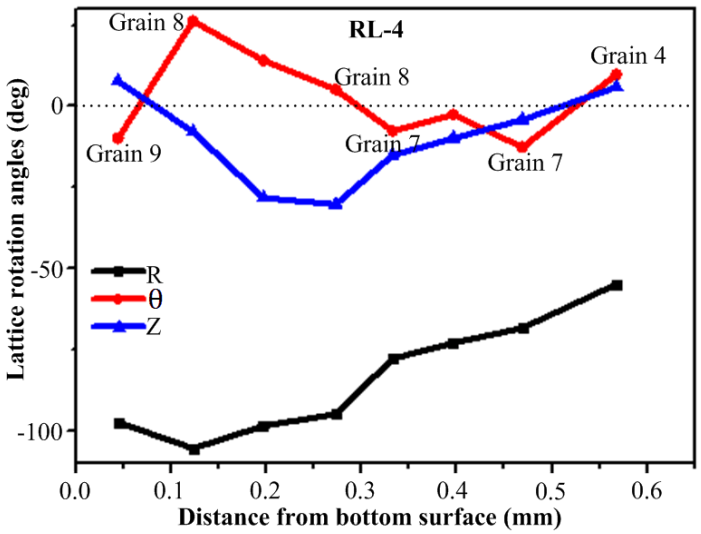

Fig. 6.14 The predicted lattice rotation angles along the RL-4 depicted in Fig. 6.5 after 45° revolution angles HPT deformation.

The grain refinement process along the axial direction is more complicated than that along the radial direction because there was small initial orientation variation in the initial state. The initial orientation variation became stronger during straining and finally led to the development of grains which were separated by boundaries of high misorientation. Raabe et al. mathematically described this corresponded to a 'positive divergence' of the reorientation field which had an intrinsic tendency to build up orientation gradients [284]. We found that there are different reasons for the development of widely different oriented grains along the axial direction during the HPT process. One is the main divergence in the R axis lattice rotation, such as, Grains 4 and 5 in Fig. 6.11(b) and Grains 2 and 4 in Fig. 6.13(a); another one is the major variation in the θ axis lattice rotation, such as, Grains 5 and 10 in Fig. 6.11(c) and Grain 8 and 9 in Fig. 6.13(d). In addition, the combined divergences along all three axes or two of the three axes can also cause the grain to subdivide, such as, Grains 3 and 4 in Fig. 6.11(a), Grains 2 and 4 in Fig. 6.13(a), and Grains 7 and 8 in Fig. 6.13(c).

In Fig. 6.5, at the right-down corner, only one large grain of Grain 10 with the major axis parallel to the axial direction could be obtained from the predicted grain map. Seeing from Fig. 6.6(j), under un-deformed condition, there was a clear initial orientation gradient in this region. However, this strong initial orientation gradient does not lead to grain fragmentation after 45°

degrees of HPT deformation as described in Figs. 6.10 and 6.12. To explain this behavior, the lattice rotations around all three axes of various simulated positions within Grain 10 were calculated and the results are presented in Fig. 6.14. Position 1 in Fig. 6.14 corresponds to the location close to the bottom surface and it extents to position 7 as the distance from the bottom surface increases. Fig. 6.14 shows that, at any stage of HPT deformation, from position 7 to position 1, the lattice rotation angles around R and θ axis increase gradually while the Z-axis lattice rotation is basically zero. This leads to a continuous change in lattice rotations along the axial direction but the bulk region undergoes bulk reorientation. Raabe et al. mathematically described this corresponded to 'zero divergence' of the reorientation field which did not have an intrinsic tendency to build up orientation gradients [284]. Therefore, the pole figure of Fig. 6.6(j) reveals that the developed orientations are spread about a single average orientation of ideal C component rather than splitting into multiple distributions. This explanation also applies to the developed three large grains on the left side of the predicted grain map in Fig. 6.5, namely, Grains 1, 4, and 6. Moreover, it is worth noting that an isolated pole exists in the pole figure of Fig. 6.6(j), which means that Grain 10 is undergoing fragmentation and will be further subdivided if more strain applied.

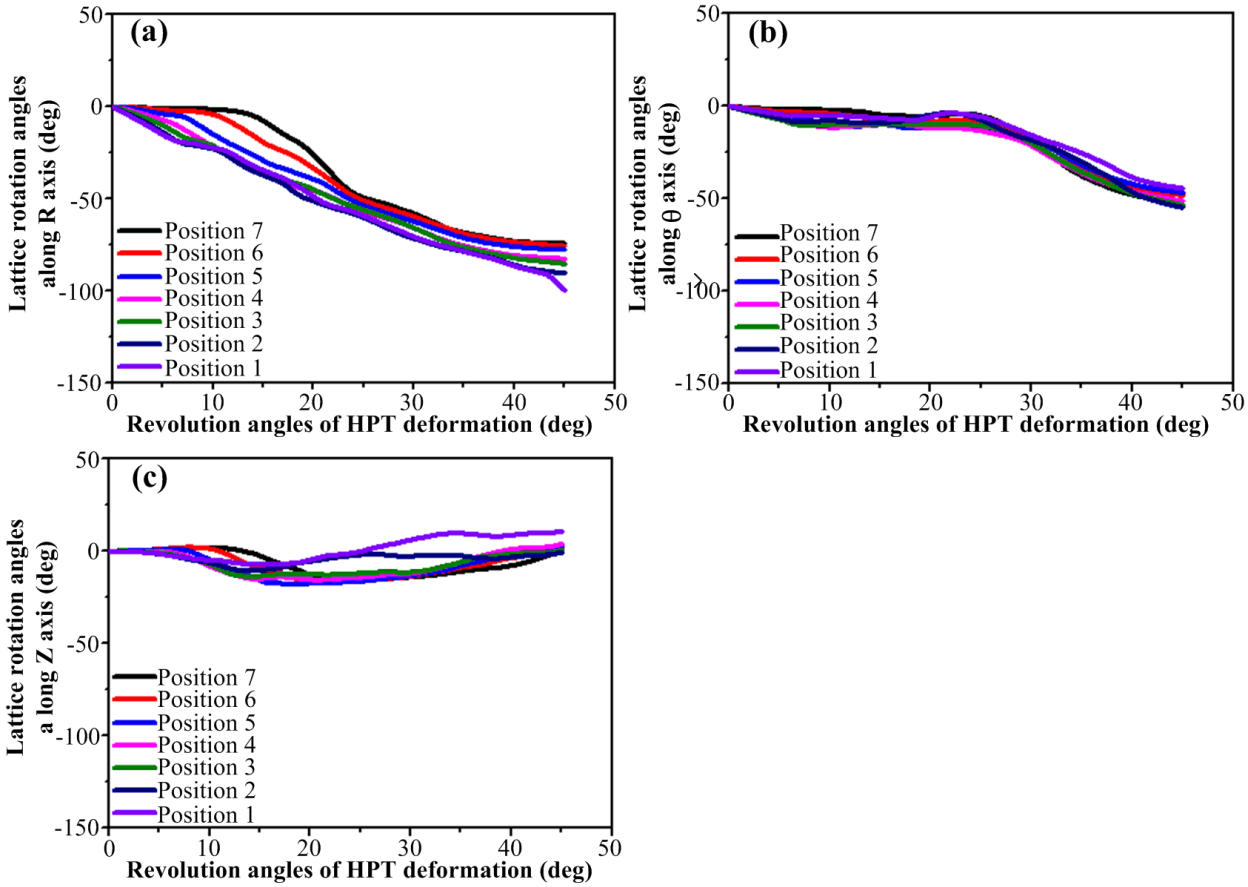

Fig. 6.15 The predicted lattice rotation results for various simulated positions in Grain 10. (a) Lattice rotations angles along the R axis. (b) Lattice rotations angles along the θ axis. (c) Lattice rotations angles along the Z axis

In plastically deformed single and polycrystalline metals, the generation of new HAGBs and grain refinement process have been the subject of many studies [153,157,159,270,284,285]. It is well established form the previous studies that lattice rotation plays a key role in the development of HAGBs and fragmentation of grains [70,85,151–153,159,161,270,284,286–288]. The main characteristics of lattice rotation during the large strain torsion deformation and HPT process were studied by many experimental measurements and numerical simulations [153,166,167,170]. These investigations revealed that the common feature of lattice rotation is that the lattice rotates predominately along the radial axis of a single-sense direction to accommodate the increasing plastic strain introduced by torsion/HPT deformation [153,166,167,170]. However, how the lattice rotation leads the initially uniformly oriented

crystals subdividing into portions with a range of different orientations is still unclear. In this study, in order to reveal the correlation between the grain subdivision procedure and lattice rotation, the lattice rotations angles around R, θ and Z axis and the orientation changes were analyzed over a set of grains predicted by the developed CPFEM model. By utilizing the analysis, we are able to determine the fragmentation model during the HPT process. It is found that in HPT there are mainly two models under which the grain fragmentation occurs and the formation of boundaries with high misorientation could be observed.

In one model, the main reason of grain subdivision lies in the R-axis lattice rotation, as shown in Figs. 6.8(a)-(b), Figs. 6.11(a)-(b) and Fig. 6.13(a), the divergence in rotation rate along radial direction contributes to the formation of different oriented grains. The occurrence of divergence in R-axis rotation rate is because the lattice does not rotate uniformly with respect to the shear deformation in HPT. This model is confirmed by Barnett and Montheillet [153]. They investigated the generation of new HAGBs in aluminium during torsion deformation by experiments and a Taylor-type model, and found that these generated HAGBs were characterized by a disorientation axis close to parallel with the sample radial direction and the main cause of the high-angle boundaries was the difference in rotation rate along the radial direction.

In the other model, the R-axis lattice rotation angles are still much larger than the other two axes in HPT, but there is only slight or even no divergence. Therefore it has few effects in determining grain refinement. Moreover, the Z-axis lattice rotation is relatively small and its influences could be basically neglected. Meanwhile, a noticeable amount of lattice rotation along the θ axis occurs and there are clear divergences in the rotation amount and (or) sense, which is supposed to contribute to the formation of grains separated by boundaries of high misorientation. This model of grain fragmentation could be widely found in this study, such as in Figs. 6.8(c)-(e), Fig. 6.11(c) and Fig. 6.13(d). It's most obviously illustrated Fig. 6.8(d), in which the grain subdivision was achieved by large amount of rotations but opposite sense about the θ axis.

6.5 Summary

In this chapter the developed CPFEM model was further employed to study the grain refinement behaviour of the initial (001) nickel single crystal during HPT process. The summaries are listed as follows:

(1) The grain maps obtained by the developed CPFEM model in the present work were capable of predicting the prominent characteristics associated with grain refinement during the HPT process. The simulation results of the local texture on the interested cut plane were in good coherence with the previously published experimental observations of single crystal and polycrystalline materials deformed by the HPT process.

(2) The development process over a set of different oriented grains bounded by high angle boundaries on the predicted grain map were extensively examined by the combination of lattice rotations angles and changes of orientation to explore the underlying mechanism. It has been found that there were mainly two models which caused the initial (001) nickel single crystal to subdivide: one is the difference in the rate of rotation along the radial direction, which is the direction of predominant lattice rotation in HPT; the other one is the divergence of rotation angles along the θ axis, even though they are much smaller than the R-axis rotations, can also contribute to the formation of grains with significantly different orientations.

Chapter 7 Investigation of Plastic Deformation Behavior of Aluminium Single Crystal during HPT by CPFEM Simulation

In the previous chapters, texture evolution and grain fragmentation of the nickel single crystals deformed by HPT were studied by CPFEM simulations. In this chapter, the developed CPFEM model is extended to simulate the HPT process of aluminium single crystal. This chapter will focus on the investigations of plastic deformation behavior along the circumferential direction and texture evolution with increasing HPT deformation will be discussed in detail.

7.1 Introduction

Crystalline matter is mechanically anisotropic. In a single crystal, it is well known that atoms should be able to slip over one another or distort in relation to one another easier in some directions than others. When the properties of a material vary with different crystallographic orientations, the material is said to be anisotropic. Alternately, when the properties of a material are the same in all directions, the material is said to be isotropic. For many polycrystalline materials the grain orientations are random before any working (deformation) of the material is done. Therefore, even if the individual grains are anisotropic, the property differences tend to average out and, overall, the material is isotropic. When a material is deformed, the grains are usually distorted and elongated in one or more directions and an initially isotropic metal therefore becomes anisotropic. An essential consequence of this crystalline anisotropy is that the associated mechanical phenomena such as material strength, shape change, ductility, strain hardening, deformation-induced surface roughening, damage, wear, and abrasion are orientation-dependent [74,199].

As HPT processing is normally applied on thin-disk shaped samples, the initial crystallographic orientation of a disk-shaped single crystal changes from position to position along the circumferential direction of the sample [48]. This will definitely lead to different plastic deformation behaviors along the sample circular direction during the HPT process. Therefore, in this chapter, the developed CPFEM model is further employed to investigate the circumferentially plastic deformation behavior of aluminium single crystal during the HPT process. Moreover, the texture evolution of the initial (001) aluminium single crystal is also presented and analyzed in detail.

7.2 Plastic deformation behavior at the Early Stage of HPT

The simulation model is basically the same as that used for the texture evolution and grain refinement studies in the previous chapters. The only differences are that aluminium single crystal was used in this chapter and the sample rotated clockwise along the axial direction. The starting material was oriented with (001) crystallographic plane lying parallel to the Z axis of the sample. The parameters of the constitutive laws for aluminium single crystal were already given in Chapter 4.

7.2.1 True Strain, Mises Stress and Critical Resolved Shear Stress

Figs. 7.1(a)-(c) shows the contour plot of true strain, Mises stress, and critical resolved shear stress (SDV 1) respectively that was recorded on the surface of (001) aluminium single crystal after a torsional strain of N=1/12 turn. Angle φ in Fig. 7.1(a) refers to the extent of material flowing away from the fixed X axis along the axial direction on the shear plane due to sample rotation. The critical resolved shear stress (CRSS) recorded in Fig. 7.1(c) represents the resistance of crystallographic slip. The CRSS of a slip system is a function of plastic strain and usually increases due to the material hardening caused by plastic deformation.

As illustrated in Fig. 7.1(a), the strain remains relatively small at the center of the sample and it increases with the distance away from the center. The maximum strain exists in the vicinity of sample edge, which is around 1.4. Moreover, it can be seen from Fig. 7.1(a) that the spatial

strain is basically homogenously distributed along the circumferential direction except for a slight difference at the edge region. The similar strain distribution on the section of the sample of different materials have been revealed previously in [265–267], which reported that the torsion deformation of a cylinder/tubular sample with respect to a [001] axis gave rise to the formation of four zones of more deformation around the circumference of the sample using a micro-macro anisotropic viscoplasticity model and experimental observations. The distribution of Mises stress in Fig. 7.1(b) becomes quite different. A distribution pattern of a four-fold symmetry is developed on the sample surface. Four more strain hardening regions separated by four less strain hardened ones with interval angles of $\varphi = 90°$ along the circumferential direction could be observed. This result differs from that obtained by classic FEM simulation as revealed in [63,66], which gave an homogenous stress distribution along the circumferential direction of the sample deformed by HPT, indicating the FEM simulations are not capable of predicting deformation anisotropy attributed to the isotropic assumption. In Fig. 7.1(c), the distribution of CRSS also presents a similar characteristic of heterogeneity along the circumferential direction with an obvious four-fold symmetry pattern on the sample surface. Four easy slipping longitudinal zones could be observed on the surface of the sample that are separated by four relatively difficult slipping regions.

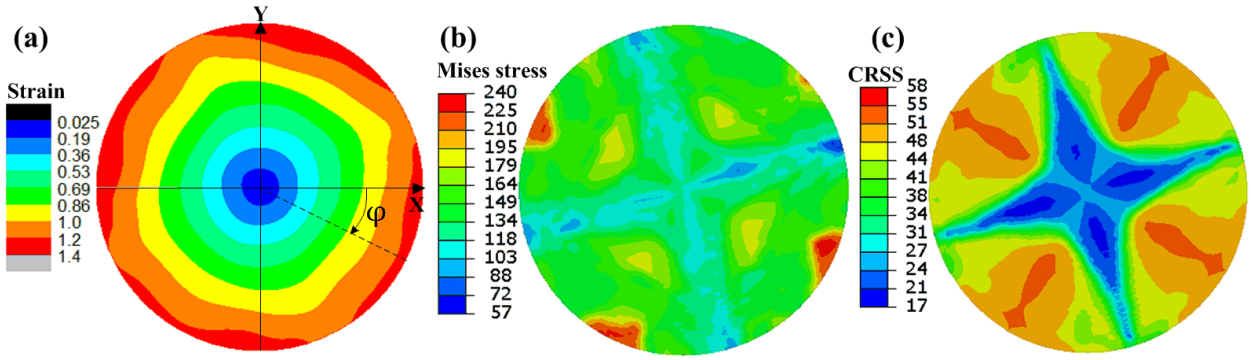

Fig. 7.1 The contour plots of (a) True strain, (b) Mises stress and (c) CRSS recorded on the surface of (001) aluminium single crystal after N=1/12 turn HPT deformation.

7.2.2 Texture Evolution along the Circumferential Direction.

The results of Mises stress and CRSS recorded in Fig.7.1 revealed the obvious plastic deformation heterogeneity around the circumference of the sample. It is well established that such plastic deformation heterogeneity is strongly correlated with the crystallographic orientations developed during plastic deformation. Therefore, the evolution of crystallographic orientation along the circumferential direction of the HPT deformed aluminium single crystal was examined in detail.

Fig. 7.2 shows the predicted {111} pole figures recorded along the circumferential direction of the initial (001) aluminium single crystal after N=1/12 turn HPT deformation. The resulting pole figures were obtained at various positions with the same distance away from the center of the sample ($R_0/R\sim=1$) but different values of φ. According to Hafok and Pippan [48], the shear direction and the initial crystallographic orientation change between individually selected positions. The resulting {111} pole figures were all recorded on the $\theta - Z$ planes where the horizontal and vertical axes of the pole figures represent the local tangential (θ) and axial direction (Z), respectively. The locations of the main components of ideal torsion texture were also presented ad visualized by different symbols in the pole figures (after [164,170,283]). For the pole figure obtained at each selected position, the thick black dots stand for the initial crystallographic orientation corresponding to the un-deformed state, while the thick red dots denote the orientation after N=1/12 turn HPT deformation. The examinations of positions occupied by black and red dots recorded in one pole figure makes it possible to inspect the lattice rotation in the polar coordinate system due to plastic deformation, which is not easy to be accomplished by experimental measurements.

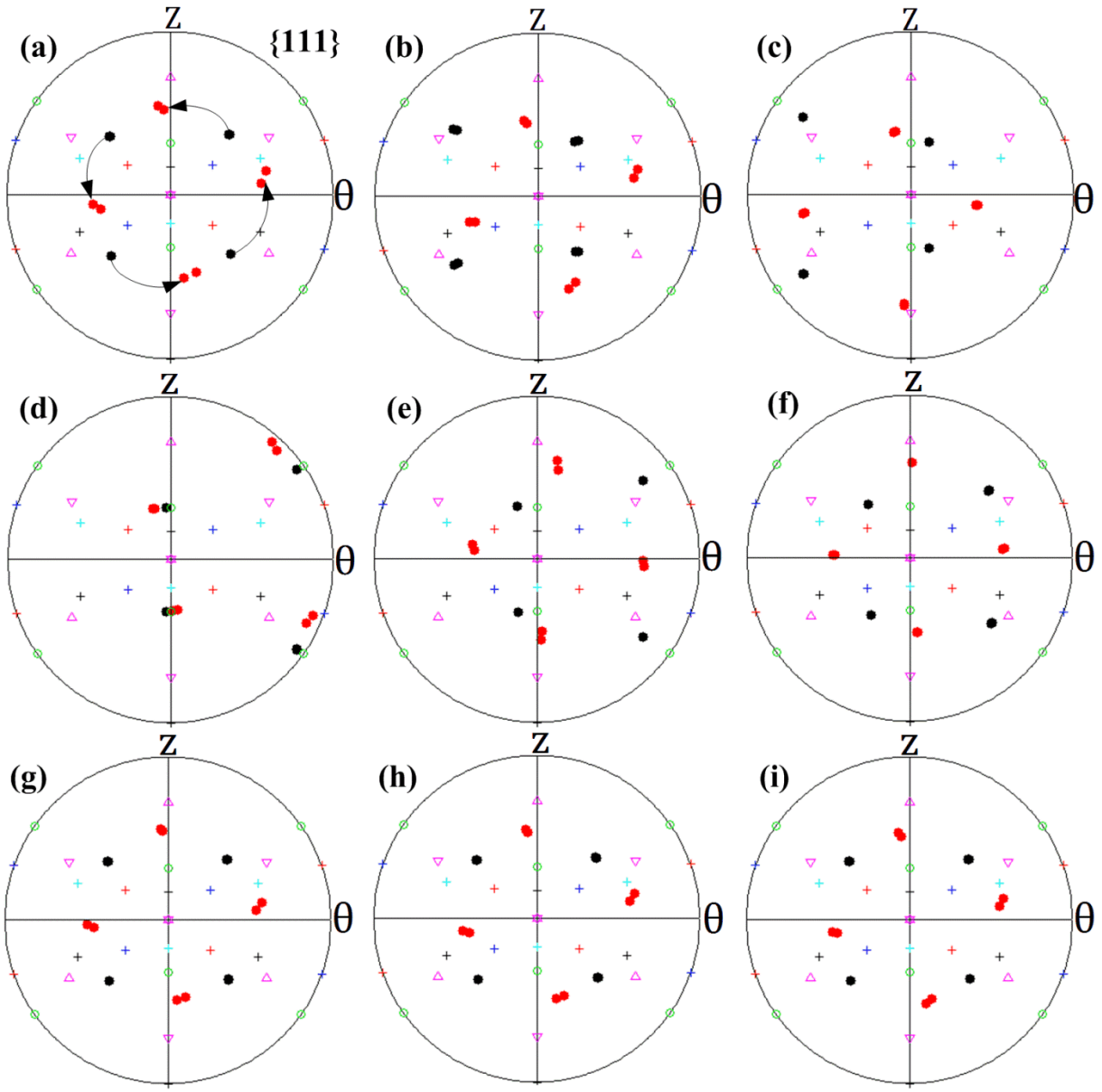

Fig. 7.2 The predicted {111} pole figures recorded along the circumferential direction of the (001) aluminium single crystal after N=1/12 turn HPT deformation. The pole figure were recorded at different sample positions with $\varphi =$ (a) $-30°$, (b) $-15°$, (c) $0°$, (d) $18°$, (e) $30°$,(f) $45°$, (g) $60°$, (h) $150°$ and (i) $-120°$ respectively.

The first pole figure represents the orientation developed at the sample position $\varphi = -30°$. In the pole figure, the initial crystallographic orientation of this position is close to the Cube orientation. The lattice rotations are observed to be mainly around the radial axis in an anti-

clockwise direction, as shown in Fig. 7.2(a), which causes the initial Cube orientation to occupy positions of rotated cube orientation. When considering the pole figures in Figs. 7.2(b)-(c), which were recorded at sample positions of $\varphi = -15°$ and $0°$ respectively, the initial orientations belonging to these positions gradually approach a certain ideal torsion texture component. The resulting orientations deviate significantly from that of $\varphi = -30°$ position. In Fig. 7.2(d), the initial orientation of the $\varphi = 18°$ position almost occupies the positions of the ideal C component. The orientation that developed after N=1/12 turn HPT deformation illustrates only a little divergence from the initial C orientation, indicating a relatively small amount of lattice rotations. Further examinations of the pole figures in Figs. 5.2(e)-(f) reveal that the initial orientations of $\varphi = 30°$ and $45°$ positions gradually leave away from the ideal C component and the resulting orientations occupy completely different crystallographic orientations in their corresponding pole figures. Figs. 7.2(a)-(f) show that crystallographic orientations of various circumferential positions that developed at small level of strain of N=1/12 turn deviate significantly from each other due to variations in the initial orientation along the circumferential direction of the (001) aluminium single crystal. The initial orientation of position $\varphi = 60°$ once more occupy the position of Cube orientation and the resulting orientation in Fig. 7.2(g) is quite similar with position $\varphi = -30°$.

Due to the similarity in texture prediction of $\varphi = 60°$ and $\varphi = -30°$positions, additional positions of $\varphi = 150°$ and $\varphi = -120°$ were investigated and the results are plotted in the same manner, as shown in Figs. 7.2(h)-(I) respectively. It is readily to see that the developed orientations recorded at these four different circumferential positions, with an interval of $90°$ in position angles φ, occupy almost the same positions in the corresponding pole figures, namely rotated cube orientation. Therefore, it can be concluded that the texture also develops a four-fold symmetry along the circumferential direction of the sample at this specific strain. Hafok and Pippan [48] investigated the texture evolution of initial (001) nickel single crystal along the circumferential direction at an equivalent strain of $1.4 \sim 1.6$ by experimental measurements and predictions using Taylor-type modelling. They also reported the phenomenon of repetition in the texture development and the evolution of a four-fold

symmetry at the early stage of HPT deformation, which agrees well with our predictions in this study using CPFEM model.

7.2.3 Lattice Rotation along the Circumferential Direction

Figs. 7.3(a)-(c) shows the contour map of lattice rotation angles around the R, θ and Z axis respectively that were recorded on the surface of the initial (001) aluminium single crystal after N=1/12 turn HPT deformation. In all the maps, positive values mean anticlockwise lattice rotations while negative angles mean clockwise rotations.

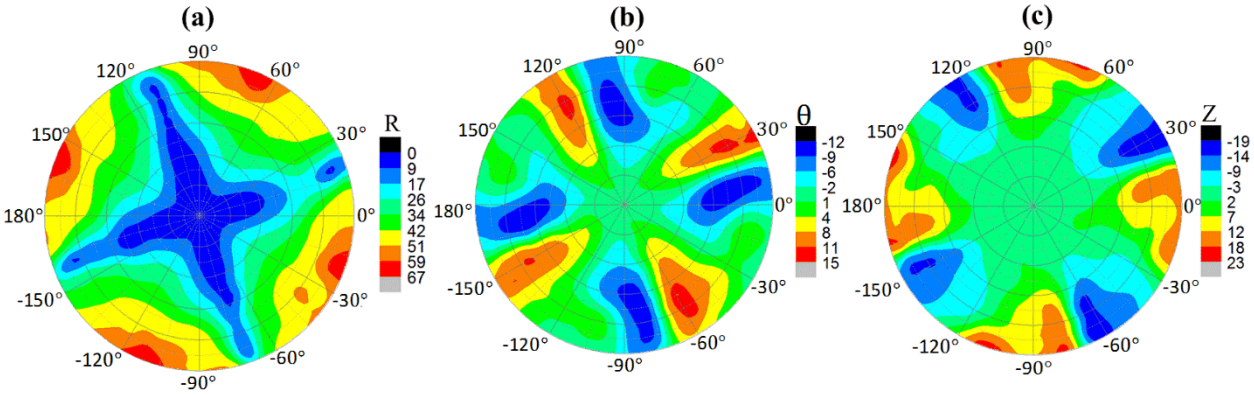

Fig. 7.3 Contour plots of lattice rotation angles recorded on the surface of the initial (001) aluminium single crystal after N=1/12 turn HPT deformation. (a) Lattice rotation angles around R axis, (b) Lattice rotation angles around θ axis and (c) Lattice rotation angles around Z axis

Fig. 7.3 shows that the lattice rotates around all three axes during the HPT process. The rotation angles around R axis are much larger than those around the θ and Z axes. The largest rotation angles around the R axis existing in the vicinity of sample edge are $\sim 65°$ compared to those of $\sim 15°$ around the θ axis and $\sim 20°$ along the Z axis. This is consistent with the result of predominant single sense rotations around the sample radial direction during the torsion deformation process reported in previously published papers [153,167,272]. It should be noted that, in this study, the sample rotated clockwise along the axial direction, the predominant R-axis rotations in Fig. 7.3(a) are found to occur in an anticlockwise direction; when the sample rotated anticlockwise along the axial direction, as in the studies in chapters 5-6, the R-axis lattice rotations occurred in a clockwise direction. This implies that the direction of the

predominant R axis rotation is determined by the direction of imposed sample rotation. Furthermore, in Fig. 7.3(a), one can see that the distribution of R-axis lattice rotations on the sample surface has the same feature of four-fold symmetry as shown in Figs. 7.1 and 7.2, where four red regions with higher value of lattice rotations, are separated by four blue regions with relatively small angles of lattice rotation. A close examination of the R-axis lattice rotation in Fig. 7.3(a) indicates that the largest and smallest lattice rotations generally occur at specific positions on the sample surface. For instance, the sample position $\varphi = 18°$ has the smallest R-axis rotation angles of less than $10°$. The initial orientation of this particular position was close to the ideal C component and the resulting orientation in Fig. 7.2(d) illustrated a limited divergence from the original C orientation. Also, the smallest Mises stress and CRSS in Figs. 7.1(b)-(c) were observed at the circumferential position of about $\varphi = 18°$. Moreover, at sample position close to $\varphi = -30°$, the largest R axis lattice could be seen with the amount of $\sim 65°$. Seeing from the pole figure in Fig. 7.2(a), this particular sample position had an initial orientation close to the Cube orientation and the increasing introduced HPT deformation caused the resulting orientation to rotate significantly away. Besides, at the position of about $\varphi = -30°$, the highest strain hardening and slip resistance were also seen in Figs. 7.1(b)-(c).

When considering the lattice rotations of the θ and Z axes on the surface of the sample, the four-fold symmetry pattern can also be observed, as shown in Figs. 7.3(b)-(c), which present the alternations of positive and negative rotations around the θ and Z direction, but the magnitude of lattice rotation angles along the θ and Z axes are much smaller.

7.2.4 Slip Traces Evolution along the Circumferential Direction

It is well known that crystalline materials deform plastically by the crystallographic slips of dislocations on discrete slip systems. In this study, the evolution of the slip traces along the circumferential direction was also investigated by the developed CPFEM model. Fig. 7.4 displays the simulated slip traces recorded at various positions along the circumferential direction of the initial (001) aluminium single crystal after N=1/12 turn HPT deformation. To save space, only the right hand side of the sample surface is shown. In Fig. 7.4, the small red circles represent the location of individually selected positions. At each position, six slip systems with the larger

magnitude of accumulative shear strain are presented. The center of all the straight trace lines is located at the integration point of the element generated at this selected position. The direction of each straight line infers the orientation of the slip trace while the length of the straight line represents the relative magnitude of accumulative shear strain. The traces of these six slip systems, from the first largest magnitude to the sixth largest magnitude, are distinguished by black, blue, red, cyan, green, and magenta, respectively. These trace lines are the projections of the spatial slip traces onto the θ-Z plane, as illustrated in the bottom right corner of Fig. 7.4, where the horizontal direction stands for the shear direction while the vertical direction represents the axial direction.

Seeing from Fig. 7.4, the simulated slip traces show significant variations along the circumferential direction of the sample. At sample position $\varphi = -30°$, the magnitudes of accumulative shear strain on the slip systems of interest are approximately the same. The six slip system could be treated as three sets which are all differently oriented. Within each set the two slip traces almost coincide with each other. At sample position $\varphi = -15°$, the slip activities are similar with $\varphi = -30°$ position except that the accumulative shear strains corresponding to the fifth and sixth largest slip systems are much smaller. At $\varphi = 0°$ position, a different slip trace is exhibited. Slip systems with the first and second largest accumulative shear strain coincide with each other and possess an accumulative shear strain that is several times larger the others. Moreover, these two slip systems tend to rotate towards the shear direction while the other slip systems of interest all orient with certain angles with each other. At the $\varphi = 18°$ position, the slip activities become completely different, here the accumulative shear strains are concentrated on two slip systems, namely a3 and d3, as defined in Chapter 5, which share the same [110] crystallographic direction. The accumulative shear strain on the dominant two slip systems are huge compared to the other slip systems and their slip traces are almost parallel to the macroscopic shear direction. Under such circumstance, the influence of the other slip systems could basically be neglected. When further examining the positions from $\varphi = 18°$ to $\varphi = 60°$, there is a tendency for the slip traces to develop gradually from dominate slip to multiple slip and the slip trace obtained at $\varphi = 60°$ position possess the similar characteristics with $\varphi = -30°$ position.

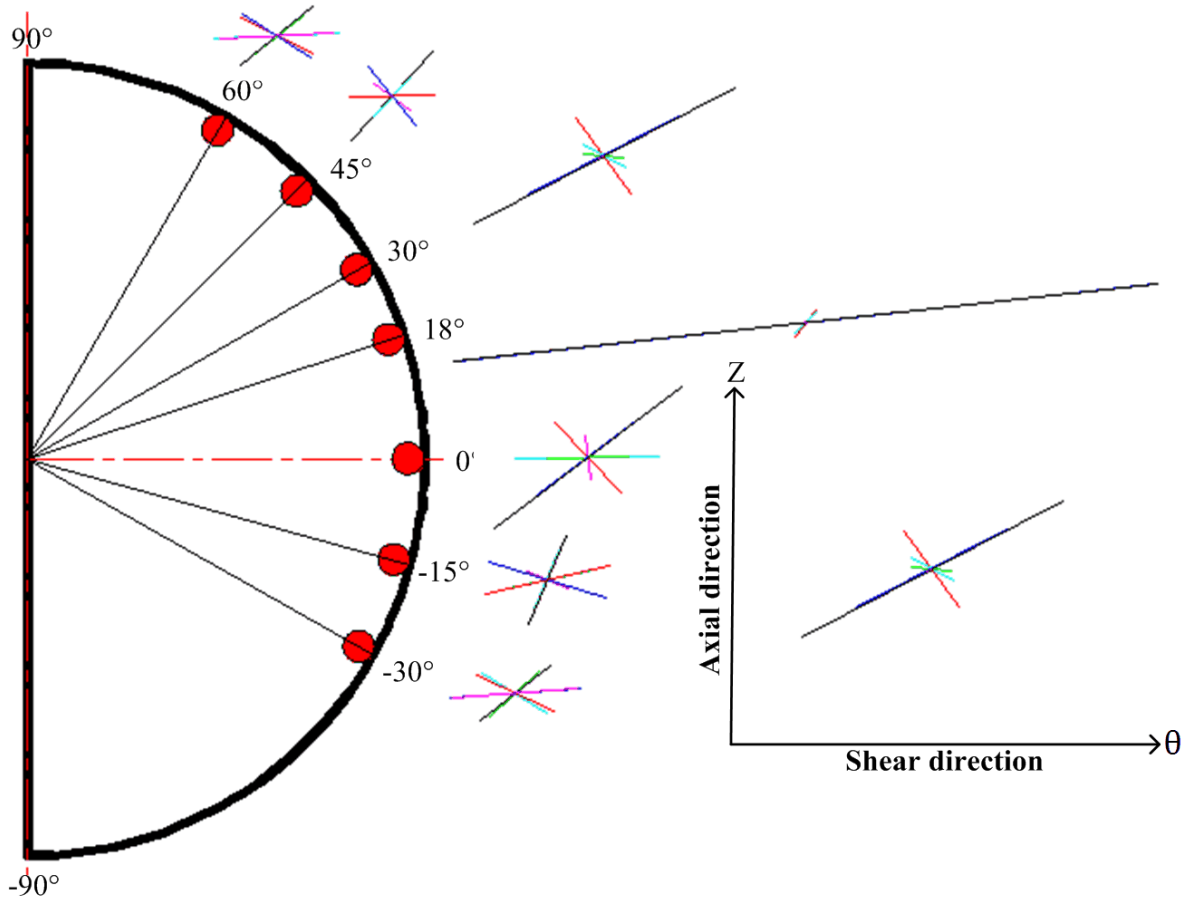

Fig. 7.4 The visualization of slip traces of various positions along the circumferential direction of the initial (001) aluminium single crystal after N=1/12 turn HPT deformation.

7.2.5 Discussion

At the early stage of HPT deformation of the initial (001) aluminium single crystal, the Mises stress and CRSS were not homogenously distributed along the circumferential direction and a four-fold-symmetry distribution pattern was observed on the surface of the sample. Four 'soft' longitudinal zones could be seen in Fig. 7.1 that were separated by four relatively 'hard' regions. Quilici et al. simply attributed such a phenomenon to the Schmid factor variations along the sample circumference [266]. To achieve a better understanding of the plastic deformation heterogeneity along the circumference of the sample, texture evolution, lattice rotation and slip activities at various circumferential positions were plotted and have been analyzed in detail.

These results are combined together to explain the differences in plastic deformation behavior along the circumferential direction during the early stage of the HPT process.

Since HPT processing was applied onto a thin-disk shaped sample, the initial crystallographic orientation of the (001) aluminium single crystal changed from position to position along the circumferential direction under un-deformed state (see the pole figures in Fig. 7.2). At the early stage of HPT deformation, due to such variations in the initial orientation, the introduced torsion strain activated different slip systems at different circumferential positions, which could be clearly observed from Fig. 7.4. It is possible that only two slip systems were active (dominant slip mode), whereas the slip mode in which many systems are active is called multiple slip mode. Single crystals deformed by different modes (dominate or multiple slip) showed different plastic deformation behaviors.

At some sample positions, for example, $\varphi = 18°$, dominant slip was the slip mode. The accumulative shear strain on the two primary slip system were significantly larger than the others and they shared the same [110] slip direction which aligned parallel to the macroscopic shear direction, as shown in Fig. 7.4. All the introduced plastic strains were concentrated into the dominant slip systems, producing a given amount of overall glide rotation (Ω^P). This resulted in the fact that the required material rotation (Ω) can be almost fully satisfied by plastic rotation (Ω^P) induced by the dominant slip and therefore the lattice rotation (Ω^*) was very small at $\varphi = 18°$ position (see Fig. 7.3(a)). This would lead to the near-initial orientation after deformation (see the pole figure in Fig. 7.2(d)). The dominant slip was basically not influenced by other slip systems and the material flowed easily. So a limited macroscopic strain hardening occurred at $\varphi = 18°$ position in Fig. 7.1(b), while relatively small slip resistance was found at the same sample position in Fig. 7.1(c).

However, at certain sample positions, such as $\varphi = -30°$, a multiple slip mode could also be activated. The activated systems possessed almost the same amount of accumulative shear strain but oriented along different directions, as shown in Fig. 7.4. Each of the slip systems of interest produced a rotation component, the resultant of which was the overall glide rotation (Ω^p) was relatively small. The lattice must rotate to generate a large Ω^* to satisfy the material

rotation (Ω) requirement, as shown at $\varphi = -30°$ position in Fig. 7.3(a), which led to a considerable change in orientation (see the pole figure in Fig. 7.2(a). The simultaneously activated slip systems interacted with each other and hindered the flow of the material. Therefore a strong macroscopic strain hardening took place at $\varphi = -30°$ position in Fig. 7.1(b) and meanwhile relatively large values of slip resistance at the same sample position could be observed in Fig. 7.1(c).

At other sample positions along the circumferential direction, the slip conditions were between these two slip modes of dominant slip and multi-slip. Accordingly, there were moderate increases in Mises stress and CRSS, as shown in Figs. 7.1(b)-(c) respectively.

7.3 Plastic Deformation Behavior with Increasing HPT Deformation

The evolution of CRSS (SDV1) with increasing HPT deformation was studied using the CPFEM simulation. Fig. 7.5 shows the distribution of CRSS on the surface of the initial (001) aluminum single crystal after subjected to increasing HPT deformation from N=1/8 turn, through N=1/2 turn, to N=2/3 turn.

After processed through N=1/4 turn, compared with N=1/12 turn deformation recorded in Fig. 7.1(c), further material hardening has occurred and the sample exhibits higher CRSS values over the total section. The central area of lower CRSS is reduced in size significantly. Moreover, the four-fold-symmetry distribution of CRSS on the sample surface can still be clearly observed in Fig. 7.5(a). The ‘hard’ and ‘soft’ regions all rotate along the circumferential direction as material flows and occupy different positions on the surface of the sample compared with that in Fig. 7.1(c), which is mainly due to that as the material rotates continuously around the axial direction during the HPT process, the crystallographic orientations change according.

When the HPT deformation proceeds to N=1/2 turn, It can be seen from Fig. 7.5(b) that there is a tendency for regions with higher CRSS to expand from sample edge towards the center and simultaneously along the circumferential direction. The regions with higher CRSS become broader. Furthermore, at the edge region of the sample, the variations in CRSS along the

circumferential direction decrease and the four-fold-symmetry distribution pattern on the sample surface becomes weak. This is mainly due to that some crystals has almost reached a saturate level of strain hardening while some crystals still undergoes further hardening, leading to that the difference in CRSS decreases.

After a large torsion deformation of N=2/3 turn is fulfilled, as shown in Fig. 7.5(c), the values of the CRSS illustrate gentle increases over the whole section and there are much higher CRSS values around the periphery of the sample than the center. Compared with the results recorded in Fig. 7.1(c) and Figs. 7.5 (a)-(b), the four-fold-symmetry distribution of the CRSS grows even weaker and could be barely seen on the sample surface at the edge of the sample. Instead, the CRSS tends to be reasonably homogenously distributed along the circumferential direction. This is supposed to be primarily attributed to the gradual expansion of the saturated strain hardening region with increasing torsion deformation in HPT.

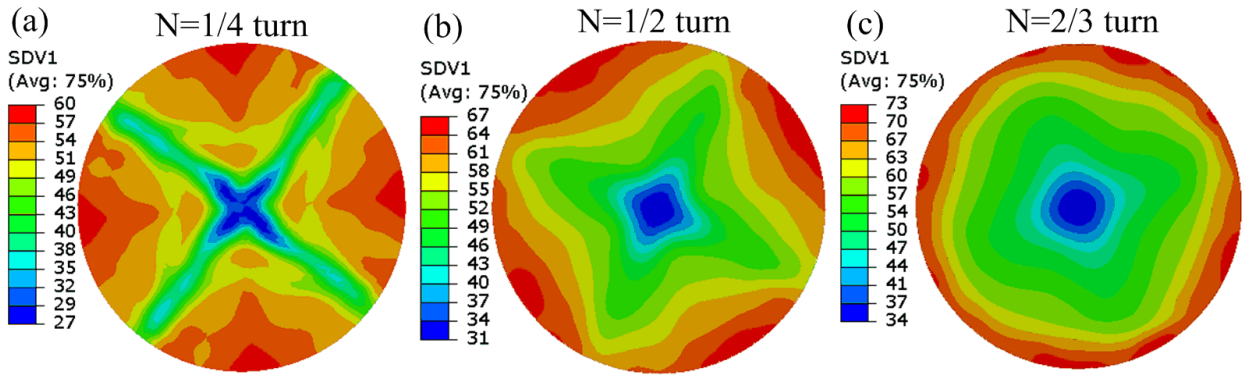

Fig. 7.5 The predicted results of CRSS recorded on the surface of the initial (001) aluminum single crystal after deformed by increasing HPT deformation of (a) N=1/4 turn, (b) N=1/2 turn and (c) N=2/3 turn.

7.4 Texture Evolution with Increasing HPT Deformation

In the un-deformed state, a small region at the edge of the sample was used as a representation to investigate the local texture evolution of the initial (001) aluminium single crystal during the subsequent deformation process. This selected region was located near the top surface on the Y=0 mm section and the coordinates of its center was X=4.5mm, Y=0 mm and Z=0.7 mm. The initial orientation of this region in the local polar coordinate system was

almost Cube orientation, as shown in Fig. 7.6(a). As the sample was deformed continuously by the constantly imposed rotation, the selected region flowed around the torsion axis on the shear plane simulating the changes in crystallographic orientation. The resulting orientations as a function of increasing applied strain predicted by the developed CPFEM model are presented in Fig. 7.6 in terms of {111} pole figures recoded on $\theta - Z$ planes. The horizontal axis and vertical axis of the pole figures represents the local circumferential and axial directions, respectively. The resulting orientations obtained at different strain levels are marked by black dots. The simulated texture will be compared with the ideal torsion texture in the following context. For the convenience of interpretation, the locations of the main torsion texture components on the {111} pole figure are visualized with different symbols. According to Kockss and Jonas[164], an {hkl} <uvw> orientation adopted here signifies that the {hkl} plane coincides with the shear plane and that the <uvw> direction is aligned with the shear direction. The A-type texture fiber are indexed as {111} <uvw>, the B-type fiber as {hkl} <110> and the C orientation as {001} <110>, which is a special position of the B fiber.

The effect of the increased torsion straining on the texture evolution is initially illustrated in Fig. 7.6(b), referring to 30° degrees of HPT deformation, where the developed orientations has rotated significantly away from the initial Cube orientation around the radial axis in an anti-clockwise direction due to the continuous lattice rotations and locate around the position of, according to [144], rotated cube orientation. Moreover, the orientations arranges as steak-like distribution in the pole figure, indicating small variations in the magnitude of lattice rotations between adjacent elements generated in the selected region. This rotated cube orientation is not stable. As the HPT deformation proceeds, the lattices are further rotated to accommodate the increasing plastic deformation. After subjected to 60° degrees of HPT deformation, one can see from Fig. 7.6(c) that the selected region has orientations dominated by C component of the ideal torsion texture which favors the alignment of {001} crystallographic planes with the shear plane and $< 01\bar{1} >$ crystallographic directions with the shear direction. Furthermore, this steak-like distribution is further elongated and becomes even more obvious in Fig. 7.6(c). The developed ideal C orientation is relatively stable. The selected region is capable of maintaining this orientation with increasing HPT deformation and the major orientations begin to initially

move away from it after a sample rotation of 85° (which is not given here). This results is confirmed by the experimental measurements of texture evolution for nickel single crystal during the HPT process recorded in [48], which reported that the C texture component was maintained over a wide range of equivalent strains ranging, indicating a stable orientation. When the sample rotation angles reach 95°, it can be seen from Fig. 7.6(d) that the predicted orientations have rotated away from the ideal C component which could barely be seen in the pole figure. The developed orientations become widely spread at this rotated position and extent somewhat towards the next preferred orientation, leading to a much wider banding distribution of the scattered poles shown in Fig. 7.6(d). The developed orientations keep on rotating with increasing plastic deformation until they reach another preferred orientation after subjected to 110° degrees of sample rotation, as shown in Fig. 7.6(e). This preferred orientation in Fig. 7.6(e) is recognized as the A_2^* component of the ideal torsion texture which aligns the {111} crystallographic planes with the shear plane and the <$11\bar{2}$ > crystallographic directions parallel to the shear direction. The steak-like distribution of the poles could once more be observed in the pole figure. The selected region is able to maintain the ideal A_2^* orientation for a moderate strain range from around 110° to about 125° revolution angles HPT deformation and then begins to deviate from it. As the sample rotation angles increase to 135°, the pole figure in Fig. 7.6(f) shows that some orientations locate close to the ideal A_2^* component while the majority of the predicted orientations have rotated significantly away from it to occupy positions that differ greatly. The resulting poles reveal a fairly scattered distribution in the pole figure of Fig. 7.6(f). After 155° degrees of HPT deformation, the pole figure in Fig. 7.6(g) shows that the resulting orientations are strongly distorted to occupy positions close to different ideal torsion texture components and a preliminary state of the torsion texture has been developed for the selected region at this particular level of straining. The strong ideal torsion texture revealed for the case of shear deformation could be captured in the pole figure of Fig. 7.6(h) where the sample undergoes 180° angles of rotation. As the HPT deformation proceeds to relatively large degrees of 240°, the developed ideal torsion texture in Fig. 7.6(h) becomes weaker and there is tendency for the resulting orientations to be randomly distributed in the pole figure of Fig. 7.6(i). It has to be noted that the results recorded in Figs. 7.6(h)-(i) were

collected from a relatively large section that spreads from the center of the sample to the edge through the whole thickness.

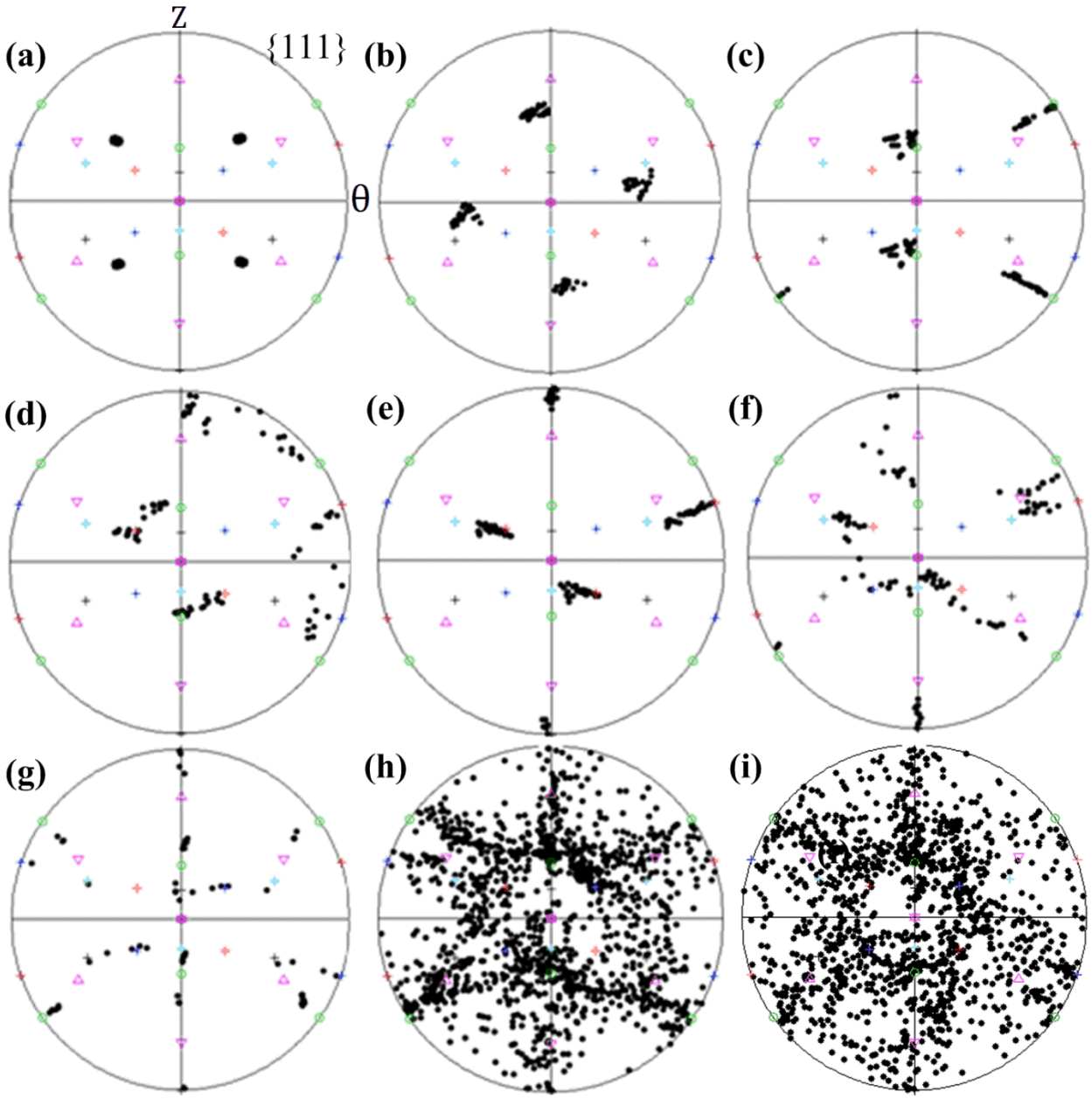

Fig. 7.6 The predicted {111} pole figures of the initial (001) aluminium single crystal as a function of increasing revolution angles HPT deformation of (a) 0°, (b) 30°,(c) 60°, (d) 95°, (e) 110°,(f) 135°, (g) 155°, (h) 180° and (i) 240°.

The results obtained for the evolution of local crystal orientations in the present work are in good coherence with the results that have been published previously for torsion/shear deformation. Rose and Stüwe [271] published experimental results for initially strongly cube oriented textured tubes of copper deformed in torsion process. They have found that the texture was simply rotated with the rigid body rotation. The plastic deformation, however, was not large. Toth and Jonas [272] showed by analytical modeling that in simple shear of Cube orientation the plastic spin was zero so that the orientation change rate was equal to the rigid body rotation rate for any rotated position of the initially cube oriented crystal, therefore the orientation change toke place solely around the sample radial axis. The same result was found in the present work, at least at the imposed rotation angle of the sample by 30°, see Fig. 7.6(b). At this particular position, the Cube orientation was rotated by nearly 60° around the radial axis, which is the axis of the rigid body rotation in HPT. However, for larger strains, the lattice rotation became very different because the rotation did not take place any more simply around the rigid body rotation axis. The crystal orientations differed greatly from the previous rotated cube orientation and then they all rotated progressively into the C component of the ideal orientation of shear textures (see Fig. 7.6(c)). Such a rotation has also been observed and modeled previously by Skorotzki and Toth et al. [144] for a nickel single crystal subjected to one pass ECAP. In that study the nickel single crystal was oriented initially almost like the orientation Fig. 7.6(b) with respect to the imposed deformation, which is mainly simple shear in ECAE. Starting from this orientation, the authors of Ref. [144] have found experimentally that the crystal rotated into the C component. It was also modeled by polycrystal simulations starting with a polycrystal with orientations near to the initial ideal position. The main predicted texture component became the C at large strains. The present study further showed that the C type orientation remained almost unchanged as the sample rotation angles increased from 60° to around 90°, which indicated that the C texture component was a relatively stable orientation in HPT. Our simulation results in Figs 7.6(b)-(d) have already been confirmed in the aforementioned references. Even if those results were obtained for other materials (copper and nickel), they deformed also with the same {111}<110> slip systems, which were used also in the present case of aluminium. For even higher strains, the present study showed that the lattice

restarted the predominant single-sense radial direction lattice rotation and led the orientations rotating close to the next preferred orientation of A_2^* after 110° revolution angles deformation (Fig 7.6(e)). Hafok and Pippan [48] also reported the similar changes of the measured orientations from one preferred crystallographic orientation to another for nickel single crystal during HPT deformation process. Then when further deformed the obvious divergences of the developed orientation occurred, which led to a fairly scattered distribution of the resulting poles in the pole figure (see Figs. 7.6(f)-(g)). For the relatively higher strains of 180° deformation, in a large studied section, the ideal torsion texture typically for FCC metals deformed by shear deformation was formed (Fig 7.6(h)). This is consistent with the experimental observations of many single crystal and polycrystalline materials deformed by HPT deformation to very large strain level [43,44,47,48,52,54]. A further increase in the strain leads to the tendency of gradually weakening of the ideal torsion texture (Fig 7.6(i)), which agrees with the experimental observations by Orlov et al. [49]. They examined the texture evolution of pure aluminium in HPT and found that the texture varied in a systematic manner with increasing strain: The texture was dominated by the orientations belonging mainly to the A fiber during the early stages of deformation. The A fiber was gradually substituted by the C component with increasing strain. With further increase in strain the volume fraction of the C component decreased the texture was found to be weakened and randomized. Moreover, Al-Fadhalah et al. [54] proposed that the stability of the ideal torsion texture at high HPT strains might be periodic in nature so that the ideal torsion texture formed, broke and then reformed , which was caused by the permanent changing of the shear direction during torsion [53].

At the early stage of HPT deformation, from the beginning to around 120° revolution angles, the series of pole figure in Figs. 7.6(a)-(e) reveal that the lattices rotated progressively with respect to the continuously introduced plastic straining, leading to the initial Cube orientation rotated progressively to the rotated cube orientation, and then to the ideal C component, followed by the A_2^* component of the ideal torsion texture. This is a consequence of the different activated slip systems at different stages of HPT deformation, as discussed in Chapter 5. However, at each rotated position, the resulting poles arranged as steak-like or banding shape distributions in their corresponding pole figures, which indicated that the selected region

experienced limited fragmentations throughout the early HPT stage. As the revolution angles realized in the HPT increased further, there was a fairly scattered distribution of the resulting poles in the pole figures in of Figs. 7.6(f)-(g) and a strong ideal torsion texture when a large section was considered (see Fig. 7.6(h). This effect is connected with increasing formation of high angle grain boundaries and the development of grains with significantly different orientations at higher deformation degrees [46], as discussed in Chapter 6. For even higher HPT strains, the developed ideal torsion texture tended to be weakened in Fig. 7.6(i). This is primarily attributed to the gradual transformation from LAGBs to HAGBs, which leads to a greater spread in orientations between neighboring crystallites and the development of overall weaken and randomized texture [51,54].

7.4 Summary

In this chapter, the investigations of plastic deformation behavior along the circumferential direction and the texture evolution of the initial (001) aluminium single crystal during the HPT process using the developed CPFEM model have been performed. The following summaries can be made:

(1) At the early stage of HPT deformation of the initial (001) aluminium single crystal, Mises stress and CRSS were non-homogenous along the circumferential direction and a four-fold-symmetry distribution pattern occurred on the sample surface. Due to the variations in the initial orientation along the circumferential direction of the disk-shaped single crystal, the introduced plastic torsion strain activated different slip systems (dominant slip or multiple slip) at different circumferential positions, which led to differences in lattice rotations and crystallographic orientation changes, and to different mechanical behaviors from position to position along the circumferential direction. This was assumed to be responsible for the development of plastic deformation heterogeneity along the circumferential direction. Such plastic deformation heterogeneity along the circumferential direction could be maintained over a wide strain range in HPT.

(2) For higher strains, the non-homogenous distribution of CRSS along the circumferential direction became weak. This is mainly due to that some crystals has almost reached a saturate level of strain hardening while some crystals undergoes further hardening. For even higher strains, the four-fold-symmetry distribution of the CRSS grew even weaker and could be barely seen on the surface of the sample due to the gradual expansion of the saturated strain hardening region during the HPT process.

(3) At the early stage of HPT deformation, the initial Cube orientation of (001) aluminium single crystal rotated progressively to the rotated cube orientation, and then to the ideal C component, followed by the A_2^* component of the ideal torsion texture, which was a consequence of the different activated slip systems at different stages of HPT deformation. The resulting poles arranged as steak-like or banding shape distributions in their corresponding pole figures. At higher strain levels, apparent divergences of the developed orientation occurred, the resulting orientations were strongly distorted to occupy positions close to different ideal torsion texture components and revealed a fairly scattered distribution in the pole figures. At even higher strain levels, a strong torsion texture was developed in a large studied section and it tended to be weakened as the torsion deformation proceeded.

Chapter 8 Conclusions and Recommendations for Future Work

8.1 Conclusions

In this work, a CPFEM model has been developed to simulate the plastic deformation behavior, texture evolution, and grain refinement of single crystals during the HPT process. It should be noted that the CPFEM simulations of HPT of single crystals have never been conducted. The following conclusions can be drawn:

(1) The 3D FEM model of the HPT process was firstly constructed. Remeshing and mapping solution method of ABAQUS software was adopted to cope with the severe mesh distorsion problem due to heavy deformation in the simulation. It has been proved that the mesh to mesh solution mapping technique could satisfy the requirement of HPT simulation. The evolutions of Mises stress and equivalent strain with increasing HPT deformation were presented. The simulated results agreed well with the experimental measurements.

(2) The crystal plasticity theory and a rate-dependent hardening law were introduced and the procedure of implementing the crystal plasticity constitutive model into the UMAT of the commercial finite element code (ABAQUS) was described. For the first time, the CPFEM model of the full scale HPT process of nickel and aluminium single crystals have been constructed.

(3) Texture evolution of nickel single crystals during the HPT process has been simulated by the developed CPFEM model. The predicted textures results were in good coherence with the previously published experimental measurements. It has been found that, different crystallographic orientations rotated towards different ideal shear texture components with respect to the torsion deformation in HPT. During this process, lattice rotated predominately along the radial direction. While for the initial Cube orientation of (001) nickel single crystal, there were a noticeable amount of rotation angles around the tangential direction and axial

direction. Moreover, lattice did not rotate uniformly during the HPT process, the rotation rate converged when approaching the main components of the ideal shear texture but it diverged while rotated away from the ideal texture components. In addition, for HPT deformation, the material spin was usually larger than other SPD processes due to severe shear deformation. The material spin requirement could be met by either lattice spin or plastic rotation rate. The lattice spin, which is the difference between material spin and plastic rotation rate, was controlled by the plastic rotation rate. Under dominant slip condition, material spin could be mainly or even fully satisfied by plastic rotation rate, and therefore the lattice rotation rate was very small or even dropped to zero, which led to limited orientation change or even stable orientation with increasing HPT deformation. While for multi-slip condition, each of the slip systems of interest could produce a rotation component that resulted in a very small or even zero overall plastic rotation rate, the lattice must rotate to generate large lattice spin in order to satisfy the material spin requirement, which led to significant orientation changes. Dominant slip and multi-slip competed against each other to minimize the total energy consumed in the system, which is responsible for texture evolution of nickel single crystal during the HPT process.

(4) Grain refinement behaviors of the nickel single crystal during the HPT process have been simulated by the developed CPFEM model. The predicted grain maps were capable of reflecting the prominent characteristics associated with grain refinement during the HPT process. The simulation results of the local texture development on the interested cut plane were in good coherence with the previously published experimental observations of single crystal and polycrystalline materials deformed by HPT. It has been found that there were mainly two reasons which were responsible for the grain fragmentation of the nickel single crystal: one was the difference in lattice rotation rate along the radial direction, which is the direction of predominant lattice rotation in HPT. The occurrence of divergence in R-axis rotation rate was because the lattice did not rotate uniformly with respect to the shear deformation in HPT; another one was the divergence of rotation angles along the tangential direction, even if much smaller than the R-axis rotations, could also contribute to the formation of grains with significantly different orientations.

(5) Plastic deformation behavior along the circumferential direction of the initial (001) aluminum single crystals at the early stage of HPT processing and its evolution with increasing HPT deformation have been simulated by the developed CPFEM model. It has been found, at the early stage of HPT process, Mises stress and CRSS were not homogenously distributed along the circumferential direction and a four-fold-symmetry distribution pattern could be observed on the sample surface. Because of the variations in the initial orientation along the circumferential direction, the introduced plastic torsion strain activated different slip systems at different tangential positions. Tangential positions deformed by different slip modes resulted in differences in lattice rotations and crystallographic orientation changes and showed different mechanical behaviors, which was assumed to be responsible for the development of plastic anisotropy on the sample surface. For higher strains, the non-homogenous distribution of CRSS along the circumferential direction became weak. This was mainly due to that some crystals has almost reached a saturate level of strain hardening while some crystals underwent further hardening. For even higher strains, such a heterogeneous distribution of the CRSS grew even weaker due to the gradual expansion of the saturated strain hardening region during the HPT process.

8.2 Recommendations for Future Work

The following investigations are recommended to be conducted to continue the research from this work.

(1) More experimental measurements of microstructure and microtexture evolution of nickel and aluminum single crystals with increasing HPT deformation need to be conducted. Further experimental validation for the CPFEM simulations needs to be carried out.
(2) The influencing factors, such as, sample dimension, frictional condition, structure elements and size, applied pressure, torsional rate and direction need to be examined by more CPFEM simulations and discussed in detail.
(3) The experiments and simulations of the bi-crystals poly-crystals during the HPT process considering the initial crystallographic orientations of the component grains need to be

carried out to investigate in depth the influence of grain boundaries with different initial orientations on the deformation behaviors during the HPT process.

(4) The CPFEM model has been proved to be a very effective and powerful tool to simulate the various plastic deformation behaviors of FCC structured materials during the HPT process in this work. It is strongly recommended that the CPFEM simulations of the HPT processes of BCC and HCP materials need to be conducted. The other deformation mechanism such as twinning needs to be considered in the crystal plasticity theory in order to accurately simulate the deformation of the BCC/HCP materials.

References

[1] Valiev RZ, Islamgaliev RK, Alexandrov I V. Bulk nanostructured materials from severe plastic deformation. Prog Mater Sci 2000;45:103–89.

[2] Verlinden B, Leuven KU, Engineering M. SEVERE PLASTIC DEFORMATION OF METALS. Metal J Metall 2004:165–82.

[3] Azushima a., Kopp R, Korhonen a., Yang DY, Micari F, Lahoti GD, et al. Severe plastic deformation (SPD) processes for metals. CIRP Ann - Manuf Technol 2008;57:716–35.

[4] Estrin Y, Vinogradov a. Extreme grain refinement by severe plastic deformation: A wealth of challenging science. Acta Mater 2013;61:782–817.

[5] Langdon TG. Twenty-five years of ultrafine-grained materials: Achieving exceptional properties through grain refinement. Acta Mater 2013;61:7035–59.

[6] Segal VM. Equal channel angular extrusion: from macromechanics to structure formation. Mater Sci Eng A 1999;271:322–33.

[7] Segal VM. Engineering and commercialization of equal channel angular extrusion (ECAE). Mater Sci Eng A 2004;386:269–76.

[8] Valiev RZ, Langdon TG. Principles of equal-channel angular pressing as a processing tool for grain refinement. Prog Mater Sci 2006;51:881–981.

[9] Segal VM. Equal channel angular extrusion of flat products. Mater Sci Eng A 2008;476:178–85.

[10] Pippan R, Scheriau S, Hohenwarter A, Hafok M. Advantages and limitations of HPT : a review. Mater Sci Forum Vols 2008;586:16–21.

[11] Zhilyaev a, Langdon T. Using high-pressure torsion for metal processing: Fundamentals and applications. Prog Mater Sci 2008;53:893–979.

[12] Pippan R, Scheriau S, Taylor a., Hafok M, Hohenwarter a., Bachmaier a. Saturation of Fragmentation During Severe Plastic Deformation. Annu Rev Mater Res 2010;40:319–43.

[13] Edalati K, Horita Z. High-pressure torsion of pure metals: Influence of atomic bond parameters and stacking fault energy on grain size and correlation with hardness. Acta Mater 2011;59:6831–6.

[14] Kawasaki M, Figueiredo RB, Langdon TG. Twenty-five years of severe plastic deformation: recent developments in evaluating the degree of homogeneity through the thickness of disks processed by high-pressure torsion. J Mater Sci 2012.

[15] Saito Y, Tsuji N, Utsunomiya H, Sakai T, Hong RG. Ultra-fine grained bulk aluminum produced by accumulative roll-bonding (ARB) process. Scr Mater 1998;39:1221–7.

[16] Lee S-H, Sakai T, Saito Y, Utsunomiya H, Tsuji N. Strengthening of sheath-rolled aluminum based MMC by the ARB process. Mater Trans JIM 1999;40:1422–8.

[17] Krallics G, Lenard JG. An examination of the accumulative roll-bonding process. J Mater Process Technol 2004;152:154–61.

[18] Lu C, Tieu K, Wexler D. Significant enhancement of bond strength in the accumulative roll bonding process using nano-sized SiO2 particles. J Mater Process Technol 2009;209:4830–4.

[19] Reza Toroghinejad M, Ashrafizadeh F, Jamaati R. On the use of accumulative roll bonding process to develop nanostructured aluminum alloy 5083. Mater Sci Eng A 2013;561:145–51.

[20] Zhilyaev a. ., Lee S, Nurislamova G., Valiev R., Langdon T. Microhardness and microstructural evolution in pure nickel during high-pressure torsion. Scr Mater 2001;44:2753–8.

[21] Horita Z, Langdon TG. Microstructures and microhardness of an aluminum alloy and pure copper after processing by high-pressure torsion. Mater Sci Eng A 2005;410-411:422–5.

[22] Yang Z, Welzel U. Microstructure–microhardness relation of nanostructured Ni produced by high-pressure torsion. Mater Lett 2005;59:3406–9.

[23] Concustell a., Sort J, Woodcock TG, Gimazov a., Suriñach S, Gebert a., et al. Enhanced microhardness in nanocomposite Ti60Cu14Ni12Sn4Ta10 processed by high pressure torsion. Intermetallics 2006;14:871–5.

[24] Xu C, Horita Z, Langdon TG. The evolution of homogeneity in processing by high-pressure torsion 2007;55:203–12.

[25] Zhilyaev a. P, Swaminathan S, Gimazov a. a., McNelley TR, Langdon TG. An evaluation of microstructure and microhardness in copper subjected to ultra-high strains. J Mater Sci 2008;43:7451–6.

[26] Xu C, Horita Z, Langdon TG. The evolution of homogeneity in an aluminum alloy processed using high-pressure torsion. Acta Mater 2008;56:5168–76.

[27] Xu C, Langdon TG. Three-dimensional representations of hardness distributions after processing by high-pressure torsion. Mater Sci Eng A 2009;503:71–4.

[28] Kawasaki M, Figueiredo RB, Langdon TG. An investigation of hardness homogeneity throughout disks processed by high-pressure torsion. Acta Mater 2011;59:308–16.

[29] Kawasaki M, Alhajeri SN, Xu C, Langdon TG. The development of hardness homogeneity in pure aluminum and aluminum alloy disks processed by high-pressure torsion. Mater Sci Eng A 2011;529:345–51.

[30] Jiang H, Zhu YT, Butt DP, Alexandrov I V, Lowe TC. Microstructural evolution, microhardness and thermal stability of HPT-processed Cu. Mater Sci Eng A 2000;290:128–38.

[31] Zhilyaev a. ., Nurislamova G., Kim B-K, Baró M., Szpunar J., Langdon T. Experimental parameters influencing grain refinement and microstructural evolution during high-pressure torsion. Acta Mater 2003;51:753–65.

[32] Sort J, Zhilyaev a, Zielinska M, Nogués J, Suriñach S, Thibault J, et al. Microstructural effects and large microhardness in cobalt processed by high pressure torsion consolidation of ball milled powders. Acta Mater 2003;51:6385–93.

[33] Kužel R, Matěj Z, Cherkaska V, Pešička J, ČíŽek J, Procházka I, et al. Structural investigations of submicrocrystalline metals obtained by high-pressure torsion deformation. J Alloys Compd 2004;378:242–7.

[34] Zhilyaev a. P, Oh-ishi K, Langdon TG, McNelley TR. Microstructural evolution in commercial purity aluminum during high-pressure torsion. Mater Sci Eng A 2005;410-411:277–80.

[35] Zhilyaev a. P, Gimazov a. a., Soshnikova EP, Révész Á, Langdon TG. Microstructural characteristics of nickel processed to ultrahigh strains by high-pressure torsion. Mater Sci Eng A 2008;489:207–12.

[36] Lugo N, Llorca N, Cabrera JM, Horita Z. Microstructures and mechanical properties of pure copper deformed severely by equal-channel angular pressing and high pressure torsion. Mater Sci Eng A 2008;477:366–71.

[37] Balogh L, Ungár T, Zhao Y, Zhu YT, Horita Z, Xu C, et al. Influence of stacking-fault energy on microstructural characteristics of ultrafine-grain copper and copper–zinc alloys. Acta Mater 2008;56:809–20.

[38] Zhang HW, Huang X, Hansen N. Evolution of microstructural parameters and flow stresses toward limits in nickel deformed to ultra-high strains. Acta Mater 2008;56:5451–65.

[39] Wang YB, Louie M, Cao Y, Liao XZ, Li HJ, Ringer SP, et al. High-pressure torsion induced microstructural evolution in a hexagonal close-packed Zr alloy. Scr Mater 2010;62:214–7.

[40] Kawasaki M, Ahn B, Langdon TG. Microstructural evolution in a two-phase alloy processed by high-pressure torsion. Acta Mater 2010;58:919–30.

[41] Wongsa-Ngam J, Kawasaki M, Zhao Y, Langdon TG. Microstructural evolution and mechanical properties of a Cu–Zr alloy processed by high-pressure torsion. Mater Sci Eng A 2011;528:7715–22.

[42] Tian YZ, Li JJ, Zhang P, Wu SD, Zhang ZF, Kawasaki M, et al. Microstructures, strengthening mechanisms and fracture behavior of Cu–Ag alloys processed by high-pressure torsion. Acta Mater 2012;60:269–81.

[43] Alexandrov I V., Dubravina A a., Kilmametov AR, Kazykhanov VU, Valiev RZ. Textures in nanostructured metals processed by severe plastic deformation. Met Mater Int 2003;9:151–6.

[44] Zhilyaev AP, Baró MD, Langdon TG, Mcnelley TR. AN EXAMINATION OF MICROTEXTURE AND MICROSTRUCTURE IN ULTRAFINE-GRAINED NICKEL. RevAdvMaterSci 2004;7:41–9.

[45] Zhilyaev AP, Kim B-K, Szpunar J a., Baró MD, Langdon TG. The microstructural characteristics of ultrafine-grained nickel. Mater Sci Eng A 2005;391:377–89.

[46] Alexandrov I V, Zhilina M V, Bonarski JT. Formation of texture inhomogeneity in severely plastically deformed copper 2006;54.

[47] Zhilyaev a. P, McNelley TR, Langdon TG. Evolution of microstructure and microtexture in fcc metals during high-pressure torsion. J Mater Sci 2006;42:1517–28.

[48] Hafok M, Pippan R. High-pressure torsion applied to nickel single crystals. Philos Mag 2008;88:1857–77.

[49] Orlov D, Bhattacharjee PP, Todaka Y, Umemoto M, Tsuji N. Texture evolution in pure aluminum subjected to monotonous and reversal straining in high-pressure torsion. Scr Mater 2009;60:893–6.

[50] Chulist R, Skrotzki W, Oertel C-G, Böhm a., Lippmann T, Rybacki E. Microstructure and texture in Ni50Mn29Ga21 deformed by high-pressure torsion. Scr Mater 2010;62:650–3.

[51] Dopita M, Janeček M, Kužel R, Seifert HJ, Dobatkin S. Microstructure evolution of CuZr polycrystals processed by high-pressure torsion. J Mater Sci 2010;45:4631–44.

[52] Arzaghi M, Fundenberger JJ, Toth LS, Arruffat R, Faure L, Beausir B, et al. Microstructure, texture and mechanical properties of aluminum processed by high-pressure tube twisting. Acta Mater 2012;60:4393–408.

[53] Korznikova E a., Mironov SY, Korznikov a. V, Zhilyaev a. P, Langdon TG. Microstructural evolution and electro-resistivity in HPT nickel. Mater Sci Eng A 2012;556:437–45.

[54] Al-Fadhalah KJ, Alhajeri SN, Almazrouee AI, Langdon TG. Microstructure and microtexture in pure copper processed by high-pressure torsion. J Mater Sci 2013;48:4563–72.

[55] Huang Y, Figueiredo RB, Baudin T, Helbert A-L, Brisset F, Langdon TG. Microstructure and texture evolution in a magnesium alloy during processing by high-pressure torsion. Mater Res 2013;16:577–85.

[56] Khereddine AY, Hadj Larbi F, Azzeddine H, Baudin T, Brisset F, Helbert A-L, et al. Microstructures and textures of a Cu–Ni–Si alloy processed by high-pressure torsion. J Alloys Compd 2013;574:361–7.

[57] Islamgaliev RK, Sitdikov VD, Nesterov KM, Pankratov DL. STRUCTURE AND CRYSTALLOGRAPHIC TEXTURE IN THE Cu-Cr-Ag ALLOY SUBJECTED TO SEVERE PLASTIC DEFORMATION 2014;39.

[58] Kim HS. Finite element analysis of high pressure torsion processing. J Mater Process Technol 2001;113:617–21.

[59] Kim HS, Hong SI, Lee YS, Dubravina A a., Alexandrov I V. Deformation behavior of copper during a high pressure torsion process. J Mater Process Technol 2003;142:334–7.

[60] Yoon SC, Horita Z, Kim HS. Finite element analysis of plastic deformation behavior during high pressure torsion processing. J Mater Process Technol 2008;201:32–6.

[61] Rosochowski A, Olejnik L. Finite element simulation of severe plastic deformation processes. Proc Inst Mech Eng Part L J Mater Des Appl 2007;221:187–96.

[62] Lapovok R, Pougis a., Lemiale V, Orlov D, Toth LS, Estrin Y. Severe plastic deformation processes for thin samples. J Mater Sci 2010;45:4554–60.

[63] Figueiredo RB, Cetlin PR, Langdon TG. Using finite element modeling to examine the flow processes in quasi-constrained high-pressure torsion. Mater Sci Eng A 2011;528:8198–204.

[64] Figueiredo RB, Pereira PHR, Aguilar MTP, Cetlin PR, Langdon TG. Using finite element modeling to examine the temperature distribution in quasi-constrained high-pressure torsion. Acta Mater 2012;60:3190–8.

[65] Figueiredo RB, Aguilar MTP, Cetlin PR, Langdon TG. Analysis of plastic flow during high-pressure torsion. J Mater Sci 2012;47:7807–14.

[66] Draï A, Aour B. Analysis of plastic deformation behavior of HDPE during high pressure torsion process. Eng Struct 2013;46:87–93.

[67] Verleysen P, Abeele F Van Den, Degrieck J. Numerical Simulation of Severe Plastic Deformation during High Pressure Torsion Processing. 2013 SIMULIA Community Conf 2013:1–9.

[68] Song Y, Wang W, Gao D, Yoon EY, Lee DJ, Kim HS. Finite element analysis of the effect of friction in high pressure torsion. Met Mater Int 2014;20:445–50.

[69] Estrin Y, Molotnikov a, Davies C, Lapovok R. Strain gradient plasticity modelling of high-pressure torsion. J Mech Phys Solids 2008;56:1186–202.

[70] Kratochvil J, Kruzik M, Sedlacek R. A model of ultrafine microstructure evolution in materials deformed by high-pressure torsion. Acta Mater 2009;57:739–48.

[71] Kratochvil J, Kruzik M, Sedlacek R. Model of structural fragmentation induced by high pressure torsion. RevAdvMaterSci 2010;25:88–98.

[72] Lee DJ, Yoon EY, Park LJ, Kim HS. The dead metal zone in high-pressure torsion. Scr Mater 2012;67:384–7.

[73] Lee DJ, Yoon EY, Ahn D-H, Park BH, Park HW, Park LJ, et al. Dislocation density-based finite element analysis of large strain deformation behavior of copper under high-pressure torsion. Acta Mater 2014;76:281–93.

[74] Wenk H-R, Houtte P Van. Texture and anisotropy. Reports Prog Phys 2004;67:1367–428.

[75] Tian YZ, Wu SD, Zhang ZF, Figueiredo RB, Gao N, Langdon TG. Comparison of microstructures and mechanical properties of a Cu–Ag alloy processed using different severe plastic deformation modes. Mater Sci Eng A 2011;528:4331–6.

[76] Tian YZ, Wu SD, Zhang ZF, Figueiredo RB, Gao N, Langdon TG. Microstructural evolution and mechanical properties of a two-phase Cu–Ag alloy processed by high-pressure torsion to ultrahigh strains. Acta Mater 2011;59:2783–96.

[77] Wei Q, Pan ZL, Wu XL, Schuster BE, Kecskes LJ, Valiev RZ. Microstructure and mechanical properties at different length scales and strain rates of nanocrystalline tantalum produced by high-pressure torsion. Acta Mater 2011;59:2423–36.

[78] Sakai G, Horita Z, Langdon TG. Grain refinement and superplasticity in an aluminum alloy processed by high-pressure torsion. Mater Sci Eng A 2005;393:344–51.

[79] Kai M, Horita Z, Langdon TG. Developing grain refinement and superplasticity in a magnesium alloy processed by high-pressure torsion. Mater Sci Eng A 2008;488:117–24.

[80] Kawasaki M, Langdon TG. Developing superplasticity and a deformation mechanism map for the Zn–Al eutectoid alloy processed by high-pressure torsion. Mater Sci Eng A 2011;528:6140–5.

[81] Kim H-K, Choi M-I, Chung C-S, Shin DH. Fatigue properties of ultrafine grained low carbon steel produced by equal channel angular pressing. Mater Sci Eng A 2003;340:243–50.

[82] Kunz L, Lukáš P, Svoboda M. Fatigue strength, microstructural stability and strain localization in ultrafine-grained copper. Mater Sci Eng A 2006;424:97–104.

[83] Balyanov a. Corrosion resistance of ultra fine-grained Ti. Scr Mater 2004;51:225–9.

[84] Ivanisenko Y, Lojkowski W, Valiev RZ, Fecht H-J. The mechanism of formation of nanostructure and dissolution of cementite in a pearlitic steel during high pressure torsion. Acta Mater 2003;51:5555–70.

[85] Hebesberger T, Stüwe HP, Vorhauer a., Wetscher F, Pippan R. Structure of Cu deformed by high pressure torsion. Acta Mater 2005;53:393–402.

[86] Xu C, Horita Z, Langdon T. The evolution of homogeneity in processing by high-pressure torsion. Acta Mater 2007;55:203–12.

[87] Edalati K, Fujioka T, Horita Z. Microstructure and mechanical properties of pure Cu processed by high-pressure torsion. Mater Sci Eng A 2008;497:168–73.

[88] Edalati K, Yamamoto A, Horita Z, Ishihara T. High-pressure torsion of pure magnesium: Evolution of mechanical properties, microstructures and hydrogen storage capacity with equivalent strain. Scr Mater 2011;64:880–3.

[89] Valiev RZ, Korznikov a. V, Mulyukov RR. Structure and properties of ultrafine-grained materials produced by severe plastic deformation. Mater Sci Eng A 1993;168:141–8.

[90] Segal VM. Materials processing by simple shear. Mater Sci Eng A 1995;197:157–64.

[91] Iwahashi Y, Wang J, Horita Z, Nemoto M, Langdon TG. PRINCIPLE OF EQUAL-CHANNEL ANGULAR PEESSING FOR THE PROCESSING OF ULTRA-FINE GRAINED MATERIALS 1996;35:143–6.

[92] Langdon TG. Influence of Pressing Speed on Microstructural Development in Equal-Channel Angular Pressing 1999;30:1989–97.

[93] Nakashima K, Horita Z, Nemoto M, Langdon TG. Development of a multi-pass facility for equal-channel angular pressing to high total strains. Mater Sci Eng A 2000;281:82–7.

[94] Segal VM. Slip line solutions, deformation mode and loading history during equal channel angular extrusion. Mater Sci Eng A 2003;345:36–46.

[95] VALIEV R. Nanostructuring of metals by severe plastic deformation for advanced properties. Nat Mater 2004;3:511–6.

[96] Beyerlein IJ, Tóth LS. Texture evolution in equal-channel angular extrusion. Prog Mater Sci 2009;54:427–510.

[97] Segal VM. Mechanics of continuous equal-channel angular extrusion. J Mater Process Technol 2010;210:542–9.

[98] Xu C, Horita Z, Langdon TG. Microstructural evolution in an aluminum solid solution alloy processed by ECAP. Mater Sci Eng A 2011;528:6059–65.

[99] Saito Y, Utsunomiya H, Tsuji N, Sakai T. NOVEL ULTRA-HIGH STRAINING PROCESS FOR BULK MATERIALSÐDEVELOPMENT OF THE ACCUMULATIVE ROLL-BONDING (ARB) PROCESS 1999;47.

[100] Zhu Y, Valiev RZ, Langdon TG, Tsuji N, Lu K. Processing of nanostructured metals and alloys via plastic deformation 2010;35:977–82.

[101] Hausöl T, Maier V, Schmidt CW, Winkler M, Höppel HW, Göken M. Tailoring Materials Properties by Accumulative Roll Bonding. Adv Eng Mater 2010;12:740–6.

[102] Su L. Microstructure, texture and vacancy-type defects in severe plastic deformed aluminum alloys. University of Wollongong, Australia, 2012.

[103] Takayama a., Yang X, Miura H, Sakai T. Continuous static recrystallization in ultrafine-grained copper processed by multi-directional forging. Mater Sci Eng A 2008;478:221–8.

[104] Nakao Y, Miura H. Nano-grain evolution in austenitic stainless steel during multi-directional forging. Mater Sci Eng A 2011;528:1310–7.

[105] Miura H, Yu G, Yang X. Multi-directional forging of AZ61Mg alloy under decreasing temperature conditions and improvement of its mechanical properties. Mater Sci Eng A 2011;528:6981–92.

[106] Beygelzimer Y, Varyukhin V, Synkov S, Orlov D. Useful properties of twist extrusion. Mater Sci Eng A 2009;503:14–7.

[107] Beygelzimer Y, Prilepo D, Kulagin R, Grishaev V, Abramova O, Varyukhin V, et al. Planar Twist Extrusion versus Twist Extrusion. J Mater Process Technol 2011;211:522–9.

[108] Kulagin R, Latypov MI, Kim HS, Varyukhin V, Beygelzimer Y. Cross Flow During Twist Extrusion: Theory, Experiment, and Application. Metall Mater Trans A 2013;44:3211–20.

[109] Orlov D, Beygelzimer Y, Synkov S, Varyukhin V, Tsuji N, Horita Z. Plastic flow, structure and mechanical properties in pure Al deformed by twist extrusion. Mater Sci Eng A 2009;519:105–11.

[110] Toth L, Arzaghi M, Fundenberger J, Beausir B, Bouaziz O, Arruffatmassion R. Severe plastic deformation of metals by high-pressure tube twisting. Scr Mater 2009;60:175–7.

[111] Wang JT, Li Z, Wang J, Langdon TG. Principles of severe plastic deformation using tube high-pressure shearing. Scr Mater 2012;67:810–3.

[112] Fonda RW, Wert J a., Reynolds a. P, Tang W. Friction stir welding of single crystal aluminium. Sci Technol Weld Join 2007;12:304–10.

[113] Shibayanagi T, Gerlich AP, Kashihara K, North TH. Textures in Single-Crystal Aluminum Friction Stir Spot Welds. Metall Mater Trans A 2009;40:920–31.

[114] Mishra RS, Ma ZY. Friction stir welding and processing. Mater Sci Eng R Reports 2005;50:1–78.

[115] Zhang YN, Cao X, Larose S, Wanjara P. Review of tools for friction stir welding and processing. Can Metall Q 2012;51:250–61.

[116] Liu HJ, Li JQ, Duan WJ. Friction stir welding characteristics of 2219-T6 aluminum alloy assisted by external non-rotational shoulder. Int J Adv Manuf Technol 2012;64:1685–94.

[117] Nishida Y, Arima H, Kim J. Rotary-die equal-channel angular pressing of an Al ± 7 mass % Si ± 0 . 35 mass % Mg alloy. Scr Mater 2001;45:261–6.

[118] Richert M, Liu Q, Hansen N. Microstructural evolution over a large strain range in aluminium deformed by cyclic-extrusion–compression. Mater Sci Eng A 1999;260:275–83.

[119] Peng T, Wang QD, Lin JB. Microstructure and mechanical properties of Mg–10Gd–2Y–0.5Zr alloy recycled by cyclic extrusion compression. Mater Sci Eng A 2009;516:23–30.

[120] Zaharia L, Chelariu R, Comaneci R. Multiple direct extrusion: A new technique in grain refinement. Mater Sci Eng A 2012;550:293–9.

[121] Farhoumand a, Khoddam S, Hodgson PD. A study of plastic deformation during axisymmetric forward spiral extrusion and its subsequent mechanical property changes. Model Simul Mater Sci Eng 2012;20:085005.

[122] Pardis N, Ebrahimi R. Deformation behavior in Simple Shear Extrusion (SSE) as a new severe plastic deformation technique. Mater Sci Eng A 2009;527:355–60.

[123] Pardis N, Ebrahimi R. Different processing routes for deformation via simple shear extrusion (SSE). Mater Sci Eng A 2010;527:6153–6.

[124] Tork NB, Pardis N, Ebrahimi R. Investigation on the feasibility of room temperature plastic deformation of pure magnesium by simple shear extrusion process. Mater Sci Eng A 2013;560:34–9.

[125] Bridgman PW. On Torsion Combined with Compression. J Appl Phys 1943;14:273–83.

[126] S. Erbel. Mechanical Properties and Structure of Extremely Strain-hardened Copper. Met Technol 1979;6:482–6.

[127] Valiev RZ, Krasiinikov NA, Tsenev NK. Plastic deformation of alloys with submicron-grained structure 1991;137:35–40.

[128] Valiev RZ. Structure and mechanical properties of ultrafine-grained metals 1997;234-236:59–66.

[129] VALIEV R. Nanostructuring of metals by severe plastic deformation for advanced properties. Nat Mater 2004.

[130] Zhilyaev AP, Oh-ishi K, Langdon TG, McNelley TR. Microstructural evolution in commercial purity aluminum during high-pressure torsion. Mater Sci Eng A 2005;410-411:277–80.

[131] Wetscher F, Vorhauer a., Stock R, Pippan R. Structural refinement of low alloyed steels during severe plastic deformation. Mater Sci Eng A 2004;387-389:809–16.

[132] Ito Y, Horita Z. Microstructural evolution in pure aluminum processed by high-pressure torsion. Mater Sci Eng A 2009;503:32–6.

[133] Nationale E, Grenoble P De. STRUCTURE AND DEFORMATON BEHAVIOUR OF ARMCO IRON SUBJECTED TO SEVERE PLASTIC DEFORMATION 1996;44.

[134] An XH, Wu SD, Zhang ZF, Figueiredo RB, Gao N, Langdon TG. Evolution of microstructural homogeneity in copper processed by high-pressure torsion. Scr Mater 2010;63:560–3.

[135] Zhilyaev AP, Nurislamova G V, Baro MD, Szpunar JA, Langdon TG. Experimental parameters influencing grain refinement and microstructural evolution during high-pressure torsion 2003;51:753–65.

[136] Vorhauer a., Pippan R. On the homogeneity of deformation by high pressure torsion. Scr Mater 2004;51:921–5.

[137] Xu C, Horita Z, Langdon TG. Evaluating the influence of pressure and torsional strain on processing by high-pressure torsion. J Mater Sci 2008;43:7286–92.

[138] Kawasaki M, Ahn B, Langdon TG. Effect of strain reversals on the processing of high-purity aluminum by high-pressure torsion. J Mater Sci 2010;45:4583–93.

[139] Xu C, Horita Z, Langdon TG. Microstructural Evolution in Pure Aluminum in the Early Stages of Processing by High-Pressure Torsion. Mater Trans 2010;51:2–7.

[140] Orlov D, Kamikawa N, Tsuji N. High pressure torsion to refine grains in pure aluminum up to saturation : mechanisms of structure evolution and their dependence on strain 2012:37–41.

[141] Zhilyaev a. P, Kim B-K, Nurislamova GV, Baró MD, Szpunar J a., Langdon TG. Orientation imaging microscopy of ultrafine-grained nickel. Scr Mater 2002;46:575–80.

[142] Fukuda Y, Oh-ishi K, Furukawa M, Horita Z, Langdon TG. The application of equal-channel angular pressing to an aluminum single crystal. Acta Mater 2004;52:1387–95.

[143] Miyamoto H, Erb U, Koyama T, Mimaki T, Hashimoto S, City O. Microstructure and texture development of copper single crystals deformed by equal-channel angular pressing 2006:37–41.

[144] Skrotzki W, Tóth LS, Klöden B, Brokmeier H-G, Arruffat-Massion R. Texture after ECAP of a cube-oriented Ni single crystal. Acta Mater 2008;56:3439–49.

[145] Goran D. Local texture and microstructure in cube-oriented nickel single crystal deformed by equal channel angular extrusion 2011:37–41.

[146] M.Hafok, A.Vorhasuer, Keckes J, R.Pippan. HPT deformation single crystal copper and nickle.pdf. Mater Sci Forum Sci 2006;503-504:621–6.

[147] M.Hafok, R.Pippan. Comparison of single crystal and polycrystal of nickle.pdf. Mater Sci Forum 2007;550:277–82.

[148] Nazarov a. a., Shenderova O a., Brenner DW. On the disclination-structural unit model of grain boundaries. Mater Sci Eng A 2000;281:148–55.

[149] Hurtado J a., Elliott BR, Shodja HM, Gorelikov DV, Campbell CE, Lippard HE, et al. Disclination grain boundary model with plastic deformation by dislocations. Mater Sci Eng A 1995;190:1–7.

[150] Ivanisenko Y, Valiev RZ, Fecht H-J. Grain boundary statistics in nano-structured iron produced by high pressure torsion. Mater Sci Eng A 2005;390:159–65.

[151] Hafok M, Pippan R. Post-shear deformation of high pressure torsion-deformed nickel under hydrostatic pressure 2007;56:757–60.

[152] Pippan R, Scheriau S, Taylor a., Hafok M, Hohenwarter a., Bachmaier a. Saturation of Fragmentation During Severe Plastic Deformation. Annu Rev Mater Res 2010;40:319–43.

[153] Barnett MR, Montheillet F. The generation of new high-angle boundaries in aluminium during hot torsion 2002;50:2285–96.

[154] Vinogradov a, Hashimoto S, Patlan V, Kitagawa K. Atomic force microscopic study on surface morphology of ultra-fine grained materials after tensile testing. Mater Sci Eng A 2001;319-321:862–6.

[155] Krasilnikov N, Lojkowski W, Pakiela Z, Valiev R. Tensile strength and ductility of ultra-fine-grained nickel processed by severe plastic deformation. Mater Sci Eng A 2005;397:330–7.

[156] Chinh NQ, Szommer P, Csanádi T, Langdon TG. Flow processes at low temperatures in ultrafine-grained aluminum. Mater Sci Eng A 2006;434:326–34.

[157] Sevillano JG, Leuven KU. LARGE STRAIN WORK HARDENING AND TEXTURES. Prog Mater Sci 1981;25:59–412.

[158] Laboratories SN, Ni D. EVOLUTION OF F . C . C . D E F O R M A T I O N STRUCTURES IN POLYSLIP. Acta Metall 1992;40:205–19.

[159] Hughes DA. HIGH ANGLE BOUNDARIES FORMED BY GRAIN SUBDIVISION MECHANISMS 1997;45:3871–86.

[160] Wetscher F, Vorhauer a., Pippan R. Strain hardening during high pressure torsion deformation. Mater Sci Eng A 2005;410-411:213–6.

[161] Hughes D a., Lebensohn R a., Wenk HR, Kumar a. Stacking fault energy and microstructure effects on torsion texture evolution. Proc R Soc A Math Phys Eng Sci 2000;456:921–53.

[162] Tsutsui K, Kume Y, Kobashi M, Kanetake N. Effect of processing temperature on microstructure of AZ61 magnesium alloy produced by compressive torsion processing. J Japan Inst Light Met 2009;59:35–40.

[163] Introduction to Texture Analysis: Macrotexture, Microtexture and Orientation Mapping-Second Edition, n.d.

[164] Kocks UF, Jonas JJ. THEORY TEXTURE DEVELOPMENT. Acta Metall 1984;32:211–26.

[165] Montheillet F. AXIAL STRESSES AND TEXTURE DEVELOPMENT Al , Cu AND a-Fe 1984;32:2077–89.

[166] Tóth LS, Gilormini P, Jonas JJ. EFFECT OF RATE SENSITIVITY ON THE stability of torsion texture. Acta Metall 1988;36:3077–91.

[167] Tóth LS, Neale KW, Jonas JJ. Stress response and persistence characteristics of the ideal orientations of shear textures. Acta Metall 1989;37:2197–210.

[168] Neale KW, Tóth LS, Jonas JJ. LARGE STRAIN SHEAR AND TORSION OF RATE-SENSITIVE FCC POLYCRYSTALS. Int J Plast 1990;6:45–61.

[169] Tóth LS, Jonas JJ, Daniel D, Bailey J a. Texture Development and Length Changes in Copper Bars Subjected to Free End Torsion. Textures Microstruct 1992;19:245–62.

[170] Havner K. Length changes during free end torsion: a rate sensitive analysis l.s. 1990;6:83–108.

[171] Britain G, Engineering M. Modelling the length changes that take place during torsion testing j. j. jonas 1993;35.

[172] Zhang HW, Huang X, Pippan R, Hansen N. Thermal behavior of Ni (99.967% and 99.5% purity) deformed to an ultra-high strain by high pressure torsion. Acta Mater 2010;58:1698–707.

[173] Bonarski BJ, Schafler E, Mingler B, Skrotzki W, Mikulowski B, Zehetbauer MJ. Texture evolution of Mg during high-pressure torsion. J Mater Sci 2008;43:7513–8.

[174] Sitdikov V, Alexandrov I. TEXTURE ANALYSIS OF - PHASE Ti SUBJECTED TO HIGH PRESSURE TORSION 2012:85–9.

[175] Skrotzki W, Klöden B, Tamm R, Oertel C-G, Garbe U, Rybacki E. Torsion Texture Measurements With High-Energy Synchrotron Radiation on NiAl. Textures Microstruct 2003;35:163–73.

[176] Cao GH, Klöden B, Rybacki E, Oertel C-G, Skrotzki W. High strain torsion of a TiAl-based alloy. Mater Sci Eng A 2008;483-484:512–6.

[177] Ivanisenko Y, Skrotzki W, Chulist R, Lippmann T, Yang K, Kurmanaeva L, et al. Information on deformation mechanisms in nanocrystalline Pd–10% Au inferred from texture analysis. J Mater Sci 2010;45:4571–7.

[178] Busquet M, Descartes S, Berthier Y. Formation conditions of mechanically modified superficial structures for two steels. Tribol Int 2009;42:1730–43.

[179] Molotnikov A. Application of Strain Gradient Plasticity Modelling to High Pressure Torsion. Mater Sci Forum 2008;584-586:1051–6.

[180] Kratochvíl J. Mechanism of Grain Refinement Induced by Severe Plastic Deformation. Mater Sci Forum 2010;667-669:617–22.

[181] Kratochvíl J, Rr Ω L. Crystal Plasticity Treated as a Quasi-Static Material Flow through Adjustable Crystal Lattice Crystal Plasticity Treated as a Quasi-Static Material Flow . . . Acta Phys Pol A 2012;122:482–5.

[182] Taylor GI. Plastic strain in metals. J Inst Met 1938;62:307–24.

[183] Van der Giessen E, Neale KW. Analysis of the inverse Swift effect using a rate-sensitive polycrystal model. Comput Methods Appl Mech Eng 1993;103:291–313.

[184] Lin G, Havner KS. A comparative study of hardening theories in torsion using the taylor polycrystal model 1996;12:695–718.

[185] Wu PD, Neale IKWI, Giessen E Van Der. SIMULATION OF THE BEHAVIOUR OF FCC POLYCRYSTALS DURING REVERSED TORSION. Int J Plast 1997;12:1199–219.

[186] Graham S, Stock SR, Ferney VC, Graham S, McDowell DL. Application of the Taylor Polycrystal Plasticity model to Complex Deformation Experiments. J Eng Mater Technol 1998;120:197–205.

[187] Kopacz I, Tóth LS, Zehetbauer MJ, Stüwe HP. Large-strain hardening curves corrected for texture development. Model Simul Mater Sci Eng 1999;7:875–9.

[188] Böhlke T, Bertram A, Krempl E. Modeling of deformation induced anisotropy in free-end torsion. Int J Plast 2003;19:1867–84.

[189] Qods F, Tóth LS, Van Houtte P. Modeling of Length Changes and Textures during Free End Torsion of Cylindrical Bars. Mater Sci Forum 2005;495-497:1609–14.

[190] Duchêne L, El Houdaigui F, Habraken AM. Length changes and texture prediction during free end torsion test of copper bars with FEM and remeshing techniques. Int J Plast 2007;23:1417–38.

[191] Böhlke T, Glüge R, Klöden B, Skrotzki W, Bertram A. Finite element simulation of texture evolution and Swift effect in NiAl under torsion. Model Simul Mater Sci Eng 2007;15:619–37.

[192] Klöden B, Oertel C-G, Skrotzki W, Rybacki E. Texture Formation and Swift Effect in High Strain Torsion of NiAl. J Eng Mater Technol 2009;131:011102.

[193] Beausir B, Tóth LS, Qods F, Neale KW. Texture and Mechanical Behavior of Magnesium During Free-End Torsion. J Eng Mater Technol 2009;131:011108.

[194] Wang H, Wu Y, Wu PD, Neale KW. Numerical Analysis of Large Strain Simple Shear and Fixed-End Torsion of HCP Polycrystals. CMC 2010;503:1–30.

[195] Taylor GI. The Mechanism of Plastic Deformation of Crystals. Part I. Theoretical. Proc R Soc A Math Phys Eng Sci 1934;145:362–87.

[196] Taylor GI. The Mechanism of Plastic Deformation of Crystals. Part II. Comparison with Observations. Proc R Soc A Math Phys Eng Sci 1934;145:388–404.

[197] Khan AS, Liu J, Yoon JW, Nambori R. Strain rate effect of high purity aluminum single crystals: Experiments and simulations. Int J Plast 2015;67:39–52.

[198] Prakash a., Weygand SM, Riedel H. Modeling the evolution of texture and grain shape in Mg alloy AZ31 using the crystal plasticity finite element method. Comput Mater Sci 2009;45:744–50.

[199] Roters F, Eisenlohr P, Hantcherli L, Tjahjanto DD, Bieler TR, Raabe D. Overview of constitutive laws, kinematics, homogenization and multiscale methods in crystal plasticity finite-element modeling: Theory, experiments, applications. Acta Mater 2010;58:1152–211.

[200] Izadbakhsh A, Inal K, Mishra RK. Crystal plasticity based finite element modelling of large strain deformation in AM30 magnesium alloy. Model Simul Mater Sci Eng 2012;20:035016.

[201] Diard O, Leclercq S, Rousselier G, Cailletaud G. Evaluation of finite element based analysis of 3D multicrystalline aggregates plasticity. Int J Plast 2005;21:691–722.

[202] Kalidindi R. INCORPORATION OF DEFORMATION TWINNING IN MODELS 1998;46.

[203] Abdolvand H, Daymond MR, Mareau C. Incorporation of twinning into a crystal plasticity finite element model: Evolution of lattice strains and texture in Zircaloy-2. Int J Plast 2011;27:1721–38.

[204] Peirce D, Asaro RJ, Needleman a. AN ANALYSIS OF NONUNIFORM AND LOCALIZED DEFORMATION. Acta Metall 1982;30:1087–119.

[205] Britain G, Press P, Division A. NONUNIFORM DEFORMATIONS IN POLYCRYSTALS AND ASPECTS OF THE VALIDITY OF 1989;37.

[206] Becker R. ANALYSIS OF TEXTURE EVOLUTION IN CHANNEL DIE COMPRESSION-I. EFFECTS OF GRAIN INTERACTION. Acta Metall 1991;39:1211–30.

[207] Search H, Journals C, Contact A, Iopscience M, Simul M, Address IP. Large strain behaviour of aluminium sheets subjected to in-plane simple shear n.d.;237.

[208] Neale KW, Inal K, Wu PD. Effects of texture gradients and strain paths on localization phenomena in polycrystals. Int J Mech Sci 2003;45:1671–86.

[209] Inal K, Simha HM, Mishra RK. Numerical Modeling of Second-Phase Particle Effects on Localized Deformation. J Eng Mater Technol 2008;130:021003.

[210] Wu PD, Huang Y, Lloyd DJ. Studying grain fragmentation in ECAE by simulating simple shear. Scr Mater 2006;54:2107–12.

[211] Li S, Kalidindi SR, Beyerlein IJ. A crystal plasticity finite element analysis of texture evolution in equal channel angular extrusion. Mater Sci Eng A 2005;410-411:207–12.

[212] Li S, Donohue BR, Kalidindi SR. A crystal plasticity finite element analysis of cross-grain deformation heterogeneity in equal channel angular extrusion and its implications for texture evolution. Mater Sci Eng A 2008;480:17–23.

[213] Kalidindi SR, Donohue BR, Li S. Modeling texture evolution in equal channel angular extrusion using crystal plasticity finite element models. Int J Plast 2009;25:768–79.

[214] Deng GY, Lu C, Tieu a. K, Su LH, Huynh NN, Liu XH. Crystal plasticity investigation of friction effect on texture evolution of Al single crystal during ECAP. J Mater Sci 2010;45:4711–7.

[215] Lu C, Deng GY, Tieu a. K, Su LH, Zhu HT, Liu XH. Crystal plasticity modeling of texture evolution and heterogeneity in equal channel angular pressing of aluminum single crystal. Acta Mater 2011;59:3581–92.

[216] Deng GY, Lu C, Su LH, Liu XH, Tieu a. K. Modeling texture evolution during ECAP of copper single crystal by crystal plasticity FEM. Mater Sci Eng A 2012;534:68–74.

[217] Li S, Sun F, Li H. Observation and modeling of the through-thickness texture gradient in commercial-purity aluminum sheets processed by accumulative roll-bonding. Acta Mater 2010;58:1317–31.

[218] Ardeljana M, Beyerleinb IJ, Knezevica M. A dislocation density based crystal plasticity finite element model: Application to a two-phase polycrystalline HCP/BCC composites. J Mech Phys Solids 2014;66:16–31.

[219] Ardeljan M, Knezevic M, Nizolek T, Beyerlein IJ, Zheng SJ, Carpenter JS, et al. A multi-scale model for texture development in Zr/Nb nanolayered composites processed by accumulative roll bonding. IOP Conf Ser Mater Sci Eng 2014;63:012170.

[220] Abaqus Analysis User's Manual. Abaqus 6.9 Documentation n.d.

[221] Dieter GE. Mechanical metallurgy. McGraw-Hill; 1976.

[222] Tabor D. The hardness of metals. Oxford University Press, Oxford; 2000.

[223] Hill R. GENERALIZED RELATIONS FOR INCREMENTAL DEFORMATION OF METAL CRYSTALS. J Eng Mater Technol 1966;14:95–102.

[224] Asaro RJ. Crystal Plasticity. J Appl Phys 1983;50:921–34.

[225] Asaro RJ, J. R. Rice. STRAIN LOCALIZATION IN DUCTILE SINGLE CRYSTALS. J Mech Phys Solids 1977;25:309–38.

[226] Roters F, Wang Y, Kuo J-C, Raabe D. Comparison of Single Crystal Simple Shear Deformation Experiments with Crystal Plasticity Finite Element Simulations. Adv Eng Mater 2004;6:653–6.

[227] Zaafarani N, Raabe D, Singh RN, Roters F, Zaefferer S. Three-dimensional investigation of the texture and microstructure below a nanoindent in a Cu single crystal using 3D EBSD and crystal plasticity finite element simulations. Acta Mater 2006;54:1863–76.

[228] Raabe D, Ma D, Roters F. Effects of initial orientation, sample geometry and friction on anisotropy and crystallographic orientation changes in single crystal microcompression deformation: A crystal plasticity finite element study. Acta Mater 2007;55:4567–83.

[229] Zaafarani N, Raabe D, Roters F, Zaefferer S. On the origin of deformation-induced rotation patterns below nanoindents. Acta Mater 2008;56:31–42.

[230] Si LY, Lu C, Huynh NN, Tieu a. K, Liu XH. Simulation of rolling behaviour of cubic oriented al single crystal with crystal plasticity FEM. J Mater Process Technol 2008;201:79–84.

[231] Huynh NN, Lu C, Si L, Tieu K. A study of microstructural evolution around crack tip using crystal plasticity finite-element method. Proc Inst Mech Eng Part J J Eng Tribol 2008;222:183–92.

[232] Peirce D, Asaro RJ, Needleman A. AN ANALYSIS OF NONUNIFORM AND LOCALIZED DEFORMATIONcin ductile single crystals. Acta Metall 1982;30:1087–119.

[233] Asaro RJ, Needleman A. TEXTURE DEVELOPMENT AND STRAIN HARDENING IN RATE DEPENDENT POLYCRYSTALS. Acta Mech Solida Sin 1985;33:923–53.

[234] Hutchinson JW. Bounds and self-consistence estimate for creep of polycrystalline materials. Proc R Soc Lond A 1976;348:101–27.

[235] Peirce D, Asaro RJ, Needleman A, Park A. OVERVIEW MATERIAL RATE DEPENDENCE AND LOCALIZED DEFORMATION IN CRYSTALLINE SOLIDS. Acta Metall 1983;31:1951–76.

[236] Toth LS. Effect of rate sensitivity on the stability of torsion textures 1988;36:3077–91.

[237] Yoon JH, Huh H, Lee YS. Finite Element Analysis of Polycrystalline Deformation with the Rate-dependent Crystal Plasticity. AIP Conf Proc 2007;908:1325–30.

[238] Choi S-H, Kim DH, Lee HW, Shin EJ. Simulation of texture evolution and macroscopic properties in Mg alloys using the crystal plasticity finite element method. Mater Sci Eng A 2010;527:1151–9.

[239] Nakamachi E. CRYSTALLOGRAPHIC HOMOGENIZATION FINITE ELEMENT METHOD AND ITS APPLICATION ON SIMULATION OF EVOLUTION OF PLASTIC DEFORMATION INDUCED TEXTURE. Acta Mech Solida Sin 2010;23:36–48.

[240] Rehrl C, Völker B, Kleber S, Antretter T, Pippan R. Crystal orientation changes: A comparison between a crystal plasticity finite element study and experimental results. Acta Mater 2012;60:2379–86.

[241] Hama T, Takuda H. Crystal plasticity finite-element simulation of work-hardening behavior in a magnesium alloy sheet under biaxial tension. Comput Mater Sci 2012;51:156–64.

[242] Wu T-Y, Bassani JL, Laird C. Latent Hardening in Single Crystals I. Theory and Experiments. Proc R Soc A Math Phys Eng Sci 1991;435:1–19.

[243] Hutchinson JW. Elastic-plastic behavior of polycrystalline metals and composites.pdf. Proc R Soc Lond A 1970;319:247–72.

[244] Bassani JL, Wu T-Y. Latent Hardening in Single Crystals II. Analytical Characterization and Predictions. Proc R Soc A Math Phys Eng Sci 1991;435:21–41.

[245] Kumar A V, Yang C. Study of work hardening models for single crystals using three dimensional finite element analysis. Int J Plast 1999;15:737–54.

[246] Siddiq A, Schmauder S. CRYSTAL PLASTICITY PARAMETER IDENTIFICATION PROCEDURE FOR SINGLE CRYSTALLINE MATERIAL DURING DEFORMATION. J Comput Allpied Mech 2006;7:1–15.

[247] Abaqus User Subroutines Reference Manual. Abaqus 6.9 Documentation n.d.

[248] Huang Y. A User-material subroutine incorporating single crystal plasticity in the ABAQUS finite element program. Mech report 178, Division of Engineering and Applied Sciences, Harvard University 1991.

[249] MOOSBRUGGER JC. CONTINUUM SLIP VISCOPLASTICITY WITH THE HAASEN CONSTITUTIVE MODEL : APPLICATION TO CdTe SINGLE CRYSTAL INELASTICITY. Int J Plast 1995;11:799–826.

[250] Zhou D, Moosbrugger JC, Morrison DJ. Finite element simulation of PSB macroband nucleation and propagation in single crystal nickel cycled at low plastic strain amplitudes. Int J Plast 2006;22:1336–66.

[251] Freund LB, Freund SS. Thin Film Materials. Cambridge University Press, Cambridge; 2003.

[252] Zhang X, Shang F. A continuum model for intermittent deformation of single crystal micropillars. Int J Solids Struct 2014;51:1859–71.

[253] Reuber C, Eisenlohr P, Roters F, Raabe D. Dislocation density distribution around an indent in single-crystalline nickel: Comparing nonlocal crystal plasticity finite-element predictions with experiments. Acta Mater 2014;71:333–48.

[254] Keller C, Habraken a. M, Duchene L. Finite element investigation of size effects on the mechanical behavior of nickel single crystals. Mater Sci Eng A 2012;550:342–9.

[255] Keller C, Hug E, Habraken a. M, Duchene L. Finite element analysis of the free surface effects on the mechanical behavior of thin nickel polycrystals. Int J Plast 2012;29:155–72.

[256] Franciosi P, Berveiller M, Zaoui A, Paris-nord U. LATENT HARDENING IN COPPER AND ALUMINIUM. Acta Metall 1980;28:273–83.

[257] Liu Q, Maurice C, Driver J, Hansen N. Heterogeneous Microstructures and Microtextures in Cube- Oriented Al Crystals after Channel Die Compression 1998;29.

[258] Akef a., Driver JH. Orientation splitting of cube-oriented face-centred cubic crystals in plane strain compression. Mater Sci Eng A 1991;132:245–55.

[259] SHAMRAY VF, BABAREKO AA, SETJUCOV OA. INFLUENCE OF THE TEXTURE ON MECHANICAL PROPERTIES OF THE Al-Li ALLOY 1441. Textures Microstruct 1999;32:341–53.

[260] Kim W., Hong S., Kim Y., Min S., Jeong H., Lee J. Texture development and its effect on mechanical properties of an AZ61 Mg alloy fabricated by equal channel angular pressing. Acta Mater 2003;51:3293–307.

[261] Yuan W, Mishra RS. Grain size and texture effects on deformation behavior of AZ31 magnesium alloy. Mater Sci Eng A 2012;558:716–24.

[262] Mao P, Liu Z, Wang C. Texture effect on high strain rates tension and compression deformation behavior of extruded AM30 alloy. Mater Sci Eng A 2012;539:13–21.

[263] Murty SVSN, Nayan N, Kumar P, Narayanan PR, Sharma SC, George KM. Microstructure–texture–mechanical properties relationship in multi-pass warm rolled Ti–6Al–4V Alloy. Mater Sci Eng A 2014;589:174–81.

[264] Wei P, Lu C, Tieu K, Deng G, Wang H, Kong N. Finite Element Analysis of High Pressure Torsion. Steel Res Int 2013;84:1246–51.

[265] Qailletaud G. Single Crystal Modeling for Structural Calculations : Part 2 — Finite Element Implementation 1991;113:171–82.

[266] S.Quilici, S.Forest GG. On size effects in torsion of multi and polycrystalline specimens.pdf 1998:325–32.

[267] Nouailhas D, Cailletaud G. Tension-torsion behavior of single-crystal superalloys: Experiment and finite element analysis. Int J Plast 1995;1:451–70.

[268] Liu Q, Hansen N. DISLOCATION COLD-ROLLED FORMATION Al SINGLE IN A 1997;45.

[269] Lu C. Crystal plasticity finite element method modelling of indentation size effect. Int J Solids Struct 2015.

[270] Quey R, Dawson PR, Driver JH. Grain orientation fragmentation in hot-deformed aluminium: Experiment and simulation. J Mech Phys Solids 2012;60:509–24.

[271] ROSE W, STUWE H. THE INFLUENCE OF TEXTURE ON THE CHANGE IN LENGTH IN TORSION TESTS. Z Met 1968;59:396–9.

[272] Th LST, Jonas JJ. Analytic Prediction of Texture and Length Changes During. Textures Microstruct 1989;10:195–209.

[273] B.Bay, Hansen N, Hughes DA, D.KUHLMANN-WILSDORP. EVOLUTION OF F . C . C . D E F O R M A T I O N STRUCTURES IN POLYSLIP. Acta Metall 1992;40:205–19.

[274] Wetscher F, Pippan R. Cyclic high-pressure torsion of nickel and Armco iron. Philos Mag 2006;86:5867–83.

[275] Klimanek P, Klemm V, Romanov a. E, Seefeldt M. Disclinations in Plastically Deformed Metallic Materials. Adv Eng Mater 2001;3:877.

[276] Romanov AE, Kolesnikova AL. Application of disclination concept to solid structures. Prog Mater Sci 2009;54:740–69.

[277] Sachtleber M, Zhao Z, Raabe D. Experimental investigation of plastic grain interaction. Mater Sci Eng A 2002;336:81–7.

[278] Tatschl a, Kolednik O. On the experimental characterization of crystal plasticity in polycrystals. Mater Sci Eng A 2003;342:152–68.

[279] Petryk H, Stupkiewicz S. A quantitative model of grain refinement and strain hardening during severe plastic deformation. Mater Sci Eng A 2007;444:214–9.

[280] Li S. A crystal plasticity-based explanation for the dependencies of grain refinement on processing route and die angle in equal channel angular extrusion. Scr Mater 2009;60:706–9.

[281] Kowalczyk-Gajewska K, Stupkiewicz S, Frydrych K, Petryk H. Modelling of Texture Evolution and Grain Refinement on Complex SPD Paths. IOP Conf Ser Mater Sci Eng 2014;63:012040.

[282] Bachmann F, Hielscher R, Schaeben H. Grain detection from 2d and 3d EBSD data--specification of the MTEX algorithm. Ultramicroscopy 2011;111:1720–33.

[283] Montheillet F, Gilormini P, Jonas JJ. Relation between axial stresses and texture development during torsion testing: A simplified theory. Acta Metall 1985;33:705–17.

[284] Raabe D, Zhao Z, Park S-J, Roters F. Theory of orientation gradients in plastically strained crystals. Acta Mater 2002;50:421–40.

[285] Utyashev FZ, Raab GI. THE MODEL OF STRUCTURE REFINEMENT IN METALS AT LARGE DEFORMATIONS AND FACTORS EFFECTING GRAIN SIZES 2006;11.

[286] Poulsen HF, Margulies L, Schmidt S, Winther G. Lattice rotations of individual bulk grains. Part I: 3D X-ray characterization. Acta Mater 2003;51:3821–30.

[287] Winther G, Margulies L, Schmidt S, Poulsen HF. Lattice rotations of individual bulk grains Part II: Correlation with initial orientation and model comparison. Acta Mater 2004;52:2863–72.

[288] Zhang Y, Wilson L. Lattice rotation in polycrystalline aggregates and single crystals with one slip system 1997;19.